Three-dimensional modelling of tidal stream energy extraction for impact assessment

Thesis submitted in accordance with the requirements of
the University of Liverpool for the degree of Doctor in Philosophy
by
Xiaorong Li

September 2016

Abstract

This research is themed around development of a tidal turbine simulation platform based on a three-dimensional oceanographic numerical modelling environment; more specifically, parameterization of effects of tidal turbine on flow current, turbulence, waves and sediment transport. In this context, the author adopts concepts in the current module, the turbulent module, the wave module and the sediment transport module of Finite-Volume, primitive equation Community Ocean Model (FVCOM) to simulate the effects of tidal turbines.

The retarding force concept is employed in the current module, working as an additional body force exerted on the water to simulate the turbine induced water deceleration. Three terms are added into the MY-2.5 turbulence closure to model turbine related turbulence generation, dissipation and turbulence length-scale interference. The built-in feature 'OBSTACLE' of the wave module is used to simulate the reduction of wave height caused by the turbine. The enhanced sediment suspension due to the turbine in motion is represented by an additional bottom shear stress term, entraining an extra portion of sediment particles from the bed into the water. Due to the fact that the bedload sediment transport module of FVCOM is not fully developed, it is not considered in this research; development of such a module is beyond the scope of this project.

Coefficients of the turbine simulation terms are calibrated based on experimental data collected in the 'Total Environment Simulator laboratory flume' at the University of Hull, in which a prototype experiment was conducted. Small scale simulations carried out using ANSYS FLUENT also provided complementary calibration data. An idealized water channel model with mesh resolution fined down to the size of the simulated turbine is built to carry out the coefficient calibration. In general, the developed turbine simulation platform is capable of predicting reliable flow velocity, turbulent level, wave height and suspended sediment transport in the far wake region of the turbine, given proper values assigned to the relating coefficients. In addition, preliminary sensitivity tests are carried out to investigate the impact of these coefficients to the model's overall prediction to reveal the model's application range.

Upon the satisfactory choices of the coefficients, the platform is applied to a 15m scale idealized single turbine case as well as a regional scale case based on the realistic

hydrodynamics off the Anglesey coast, north-west of Wales. A series of single turbine tests are carried out with and without the turbine implementations, i.e. the coefficients represent turbine effects being switched on and off, in order to reveal the differences between the baseline case (no turbine) and case with turbine effects. Under realistic natural tidal and wave conditions, the Anglesey coast case showcases impact from a large scale turbine farm to both local and regional processes.

Contents

List of Figures

List of Tables

Acknowledgement

I would like to express my great appreciation and gratitude to o the following persons who have contributed in making this work possible.

Dr. Ming Li for his continued guidance, advice and support throughout the project.
Prof. Peter Thorne for his ideas and advice.
Prof. Judith Wolf for providing model driving data, patient discussion and Fortran code for Lagrangian particle tracking.
Dr. Stuart McLelland, **Dr. Laurent Amoudry** and **Miss Laura-Beth Jordan** for providing experimental data.
Mr. QingYang Song for advising on wave modelling in FVCOM.
Mr. Sufian Sufian for advising on VBM settings.
Mr. Cliff Addison and **Mr. Dave Love** for their HPC support.
Prof. Richard Simons and **Dr. Francisco Alejandro Diaz De la O** for their opinions and advice on improving the quality of this thesis.

This work has been aided by the use of N8 HPC access. I would also like to acknowledge the use of data made available by the National Oceanography Centre (NOC), British Oceanographic Data Centre (BODC), the European Centre for Medium-Range Weather Forecasts (ECMWF) and the Centre for Environment, Fisheries and Aquaculture Science (Cefas).

I would like to thank my colleagues and friends for their support in numerous ways.

Great thanks to my family for being supportive and caring.

I would also like to give considerable thanks to China Scholarship Council (CSC) for providing my research studentship.

Chapter 1

Introduction

1.1 Background

As a response to the natural energy resource shortage and worldwide climate change, due in part to burning of fossil fuels to fulfil ever growing energy requirements, clean and renewable alternatives have been gaining significant attention. For example, the UK is aiming for 15% of the country's total energy production to be produced from renewable resources by 2020 [13]. In this regard, kinetic energy carried by ocean flows, known as 'tidal stream energy', is considered to be a very promising avenue of investigation, particularly due to its consistent predictability and availability. At the time of writing, 119 Tidal Energy Converter (TEC) concepts, developed by different companies, are listed on the European Marine Energy Centre (EMEC)'s website[1], with full-scale tests of such devices currently underway in coastal waters around the world. The Roosevelt Island Tidal Energy (RITE) project, one of the leaders in this field, began the process of commercialization of tidal stream energy in 2012. In the UK waters, the natural large tidal range means it is particularly advantageous to develop tidal stream schemes. The Carbon Trust believes that practical and economic sources of tidal power could meet 5.5% of UK's current electricity demand (this amounts to 21TWh per year based on 381TWh of total electricity generated in the UK in 2010) [118]. Although still in its infancy in terms of development, 1GW installation capacity has already been permitted in recent years. In other countries, like in China, despite having generally lower tidal ranges, a number of hot spots with strong tidal currents also provide considerable potential of energy sources that can be harvested through the tidal stream devices.

However, the present understanding on impacts from such device on the ocean environment is still at its early stage, most of it is obtained through laboratory experiments and numerical simulations. Observational data collected from a site experiment through which the short-term and long-term impacts can be directly analysed is not yet available, despite the number of on-site projects undergoing around the world. Laboratory experiments and Computational Fluid Dynamics (CFD) simulations are often used to

[1] http://www.emec.org.uk/marine-energy/tidal-developers/

investigate the potential performance and related impacts from any particular turbine design. However, they are limited in terms of experiment scale, flow complexity and accuracy of device representation method. Consequently, they often concentrate on small scale and near field studies, and most are carried out in the context of steady flow with very simple flow structure which is rarely observed in coastal waters. In addition, these studies focus largely on single turbine, rather than large scale arrays which are considered to be a more realistic operating scheme. On the other hand, large scale oceanographic numerical models are able to simulate a desired water region with fairly realistic ocean dynamics outputs which are particularly useful in predicting impacts from the devices on the ocean circulation, wave propagation, sedimentation and hence long term morphological evolution at the adjacent coastal region. But it is very challenging to realistically represent turbine devices in such models, mainly due to the mesh resolution usually used in these models. Currently available turbine modelling in oceanographic numerical models employs far too simple representations without systematic calibration. Therefore, there is a clear lack of suitable modelling systems which are able to represent a turbine array, operating in realistic ocean environment; this leads to the aforementioned knowledge gap in understanding the impacts from these devices to the surroundings. The present study aims to fill in this gap and develop a new cross-scale modelling system to improve current knowledge of such crucial process that could affect our society in the long term.

The large scale tidal turbine simulation system developed herein, as well as the revealed impacts of tidal turbine farms on hydrodynamic and sediment transport processes, are expected to be interesting and useful for engineers, governmental departments, institutes and companies that focus on the environmental impacts of tidal turbine systems.

1.2 Aims and objectives of the study

The main aim of this project is to develop a three-dimensional numerical representation of a large scale array of tidal stream devices that is often the envisaged optimal operation scheme into the future in a three-dimensional oceanographic numerical environment. This is carried out based on understandings obtained through analyzing experimental and detailed CFD computational results. Finally, the newly developed three-dimensional oceanographic model is applied to a coastal site to investigate the effects of large scale arrays on their surrounding marine environment.

Objectives:

1. Experimental data analysis

   Analyse the most recent available experimental laboratory data to formulate a

comprehensive dataset for model calibration.

2. CFD modelling of single turbine operation

   Develop CFD models for single turbine operation in combined wave-current condition to provide complementary data and extra parameterisation for ocean model calibration.

3. Tidal stream device parameterisation in a three-dimensional large-scale wave-current-sediment fully coupled oceanographic model

   Parameterize tidal stream devices into 'engineering' parameters that can be used in oceanographic models and implement them in one of the available open source packages — Finite Volume Coastal Ocean Model (FVCOM). Systematic calibration of the turbine modelling platform will be carried out.

4. Application of the model

   Investigate impacts from large scale arrays of tidal stream devices on ocean circulation at offshore and impacts on near shore hydrodynamics, wave dynamics and sediment transport using the developed turbine modelling platform.

1.3 Structure of the thesis

The overall structure of this thesis is given as follows:

Chapter 2 provides relevant basic information about tidal stream energy devices, coastal processes upon which this research focuses, discusses possible impacts of tidal stream energy devices on coastal processes, recalls device representation methods used in currently available large-scale research through literature review and points out questions this research aims to answer.

Chapter 3 gives details of the three-dimensional numerical model; where the original modules of current, turbulence, waves and sediment transport and the numerical representation of tidal stream energy devices in each of these modules are introduced in detail.

Chapter 4 provides information about the laboratory environment in which the experimental measurements were taken as well as the settings of CFD simulations. Coefficients related to the numerical representation of tidal stream energy devices in FVCOM are calibrated in this chapter based on experimental data and CFD calculated results. The model calibration work is carried out in an idealized water channel model built within FVCOM.

Chapter 5 answers the scale-up question: how the tidal stream energy device related parameters in FVCOM should vary according to the physical scale of the model. Sensitivity of the model to the variation of the turbine related coefficients is also discussed in this chapter.

Chapter 6 records benchmarking single turbine tests discussing the significance of the device simulation related coefficients. This chapter also focuses on the application of the model in the N-W Welsh coastal area. Calibration of the model and effects of the tidal stream energy device array on current, turbulence, waves, bottom shear stress and suspended sediment transport are presented in this chapter.

Chapter 7 gives the concluding remarks of the overall research outcomes and highlights recommendations for future research.

Chapter 2

Literature review

2.1 Introduction

After giving a list of major tidal turbine designs, this literature review focuses on three major topics: physical processes in coastal regions, impacts caused by tidal turbines in both the near and far fields and tidal turbine modelling approaches developed so far. Based on the review, the rationale of the present research is discussed in the end.

2.2 Tidal stream device types

This research aims to study the impacts of devices that are designed particularly to exploit tidal stream energy, i.e. the kinetic energy carried by the sea currents. So far, six major types of such device are widely recognized: (a) Horizontal Axis Tidal Turbine (HATT), (b) Vertical Axis Tidal Turbine (VATT), (c) Oscillating hydrofoil, (d) Enclosed tips, (e) Archimedes screw and (f) Tidal kite. Figure 2.1 gives one example of each of the device types. Detailed introduction of these devices can be found on EMEC's website[1], with animated videos illustrating how they interact with tidal currents.

It should be noted that they influence the adjacent hydrodynamics and sediment transport in very different ways. For example, the swiping area of a HATT is perpendicular to the coming flow. It uses lift force of the passing flow to generate torque. A 'w' shaped x-direction velocity profile can be observed closely behind the turbine. However, blades of a VATT are parallel to the turbine axis which is perpendicular to the seabed and are pushed by the flow to rotate around the vertical axis. The swiping area of a VATT is therefore a cylinder which exerts an influence on the passing flow rate identically along its height. The scenario may be even more different when the other four types of tidal stream devices are considered. So far, among these different schemes, the HATT design has been widely recognised as the most viable and many developments have been made based on this concept. Therefore, this research focuses on HATT devices.

[1] http://www.emec.org.uk/marine-energy/tidal-devices/

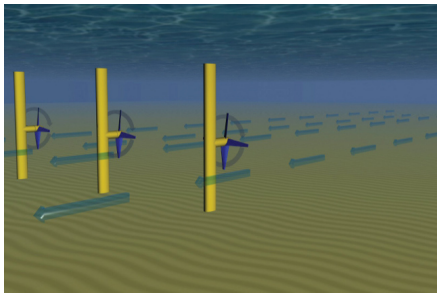

(a) HATT

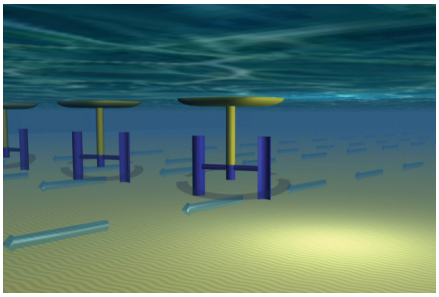

(b) VATT

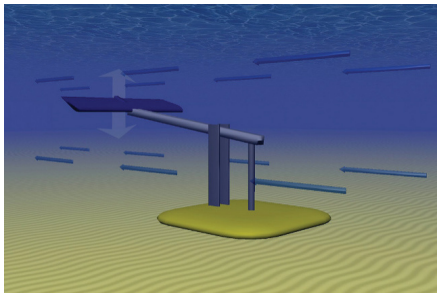

(c) Oscillating hydrofoil

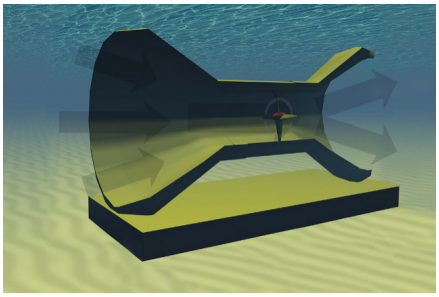

(d) Enclosed tips

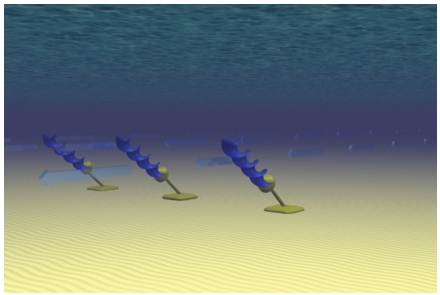

(e) Archimedes screw

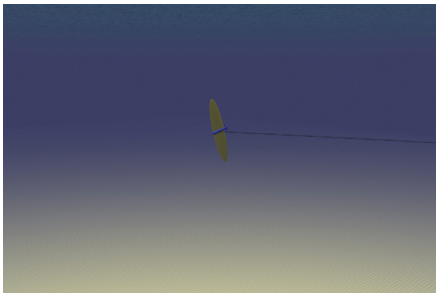

(f) Tidal kite

Figure 2.1: Tidal stream device types (Source: AQUARET)

2.3 Coastal processes

2.3.1 Current

Current in the ocean is the general movement of seawater. It can be generated by a number of sources such as tides, waves, winds and pressure gradients, among which tidal current is the main focus in this work. In a numerical model, a typical tidal flow includes a logarithmic profile across the depth at a given tidal phase with the near-bed boundary layer described via a prescribed bed roughness. Under the presence of waves, the logarithmic profile is bound to be changed and the changes are dependent on the propagation direction of the waves in relation to the carrying current. This is discussed in more detail in Section 2.3.3. In coastal areas, waves often bring obvious cross-shore and long-shore velocities. The cross-shore flow (undertow) distribution typically has an onshore flow near the surface and a returning offshore flow close to the bed. The long-shore flow, however, is more likely to have a typical tidal current profile with a logarithmic distribution. Hence, the overall flow in a coastal area is often found to have a three-dimensional structure.

In terms of flow speed at potential tidal stream energy extraction sites, recent surveys suggest that the flow speed at such sites is often high (>1.0m/s) most of the time to be suitable for energy generation. For example, current speed at one of the well-known prospective sites —the Pentland Firth —is reported to exceed 1m/s for 80% of each tidal cycle [105]. Also, a tidal current power plant is planned at the eastern shoreline of Taiwan where the strong Kuroshio current passes by and leaves a characteristic speed of 1.0-1.5m/s [56].

2.3.2 Waves

Surface waves can be classified into a variety of types according to their period or wave length. From the longest to the shortest in terms of wave length, trans-tidal waves, tides, storm surges, tsunamis, seiches, infra-gravity waves, wind-generated surface gravity waves and capillary waves can be observed in the ocean [54]. As far as a coastal region is concerned, short period surface waves largely generated by wind are of the greatest importance. Wind-generated surface waves are characterized by their period of 0.25-30s and corresponding wave length of 0.1-1500m [54].

Waves can normally be defined by amplitude, frequency and phase. In nature, definitions of wave characteristics are given to describe a single wave in detail. For example, wave height or amplitude is defined as the vertical distance between the highest and lowest surface elevation in a wave. In oceanographic and coastal modelling, even though the definitions still represent the same physical meanings, waves are described statistically using their power spectrum. A stationary wave spectrum characterises frequency dependent wave power during a certain period, and makes it possible to

describe the ocean surface composed of random waves. Under the spectrum method, significant wave height, peak period and dominant angle are the most commonly used terms.

Waves in the nature or in the spectrum of a numerical model undergo transformation constantly during the propagation process due to reasons such as the change of water depth and the encounter of obstacles which happen very often in coastal regions. The typical resulting phenomena are wave shoaling, wave breaking, reflection, refraction and diffraction. These processes are commonly considered in the state-of-the-art wave models.

Tidal turbines, even though are submerged in the water (sometimes quite deep), interfere with wave transmission. The aforementioned behaviour of the flow velocity field under the presence of turbines either facilitate or partially block the transmission of the waves, depending on the wave propagation direction, leading to changes in wave height, wave period and wave direction [113].

2.3.3 Wave-current interaction

Current and waves are not independent processes in the ocean or coastal waters. They interact with and exert impacts on each other[16, 90, 134]. Tidal stream turbines are supposed to be installed at sites with strong tidal flows. Likely sites are commonly exposed to sea waves. Studies, both experimental [60, 61, 63, 83, 122] and numerical [18, 62, 87, 121], on wave-current interaction revealed that the non-linear effects between the aforementioned two components have significant influence on the vertical profile of the current. For example, it was concluded in [87] that in the presence of following waves, the current velocity between the wave crest and trough was increased while it was reduced below the wave trough. And the significance of the changes is related to the wave height. Scenarios of opposing and perpendicular waves are also discussed in detail in [87]. A wave-induced streaming layer in the direction of wave propagation near the bottom was also pointed out by [18] and was believed to have significant influence on sediment transport. An increase of 40% in sediment transport rate, which was believed to be caused by the wave-induced streaming, was observed in [18] under propagating waves.

Realizing the changes currents and waves may impose on each other, [49] and [50] assessed wave energy resources at the north-west European sea and tidal energy potential along the Anglesey coast numerically under both wave-only/current-only and wave-current coupled scenarios respectively, aiming to find out the magnitude of significance of these two processes on each other in terms of energy potential prediction. It was concluded that both impacts of tides on wave energy estimation and consequences of waves on tidal energy evaluation are significant. The difference in terms of percentage of the energy calculated under the wave-only or current-only scenario can be over 10%

and 15% respectively.

It is, therefore, considered as worthwhile to parameterize tidal stream devices to predict their impacts on the surrounding environment in a current-wave coupled numerical modelling system.

2.3.4 Sediment transport

Sediment particles tend to rest on the sea bed due to gravity. When water flows over the surface of sediment, it causes two forces on sediment grains: drag force and lift force. Another force sediment particles experience in the water is buoyancy, which is an upward force exerted by the water. The balance of these forces can be expressed in a dimensionless form which is known as the Shields parameter:

$$\theta = \frac{\tau_0}{(\rho_s - \rho_0)gd} \tag{2.1}$$

where g is the acceleration due to gravity; d is the diameter of the sediment particles; ρ_s is the density of the sediment particles; ρ is the density of water and τ_0 is the shear stress experienced by the particles.

Sediment transport, in the form of bedload, which takes place just above the bed and reacts instantaneously to the local conditions [102], occurs once the shear stress reaches a threshold: the critical shear stress τ_c. This can also be expressed in terms of Shields parameter as the critical Shields parameter θ_c [111].

Another form of sediment movement is suspended transport in which sediment particles are carried by the water over large spatial and temporal scales [102]. An important term associated with suspended sediment transport is settling velocity (w_s) which depicts how fast sediment particles fall in fluids. It depends upon particle properties, such as particle size, the shape and density of the particles, as well as the viscosity and density of the fluid. Bed shear stress is another important factor that influences suspended sediment transport. Again, once it reaches a critical value, sediment particles settled on the seabed are picked up and become suspended in the water.

Turbulence induced mixing also has impacts on suspended sediment transport in terms of particle pick-up and turbulent diffusion of particles. Intuitively, as the turbulence level increases, eddies close to the bed and mixing effects of the water become stronger. Hence, the sediment particles get to be transported from the near-bed saturated layer into the water column at a faster speed. Also, three dimensionally, a high turbulent level facilitates the diffusion of particles in the water column, promoting the form of a well-mixed condition.

A functioning turbine in the water, as mentioned before, would accelerate the water close to the bed and therefore increase the bed shear stress exerted on local sediment particles. It would also largely increase the turbulent level by inducing a large velocity gradient as well as mechanical turbulence brought up by the motion of the blades.

2.4 Impacts of HATTs

Impacts from extracting energy from the tidal stream can be generalized as impacts from four main stages: transportation, installation, operation and maintenance as well as decommissioning. In this section, only the impacts incurred during the operation stage are reviewed. Impact of HATTs on the surrounding environment can be further categorized into that caused by the supporting structure and that caused by the rotating rotor which captures the energy and slows down the water leading to a wake downstream of the device. As the wake recovers, different features are displayed longitudinally along the wake from the point immediately downstream of the structure to the point where the wake is dissipated, according to which near wake and far wake are differentiated. Effects brought up by the interaction of the rotor and the passing flow are not simply limited to water velocity changes. Other physical processes, such as turbulence level, surface waves and sediment transport, may also be affected to some extent. This section, through reviewing published works, discusses possible impacts of HATTs on their neighbouring environment.

2.4.1 Impacts of the supporting structure

Rotors of a HATT are normally mounted on a supporting structure which is firmly fixed onto the sea floor (Figure 2.2). The supporting structure keeps the entire device in place and is necessary. Like all other structures or objects seated on the seabed, e.g. bridge piers, the supporting structure of a HATT alters the dynamics of the passing flow as well as that of sediment transport. However, due to the difficulty of separating the supporting structure of a HATT from the entire device during the tests, impacts of the supporting structure are rarely discussed independently either in small-scale studies, i.e. laboratory and CFD simulations, or oceanographic-scale simulations. In fact, instead of being mounted on the floor, the representative devices are usually hung in the water in many experimental studies [58, 70, 117].

The drag force exerted on the flow by the supporting structure was omitted in [37] for the reason that 'the cross-sectional area of the support structure would be very much smaller than the swept area of the turbine and thus the support structure drag force would be negligible compared to the turbine thrust'. Following the same argument and given the fact that reliable data for calibration is not currently available, the supporting structure of the device is not presented in the hydrodynamic simulations in this research.

However, supporting structures do lead to local bed scour in the near-wake field (see Section 2.4.2). [26] summarized the scouring patterns of different supporting structure geometries. [53] separated the supporting structure from the whole device and tested the local scour associated with it in terms of scour depth downstream of the turbine. The results showed that the local scour induced by the supporting structure is much

(a) SeaGen

(b) AR1500

Figure 2.2: Examples of HATTs and their supporting structures

smaller than that caused by a fully operational turbine, when a fully operational turbine could lead to a scour depth of approximately 30-35% of the rotor diameter. Therefore, the scouring effect of the supporting structure are considered in this research. The local scour caused by the supporting structure is integrated into the total turbine-related scour by modifying the bottom shear stress calculation. The same issue concerning Turbulent Kinetic Energy (TKE) computation was also pointed out in a CFD based research project, which aimed to adapt the turbulence closures for turbine simulation [106]. A similar approach was applied in [106] to compensate eddies from support structures by integrating the extra TKE into a source term added to the turbulence closure equations.

2.4.2 Near-wake field impacts

Within the near wake, research focus is put on wake recovery in terms of free-surface elevation, depth-averaged flow rate, vertical velocity profiles, TKE level, etc. a few diameters downstream of the device. Such understandings are mostly obtained through laboratory experiments and small scale CFD simulations, due to the lack of on-site observation. In fact, such laboratory and numerical investigations merit in a way that various upstream conditions can be created easily and, thus, experiments providing information concerning impacts of HATTs over a wide range of surrounding circumstances are achievable at a relatively low cost. Results of such tests can serve as useful calibration input for HATT parameterization in oceanographic scale models.

Hydrodynamics

The typical logarithmic current velocity profile is shown to be perturbed by the introduction of tidal turbines in a way that turbines slow the incoming water down, resulting in the acceleration of the surrounding water, i.e. water flows around the turbine [81]. Depending on various features of the device, e.g. dimension, blade shape, rotation speed, etc., the perturbation differs [58, 70, 80, 117].

One of the major changes an HATT causes to its passing flow is the reduction of flow

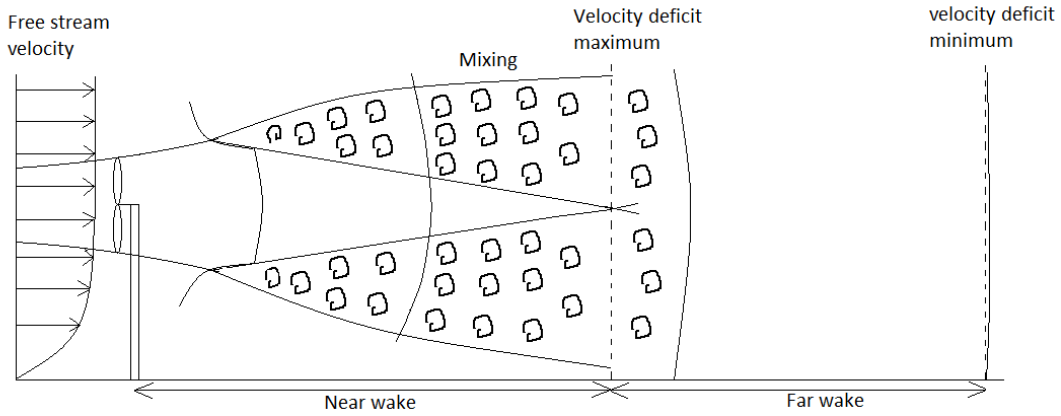

Figure 2.3: A wind turbine wake velocity profile (produced based on Figure 6 in [3])

velocity. Water at the immediate downstream region of an HATT normally moves at a lower speed than the free stream mainly due to energy loss and the blockage effect of the device. This region is commonly known as the wake. A wake can be further categorized into near wake and far wake based on the velocity gradient condition. The longitudinal limit of near wake is defined as the point at which the shear layer (Figure 2.3) reaches the centreline turbine axis [80]. [123] reported that near wake is usually observed within 2-5 rotor diameters downstream of a wind turbine. A similar extent of near wake was also observed for porous disc rotor simulators (a porous disc rotor simulator is a thin porous disc which replicates flow deceleration caused by tidal turbines) [5, 80]. However, it should be noted that the extent of near wake is very likely to be dependant on the medium and the configuration of the turbine. For instance, it was observed in [70] to be 2D (D — Diameter of the turbine) when the ambient turbulent intensity was 25% and 5D when the turbulent intensity was reduced to 8%.

Experimental and CFD work studying the evolution of free-surface elevation, and velocity structure along the depth in the near wake in detail can be found in [4, 5, 48, 58, 70, 80, 82, 114, 117, 128], among which [58, 70, 117] used scaled rotors and the others used porous disc rotor simulators.

To study the evolution of free-surface elevation and depth-averaged velocity around an energy absorption disc, [114] built a water flume model using ANSYS FLUENT [39]. The dimension of the flume was 10m (L) $\times$ 1.5m (W) $\times$ 1.0m (D). When approximately 10% of the total kinetic energy was dissipated due to the presence of the disc, a drop of free surface of 0.1m (10% of the water depth) behind the energy extraction site was observed, accompanied by an increase of water level by 0.05m (5% of the water depth) in the upstream region. The normalised depth-averaged velocity deficit peaks at 1.2% right after the disc. The changes to surface elevation and the depth-averaged velocity in the wake region gradually reduces, yet it is not fully recovered at 6D downstream of the disc.

To study the wake behaviours behind a scaled HATT, [117] conducted an experiment in a 3.7m (L) $\times$ 1.4m (W) $\times$ 0.8m (D) flume. The diameter and tip speed ratio of the model HATT were 0.5m and 6.15 respectively. The data show that along the length of the channel, a typical development of streamwise velocities behind a turbine can be found. A W-shaped velocity profile with the opening facing the right-hand side can be measured immediately downstream the turbine. The largest velocity deficit can be found at the tip of the blades. These two jets of large velocity deficit gradually merge into a single one as the wake recovers. Flow speed above and below the highest and lowest points of the turbine is increased as the water seeks to go around the turbine. In this particular case where the inlet flow rate is 1.0m/s, the flow speed is reduced to 0.35m/s at the tip of the blades and it is increased to 1.2m/s in areas beyond the tips. Velocity profiles observed from the longitudinal slice of the channel demonstrate similar characteristics. They are, however, dependent on the proximity of the turbine to the surface/bed and thus can be less symmetrical.

Turbulence characteristics

Water flow within the near wake features a high turbulent level. Apart from the background turbulence, turbines bring in extra turbulence: flow accelerates and decelerates around blades, turbulent mixing in the wake and its interaction with the free stream [80] and mechanical turbulence resulted from the rotating motion of the turbine [120]. Figure 2.4 demonstrates a swirl angle of the flow to the free stream caused by the rotation of the rotor in the near wake. The persistence of this swirl effect is believed to be weak and decays swiftly in the downstream [92]. Another phenomenon observed within the near wake region is the vortex shed from the tip of the rotor (tip vortex, see Figure 2.5). A tip vortex can persist beyond the near-wake region, especially when the ambient turbulent level is low [92]. The turbulence level of a tip vortex varies depending on the design of the blades. [107] characterized the turbulence in the wake of two HATTs with different blade designs, one with narrower blades and the other one with wider blades. It was observed that the vortex shed from the tip was significantly greater in magnitude for the wider-blade design and TKE measured downstream of the wider-blade design is twice as much as that of the narrower-blade design.

Using a scaled turbine, [117] observed W-shaped TKE profiles within a certain distance downstream of the turbine. The highest turbulence level occurs at the tips of the blades. The aforementioned mechanical turbulence, however, is generally missing in some of the laboratory and CFD studies in which porous discs are submerged as substitutes for turbines [4, 5, 6, 48, 80, 81, 82, 114]. The mechanical turbulence also tends to be omitted in oceanographic scale studies, owing to the resolution of meshes normally used in large scale oceanographic models [1, 19, 20, 30, 33, 37, 71, 91, 96, 99, 119, 136].

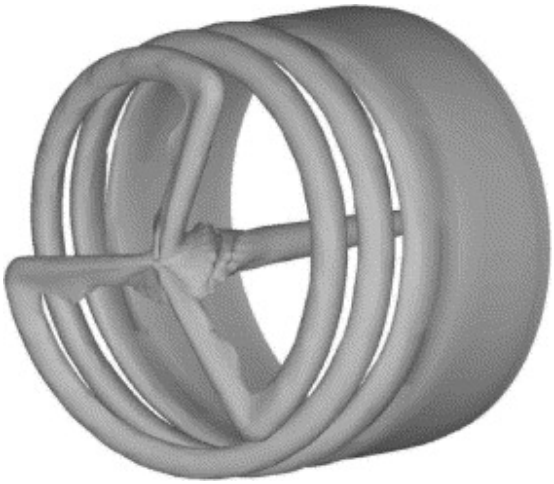

Figure 2.4: Swirling flow behind a wind turbine [110]

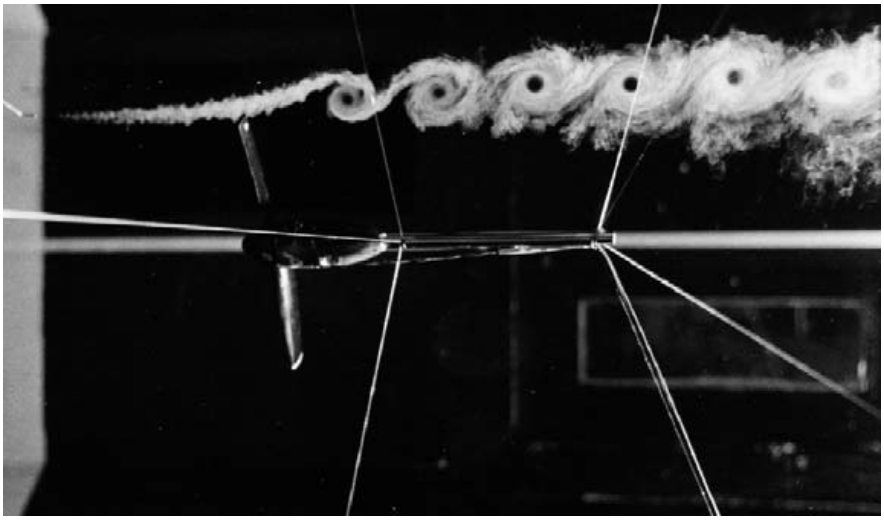

Figure 2.5: Visualisation of tip vortex behind a windmill [2]

Waves

Velocity recovery and turbulence dissipation are two of the many processes experienced behind a rotating HATT. As the most important variables reflecting hydrodynamic changes behind a turbine, they are the most reported. Up until the time of writing, results and understandings regarding impacts of HATTs on surface waves are sparse. Realizing the fact that tidal turbines are going to be installed in coastal regions where waves are not less visible and important than the current, researchers have started to examine the power efficiency of tidal turbines under wave-current interactive systems [7, 8, 32, 38, 40, 44, 67, 68, 76, 130].

On the impact assessment side, even less attention has been given to the significance of wave-current combined flow on wake recovery or impacts of HATTs on surface waves. [88] studied changes of wake recovery of a turbine subjected to opposing waves and drew a very basic conclusion that waves facilitate the wake recovery and the more energy the waves contain, the more wake recovery occurs. [113] also studied the effect of turbines under wave-current coupled flows. It simulated a turbine in a 7m long, 1.4m wide and 0.78m deep flume. The diameter of the turbine was 0.5m which gave a blockage ratio of 16% and the turbine was placed midway along the depth. A mono-chromic wave was imposed on a current with mean velocity of 0.9m/s, following the current. The wave had a wave height of 86mm, a period of 0.75s and a wavelength of 2m. Impacts of the turbine on the wave was assessed after the calculated velocity profiles were validated by comparing them with data collected in a laboratory [32]. It was observed that the overall wave height was reduced by 17% during one wave cycle. The wave length was also reported to be affected by the turbine —it was increased by 19%.

Sediment transport

Flow dynamics within the near-wake field can have significant influence on local bed scour. In fact, the interaction between the tidal stream device and the local sediment environment has been identified as a key issue awaiting investigation [23]. [114] observed a considerable flow acceleration around the energy extraction site which was believed by [27] to increase bed scour. [27] hence conducted a three-dimensional simulation of a three-blade rotor operating at various depths (0.9D, 1.1D, 1.3D and 1.5D above the bed) in a uniform flow using a CFD solver package OpenFOAM to reveal the impacts of the rotor on the three velocity components below the rotor tip and the boundary layer in the near-wake region. The results revealed that (1) the maximum steam-wise velocity component below the rotor tip is around 1.07 times of the background inlet flow; (2) the radial velocity component due to the blockage of the rotor plane and the tangential velocity component caused by the rotation of the blade, even though are increased under the presence of the rotor, make small contribution to the magnitude of the velocity and thus have negligible impacts on scouring; (3) the flow rate within

the boundary layer is increased while the velocity gradient is reduced. The changes to the boundary layer are still obvious even when the rotor hub is located 1.5D above the seabed. While noting that the flow acceleration may result in increased turbulence level and hence larger shear stress imposed on the seabed which causes the sediment to transport, the effects of these aforementioned changes on local bed scouring are not quantified in [27].

The local scour associated with a fully operational turbine with a supporting structure was quantified in terms of scour depth downstream of the turbine in [53]. Two experiments, clear water ($u^*/u^*_{cr} = 0.6$) and live-bed ($u^*/u^*_{cr} = 2.1$), were carried out in a 15m (L) and 0.9m (W) tilting water flume. The diameter of the turbine was 0.15m and the hub of the turbine was located 0.86D above the bed. It was reported that, after approximately 2.0-2.5h of run time, the maximum scour depth of the clear water case was 15% of the rotor diameter and that of the live-bed case was 1.5 times deeper (24% of the rotor diameter). Similar scour and sediment transport pattern was also observed in [58]. [58] also pointed out that the vertical variation of the turbine location, i.e. the height of the turbine hub, leads to variations in bed shear stress which directly affects the sediment transport pattern and morphological evolution. However, not too much detail was given in [58].

Two laboratory scale CFD cases were run in [113] to looked at bottom shear stress changes in the vicinity of two turbine rotors with different blockage ratios. In these two cases, the dimension of the flume was 6.0m long, 4.2m wide and 0.85m deep. Diameter of the rotor was 0.5m and it was placed at the mid-depth of the water. The two blockage ratios were 5.3% and 16%, respectively. The inlet flow speed was 0.9 m/s. It was found in this research that the bottom shear stress of a large area in the vicinity of the rotor was affected. For the larger blockage case, along the centreline, the bottom shear stress started to increased at -0.5D and the enhancement peaked at the turbine location (0D) due to flow diversion. A second peak which was due to vortex generation was observed at 2.5D behind the turbine following a gentle weaken of enhancement. The two peaks have about the same value and are about 9 times larger than the background bottom stress. The investigation stopped at 6D downstream where the stress on bed was still 6 times larger than the background stress. The smaller blockage case demonstrated similar trend. But the overall stress is 19% smaller than the larger blockage case.

2.4.3 Far-wake field impacts

The far wake is the region beyond the near wake, where the research focuses on HATTs' impacts on large scale coastal hydrodynamics. Such research, as mentioned in Section 1.1, relies heavily on oceanographic scale modelling tools due to the spatial and temporal scales involved.

Impacts on coastal hydrodynamics

Nowadays, many prototype tidal stream device projects, as mentioned in Section 1.1, are being carried out around the world, despite our immature understandings of the possible effects tidal stream devices may bring up to the marine environment. Some of the projects studied potential environmental and ecological disturbance of tidal turbines through on-site observations [93, 133]. However, hydrodynamic impact analysis has yet to be a primary focus of any of these projects. Thus, hydrodynamic changes caused by tidal stream devices are usually obtained through lab experiment and numerical modelling.

As tidal stream devices are designed to exploit kinetic energy carried by the ocean to which the tides contribute the most, tidal variables, such as tidal amplitude, phase, surface elevation and tidal current velocity, are receiving the most attention as far as impacts of such devices are concerned.

Disturbance of such devices to their surrounding environment is usually case-specific: it varies along the unique topography in the vicinity of the devices, the coastline of the study domain, the meteorology of the area and so forth. Thus, many case studies predicting large-scale and long-term influence of tidal stream devices at acknowledged promising energy extraction sites are conducted, using two-dimensional numerical models [1, 33, 37, 71, 91, 99, 104, 119].

A two-dimensional model was applied in [33] to simulate turbines along the Georgia coast, USA. The impacts on hydrodynamics were obtained under the scenario where the power extracted was 11.8MW (45% of the available kinetic power). It was discovered that the maximum drop of velocity downstream of the turbine array was 0.72m/s. The change of the water level was less than 0.05m which is not particularly significant. The implementation of the turbine array also caused the high tides to be delayed by up to approximately 10 minutes. Similar patterns were also recorded in the other works mentioned above. Impacts of the array on water level were also examined in the rest of the work listed above. Again, only slight changes were observed. These results suggest that the impacts are largely within the local region and the regional changes are small.

Impacts on sediment transport

The perturbation of turbine arrays on bedload and suspended sediment transport in the Alderney Race was investigated by [119] through looking at changes caused to the critical stress excess ($\tau - \tau_c$) and erosion and deposition flux difference (E-D). A two-dimensional model was applied. It was discovered that the presence of turbine arrays reduced the bottom stress within the turbine farms which is opposite to what was observed in the near-wake region(Section 2.4.2). It was also concluded in this work that the turbines did not change the spatial deposit pattern of suspended sediment, but they did influence the magnitude. Further, it was observed that the modification of

the suspended sediment pathways was due to the change of flow field rather than that of the erosion and deposition condition. Again, using a two-dimensional model, [71] focused on perturbation of bed shear stress caused by a turbine array in a case study in the Pentland Firth. The main difference between these two researches, in terms of model setting up, is the mesh size deployed. The mesh sizes around the device array in [119] and [71] were 150m and 18m, respectively. The fine resolution around the device farm used in the latter study allowed each turbine within the farm to be represented individually, which made observation of simulated hydrodynamics within the near-wake zone possible. However, reduction of bed shear stress within the turbine array was again reported in [71]. It should be noted that the reduction of bed shear stress was derived directly from water velocity reduction in both research.

With a two-dimensional model employed, [99] assessed potential impacts of a turbine array on sedimentary processes along the Anglesey coast. As an enhancement of the above-mentioned studies, wave-induced bed shear stress was included in the analysis, yet assumed no wave-current interaction. The concept of 'natural intra-seasonal variability' was introduced to quantify impacts of energy extraction on oceanographic processes. It was discovered that at the location of energy extraction, bedload transport was the most affected — it was reduced to 82% of its baseline value when 141MW power was removed by the turbines. A marginal impact (less than 2% for the 141MW array) was detected at a point 10km away from the farm site.

Impacts on large-scale morphology

As the first published study concerning impacts of tidal stream devices on large-scale morphology, [85] carried out research using a 1D numerical model, emphasising dependency of sediment transport changes due to energy extraction on tidal symmetry at the device location. The research was based on a case study conducted in the Bristol Channel. A 250MW tidal stream device farm west of Hinkley Point was configured implementing bulk method (box the turbine array up) according to one of the leading HATT concepts — 'Seagen'. The farm was parameterized as an additional bed friction source term (See Section 2.5.1). The main conclusions of this research are:

1. The magnitude of bed level change is damped by the introduction of the turbine farm compared with the natural scenario, regardless of the location of energy extraction;

2. Extracting energy from a region of strong tidal asymmetry has more significant effects on bed level change compared with extracting energy from a tidal symmetry region;

3. Bed level change resulting from energy extraction is evident up to a distance of 50km from the device location rather than being restricted to the vicinity of the

array;

4. The bed level change is of the order of 3-4m over 30 years which is the typical life cycle of a tidal stream device.

Based on parameterization of the tidal stream device as additional bed friction, [84] investigated impacts of tidal device arrays on the sediment dynamics of headland sand banks where strong tidal flow often occurs and hence are identified as potential tidal stream energy exploitation sites. A two-dimensional model was used to investigate the complex hydrodynamics and sediment transport. Again, the farm was presented in the model applying the bulk method. An idealized case simulating a headland within a 60km long and 50km wide channel led to the conclusion that the sedimentation pattern which results in the formation of one sand bank on each side of the headland is qualitatively similar but is reduced in magnitude after including the turbine array. The model was then applied to a case study around the Alderney island south of which sand banks are likely to form. The main aim of this study was to predict the changes caused by a 300MW turbine array on the sand banks south of the Alderney island. An erosion of 2mm over a spring-neap tidal cycle which corresponds to 10% of the deposition calculated by the background case was observed to the sand banks.

2.5 Modelling turbines in an oceanographic model

This section reviews how turbines are parameterized in modules of a large-scale oceanographic model. To include tidal stream turbines into an oceanographic model, modifications often have to be carried out to the model system. Overall, two different approaches can be found in the literature, including implementing an additional bottom friction on the seabed and simulating the effects of turbines by modifying the flow motion with added turbine-induced forces. Both methods have their advantages and disadvantages when compared against the reality. The present review will examine each method in detail and highlight their characteristics and suitability.

2.5.1 Additional bottom friction

In the two-dimensional numerical model used in [115], natural energy dissipation due to the seabed was computed by:

$$P = \iint_A \rho C_d \left|\bar{u}\right|^3 dA \tag{2.2}$$

where C_d is the quadratic bottom friction coefficient (drag coefficient), u is the tidal current speed, and A is the area of the tidal turbine farm.

In analogue, the turbines can be simulated as an enhanced bed roughness that dissipates energy in the form of Equation 2.2. The total energy dissipated over the

device farm is therefore the sum of the natural dissipation and the energy extracted by the farm:

$$P = \iint_A \rho(C_d + C_{dt}) \left|\bar{u}\right|^3 dA \tag{2.3}$$

where C_{dt} is the friction coefficient associated with the turbines.

This method was also adopted by [59, 124]. This concept was also adopted in [19] where, instead of the bottom friction coefficient, the bed shear stress (τ) is increased when tidal stream devices are present. The relation between the bottom friction coefficient and the bed shear stress is explained in Section 3.3.1. [91] also implemented the 'additional shear stress' method in a two-dimensional numerical model. However, in this work, the bed shear stress was calculated from the thrust of the turbine ($\tau = T/A$, one could refer to Equations 2.12 and 2.13 for the calculation of T). The advantage of this method is that the link between the averaged energy output of the devices and the value of C_{dt} is straightforward. Thus, it is very easy to control the installed capacity. This is of importance since the relationship between energy output and impacts is often of significant interest. However, using this method, the drag of the devices is exerted on the seabed, rather than in the water body, rendering the effects predicted unrealistic.

2.5.2 Linear Momentum Actuator Disc Theory (LMADT)

This line of research started with early power potential assessment work aiming to find suitable energy extraction sites around world coastal waters as well as to calculate maximum exploitable power at various sites. One of the widely recognized methods is the 1D Linear Momentum Actuator Disc Theory (LMADT), which was initially used in the wind power industry [12]. This theory was later adopted in the study domain of tidal power after it was modified to accommodate properties of water flows and was expanded into a more general LMADT framework that takes into account multi-dimensions and boundary features of regions from where the energy is extracted [42, 43, 55, 129].

Figure 2.6 shows a sketch of a two-dimensional approximation to the flow passing an actuator disc (representing tidal devices). LMADT, developed under the assumptions that the cross-flow is negligible and that there is no pressure loss downstream of the disc, gives the thrust coefficient (C_T) and power coefficient (C_P) of the turbine in the form:

$$C_T(\alpha) = \frac{T}{\frac{1}{2}\rho U^2 s_t} = (\tau^2 - \alpha^2) \tag{2.4}$$

$$C_P(\alpha) = \frac{P}{\frac{1}{2}\rho U^3 s_t} = \beta(\tau^2 - \alpha^2) \tag{2.5}$$

where T and P are the thrust force on the disc and the power taken by the disc respectively; ρ is the density of the water; U is the water velocity upstream of the device; s_t is the area occupied by the disc; $\alpha = U_w/U$, $\beta = U_t/U$, $\tau = U_2/U$ and U_w, U_t and U_2

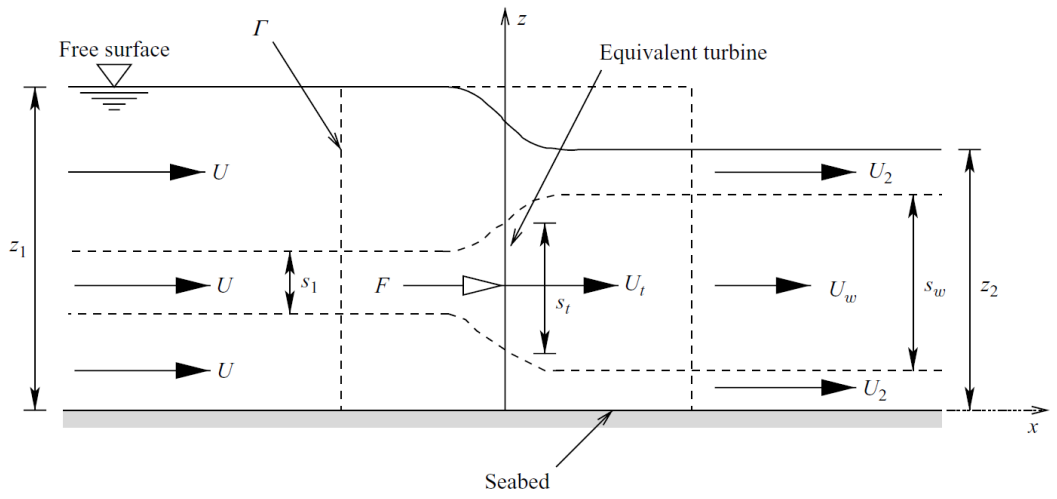

Figure 2.6: Sketch of a two-dimensional approximation to the flow past an actuator disc [129]

are water velocities within the streamtube containing the disc but far downstream of the device, water velocity across the disc and water velocity outside the stream tube far downstream of the disc, respectively.

This work was later extended by [35] to include downstream mixing which is another source of energy loss (P_w) apart from energy extraction (P) and discussed the efficiency of the device ($P/(P+P_w)$) under various blockage ratios and Froude numbers. The energy loss caused by these two processes is reflected by change in water depth upstream and downstream of the device ($\Delta z = z_1 - z_2$) which is given by:

$$\frac{1}{2}(\frac{\Delta z}{z_1})^3 - \frac{3}{2}(\frac{\Delta z}{z_1})^2 + (1 - Fr^2 + \frac{C_T B Fr^2}{2}) \times \frac{\Delta z}{z_1} - \frac{C_T B Fr^2}{2} = 0 \qquad (2.6)$$

where B is the blockage ratio of the device and $Fr = U/\sqrt{gz_1}$ is the Froude number.

In the same work, the extended LMADT was applied in conjunction with a depth-averaged numerical model to describe tidal devices in a water channel, in which the relative water depth change ($\Delta z/z_1$) across the device is implemented into the numerical model as a boundary condition representing the devices. Results with good agreement to that calculated by analytical models were obtained.

LMADT provides 'a theoretical argument that links a tidal device, defined by a blockage ratio and porosity, to the equivalent momentum sink that the device should impart within a depth-averaged domain' [35]. It helps to distinguish between power available to the turbines which is normally calculated based on the undisturbed kinetic energy flux [15] and the power extracted by the turbines. However, due to the many assumptions required, LMADT is a near-field approximation. The implementation of LMADT within a numerical model is only acceptable when the lengthscale of the wake behind the turbine/turbine array is much smaller than the mesh size. Also, even though

the link between tidal device and the momentum sink proposed by the LMADT is relatively solid, the calculation requires the blockage ratio (B) and the wave velocity coeffcient (α) to be prescribed; and they are often assigned arbitrarily by the modellers, which weakens the link extensively.

2.5.3 Additional retarding force

[30] proposed a new method to parameterize tidal stream devices in which the act of power extraction was regarded as an additional retarding force exerted on the water body. The retarding force (F) on the water as it passes through the device is given by:

$$F = -\frac{P_{ext}}{U} \tag{2.7}$$

where P_{ext} is the power being extracted and U is the velocity of the passing water.

This concept is widely adopted in site-specific large-scale impact assessment work at the Georgia coast, USA [33], the Bristol channel [1], the Tory Channel [91], the Shannon Estuary [37], the Alderney Race [119], the Pentland Firth [71] and the north-west coast of Anglesey [99] and to an idealized model of a channel connecting a bay to an ocean [136].

Among these work, [33] considered P_{ext} as a fraction of the kinetic power density P of the passing flow at the extraction location as:

$$P_{ext} = C_{ext} \cdot P \tag{2.8}$$

where C_{ext} is a coefficient denoting the fraction of power being extracted, and P is given by:

$$P = \frac{1}{2}\rho U^3 \tag{2.9}$$

Combining Equations 2.7, 2.8 and 2.9 results in the retarding force terms being added into the momentum equations in x and y directions, respectively, as:

$$F_x = -\frac{1}{2}\rho C_{ext} u \left|\vec{U}\right| \tag{2.10}$$

$$F_y = -\frac{1}{2}\rho C_{ext} v \left|\vec{U}\right| \tag{2.11}$$

where F_x, F_y, u and v denote the retarding force and the velocity components in x and y directions, respectively.

Alternatively, in the rest of the work within which the concept of retarding force was applied [1, 37, 71, 91, 99, 119, 136], the retarding force terms are calculated from the turbine thrust as:

$$F_x = T_x = -\frac{1}{2}\rho C_T A u \left|\vec{U}\right| \tag{2.12}$$

$$F_y = T_y = -\frac{1}{2}\rho C_T A v \left|\vec{U}\right| \tag{2.13}$$

where T_x and T_y are the thrust of the turbine in x and y directions, respectively, and C_T is the thrust coefficient of the turbine. It should be noted that the thrust coefficient is a function of the turbine design. It is an important indicator of the performance of a turbine and is normally measured and provided by the developer. The value of C_T was kept as a constant in [1, 37, 136] whereas, in [71, 91, 119], 'cut-in' and design speeds were introduced, below or above which, C_T had different values.

This 'additional retarding force' concept, in general, as noted in [30], is more scientifically rigorous in comparison with the 'additional bottom friction' method. Also, the extension of this concept to three-dimensional is more logically feasible when compared to the other two ways mentioned above. Regarding the two approaches realizing the 'additional retarding force' concept, the latter, as argued in [91], 'is more complete in that it allows for inefficiencies in power extraction'. The energy removed from the flow goes partially to the turbulence generated, instead of entirely to power generation. F_x and F_y calculated based on C_T reflect directly the force the turbine exerts on the flow. Therefore, the work done by F_x and F_y in this case includes both power extracted by the turbine and the power dissipated due to the incurring of turbulence. On the contrary, F_x and F_y calculated through C_{ext} are associated specifically with power extracted by the turbine. Power dissipation due to turbulence generated is not included. Impacts predicted, hence, can be underestimated. Also, the introduction of C_T links the retarding force with the actual design of the selected device. However, as C_T is a coefficient indicating the general performance of the device, it is difficult to split it up to a set of coefficients to be applied to each layer of the water column, which is particularly important when a three-dimensional numerical model is employed. In fact, most of the work employing the latter approach used two-dimensional models [1, 37, 71, 91, 99, 119] except for [136]. However, the additional retarding force term was applied in only one of the sigma layers in each simulation in [136], assuming that the turbine occupied only one single sigma layer. This is not entirely correct when the height of each of the sigma layers is smaller than the diameter of the turbine. Further, the values of C_T were chosen arbitrarily in all these studies, which means, rather than real turbine designs, the retarding force exerted on the passing flow is linked to conceptual turbines which provided no data for model validation. In contrast, the value assignment of the coefficient C_{ext} in the former approach is more flexible as it is not related to a specific turbine design rigorously. Thus, it can be easily extended into three-dimensional. However, the value of C_{ext} still needs to be calibrated. In [33], the two retarding force terms given by approach one were implemented in a two-dimensional numerical model and the value of C_{ext} was decided iteratively through successive model runs until the desired power removal was achieved. This is the only work, among all above-mentioned work, that carried out calibration for the coefficient involved.

Apart from the work mentioned above which focus on site-specific large-scale im-

pact assessment, [101] also adopted the second approach of 'additional retarding force' in a three-dimensional model. More impressively, this work initially addressed turbulence perturbations in the model (see Section2.5.4). A laboratory scale water channel (21m(L) $\times$ 1.35m(W) $\times$ 0.3m(D)) was used to test the reliability of the extended model. However, the application of the additional force term is not explicitly presented in this work. Whether the body force is applied to one or more of the vertical layers is unclear.

Among the work mentioned in this section, [37], [71], [99] and [101] treated turbines in the array individually while arrays were boxed up arbitrarily in the other studies. For example, [1] simulated a turbine array in the Severn Estuary using a one-dimensional and two-dimensional linked model. The array was configured with $2000 \times 10m$ diameter turbines in an area of 7.2 km^2 when the finest grid size of the computation mesh was 200m which was far larger than the diameter of an individual turbine. Clearly, the wake within the device farm is masked by boxing up the array. The possible changes in physical processes in the near field, such as wave height modulation and bottom shear stress increase, which should as well be parameterized into the model, are consequently skipped.

2.5.4 Modification of turbulence closures

Until the time of writing, little attention has been paid to turbulence closures in oceanographic models in terms of parameterizing impacts of tidal turbines on turbulence within the wake. Similar work, however, has been carried out extensively to study the wake of canopy. [97] pointed out that apart from the conventional shear production term ($P_s \propto (u_z^2 + v_z^2)$), canopy causes an additional 'wake production' term enhancing TKE (k) production within the wake and TKE generated through this process is at length scale much smaller than the typical length scales of the shear-generated eddies, short-circuiting the natural eddy cascade. It also pointed out that because the wake generated TKE is of smaller length scale, the wake energy is dissipated more rapidly to heat; in other words, the dissipation rate (ϵ) for large-scale TKE in the canopy is accelerated.

These processes were later modelled in a two-equation turbulence closure with a source term ($P_{p1} \propto |u|^3$) and a sink term ($P_d \propto |u| \cdot k$) for k added in the turbulence transport controlling equations, accounting for the production and dissipation by the short-circuited eddy cascade respectively [46] . At the same time, the enhancement of TKE dissipation was modelled by an additional source term on the right-hand side of the ϵ equation: $P_{\epsilon 1} \propto \frac{\epsilon}{k}(P_{p1} - P_d)$. The authors of the same work, however, pointed out that even though P_{p1} has a clear physical meaning being the kinetic energy lost by the perturbation of canopy that is converted into TKE, the other two terms, P_d and $P_{\epsilon 1}$, have no clear physical basis. Nevertheless, these additional terms are adopted in some later researches [103, 109, 98].

On the other hand, [28] proposed a general approach to adjust the dissipation rate.

A production range time scale related TKE transfer rate from large-scale turbulence to small-scale turbulence was added onto the right-hand side of the ϵ equation: $P_{\epsilon 2} \propto \frac{P_s^2}{k}$ (see P_s in Section 3.3.2), rationale being 'to allow the dissipation rate to respond to the mean strain more effectively'. In other words, the dissipation rate is enhanced when the shear production of TKE (P_s) is strong and vice versa. This approach was tested in the same paper for several problems and good results were obtained. $P_{\epsilon 2}$ was later implemented in the area of wind turbine research [36, 94]. In [36], an extended turbulence closure featuring the additional dissipation term $P_{\epsilon 2}$ was tested over three wind turbines and it was shown to produce much better results than the original turbulence closure, particularly in the near wake, where rapid changes in turbulent kinetic energy production and dissipation rates were observed.

In the research area of tidal turbines, $P_{\epsilon 2}$ was applied in a CFD based research, combined with a TKE production augmenting term $P_{p2} = \zeta_s P_s$ (ζ_s is a coefficient) added onto the k transport equation which modelled the total effects of tidal turbines on TKE production [106]. The combination was able to produce correct wake turbulence as long as the coefficients are tuned properly. Three of the above mentioned terms, P_{p1}, P_d and $P_{\epsilon 2}$, were applied in an oceanographic model to parameterize impacts of tidal turbines on turbulence generation and transport in the wake in [101]. Again, good results were obtained given the related coefficients were chosen properly.

2.6 Summary

This chapter gives basic information on tidal stream device types and coastal processes this research focuses on. More importantly, this chapter reviews relevant work to identify hydrodynamic impacts associated with tidal stream energy exploitation. Comprehensive understanding of potential hydrodynamic impacts caused by extensive implementation of such technology is obtained. Most of the reviewed works were based on laboratory or numerical experiments. In general, the velocity immediately behind the device is reduced with water going around the device accelerated, forming a W-shaped flow field within a certain distance downstream of the turbine. Turbulence in the vicinity of the device is increased due to larger velocity gradient induced by the turbine as well as mechanical turbulence shed from the rotating motion of the rotor. Less research focus on the influence of tidal turbines on waves and sediment is found. The available studies demonstrate dropped wave height and enhanced sediment scour around the turbine. These observations provide important guidelines and inputs for turbine implementation in oceanographic models.

Methods for tidal stream device representation in oceanographic models are also reviewed in this chapter. The aforementioned large scale modelling based work provides a general framework for simulating energy generation of turbines in a numerical model. However, there are still challenges to produce reliable predictions using such methods.

Most of the work published in this area relies on two-dimensional models. An immediate shortcoming of any two-dimensional model is it confuses the physical meanings of turbine representation methods. For instance, the additional retarding force which is supposed to be exerted on a certain part of the water body would be implemented vertically uniform over the water column and, therefore, could be equally regarded as additional bottom friction in a two-dimensional model. Further, two-dimensional models could result in incomplete prediction of the vertical flow structure downstream of the turbine and hence the mixing in the wake. Local to the turbines, there are significant changes to the flow field with increased flow rate around the turbines that mixes with the slower moving water which has passed through the rotor plane [104]. The effects of flow above and below the plane of extraction and the complex mixing process cannot be modelled accurately with any depth-integrated model [20]. (Objective 3 of this research listed in Section 1.2 responds to this knowledge gap.)

The 'additional retarding force' method for turbine-induced velocity reduction was indeed implemented in a three-dimensional model [136]; however, in each simulation the additional force term was applied in only one of the sigma layers, which assumed that the turbine occupied only a single layer. Hence, the evolving vertical velocity structure formed due to the disturbance of the turbine was not captured in this manner. [101] developed a relatively thorough three-dimensional parameterization which not only captured the details of the vertical velocity structure but also took the disturbance of turbines on the turbulence equilibrium into consideration in the Regional Ocean Modelling System (ROMS). Calibration of the coefficients was carried out based on a set of experimental data. The turbulence closure module to which the research made modification was the $k - \epsilon$ module. However, despite using a large-scale ocean circulation model, the validation case simulated a small-scale rectangular water channel (rotor diameter was 100mm). The system was yet to be applied to larger scale models. (Objective 3 of this research listed in Section 1.2 responds to this knowledge gap.)

Also there is scope for development in this line of research as not too much emphasis has been put on wave-current interaction and implementation of effects of turbines on waves and sediment transport in corresponding numerical modules. Little research has looked at changes on waves. All the reviewed work that focused on impacts on sediment dynamics and large-scale morphology assumed that changes to the flow pattern are sufficient to account for the potential impacts caused by turbines on bottom stress and sediment transport and reported results contradict observation of local scour in the near-wake. (Objectives 3 & 4 of this research listed in Section 1.2 respond to this knowledge gap.)

Lack of calibration is another outstanding issue. Among the existing studies, work that calibrated the turbine simulation related coefficients before model application are sparse. Aside from ensuring that the hydrodynamic conditions match on-site measure-

ments prior to the inclusion of turbines in the model, little other calibration work is done. This is primarily due to the lack of observational data after the installation of tidal turbines. The philosophy is that the models are regarded as functionally accurate as long as they have the ability to reproduce the background hydrodynamic conditions, provided good quality bathymetry distribution, open boundary condition and meteorological condition etc. Hence, based on the proven properly functioning model, as long as the representation of the turbine is sound, the modified model predicted results are assumed reliable. Unfortunately this is seldom the case as all turbine implementation methods require arbitrary choice of values of coefficients which decide directly the significance of the impacts predicted. Thus, calibration of these coefficients is considered as necessary in this research. (Objectives 1 & 2 of this research listed in Section 1.2 respond to this knowledge gap.)

Responding to the knowledge gaps summarized above, this research aims to develop a three-dimensional thorough turbine simulation platform. Based on a three-dimensional wave-current-sediment fully coupled oceanographic model, the first approach regarding the 'additional retarding force' method is implemented in the present research three-dimensionally to mimic the flow field behind the turbine. The turbulence closure is modified based on the scheme proposed in [101] to account for influence of turbines on downstream turbulence. Impacts on waves is also considered in this research and the implementation is realized through modification of wave energy flux across the device. This research also aims to verify the necessity of modifying the bottom shear stress calculation which simulates the local scour caused by turbines and provides a way of doing so. The related coefficients are calibrated based on laboratory measurements and CFD calculations. Scaling-up which lays the foundation for large-scale application of the turbine simulation platform is discussed. This research also aims to cover the discussion of impacts of variations of the turbine simulating coefficients on the overall prediction of the model. The extended model is then applied to the Anglesey coast to study the large-scale influence of turbine arrays.

One simplification over the supporting structure is made in this research after the discussion in Section 2.4.1: Impacts of the supporting structure on the passing flow and the mixing downstream is not accounted for in this research. However, its more obvious impacts on local scour is integrated into the address of bed shear stress.

Chapter 3

Modelling system

3.1 Introduction

In order to study the processes in both the near field and far field in the region affected by the turbine, two distinct modelling systems are used in the present work: the FLUENT based Computational Fluid Dynamics (CFD) modelling system to resolve the near field processes, particularly under wave-current coupled conditions, and the Unstructured Grid Finite Volume Community Ocean Model (FVCOM) [25] to simulate the far field to coastal region with large-scale turbine farms implemented. In particular, the turbine parameterization in FVCOM is based on available data and CFD modelled results.

Until now, there is no single model that is capable of simulating both near field and far field flow dynamics, turbulence characteristics and sediment transport processes, due to the fact that the basic assumption in oceanographic models, the linearised pressure distribution in vertical direction, violates the complex nature of the water in the near field region, while the computational costs and uncertainties in a CFD model are too great to cover the entire far field region. The combined approach provides the best possible opportunity to represent the physical processes at both scales accurately.

3.2 ANSYS FLUENT — a CFD solver

A wide range of CFD solver packages have been developed throughout application history, such as OpenFOAM, ANSYS FLUENT and STAR-CCM+. The package used in this research is ANSYS FLUENT (Version 14.5).

3.2.1 Modelling basic fluid flow

FLUENT solves the three-dimensional Reynolds-averaged Navier-Stokes (RANS) equations which can be written in tensor form as follows:

$$\frac{\partial \rho}{\partial t} + \frac{\partial \rho \bar{u_i}}{\partial x_i} = 0 \tag{3.1}$$

$$\frac{\partial(\rho \bar{u_i})}{\partial t} + \frac{\partial(\rho \bar{u_i} \bar{u_j})}{\partial x_j} = -\frac{\partial \bar{P}}{\partial x_i} + \frac{\partial}{\partial x_j}[\mu(\frac{\partial \bar{u_i}}{\partial x_j} + \frac{\partial \bar{u_j}}{\partial x_i}) - \frac{2}{3}\mu \frac{\partial u_l}{\partial x_l}\delta_{ij}] + \frac{\partial}{\partial x_j}(-\rho \overline{u_i' u_j'}) + F_i \tag{3.2}$$

where ρ is the water density; t is time; μ is the molecular viscosity; δ_{ij} is the Kronecker delta and F_i are external body forces in the i directions (x, y, z). $\bar{u_i}$ $(\bar{u}, \bar{v}, \bar{w})$ and u_i' (u', v', w') are the time-averaged (mean) and fluctuating water velocities in the x_i (x, y, z) directions, respectively. The combination of these two velocity components forms the instantaneous (exact) velocities:

$$u_i = \bar{u_i} + u_i' \tag{3.3}$$

Likewise, $\bar{P}$ is the time-averaged static pressure and for all scaler variables:

$$\phi = \bar{\phi} + \phi' \tag{3.4}$$

where ϕ denotes a scaler quantity such as pressure and $\bar{\phi}$ and ϕ' are the mean and fluctuating components of a scaler variable.

The Reynolds stress terms, $-\rho\overline{u_i' u_j'}$, which appear on the right hand side of Equation 3.2 represent the effects of turbulence and need to be modelled in order to close the RANS equations.

3.2.2 Modelling turbulence

To model the Reynolds stress terms in Equation 3.2, FLUENT provides a good variety of turbulence closures which can be in general grouped into two approaches: one is to employ the Boussinesq hypothesis to relate the Reynolds stresses to the mean velocity gradients and the other one is to solve transport equations for each of the terms in the Reynolds stress tensor, namely Reynolds Stress Model (RSM). The first approach which includes the popular two-equation models such as $k-\epsilon$ and $k-\omega$ is widely adopted in engineering calculations. The second approach which requires seven additional transport equations to be solved in three-dimensional problems is expected to perform better than the first approach in certain conditions. However, it normally requires 50-60% more CPU time and 15-20% more memory per iteration compared to the $k-\epsilon$ and $k-\omega$ models [39]. Thus, the RSM is not used in this research.

There is another turbulence closure, namely Shear-Stress Transport (SST) $k-\omega$ Model, which combines the robust and accurate formulation of the $k-\omega$ closure in the near-wall region with the free-stream independence of the $k-\epsilon$ closure in the far field. The traditional two-equation turbulence closures, $k-\epsilon$ and $k-\omega$, and the SST $k-\omega$ closure were compared in [47, 72] and it was reported that the SST $k-\omega$ closure produced the highest accuracy in terms of predicting near field turbulence of turbines. Therefore, turbulence in the present research is calculated based on the Shear Stress Transport (SST) $k-\omega$ turbulence closure. For completeness, the (SST) $k-\omega$ closure is introduced as following:

Transport equations for the $SST\ k-\omega$ model

In the $SST\ k-\omega$ closure, the turbulent kinetic energy, k, and the specific dissipation rate, ω, are defined as:

$$k = \frac{1}{2}\overline{u_i' u_i'} \tag{3.5}$$

$$\omega = \epsilon / k \tag{3.6}$$

where ϵ, the turbulence dissipation rate, is defined as:

$$\epsilon = \frac{\mu}{\rho} \cdot \overline{\frac{\partial u_i'}{\partial x_j}(\frac{\partial u_i'}{\partial x_j} + \frac{\partial u_j'}{\partial x_i})} \tag{3.7}$$

The calculations of these terms are based on the following transport equations:

$$\frac{\partial}{\partial t}(\rho k) - \frac{\partial}{\partial x_i}(\rho k u_i) = \frac{\partial}{\partial x_j}(\Gamma_k \frac{\partial k}{\partial x_j}) + G_k - Y_k \tag{3.8}$$

$$\frac{\partial}{\partial t}(\rho \omega) - \frac{\partial}{\partial x_i}(\rho \omega u_i) = \frac{\partial}{\partial x_j}(\Gamma_\omega \frac{\partial \omega}{\partial x_j}) + G_\omega - Y_\omega + D_\omega \tag{3.9}$$

where G_k represents the generation of k due to mean velocity gradients; G_ω represents the generation of ω; Γ_k and Γ_ω represent the effective diffusivity of k and ω, respectively; Y_k and Y_ω represent the dissipation of k and ω due to turbulence; D_ω is the cross-diffusion term. Calculation of these terms are described as below:

Modelling the effective diffusivity

$$\Gamma_k = \mu + \frac{\mu_t}{\sigma_k} \tag{3.10}$$

$$\Gamma_\omega = \mu + \frac{\mu_t}{\sigma_\omega} \tag{3.11}$$

where μ_t is the turbulent viscosity computed as following:

$$\mu_t = \frac{\rho k}{\omega} \frac{1}{max[\frac{1}{\alpha^*}, \frac{\Omega F_2}{a_1 \omega}]} \tag{3.12}$$

where $\Omega = \sqrt{2\Omega_{ij}\Omega_{ij}}$, $\Omega_{ij} = \frac{1}{2}(\frac{\partial u_i}{\partial x_j} - \frac{\partial u_j}{\partial x_i})$ is the mean rate-of-rotation tensor; α^* damps the turbulent viscosity causing a low-Reynolds-number correction and it is given as:

$$\alpha^* = \alpha^*_\infty (\frac{\alpha^*_0 + Re_t/R_k}{1 + Re_t/R_k}) \tag{3.13}$$

where

$$\alpha^*_0 = \frac{\beta_i}{3} \tag{3.14}$$

$$Re_t = \frac{\rho k}{\mu \omega} \tag{3.15}$$

Terms σ_k and σ_ω in Equation 3.10 and 3.11 are the turbulent Prandtl numbers for k and ω, respectively, calculated as following:

$$\sigma_k = \frac{1}{F_1/\sigma_{k,1} + (1 - F_1)/\sigma_{k,2}} \tag{3.16}$$

$$\sigma_\omega = \frac{1}{F_1/\sigma_{\omega,1} + (1-F_1)/\sigma_{\omega,2}} \tag{3.17}$$

The blending functions, F_1 and F_2, are given by

$$F_1 = tanh(\Phi_1^4) \tag{3.18}$$

$$\Phi_1 = min[max(\frac{\sqrt{k}}{0.09\omega y}, \frac{500\mu}{\rho y^2 \omega}), \frac{4\rho k}{\sigma_{\omega,2} D_\omega^+ y^2}] \tag{3.19}$$

$$D_\omega^+ = max[2\rho \frac{1}{\sigma_{\omega,2}} \frac{1}{\omega} \frac{\partial k}{\partial x_j} \frac{\partial \omega}{\partial x_j}, 10^{-20}] \tag{3.20}$$

$$F_2 = tanh(\Phi_2^2) \tag{3.21}$$

$$\Phi_2 = max[2\frac{\sqrt{k}}{0.09\omega y}, \frac{500\mu}{\rho y^2 \omega}] \tag{3.22}$$

where y is the distance to the next surface.

Values of constants in the above equations are: $a_1 = 0.31$, $\sigma_{k,1} = 1.176$, $\sigma_{k,2} = 1.0$, $\sigma_{\omega,1} = 2.0$, $\sigma_{\omega,2} = 1.168$, $\alpha_\infty^* = 1$, $\beta_i = 0.072$, $R_k = 6$.

Modelling the turbulence production

Production of k (G_k)

$$G_k = \mu_t S^2 \tag{3.23}$$

$$S = \sqrt{2 S_{ij} S_{ij}} \tag{3.24}$$

$$S_{ij} = \frac{1}{2}(\frac{\partial u_j}{\partial x_i} + \frac{\partial u_i}{\partial x_j}) \tag{3.25}$$

Production of ω (G_ω)

$$G_\omega = \frac{\alpha}{\nu_t} G_k \tag{3.26}$$

$$\alpha = \frac{\alpha_\infty}{\alpha^*}(\frac{\alpha_0 + Re_t/R_\omega}{1 + Re_t/R_\omega}) \tag{3.27}$$

$$\alpha_\infty = F_1 \alpha_{\infty,1} + (1-F_1)\alpha_{\infty,2} \tag{3.28}$$

$$\alpha_{\infty,1} = \frac{\beta_{i,1}}{\beta_\infty^*} - \frac{\kappa^2}{\sigma_{\omega,1}\sqrt{\beta_\infty^*}} \tag{3.29}$$

$$\alpha_{\infty,2} = \frac{\beta_{i,2}}{\beta_\infty^*} - \frac{\kappa^2}{\sigma_{\omega,2}\sqrt{\beta_\infty^*}} \tag{3.30}$$

$$\nu_t = \frac{\mu_t}{\rho} \tag{3.31}$$

where μ_t is the turbulent viscosity calculated according to Equation 3.12, α^* is the damping coefficient calculated according to Equation 3.13, F_1 computed according to Equation 3.18.

Values of newly introduced constants are $\alpha_0 = \frac{1}{9}$, $R_\omega = 2.95$, $\beta_{i,1} = 0.075$, $\beta_{i,2} = 0.0828$, $\beta_\infty^* = 0.09$, $\kappa = 0.41$.

It should be noted that the $SST\ k-\omega$ model does not include the additional turbulence generation at the tip of the blade as highlighted by previous research due to the fact that the tip vortex shed from the tip of turbine blades is not simulated by the turbine representation method (see Section 3.2.4). The model is therefore likely to under-predict the turbulence level in the near field region. For example, due to the same reason, the TKE level was found to be under-estimated by 40% at 2D-6D downstream of the rotor simulated in [106]. The extent of under-estimation, however, is case dependant. Results in Section 4.3.1 of the present study suggest an under-estimation of 17% in the near wake for the turbine rotor and scenario simulated.

Modelling the turbulence dissipation

Dissipation of k (Y_k)

$$Y_k = \rho\beta^* k\omega \tag{3.32}$$

$$\beta^* = \beta^*_\infty(\frac{4/15 + (Re_t/R_\beta)^4}{1 + (Re_t/R_\beta)^4}) \tag{3.33}$$

Dissipation of ω (Y_ω)

$$Y_\omega = \rho\beta\omega^2 \tag{3.34}$$

$$\beta = F_1\beta_{i,1} + (1 - F_1)\beta_{i,2} \tag{3.35}$$

where Re_t is given by Equation 3.15 and the newly applied constants are $R_\beta = 8$, $\beta^*_\infty = 0.09$.

3.2.3 Modelling waves

In the present study, the Volume of Fluid (VOF) method is used to simulate the wind-wave-induced free surface effects.

The VOF model

The VOF model is for free-surface representation and its formulation relies on the fact that the modelled phases are not immiscible. It calculates the fractions ($\alpha_i, 0 < \alpha_i < 1$) of the simulated phases (water and air in the present research) in each computational cell and in each control volume. The volume fractions of all phases sum to unity. Based on the local value of α_i, the appropriate properties and variables will be assigned to each control volume within the domain.

A single momentum equation which is dependent on the volume fractions of all phases through the properties ρ and μ is solved throughout the calculation domain, and the computed velocity field is shared among the phases. The momentum equation is given by

$$\frac{\partial}{\partial t}(\rho\vec{v}) + \bigtriangledown \cdot (\rho\vec{v}\vec{v}) = -\bigtriangledown p + \bigtriangledown \cdot \left[\mu(\bigtriangledown\vec{v} + \bigtriangledown\vec{v}^T)\right] + \rho\vec{g} + \vec{F} \tag{3.36}$$

where ρ is the volume-fraction-averaged density $\rho = \sum \alpha_i \rho_i$ (i is the ith phase simulated, e.g. water and air in the present research) and μ the volume-fraction-averaged viscosity calculated in the same manner.

A continuity equation for the volume fraction of one (or more) of the phases helps to track the interface(s) between the phases. For the ith phase, this equation takes the form of the following:

$$\frac{\partial \alpha_i}{\partial t} + \vec{v} \cdot \bigtriangledown \alpha_i = 0 \tag{3.37}$$

Additional scaler equations, such as those solving turbulence quantities, are also processed applying the shared-fields approach, i.e. only a single/a single set of transport equations is solved and the variables (e.g., k and ω) are shared by the phases throughout the domain.

The wave generation boundary conditions

The open channel wave boundary condition enables the simulation of wave propagation. It is an upstream boundary condition applied to the velocity inlet of the VOF model. FLUENT provides a good variety of wave theories such as first order linear wave theory and second/higher order Stokes wave theories. The choice of wave theory should be made based on Ursell number ($U_r = \frac{HL^2}{d^3}$) and wave steepness (H/L), where H, L and d are wave height, wave length and water depth, respectively. Linear wave theory is suitable when $U_r < 40$, given $H/L < 0.04$ and second/higher order Stokes wave theories are more appropriate when $U_r < 40$ and $H/L > 0.04$ [52].

In FLUENT, the wave number (k) is given by:

$$k = \frac{2\pi}{L} \tag{3.38}$$

The vector form for the wave number is:

$$\vec{K} = k_x \hat{x} + k_y \hat{y} \tag{3.39}$$

where k_x and k_y are wave numbers in the $\hat{x}$ and $\hat{y}$ directions, respectively, and are defined by:

$$k_x = k\cos\theta \tag{3.40}$$

$$k_y = k\sin\theta \tag{3.41}$$

where θ is the wave heading direction. The wave speed c is defined as:

$$c = \frac{\omega}{k} \tag{3.42}$$

where ω is the wave frequency.

For linear waves, the time-dependent surface elevation is given as:

$$\zeta(X,t) = A\cos\alpha \tag{3.43}$$

where

$$\alpha = k_x x + k_y y - \omega t + \epsilon \tag{3.44}$$

in which A is the wave amplitude, x and y are space coordinates in the $\hat{x}$ and $\hat{y}$ directions, respectively, ϵ is the phase difference and t is time.

The wave frequency ω is related to wave number and water depth as following for shallow/intermediate waves:

$$\omega = \sqrt{gk\tanh(kd)} \tag{3.45}$$

The wave induced velocity components in the $\hat{x}$, $\hat{y}$ and $\hat{z}$ directions are described as follows for shallow/intermediate waves:

$$\begin{pmatrix} u \\ v \end{pmatrix} = \frac{gkA}{\omega} \frac{\cosh[k(z+d)]}{\cosh(kd)} \begin{pmatrix} \cos\theta \\ \sin\theta \end{pmatrix} \cos\alpha \tag{3.46}$$

$$w = \frac{gkA}{\omega} \frac{\cosh[k(z+d)]}{\cosh(kd)} \sin\alpha \tag{3.47}$$

For higher order (second to fifth orders) wave theories, the generalized expression for surface elevation is:

$$\begin{aligned} \zeta(X,t) = {} & A\cos\alpha + A^2k(b_{22} + A^2k^2b_{24})\cos 2\alpha + A^3k^2(b_{33} + A^2k^2b_{35})\cos 3\alpha \\ & + A^4k^3b_{44}\cos 4\alpha + A^5k^4b_{55}\cos 5\alpha \end{aligned} \tag{3.48}$$

The generalized expression for the associated velocity potential is:

$$\Phi(X,t) = c \begin{bmatrix} A(a_{11} + A^2k^2a_{13} + A^4k^4a_{15})\cosh kd \sin\alpha + \\ A^2k(a_{22} + A^2k^2a_{24})\cosh 2kd \sin 2\alpha + \\ A^3k^2(a_{33} + A^2k^2a_{35})\cosh 3kd \sin 3\alpha + \\ A^4k^3(a_{44})\cosh 4kd \sin 4\alpha + \\ A^5k^4(a_{55})\cosh 5kd \sin 5\alpha \end{bmatrix} \tag{3.49}$$

The wave frequency is:

$$\omega = [gk(1 + A^2k^2c_3 + A^4k^4c_5)\tanh kd]^{1/2} \tag{3.50}$$

The wave induced velocity components are:

$$u = \frac{\partial\Phi}{\partial x}\cos\theta \tag{3.51}$$

$$v = \frac{\partial\Phi}{\partial x}\sin\theta \tag{3.52}$$

$$w = \frac{\partial\Phi}{\partial z} \tag{3.53}$$

When wave-current interaction is taking place, the effective wave frequency (ω_e) is defined as:

$$\omega_e = \omega + \vec{K}\vec{U} \tag{3.54}$$

where $\vec{U}$ is the averaged velocity of the flow current.

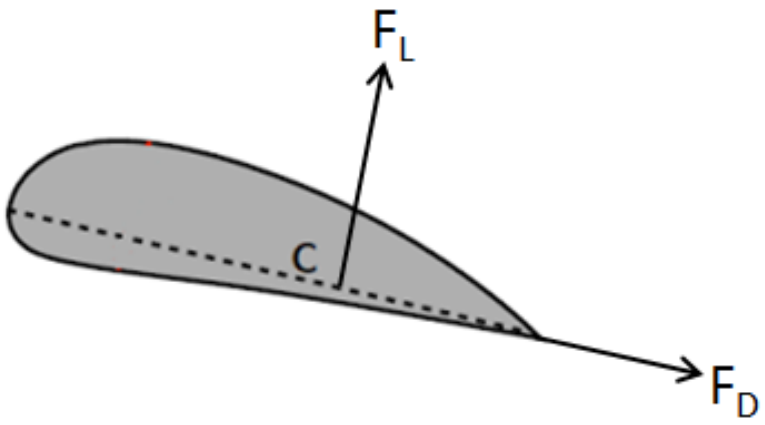

Figure 3.1: Schematic diagram of the lift and drag forces.

The final velocity vector is represented as:

$$\vec{V} = \vec{U} + u\hat{x} + v\hat{y} + w\hat{z} \tag{3.55}$$

Once the wave is generated at the upstream boundary, it will propagate downstream governed by the fluid dynamics until it reaches the downstream boundary and dissipates outside the domain. In addition to the waves, the steady current is also produced by a given inflow velocity at the upstream boundary.

3.2.4 Representation of HATT

The Virtual Blade Model (VBM) is adopted in this research to simulate HATT in FLUENT. It requires a reasonable computational cost, but still models the turbulent wake downstream of a turbine with acceptable approximation [78]. In VBM, the actual blades are not directly present. Instead, the rotor is simulated inside a rotor disk fluid zone across which the virtual blades swipe. The virtual blades are achieved through adding a body force in the x, y and z direction. This method is an application of a built-in blade simulating scheme — Blade Element Method (BEM) — within ANSYS FLUENT. In BEM, each blade is divided into small sections from root to tip. The lift and drag forces exerted on each segment (see Figure 3.1) are calculated based on the blade design as well as the lift and drag coefficients of each section:

$$f_{L,D} = c_{L,D} \cdot c(r/R) \cdot \frac{\rho \cdot V_{tot}^2}{2} \tag{3.56}$$

where $c_{L,D}$ is lift/drag coefficient specified by the user; $c(r/R)$ is the chord length; ρ is the fluid density and V_{tot} is the fluid velocity relative to the blade.

The lift and drag forces are then averaged over a full turbine rotation to calculate the force on each cell in the discretized domain:

$$F_{L,D_{cell}} = N_b \cdot \frac{dr \cdot d\theta}{2\pi} \cdot f_{L,D} \tag{3.57}$$

$$\vec{S}_{cell} = -\frac{\vec{F}_{cell}}{V_{cell}} \tag{3.58}$$

where N_b is the number of blades and V_{cell} is the volume of a grid cell.

Developed initially to model the aerodynamics of rotors [137], VBM has been applied in a number of tidal turbine studies [9, 10, 78, 113, 120]. The major disadvantage of VBM, as pointed out by [113], is that the flow characteristics in the near-wake field is poorly captured due to two reasons: first, the blade geometry is not directly present and second, the effects of the blade on the flow is averaged over a full rotation circle. Another noticeable problem with VBM is that among the three sources of turbulent mixing downstream of the rotating turbine, the ambient turbulence, the wake edge shear generated turbulence and the mechanical turbulence caused by the blade in the form of tip and hub vortex and the blade trailing edge wake [22], the last one is not yet accounted for in the VBM approach, which leads to under-predicted TKE level behind the turbine as mentioned above. However, the overall performance of the approach is satisfactory, as shown in later chapters. For the present study, the CFD model is used to generate calibration data for the oceanographic model in the far field simulation. Its accuracy within 1D-4D distance from the turbine is less critical as discussed in later sections.

3.3 Three-dimensional FVCOM — The Unstructured Grid Finite Volume Community Ocean Model

FVCOM is selected to model the impacts of tidal stream devices on the coastal region in this research. FVCOM is a three-dimensional, free surface, terrain-following oceanographic scale model for solving shallow water equations numerically using the finite-volume method [25]. There are several considerations for choosing FVCOM as the basic modelling tool in the present work: firstly, the model system includes fully coupled wave-current-sediment modules that is critical for any realistic far field modelling at a coastal regional scale; secondly, the unstructured triangular mesh which is advantageous to mesh size transition is used to discretise computational domains. Such a treatment in spatial descretisation is particularly important in the present model so that the mesh can be refined to particular high resolution around individual turbine site to resolve the small-scale impacts and maintain a smooth transition to a fairly large mesh size at far region so that the total computational costs can be restricted; thirdly, the FVCOM is maintained as an open source code so that the users can access the full model system without any restrictions, which make the necessary modification

of the code straightforward; fourthly, FVCOM comes with a three-dimensional turbulence closure 'MY 2.5' which is suitable for implementing the turbine effects as well as oceanographic scale simulations.

3.3.1 Modelling current

In Cartesian coordinates, without taking into consideration snow and ice, the governing equations of FVCOM are:

$$\frac{\partial u}{\partial t}+u\frac{\partial u}{\partial x}+v\frac{\partial u}{\partial y}+w\frac{\partial u}{\partial z}-fv=-\frac{1}{\rho_0}\frac{\partial(P_H+P_a)}{\partial x}-\frac{1}{\rho_0}\frac{\partial q}{\partial x}+\frac{\partial}{\partial z}(K_m\frac{\partial u}{\partial z})+F_x \quad (3.59)$$

$$\frac{\partial v}{\partial t}+u\frac{\partial v}{\partial x}+v\frac{\partial v}{\partial y}+w\frac{\partial v}{\partial z}+fu=-\frac{1}{\rho_0}\frac{\partial(P_H+P_a)}{\partial x}-\frac{1}{\rho_0}\frac{\partial q}{\partial y}+\frac{\partial}{\partial z}(K_m\frac{\partial v}{\partial z})+F_y \quad (3.60)$$

$$\frac{\partial w}{\partial t}+u\frac{\partial w}{\partial x}+v\frac{\partial w}{\partial y}+w\frac{\partial w}{\partial z}=-\frac{1}{\rho_0}\frac{\partial q}{\partial z}+\frac{\partial}{\partial z}(K_m\frac{\partial w}{\partial z})+F_w \quad (3.61)$$

$$\frac{\partial u}{\partial x}+\frac{\partial v}{\partial y}+\frac{\partial w}{\partial z}=0 \quad (3.62)$$

where x, y, and z are the east, north, and vertical axes in the Cartesian coordinate system; u, v, and w are the three velocity components in the x, y, and z directions respectively; ρ_0 is water density; P_a is the air pressure at sea surface; P_H is the hydrostatic pressure; q is the non-hydrostatic pressure; f is the Coriolis parameter and K_m is the vertical eddy viscosity coefficient. F_x, F_y represent the horizontal momentum, thermal, and salt diffusion terms. The total water column depth is $h=H+\zeta$, where H is the bottom depth and ζ is the height of the free surface.

The surface and bottom boundary conditions for u, v, and w are:

$$K_m(\frac{\partial u}{\partial z},\frac{\partial v}{\partial z})=\frac{1}{\rho_0}(\tau_{sx},\tau_{sy}), w=\frac{\partial\zeta}{\partial t}+u\frac{\partial\zeta}{\partial x}+v\frac{\partial\zeta}{\partial y}+\frac{E-P}{\rho}, \qquad z=\zeta(x,y,t) \quad (3.63)$$

$$K_m(\frac{\partial u}{\partial z},\frac{\partial v}{\partial z})=\frac{1}{\rho_0}(\tau_{bx},\tau_{by}), w=-u\frac{\partial H}{\partial x}-v\frac{\partial H}{\partial y}, \qquad z=-H(x,y) \quad (3.64)$$

where (τ_{sx},τ_{sy}) and $(\tau_{bx},\tau_{by})=C_d\sqrt{u^2+v^2}(u,v)$ are the x and y components of surface wind and bottom stresses. The drag coefficient C_d is determined by matching a logarithmic bottom layer to the model at a height z_{ab} above the bottom:

$$C_d=max\left(\frac{k^2}{ln^2\left(\frac{z_{ab}}{z_0}\right)},0.0025\right) \quad (3.65)$$

where $k=0.4$ is the von Karman constant and z_0 is the bottom roughness parameter.

3.3.2 Modelling turbulence

FVCOM contains a three-dimensional MY-2.5 turbulence closure module which is used in the current research and the controlling equations of this module are briefly introduced as following:

$$\frac{\partial q^2}{\partial t} + u\frac{\partial q^2}{\partial x} + v\frac{\partial q^2}{\partial y} + w\frac{\partial q^2}{\partial z} = 2(P_s + P_b - \varepsilon) + \frac{\partial}{\partial z}(K_q\frac{\partial q^2}{\partial z}) + F_q \tag{3.66}$$

$$\frac{\partial q^2 l}{\partial t} + u\frac{\partial q^2 l}{\partial x} + v\frac{\partial q^2 l}{\partial y} + w\frac{\partial q^2 l}{\partial z} = lE_1(P_s + P_b - \frac{\tilde{W}}{E_1}\varepsilon) + \frac{\partial}{\partial z}(K_q\frac{\partial q^2 l}{\partial z}) + F_l \tag{3.67}$$

where $q^2 = (u'^2 + v'^2)/2$ is the turbulent kinetic energy; l is the macroscale; K_q is the vertical eddy diffusion coefficient of the turbulent kinetic energy; F_q and F_l represent the horizontal diffusion of the turbulent kinetic energy and macroscale; $P_s = K_m(u_z^2 + v_z^2)$ and $P_b = (gK_h\rho_z)/\rho_0$ are the shear and buoyancy production terms of turbulent kinetic energy; $\varepsilon = q^3/B_1 l$ is the turbulent kinetic energy dissipation rate; $W = 1 + E_2 l^2/(\kappa L)^2$ is a wall proximity function where $L^{-1} = (\zeta - z)^{-1} + (H + z)^{-1}$; $\kappa = 0.4$ is the von Karman constant. F_q and F_l are parameterized using the Smagorinsky eddy parameterization method [108]. A constant value can also be assigned to the horizontal diffusion coefficient in FVCOM, which means the turbulence closure model can be run with both F_q and F_l set to zero.

The turbulent kinetic energy and macroscale equations are closed by defining:

$$K_m = lqS_m, \quad K_h = lqS_h, \quad K_q = 0.2lq \tag{3.68}$$

Terms S_m and S_h are stability functions calculated through:

$$S_m = \frac{0.4275 - 3.354G_h}{(1 - 34.676G_h)(1 - 6.127G_h)} \tag{3.69}$$

$$S_h = \frac{0.494}{1 - 34.676G_h} \tag{3.70}$$

where $G_h = \frac{l^2 g}{q^2 \rho_0}\rho_z$. This is the simplified version of the MY-2.5 turbulent model in which S_m and S_h depend only on G_h. An upper bound of 0.023 for the case of unstable ($\rho_z > 0$) stratification and a lower bound of -0.28 for the case of stable ($\rho_z < 0$) stratification are assigned to G_h [41].

The surface and bottom boundary conditions for the turbulent kinetic energy and macroscale equations are:

$$q^2 l = 0, \quad q^2 = B_1^{\frac{2}{3}} u_{\tau s}^2, \qquad z = \zeta(x, y, t) \tag{3.71}$$

$$q^2 l = 0, \quad q^2 = B_1^{\frac{2}{3}} u_{\tau b}^2, \qquad z = -H(x, y) \tag{3.72}$$

where $u_{\tau s}$ and $u_{\tau b}$ are the water friction velocities associated with the surface and bottom. Since $q^2 \neq 0$ at the surface and bottom, $l = 0$ at both boundaries, which means K_m, K_h and K_q are always 0 at the surface and bottom.

3.3.3 Modelling waves

To simulate surface wave propagation, Simulating Waves Nearshore (SWAN) [17] is integrated with FVCOM. The reason to choose SWAN is based on a few considerations: firstly, SWAN is designed for simulating wave propagating in coastal regions, with nearly all processes included, e.g. shoaling, breaking, diffraction, refraction, wave-wave interaction and wave-current interactions. Secondly, the same unstructured mesh used by FVCOM can be used directly by SWAN, which saves considerable efforts in data storage and exchange between modules. Thirdly, the inclusion of tidal stream turbines in the module can be implemented straightforwardly in SWAN as discussed in later sections.

The governing equation of the wave action density spectrum is given as follows:

$$\frac{\partial N}{\partial t} + \bigtriangledown \cdot \left[\left(\vec{C}_g + \vec{V}\right) N\right] + \frac{\partial C_\sigma N}{\partial \sigma} + \frac{\partial C_\theta N}{\partial \theta} = \frac{S_{tot}}{\sigma} \tag{3.73}$$

where N is the wave action density spectrum, t is the time, $\vec{C}_g$ is the group velocity vector, $\vec{V}$ is the ambient water current vector, σ is the relative frequency, θ is the wave direction and C_σ and C_θ are the wave propagation velocities in frequency space and directional space respectively. $S_{(tot)}$ is the source-sink term considering wind-induced wave growth, wave decay due to white capping, wave decay due to bottom friction and wave decay due to depth-induced wave breaking. More details are available in the SWAN technical manual [116].

3.3.4 Bottom boundary layer

Due to the presence of surface waves, the bottom boundary layer is affected and the shear stress is much higher than that due to current alone [65]. To take this into account, a special treatment is needed close to the bed, which is implemented in the bottom boundary layer module (BBL). BBL calculates the bottom shear stresses under the condition of combined waves and currents. The calculation of bottom shear stress is important as it influences the flow field as well as determines the suspension rate of suspended sediment and the transport rate of bedload sediment. The BBL module developed by [127] based on the theory proposed by [69] was converted into an unstructured-grid finite-volume version and implemented in FVCOM. It is, hence, used in the present research. This section discusses this BBL model in brief. More details can be found in [127].

The BBL model calculates the current component of the maximum wave-current combined bottom shear stress (τ_c), the wave component of the maximum wave-current combined bottom shear stress (τ_w) and the maximum wave-current combined bottom shear stress due to waves and currents (τ_{cw}):

$$\tau_c = u_{*c}^2 \tag{3.74}$$

$$\tau_w = u_{*w}^2 \tag{3.75}$$

$$\tau_{cw} = u_{*cw}^2 \tag{3.76}$$

where u_{*c}, u_{*w} and u_{*cw} are friction velocities due to current, waves and combined waves and current respectively calculated iteratively according to [69] as following:

$$u_{*c} = \frac{u_{*cw}}{2} \frac{ln(\frac{z_r}{\delta_{wc}})}{ln(\frac{\delta_{wc}}{z_0})}(-1 + \sqrt{1 + \frac{4\kappa ln(\frac{\delta_{wc}}{z_0})}{ln(\frac{z_r}{\delta_{wc}})^2} \frac{u_{cr}}{u_{*cw}}}) \tag{3.77}$$

where u_{cr} is current velocity at reference elevation z_r from the current model; δ_{wc} is wave boundary layer (WBL) thickness determined by:

$$\delta_{wc} = \begin{cases} 2\kappa u_{*cw}/\omega_r & for \quad C_\mu u_{br}/(k_N \omega_r) > 8 \\ k_N & for \quad C_\mu u_{br}/(k_N \omega_r) < 8 \end{cases} \tag{3.78}$$

where u_{br} and ω_r are wave-orbital velocity amplitude outside WBL and angular wave frequency respectively from the wave model; $k_N = 30.0 z_0$ is the equivalent Nikuradse roughness of the bottom; the total bottom roughness length z_0 is calculated as follows:

$$z_0 = z_{0N} + z_{0ST} + z_{0BF} \tag{3.79}$$

where z_{0N}, z_{0ST} and z_{0BF} are roughness lengths associated with grain roughness, sediment transport and bedform respectively. They are estimated as:

$$z_{0N} = 2.5 D_{50}/30 \tag{3.80}$$

$$z_{0ST} = \alpha D_{50} a_1 \frac{T_*}{1 + a_2 T_*} \tag{3.81}$$

$$z_{0BF} = a_r \eta_r^2 / \lambda_r \tag{3.82}$$

where $\alpha = 0.056$, $a_1 = 0.068$ and $a_2 = 0.0204 ln(100 D_{50}^2) + 0.0709 ln(100 D_{50})$ are sediment-transport coefficients according to [132]; D_{50} is the median grain diameter; a_r is set as 0.267 which was suggested in [86]; T_* is the ratio of τ_{cw} calculated from the previous time step and the bottom critical erosion stress τ_{ce}; η_r and λ_r are ripple height and ripple wavelength calculated using information from the previous time step according to [131].

Term C_μ in Equation 3.78 is calculated according to:

$$C_\mu = (1 + 2\mu |cos(\phi_{cw})| + \mu^2)^{1/2} \tag{3.83}$$

where ϕ_{cw} is the angle between current direction and direction of wave propagation and μ is defined as:

$$\mu = \tau_c / \tau_w = \frac{u_{*c}^2}{u_{*w}^2} \tag{3.84}$$

The determining factor in Equation 3.78 is also used to calculate f_{wc}, namely wave friction factor, which is used in u_{*w} calculation:

$$u_{*w} = (0.5 f_{wc} u_{br}^2)^{1/2} \tag{3.85}$$

$$f_{wc} = \begin{cases} C_\mu exp\left\{7.02(\frac{C_\mu u_{br}}{k_N \omega_r})^{-0.078} - 8.82\right\} & for \quad 0.2 < C_\mu u_{br}/(k_N \omega_r) < 10^2 \\ C_\mu exp\left\{5.61(\frac{C_\mu u_{br}}{k_N \omega_r})^{-0.109} - 7.30\right\} & for \quad 10^2 < C_\mu u_{br}/(k_N \omega_r) < 10^4 \end{cases} \tag{3.86}$$

The maximum wave-current combined bottom shear stress due to waves and currents (τ_{cw}) is then defined as:

$$u_{*cw} = (C_\mu u_{*w}^2)^{1/2} \tag{3.87}$$

3.3.5 Modelling suspended sediment transport

The suspended sediment transport is calculated in FVCOM by integrating flow velocity and suspended sediment concentrations over the depth. The controlling equation for the concentration-based suspended load calculation is as following:

$$\begin{aligned} \frac{\partial C_i}{\partial t} + \frac{\partial u C_i}{\partial x} + \frac{\partial v C_i}{\partial y} + \frac{\partial \left(w - w_i\right) C_i}{\partial z} = \frac{\partial}{\partial x}\left(A_H \frac{\partial C_i}{\partial x}\right) \\ + \frac{\partial}{\partial y}\left(A_H \frac{\partial C_i}{\partial y}\right) + \frac{\partial}{\partial z}\left(K_h \frac{\partial C_i}{\partial z}\right) \end{aligned} \tag{3.88}$$

where C_i is the concentration of the ith sediment class; A_H the horizontal eddy viscosity; K_h the vertical eddy viscosity and w_i the settling velocity of the ith sediment class. A sediment flux boundary condition is used at the bottom as:

$$K_h \frac{\partial C_i}{\partial z} = E_i - D_i \tag{3.89}$$

where E_i and D_i are the erosion and depositional rates respectively. The erosion rate E_i is calculated as following:

$$E_i = \triangle t Q_i \left(1 - P_b\right) F_{bi} \left(\frac{\tau_b}{\tau_{ci}} - 1\right) \tag{3.90}$$

where Q_i is the erosive flux; P_b the bottom porosity; F_{bi} the fraction of the ith sediment class in the bottom; τ_b the bottom shear stress and τ_{ci} the critical shear stress of the ith sediment class. Without waves, the calculation of bottom shear stress τ_b is explained in Section 3.3.1. With waves, it equals τ_{cw} introduced in Section 3.3.4. The depositional rate D_i is calculated by solving the convection-diffusion equation.

It should be noted that total sediment transport consists of suspended and bedload sediment transport. However, bedload sediment transport is not yet considered in this research due to the reason that the bedload sediment transport module of FVCOM is not fully developed. Two published works in the literature that modelled bedload sediment transport using FVCOM reported development of the bedload sediment transport module [31, 135]. However, it is beyond the scope of this project to develop the bedload sediment transport module itself. Therefore, bedload sediment transport is recommended as future work.

3.3.6 Wave-current-sediment coupling

FVCOM includes a wave-current-sediment fully coupled system. Figure 3.2 is the flow chart of the coupling scheme. After initialization, the wave model starts to solve the wave dynamics, providing information of significant wave height (H_s), wave direction (Dir), average wave length (L), surface wave relative peak period (T_p), wave bottom orbit velocity (U_b), bottom wave period (T_b) and so on.

The interactions between the current model and the wave model are achieved through radiation stress terms according to Mellor's theory [73, 74, 75]. The momentum equations in the current model (Equation 3.59 and Equation 3.60) become:

$$\begin{aligned}\frac{\partial u}{\partial t}+u\frac{\partial u}{\partial x}+v\frac{\partial u}{\partial y}+w\frac{\partial u}{\partial z}-fv=&-\frac{1}{\rho_0}\frac{\partial(P_H+P_a)}{\partial x}-\frac{1}{\rho_0}\frac{\partial q}{\partial x}\\&+\frac{\partial}{\partial z}(K_m\frac{\partial u}{\partial z})+F_x-\frac{\partial S_{xx}}{\partial x}-\frac{\partial S_{xy}}{\partial y}+\frac{\partial S_{px}}{\partial z}\end{aligned} \tag{3.91}$$

$$\begin{aligned}\frac{\partial v}{\partial t}+u\frac{\partial v}{\partial x}+v\frac{\partial v}{\partial y}+w\frac{\partial v}{\partial z}+fu=&-\frac{1}{\rho_0}\frac{\partial(P_H+P_a)}{\partial x}-\frac{1}{\rho_0}\frac{\partial q}{\partial y}\\&+\frac{\partial}{\partial z}(K_m\frac{\partial v}{\partial z})+F_y\frac{\partial S_{yx}}{\partial x}-\frac{\partial S_{yy}}{\partial y}+\frac{\partial S_{py}}{\partial z}\end{aligned} \tag{3.92}$$

where S_{xx}, $S_{xy}=S_{yx}$, S_{yy}, S_{px} and S_{py} are radiation stress terms. The detailed form of these radiation stress terms is introduced in [74].

Results from the current model, velocities (u, v) and surface elevation (ζ) in particular, provide the wave model feedback for the next time step calculation. Results from the above mentioned models then will be sent to the bottom-boundary layer (BBL) model (see Section 3.3.4) to calculate the bottom stresses under the combined influence of waves, current and, theoretically, sediment transport. These stresses are then used to solve the momentum equations in the current model and suspended and bedload transport in the sediment transport model.

3.3.7 Numerical method of FVCOM

Grids

FVCOM discretizes its calculation domains into unstructured triangles on the horizontal plane and divides the water column into layers using a terrain-following σ-coordinate system. Figure 3.3 illustrates the unstructured triangular grid design in FVCOM. Solid circles are mesh nodes on which scaler variables such as water depth and free surface elevation are calculated. Three nodes decide an unstructured triangle. Lines connecting nodes are the sides of triangles. Another typical calculation location is the centroid of the triangles denoted by circles with crosses in Figure 3.3. Calculation of u and v takes place on centroids. Using a finite volume approach, variables at the centroids are calculated based on the net flux through the three sides of the triangles. The triangles are consequently also called the 'momentum control elements'. Meanwhile, the shaded

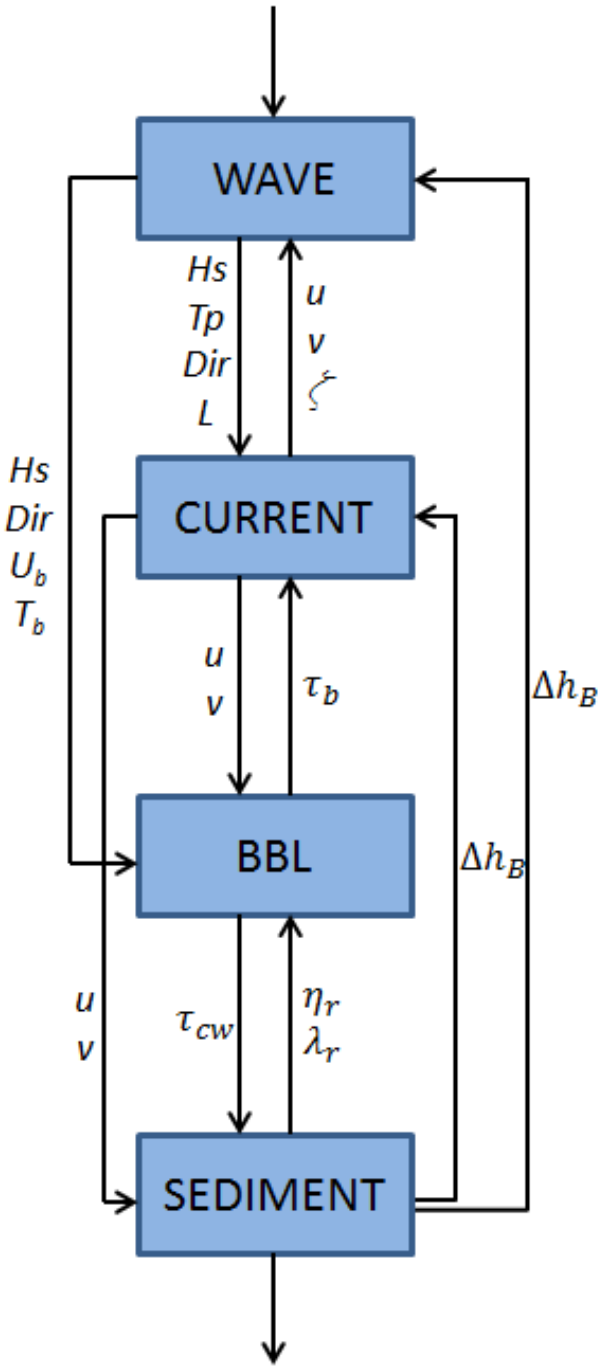

Figure 3.2: Coupling scheme of waves, current and sediment transport in FVCOM [24].

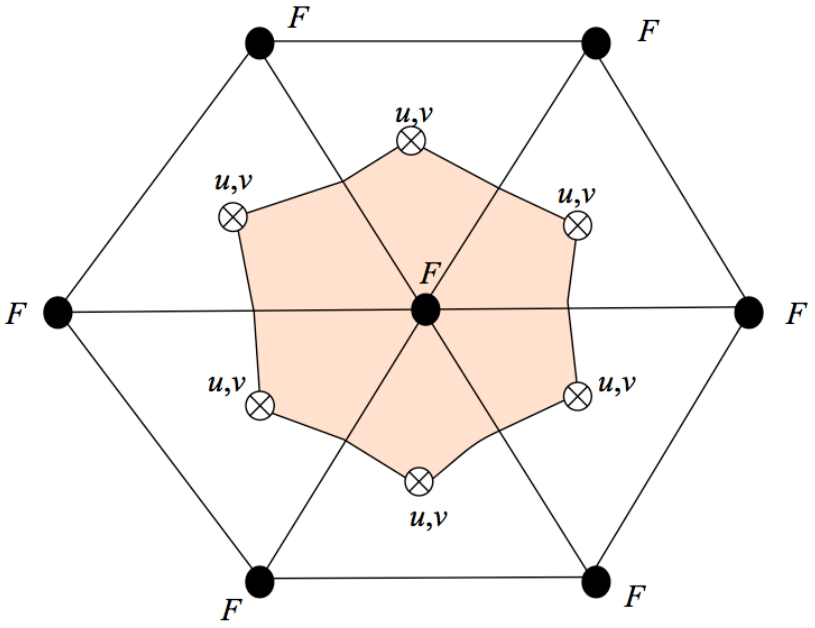

Figure 3.3: Unstructured triangular grids design in FVCOM [24].

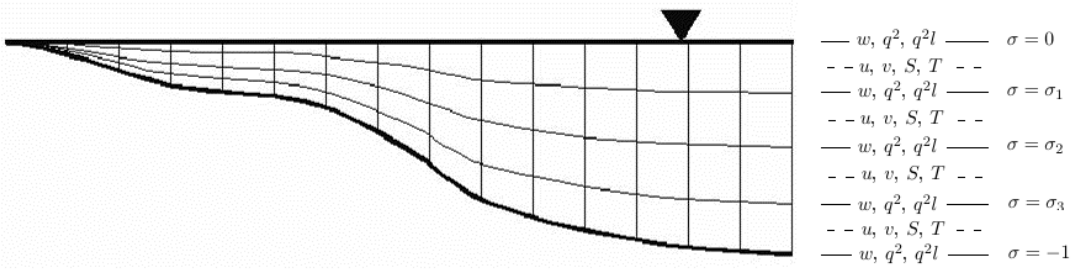

Figure 3.4: An example of σ-coordinate and locations of variables in the σ-coordinate.

area surrounded by lines connecting the centroids and the mid-points of the sides is a 'tracer control element'. A net flux through the sides of a 'tracer control element' determines the scalar variables being calculated. Figure 3.4 shows an example of σ-coordinates. All variables, except for vertical velocity (w) and turbulence variables such as q^2 and q^2l, are placed at the mid-level of each σ layer.

Discrete procedure

FVCOM applies a mode-split approach to solve the two-dimensional external mode and three-dimensional internal mode using two distinct time steps. The free surface elevation (ζ) is computed using vertically integrated equations in the two-dimensional external mode. The three-dimensional equations are then solved under the given free

surface elevation. A mode-split approach requires an adjustment to be made in every internal time step to ensure the conservation of the volume transport throughout the water column, unless the times steps of the two modes are equal to each other (see [24] for detailed explanation). In FVCOM, the correction is to adjust the internal velocities by distributing the difference between the external and vertically integrated internal water transport uniformly throughout the water column.

3.4 Representation of HATT in FVCOM

The aforementioned FVCOM provides this study the platform on which the HATT modelling is conducted. This section describes the modifications made to FVCOM to incorporate HATT's effects on current, turbulence, surface waves and sediment transport modelling.

3.4.1 Modelling HATT in current module

Deceleration of the passing flow, largely due to energy loss around the turbine as well as the blockage effect of the device, is widely recognized as the impact of a turbine on its ambient current. In this work, the energy extraction process is modelled based on the additional sink term put forward by [33] as:

$$F_u = -C_{ext} \cdot \frac{1}{2} \cdot \rho \cdot u \left|\vec{V}\right| \tag{3.93}$$

$$F_v = -C_{ext} \cdot \frac{1}{2} \cdot \rho \cdot v \left|\vec{V}\right| \tag{3.94}$$

where F_u and F_v are the additional sink term components per unit area; C_{ext} is the energy extraction coefficient which determines the strength of the sink term. These two terms are added onto the right hand side of Equations 3.59 and 3.60 respectively. It should be noted that the purpose of these modifications is not to simulate detailed hydrodynamics immediately around each individual turbine, but to represent the modified flow field at 4D-6D away from the turbine further downstream, i.e. the far field. The complex flow-structure interactions in the near field violate the basic assumption in oceanographic models like FVCOM, i.e. the pressure distribution across water depth is linear, resulting in the exclusion of non-hydrostatic pressure terms. This particular difficulty means that the predictions from FVCOM are hardly valid within the near field. But further downstream, i.e. 6D away from the structure, most existing data and available CFD modelling results suggest that the pressure distribution starts to recover towards a linear one. Therefore, the aim of the proposed modifications in the above-mentioned equations is to introduce accurate turbine effects to the passing flow beyond a far-field distance (6D) downstream of the device.

The present study identifies each individual turbine structure within a farm, rather than treating the entire turbine farm as a whole as discussed in previous studies. It is

therefore proposed that an unstructured mesh is used with particularly fine resolution at each turbine device site. In the present study, mesh size at the turbine sites is the diameter of the simulated device in each case. The triangular element in which the turbine device sits is selected to exert the energy extraction coefficient set (C_{ext}) across the water depth. Energy extraction coefficient of each sigma layer is treated individually in order to achieve a full three-dimensional representation of the flow field. Such an approach is very different from previously mentioned two-dimensional studies and the three-dimensional study in which a single value was assigned to one of the layers, both of which failed to distinguish the velocity difference across various depths due to the turbine presence.

It should be noted that FVCOM is a mode-split model which calculates the velocity in both the two-dimensional external and three-dimensional internal modes. To ensure the consistency of the two modes, an adjustment is made in every internal time step to the three-dimensional internal mode, according to the results of the two-dimensional mode. Therefore, the sink term is also added into the two-dimensional external mode. The corresponding depth averaged C_{ext} is used in the two-dimensional mode. The effective velocity terms modifying the velocity involved in the sink term calculation based on the angle between the hub of the turbine and the flow direction proposed by [1] is not adopted in this research, as it is assumed that the turbine may rotate to maintain a normal angle towards the incoming flow. Tidal turbines usually have an operational velocity window below which no power is generated and above which the power output is thresholded to the rated power output. The parameterization of this power limitation is discussed in detail in [91]. However, as the operating window is application-specific and this work simulates a hypothetical turbine, the limit on power output is not accounted for in the present study.

3.4.2 Modelling HATT in turbulent module

As mentioned in Section 2.5.4 there are three turbine incurred turbulence perturbations that are not accounted for in standard turbulence closures. In short, processes to be considered can be classified into three categories:

- Turbine-induced turbulence generation, P_{tp}

  The strong velocity gradient can generate additional turbulence in the wake region. Meanwhile, the swirling wake and the tip vortex within the near-wake also add kinetic energy to turbulence. The first type of turbulence is intrinsically handled by the shear production term P_s commonly seen in any 2-equation turbulence closure model, whereas the second type of TKE production needs an additional source term of TKE to be added onto the k transport equation when the details of turbine motion are not explicitly described. In the present research, following

[101], this additional source term of k is defined as proportional to the cube of flow velocity:

$$P_{tp} = C_{tp} \cdot \frac{u^3}{\Delta x} \tag{3.95}$$

- Turbine-induced turbulence dissipation, P_{td}

  The presence of a turbine is also believed to produce TKE of smaller length scale which can facilitate TKE dissipation into heat. This term is defined as proportional to the flow velocity multiplied by TKE in the present research following [101]:

$$P_{td} = C_{td} \cdot \frac{u \cdot k}{\Delta x} \tag{3.96}$$

- That of an interference for the turbulence length-scale (L), P_l

  Under the presence of a turbine, the turbulence field within the turbine near-wake will exhibit a reduced spectrum of length-scale due to the 'short-circuiting' of natural eddy cascade. As suggested by [101], this phenomenon could be addressed as enhancement of turbulence dissipation rate (ϵ) as mentioned in Section 2.5.4. However, because the present research uses the MY-2.5 turbulence closure which solves instead the TKE and length scale equations, a similar additional term defined as proportional to the TKE shear production is added to the right-hand side of the l equation:

$$P_l = C_l \cdot P_s \tag{3.97}$$

Terms C_{tp}, C_{td} and C_l in the aforementioned equations are coefficients decided empirically through parameter studies. The above mentioned terms are activated only at turbine locations.

3.4.3 Modelling HATT in wave module

More recent studies highlight the changes of wave dynamics around turbine sites, including the wave height reduction and wave length increase [113]. Such changes reflect the variation in energy propagation due to the presence of turbines underneath the water surface. In the present study, the wave height drop due to the inclusion of turbines is modelled using one of the built-in features of SWAN — OBSTACLE.

An obstacle is represented by a line between two locations across which wave energy is absorbed and dissipated as required (see Figure 3.5). Such an obstacle would reduce the wave height of waves propagating through or over the obstacle all along its length. The numerical realization of obstacles is given as the additional sink term as explained below.

The wave model will first determine which grid lines of the mesh cross the obstacle. In calculating the action densities for the target grid point (point 0 in Figure 3.6), if the line between the two grid points crosses the obstacle, the contribution of the

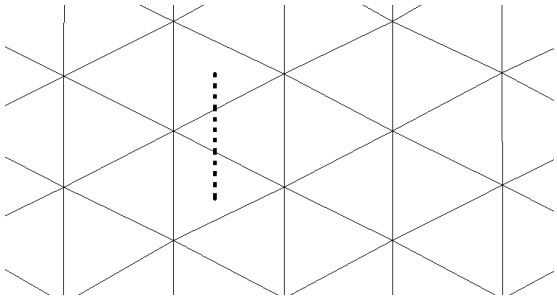

Figure 3.5: An obstacle as a line in computational grid.

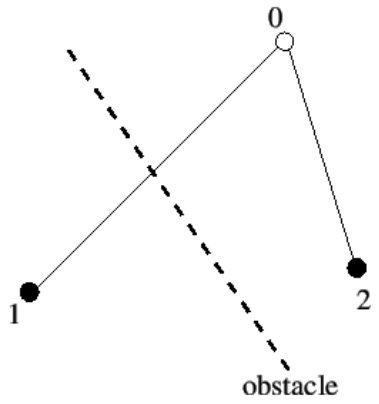

Figure 3.6: Schematic sketch of wave energy transmission in SWAVE.

neighbouring grid point (point 1 in Figure 3.6) is reduced by a constant transmission coefficient K_t. The value of K_t is decided by the user through parameter studies. When there is no obstacle crossing in between, the contribution from the neighbouring point in the computation of the target point is not reduced; K_t is taken as 1 in the calculation. See connection between point 2 and point 0 in Figure 3.6 as an example.

Applying OBSTACLE to model the effects of turbines on waves, the obstacles in the model take the diameter of the simulated turbine as their length, although the length of the obstacles should not cause any difference as long as the ends are in the same triangles. The obstacles are placed in a way that they pass through the centres and cross two sides of the triangles selected to exert retarding force, i.e. to locate turbines. The numerical realization procedure of OBSTACLE has also made the directions of the obstacles not a big concern; the results should be the same as long as the obstacles cross the same grid lines.

3.4.4 Modelling HATT in sediment module

Among the research reviewed in Section 2.4, some studies have already started to put attention on modelling the effects of tidal turbines on sediment transport. However, only the secondary effects on the sediment transport due to flow rate reduction were

analysed in these studies. The swirling effect of the turbine has not yet been considered. Unfortunately, laboratory experiment or CFD simulation is hardly found. This study, therefore, considers that the rotation of the turbine blades affects the immediate sediment transport in two ways: (1) it enhances the vertical transport of suspended sediment due to the additional vertical mixing caused by the rotating blades and (2) it increases the bottom shear stress and, consequently, the erosion rate at the bottom. The first influence is largely taken into account by enhancing turbulent mixing in the water column as shown previously. The additional bottom shear stress is assumed to have a similar form as equation $(\tau_{bx}, \tau_{by}) = C_d\sqrt{u^2 + v^2}(u, v)$ mentioned in Section 3.3.1, but also takes the vertical location of the turbine into account. This concept has the form as following:

$$\tau_r = C_r * U_r^2 * \frac{D}{z} \tag{3.98}$$

where τ_r is the additional bottom shear stress caused by the rotation of the turbine; C_r is a coefficient analogue to C_d; U_r is the tip speed of the turbine; D the diameter of the turbine and z is the distance between the lower tip of the blade and the sea bed. A simple linear combination of τ_b and τ_r is applied, leading to the total bottom shear stress (τ_{bt}) as:

$$\tau_{bt} = \tau_b + \tau_r \tag{3.99}$$

The value of C_r is chosen by the user.

3.5 Summary

This chapter introduced two different numerical modelling systems used in the present research — ANSYS FLUENT and FVCOM. As a small scale CFD solver, ANSYS FLUENT allows the geometry of the simulated objects, in this case tidal turbines, to be resolved in the mesh. However, instead of directly resolving the structure of the turbine in the mesh, the present study uses VBM to implement the rotational motion of turbine blades on a disc in the mesh, which is a good trade-off between accuracy and computational effort. The small-size mesh grid used in ANSYS FLUENT also means that turbulence, which is often a sub-grid process in oceanographic models, can be resolved and hence simulated at a higher level of accuracy. Among the available turbulence calculation approaches, $SST\ k-\omega$ closure in the middle range is used in the present research, again providing a good balance between accuracy and computational effort.

The three-dimensional oceanographic scale model, FVCOM, based on which the turbine simulation platform is developed is a thorough ocean-coast modelling package, including, but not limited to, fully coupled wave-current-sediment modules, a three-dimensional turbulence closure and a bottom boundary layer module devoted especially to the calculations near the bed under the presence of surface waves. The development of

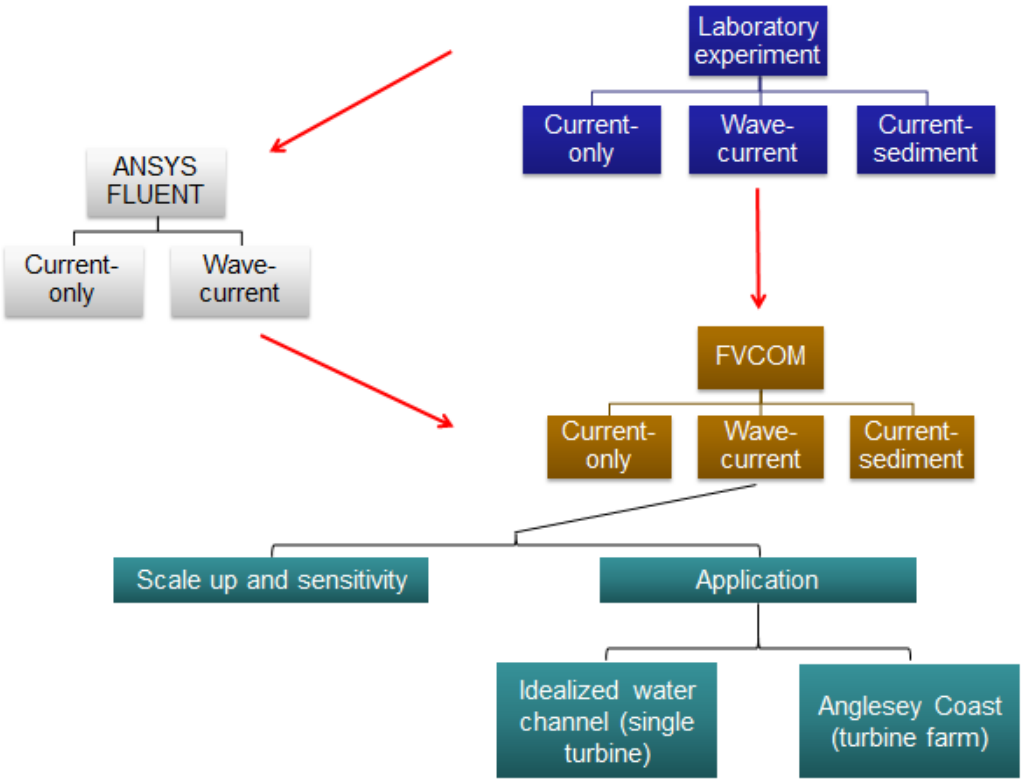

Figure 3.7: Work flow of the following chapters.

the turbine simulation platform involves the modules mentioned above. In summary, a body force is employed in the current module to simulate the turbine-induced water deceleration. Three terms are added into the three-dimensional MY-2.5 turbulence closure to model turbine-related turbulence generation, dissipation and turbulence length-scale interference. The built-in feature 'OBSTACLE' of the wave module is used to simulate the reduction of wave height caused by the turbine. An additional bottom shear stress term is added to represent the enhanced sediment suspension due to turbines in motion.

Figure 3.7 provides a flow chart for the work in the following chapters. Experimental work and ANSYS FLUENT (CFD) simulations, together providing data for coefficient calibration of the FVCOM model, are introduced in Chapter 4. In Chapter 5, the turbine-related coefficients for different physical scales are tested and the model's prediction over various values of the coefficients are studied. Application of the turbine simulation platform, to both a water channel (single turbine) and a UK coastal area (turbine farm), is introduced in Chapter 6.

Chapter 4

Model Calibration

4.1 Introduction

This chapter calibrates the coefficients involved in tidal stream device representation in the current, turbulence, waves and sediment modules of FVCOM according to experimental data and small scale CFD (ANSYS FLUENT) simulation results. The laboratory measurements include current-only [58], wave-current and current-sediment [95] conditions, providing the most reliable data for numerical model calibration and validation. However, these data are limited to a relatively small area around the rotor and measurements of certain variables. Therefore the small scale CFD solver ANSYS FLUENT is used to replicate the experiments and provide a wider range of data for FVCOM model calibration. Detailed discussion of FVCOM model calibration is presented in this chapter, after validation of the small scale CFD models.

4.2 Experimental conditions

The experiments took place at the University of Hull using their 'Environment Simulator Laboratory Flume' [58]. The flume is 11m long, 1.6m wide and 0.8m deep. A horizontal axis rotor with a diameter of 0.2m is mounted on a thin, rigid support that can be vertically re-located. Figure 4.1 provides a stream-wise view of the flume as well as the rotor. Figure 4.2 shows a side-view of the rotor and its housing structure. It can been seen that the rotor is connected to a rather thick cylinder which is part of the housing structure and the cylinder extends to about 1D downstream of the rotor. Details of these experiment settings are given below. Hydrodynamic and rotor settings are also listed concisely in Table 4.1.

4.2.1 Experiment - current only

In the current-only case, the water depth was 0.6m and the rotor was positioned at 300mm above the bed. The tip speed ratio (TSR) of the rotor was 5.5. The inlet flow velocity was 0.5m/s. The flume bed was constructed from marine plywood boards with

Figure 4.1: The 'Environment Simulator Laboratory Flume' and the rotor (provided by the University of Hull).

Figure 4.2: A side-look of the rotor and its housing structure (provided by the University of Hull).

Table 4.1: Hydrodynamic and rotor settings of the University of Hull experiments

Case name	Inlet flow rate	Wave period	Wave height	Hub location	Rotor diameter	TSR
Current-only	0.5 m/s	-	-	300mm above bed	0.2m	5.5
Wave-current	0.3 m/s	1s	0.15m	200mm above bed		
Current-sediment	0.5 m/s	-	-	150mm above sediment layer		

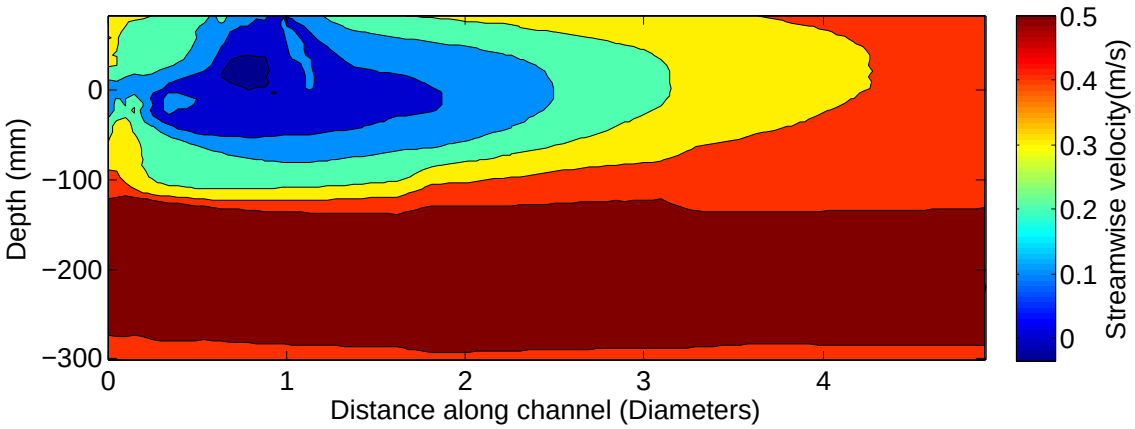

Figure 4.3: Streamwise velocity contour of the current-only case measured in the University of Hull experiment.

sand ($D_{50} = 425um$) fixed onto them to maintain a scaled bed roughness. Figure 4.3 is a contour image of the streamwise velocity of the current-only case produced based on the data collected in the laboratory. Measurements of velocities in three directions and TKE were taken along the centreline within 5D downstream of the rotor using a two-camera Particle Image Velocimetry (PIV) system, despite the fact that the flume length behind the rotor was much longer than 5D. On the figure, 0mm on the vertical axis represents the location of the rotor hub and depth below the hub is denoted by negative values. The contour shape around 1D downstream of the rotor and above 0mm clearly reflects the existence of the supporting structure as well as its effects on the water velocity. Due to the supporting structure, the streamwise velocity around the depth of 0mm drops to about 0m/s at 1D downstream of the rotor. The effects of the housing structure could reach beyond 1D behind the rotor.

4.2.2 Experiment - wave-current

In the combined wave with current case, the water depth was kept as 0.6m, the rotor was positioned at 200mm above the bed. The tip speed ratio (TSR) of the rotor was again 5.5. The bed roughness was kept the same as mentioned above. The inlet flow velocity reduced to 0.3m/s in this case. A sinusoidal wave with wave period of 1s and wave height of 0.15m was imposed at the inlet propagating in the same direction as the steady flow. The wave was generated using a wavemaker consisting of wave paddles. Measurements of velocities were taken along the centreline within 4D downstream of the rotor, using the same PIV system.

4.2.3 Experiment - current-sediment

In the current-sediment experiment, the water level was set at 0.5m above the rigid floor of the flume. A layer of sediment of 0.1m thick was placed on the floor of the flume. The sediment layer consisted of sand of about $425\mu m$ with density of 2650 kg/m^3. The rotor was located 0.15m above the surface of the sediment layer. The tip speed ratio (TSR) of the rotor was again 5.5 and flow velocity at the inlet was 0.5m/s ($u^*/u^*_{cr} = 5.9$). Measurements of streamwise velocity and sediment concentration were taken along the centreline at 5D, 7.5D, 10D, 12.5D and 15D downstream of the rotor, using an Acoustic Doppler Velocimeter (Nortek Vectrino). The suspended sediment concentration was measured using a Bedform and Suspended Sediment Imager [77].

4.3 CFD model validation

4.3.1 Current-only case

Model setup

This case models the current-only experiment aforementioned. The flume has the same dimension as the one in the laboratory. The water velocity is specified as a uniform speed of 0.5m/s at the inlet (upstream boundary). The rotor is located 300mm above the bed and 6.6m downstream from the inlet. Figure 4.4 and Figure 4.5 show the computational mesh for the channel and the rotor cross-section respectively. The calculation domain is discretized into 1.36M Hexa cells. Figure 4.6 shows the details of mesh distribution around the turbine rotor. The area the virtual blades swipe over is discretised by ring-shaped cells. The centre of the ring, where the hub is, is blocked by a shaft which simulates the cylinder which had significant influence on the near-field wake dynamics in the laboratory experiment.

Essential configurations of VBM, i.e. geometrical setup and running parameters of the rotor, are specified according to previous research [113] and are listed in Table 4.2 and Table 4.3, respectively. These settings are validated and shown to produce results that agree well with experimental measurements [113].

Table 4.2: Geometrical setup of the rotor

Radius (r/R)	Chord (m)	Twist (deg)
0.2	0.025	19
0.3	0.022	1
0.4	0.02	6
0.5	0.018	4
0.6	0.015	2
0.7	0.015	1.5
0.8	0.01	0.8
0.9	0.008	0.4
1.0	0.008	0

Table 4.3: Running parameters of the rotor

Parameter name	Value
Number of blades	3
Rotor radius	0.1m
TSR	5.5
Tip effect	96%
Blade pitch	4
Blade flapping	0

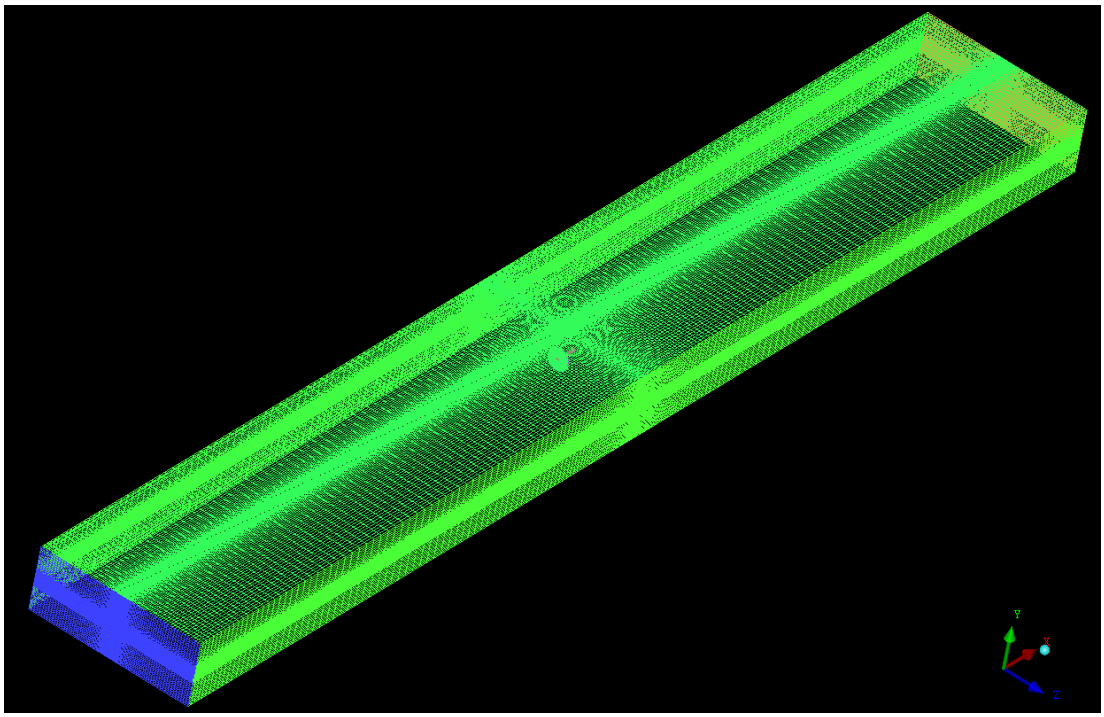

Figure 4.4: Surface mesh of the flume. The body mesh and mesh for the flume bed are deactivated.

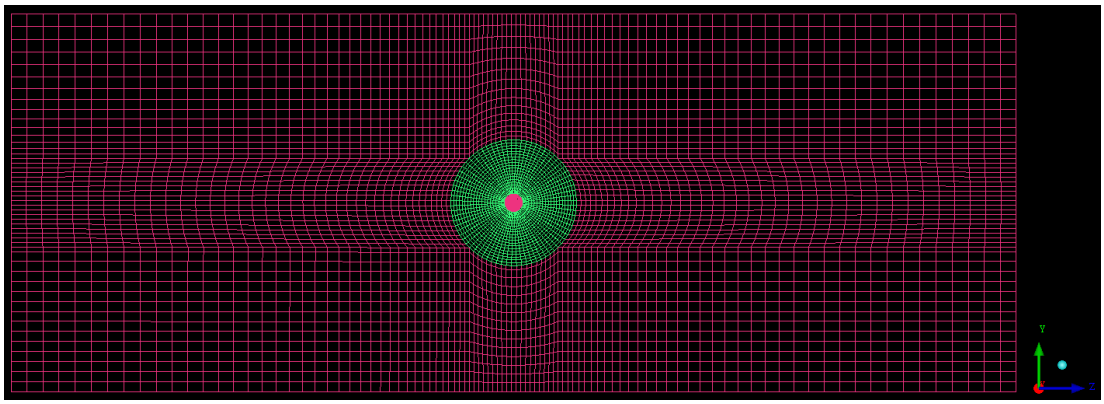

Figure 4.5: Mesh of the rotor cross-section.

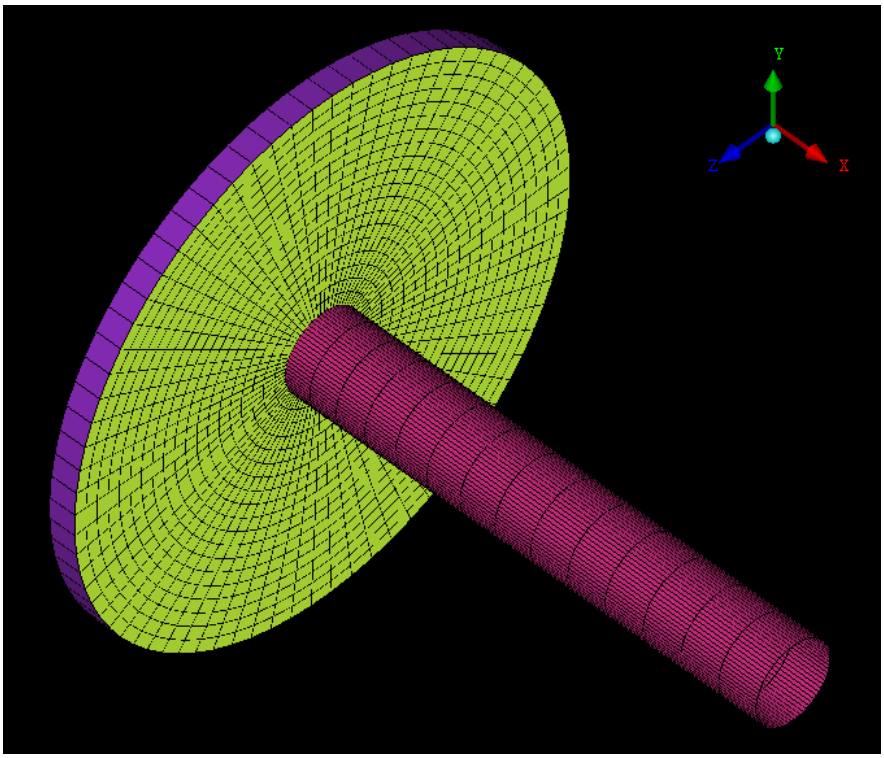

Figure 4.6: Shape and mesh of the disk on which VBM is implemented to simulate the rotor.

Table 4.4: $\%_{RMSE}$ for the two CFD cases against the experimental data

Cases	Velocity					TKE				
	1D	2D	3D	4D	5D	1D	2D	3D	4D	5D
Current-only	5.7	-	14.3	18.4	20.8	12.8	-	13.9	15.8	17.3
Wave-current	21.5	15.5	17.9	17.8	-	-	-	-	-	-

Results and discussion

As mentioned in the introduction, CFD models created here are mainly to produce a wider range of data for FVCOM model calibration. Hence, instead of discussing the hydrodynamic alterations brought up by the rotor, this section aims to validate the CFD model by comparing the predictions against the measurements [58], so that the results calculated by the CFD model can be used with confidence. Two diagnostic variables, streamwise water velocity and TKE, are selected to validate the model.

Velocity validation results are presented in Figure 4.7. It can be seen that the shaft modelled has effectively brought the velocity at the hub at 1D downstream of the rotor down to 0m/s which agrees with the observation in the laboratory. The velocity profiles at the other locations also match well with the laboratory data with root mean square error percentage ($\%_{RMSE}$) of 14.3 at 3D, 18.4 at 4D and 20.8 at 5D (These values are also presented in Table 4.4). $\%_{RMSE}$ is calculated according to the method described in [101]. However, the model predicted velocity below the rotor is consistently slightly slower than the measured data. This is largely due to the under-predicted near bed boundary layer effects in the model. In addition, the omission of experimental data within the region above the rotor also means the performance of the model in this area is uncertain. However, the overall agreements between the computed and measured velocities are considered to be satisfactory at all sites and the CFD model can be used to produce calibration data for the large scale FVCOM simulations.

The computed TKE results are compared with the measured data in Figure 4.8. At 1D downstream of the rotor, the modelled data follow the measurements very well, including the maximum and minimum values of TKE around the rotor position. Further downstream at 3D, 4D and 5D, the model predicted TKE profile shapes agree with those measured in the laboratory ($\%_{RMSE}$ refer to Table 4.4), i.e. the model is able to reproduce the enhanced turbulence at the rotor intercepted levels. The values at these levels, however, tend to be under-estimated by 15-20%. This is likely due to the CFD model not accounting for turbulence generated at the tip of rotor blades when in motion as mentioned in previous chapters. Similar findings are reported in [106] in which the TKE level is found to be underestimated by about 40% at 2D-6D downstream of the rotor simulated.

In general, the CFD predicted velocities in the region >4D downstream of the turbine can be used with confidence in later FVCOM model calibration while the TKE levels need to be used with caution.

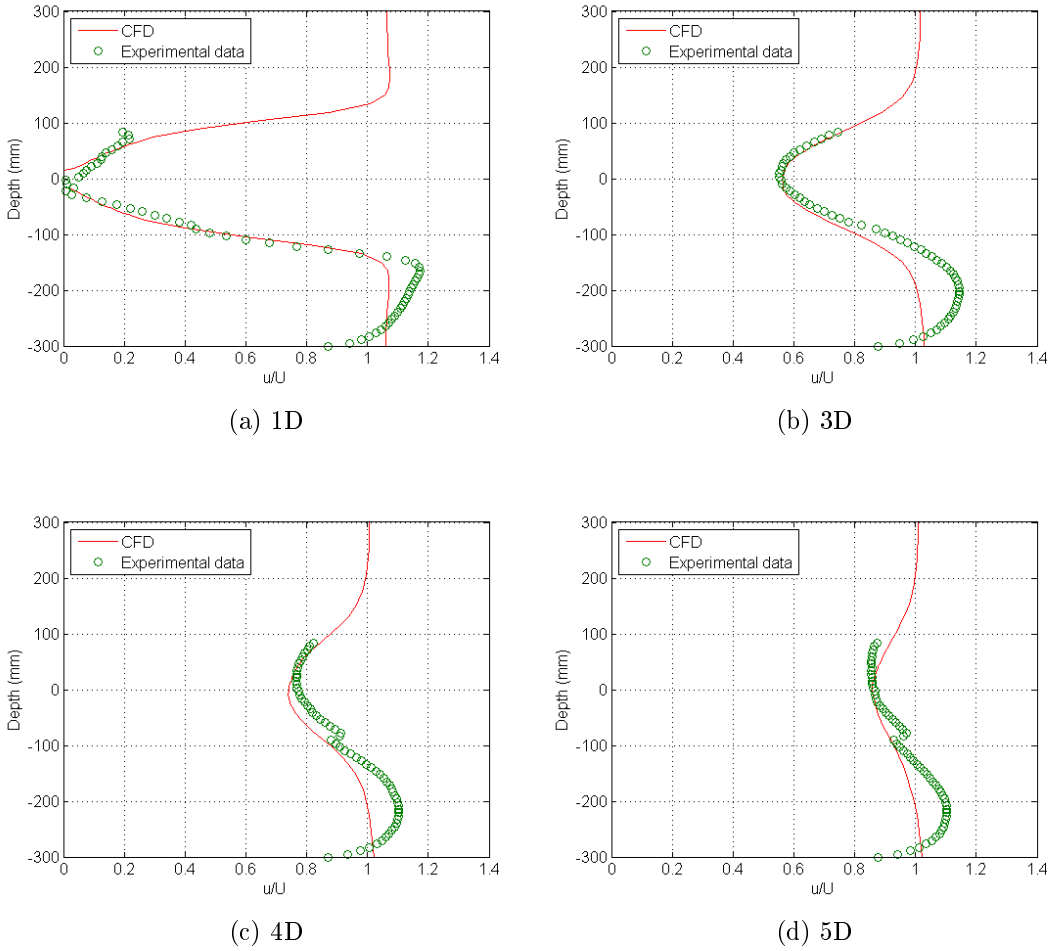

(a) 1D (b) 3D

(c) 4D (d) 5D

Figure 4.7: Normalized velocity profiles of the CFD case against those measured in the laboratory at 1D, 3D, 4D and 5D downstream of the rotor.

4.3.2 Wave-current cases

Model setup

Similar to the steady current case, the wave-current test aims to supplement the limited measurements taken in the laboratory. The numerical flume created in this case is 3.1m in length to reduce the computational time required. The total height of the flume is increased to 0.9m while the water depth is still 0.6m to accommodate the surface changes. The extra 0.3m above the water is defined as air zone which is required for multi-phase simulations. The width of the flume remains the same, so is the rotor design and running parameters. However, the rotor is located 200mm above the bed and the inflow velocity is set at 0.3m/s. These are set according to the properties of

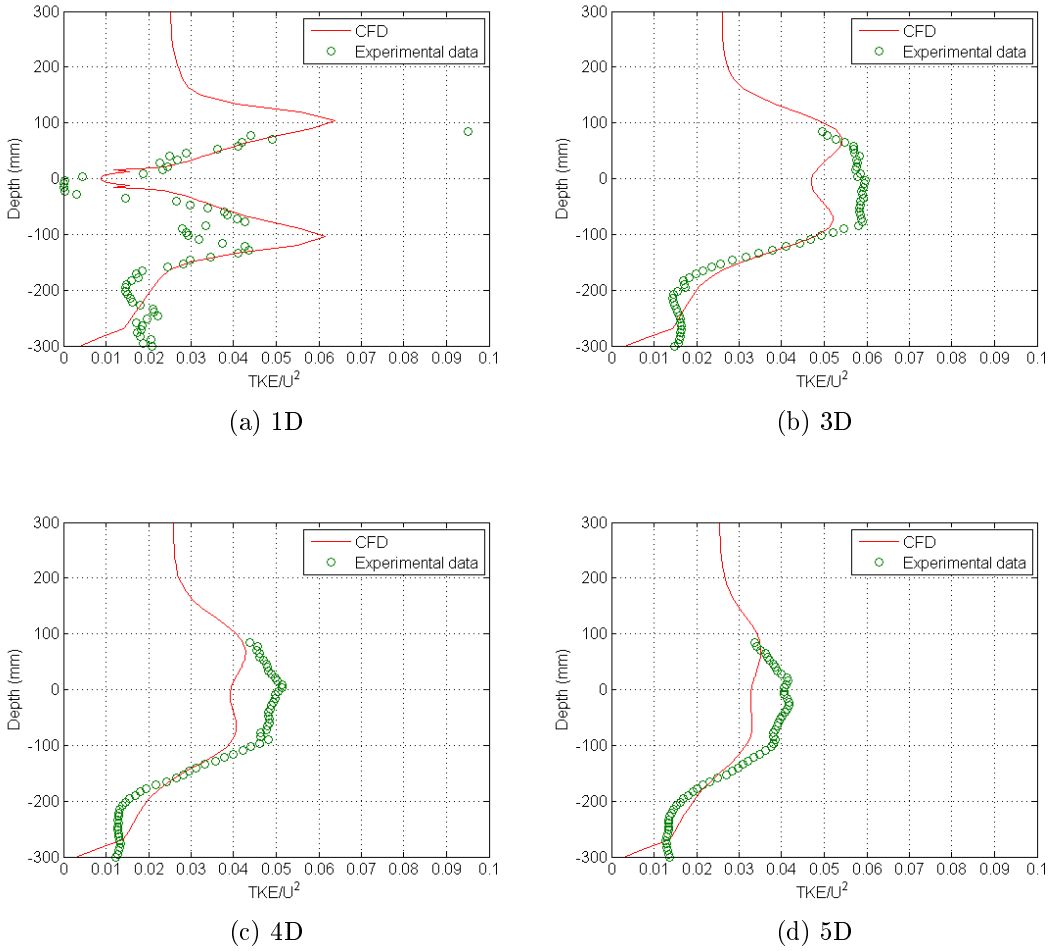

(a) 1D (b) 3D

(c) 4D (d) 5D

Figure 4.8: Normalized TKE profiles of the CFD case against those measured in the laboratory at 1D, 3D, 4D and 5D downstream of the rotor.

the provided data (see Table 4.1). The entire calculation domain is descretized to 1.8M Hexa cells with a vertical resolution of 2mm ($\leq$ 1/30 wave height) to reduce intrinsic wave decay as it propagates to the minimum. To reduce the wave energy being reflected back into the flume from the exit, three porous zones, with thickness of 0.2m, 0.2m and 0.1m, are set at the outlet boundary, with porosity declining from 0.95 to 0.9 to 0.8.

In total, five different cases are tested in this section, for different purposes: Case 1 is to test the reliability of waves produced by FLUENT. A linear wave (wave height of 0.06m) is used in this case, as it is easier to validate a linear wave; Case 2 is to provide the baseline conditions against which results of Case 3 are compared; Case 3 is to observe the changes incurred by the rotor on wave dynamics. Velocity profiles behind the rotor of Case 3 are compared against laboratory measurements to validate the rotor design and running parameters. Wave height in Case 2 and Case 3 is 0.15m. Case 4 and Case 5, on the one hand, have the same purposes as Case 2 and Case 3, respectively. On the other hand, by only reducing the wave height to 0.06m, they are also designed

Table 4.5: Settings of wave-current CFD cases

Case name	Rotor	Wave period	Wave height	Inlet fow rate
1	No	1s	0.06m	0.0m/s
2	No	1s	0.15m	0.3m/s
3	Yes	1s		
4	No	1s	0.06m	
5	Yes	1s		

to provide calibration data for FVCOM-SWAN cases (see Section 4.4.2), in which the wave height is 0.06m. 0.06m, instead of 0.15m, is used in the FVCOM-SWAN cases because the FVCOM-SWAN system was found unstable when the wave height was set to 0.15m.

Settings of these five cases are presented in Table 4.5. The inclusion of Case 2 and Case 4 is to avoid false interpretation caused by possible intrinsic wave height drop along the channel. Intrinsic wave height drop is very commonly observed in FLUENT simulations. The possible causes could be insufficient mesh resolution, insufficient time resolution, incorrect choices of solution methods, etc.

Results and discussion

Figure 4.9 shows the velocity profiles of case 1 under wave trough and peak. The two black dashed lines on Figure 4.9 indicate the theoretical fluctuation range of the free surface: 0.4 ± 0.03m. It is clear that the calculated fluctuation range agrees with the theoretical one well. Also, the two profiles are symmetrical below the free surface, which is typical for linear waves. However, close to the free surface, the velocity is larger at peak. One possible explanation of this is that the sampling point did not capture the lowest point of the trough. Nevertheless, it can be seen from Figure 4.10 that the calculated free surfaces follow the theoretical ones very well. Since the main focus of this research with respect to surface waves is wave height, and wave height in FLUENT is derived from free surfaces, the performance of FLUENT in terms of simulating surface waves is considered as satisfactory.

2nd-order Stokes wave theory was used in Case 2 and 3, being coupled with steady current. These two cases differ from each other with respect to the presence of rotor. Without rotor, Case 2 provides the undisturbed hydrodynamics, in comparison to which changes to the hydrodynamics incurred by the rotor can be observed in Case 3, where the rotor is present. Velocity profiles behind the rotor predicted by Case 3 are validated against observed data collected at the University of Hull.

Figure 4.11 shows the comparison of computed wave-period-averaged stream-wise flow velocity against the measured data. It should be noted that there are overlaps in the measured profiles. This is because in the laboratory, the centreline slice on which

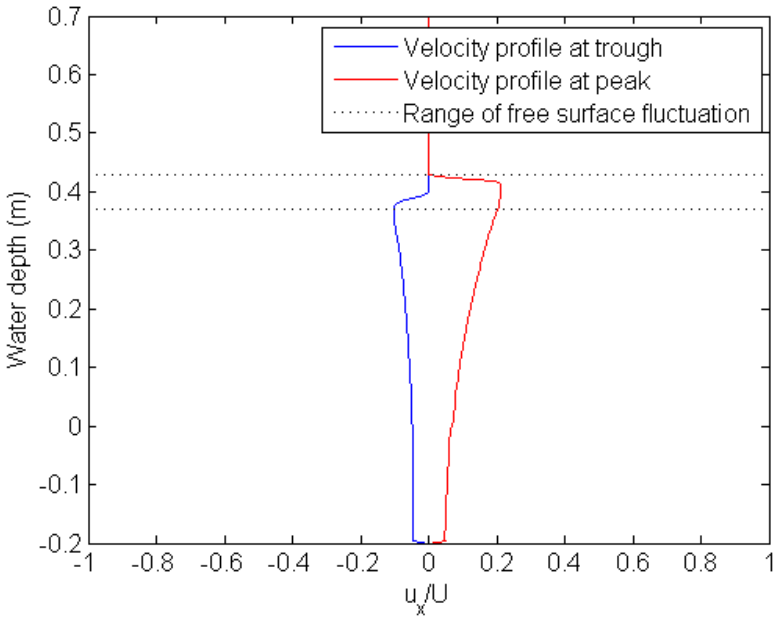

Figure 4.9: Velocity profiles of Case 1 at trough and peak.

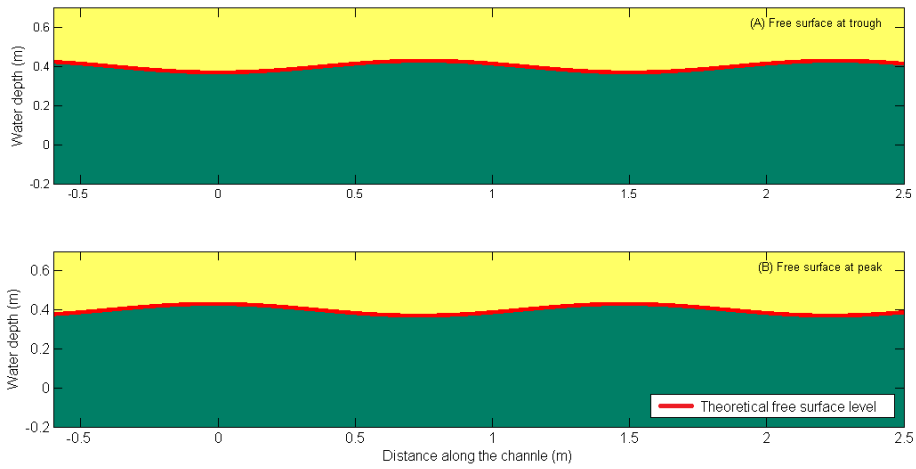

Figure 4.10: Free surfaces of Case 1 at moments when (A) trough and (B) peak pass the turbine site. Areas coloured by yellow and green are air and water zones, respectively. Red solid lines denote the corresponding theoretical free surfaces. Rotor is located at 0m on the Distance axis.

the velocities were measured was divided into 9 sub-slices and each of these sub-slices overlaps with its neighbour sub-slices. The overlaps provide a way to ensure the sub-slices are aligned correctly. The computed velocity profiles at all 4 locations (1D-4D) downstream of the rotor agree well with the measurements at the rotor swiping layers ($\%_{RMSE}$ refer to Table 4.4. The $\%_{RMSE}$ is calculated based on Equation 4.1 for each location.). In contrast to the current-only case, the wave-current model over-estimates the velocities in the region below the rotor. This over-estimation is likely due to a slightly over-predicted near bed wave boundary layer effect which was absent in the current-only model. Also, the rotor is located 100 mm closer to the bed in the wave-current case, which might have caused a larger blockage effect to the flow squeezing through the area below the rotor. Unfortunately the hub location was a property of the provided data and could not be altered. In general, the model is able to predict reliable velocities behind the turbine and hence wave properties.

$$\%_{RMSE} = \frac{\sqrt{\frac{1}{n}\sum_{i=1}^{n}(q_i - q_{iest})^2}}{q_{max} - q_{min}} \times 100 \tag{4.1}$$

where n is the number of records in the validation data; q_i is the validation data; q_{iest} is the calculated result; q_{max} and q_{min} are the maximum and minimum records in the calculated result respectively.

Free surfaces at trough and peak of Case 2 and Case 3 are drawn and presented in Figure 4.12. Rotor is place at 0m. It can be seen from Figure 4.12 that the wave height is reduced when the rotor is present and the reduction is roughly 3%. The wave height drops partly because the flow velocity close to the free surface is increased. On the other hand, wave length is slightly increased under the influence of the rotor.

The same behaviours are observed in [113]. The changes detected in the present research, however, are small compared to those reported in [113]. Wave height was reported to be reduced by 13% in [113]. This is possibly because the wave height of the imposed wave itself is rather small in the present research. Also, the blockage ratio, which is defined as the ratio between the swiping area of the rotor and the area of the cross section of the water channel, of the rotor in the present research is 3.3% whereas it was 16.5% in [113]. Proximity of the rotor to the free surface is likely another factor determining the influence of the rotor on the passing waves: a closer proximity to the free surface is expected to result in more significant effects. The rotor of the present research is located relatively far from the free surface.

Free surfaces at trough and peak of Case 4 and Case 5 are shown in Figure 4.13. Again, the presence of the rotor is causing the wave height to drop and the wave length to increase. The wave height drop is again roughly 3% in this case. As the main purpose of this case is to provide calibration data for FVCOM-SWAN cases, more detailed results are put in Section 4.4.2, along with analysis of FVCOM-SWAN predicted results.

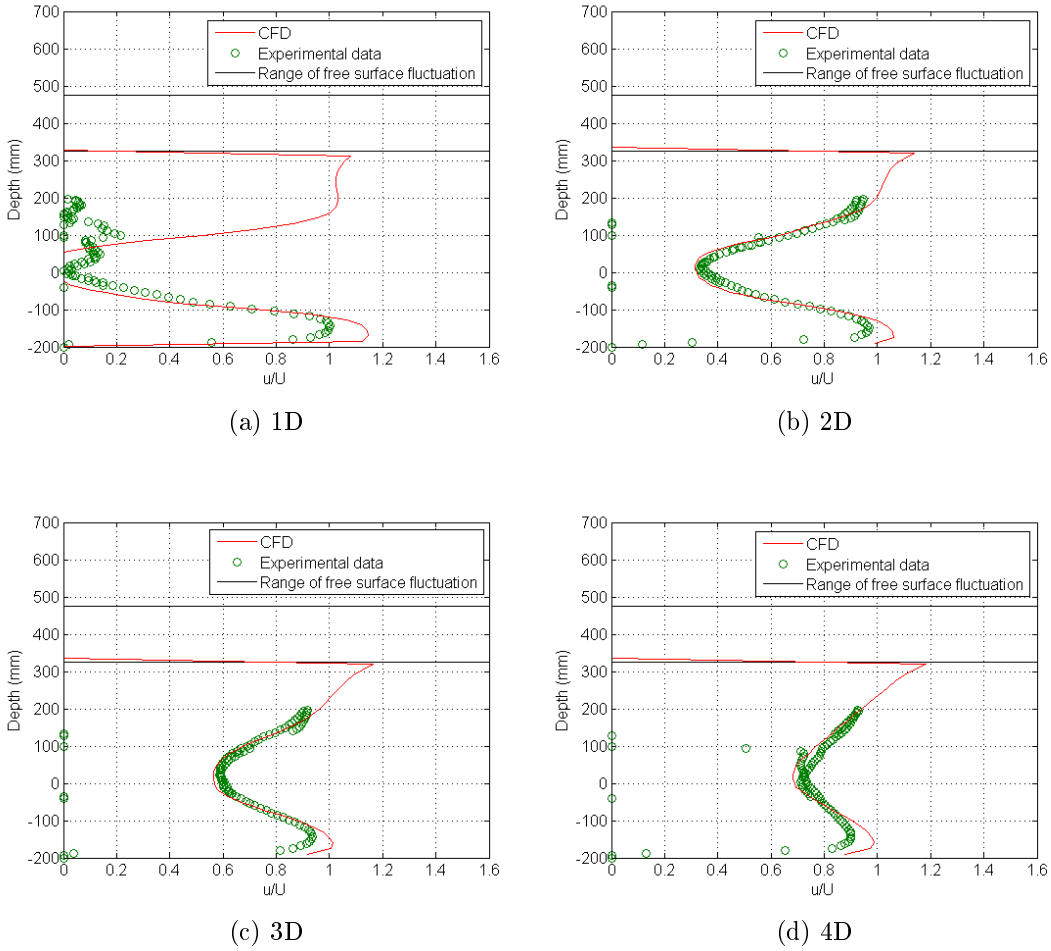

(a) 1D

(b) 2D

(c) 3D

(d) 4D

Figure 4.11: Normalized velocity profiles of Case 3 against those measured in the laboratory at 1D, 2D, 3D and 4D downstream of the rotor.

4.4 FVCOM calibration

4.4.1 Hydrodynamic modelling

Model set-up

In order to calibrate the coefficients involved, FVCOM models are setup to resemble the experimental environment in the laboratory and the ANSYS FLUENT (CFD) simulations. The mesh covering the computational domain has 5,320 nodes and 10,254 elements in total. The spatial resolution of the mesh is uniform in both stream-wise and cross-stream directions with a mesh size of 0.2m (diameter of the simulated turbine). Vertically, the water column is evenly divided into 50 sigma layers. A uniform flow speed is achieved through maintaining a constant water level difference between the two ends of the channel.

To represent a single turbine, a triangle in the calculation domain is selected to exert the energy extraction coefficient (C_{ext}) set along the water depth. Energy extraction

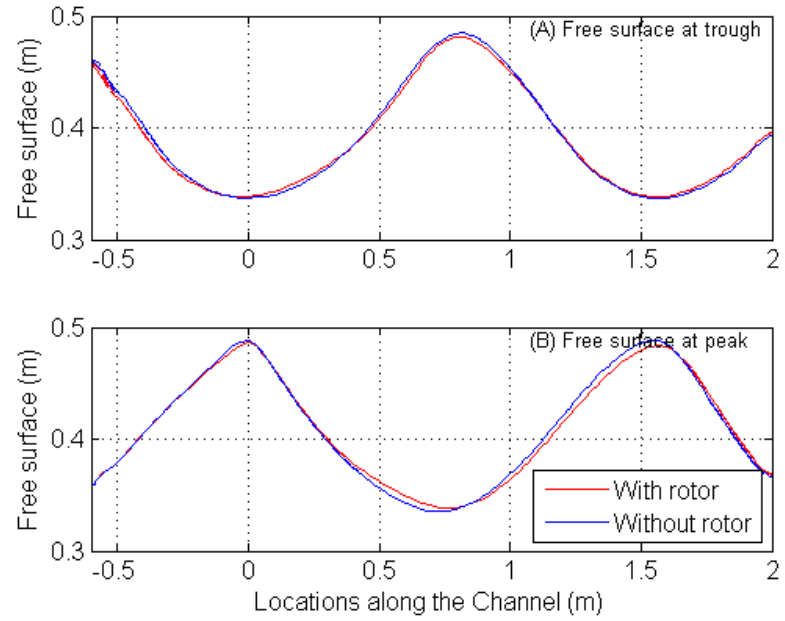

Figure 4.12: Free surfaces of Case 2 (Without rotor) and Case 3 (With rotor) at trough (A) and peak (B). Rotor is place at 0m on the 'Location' axis.

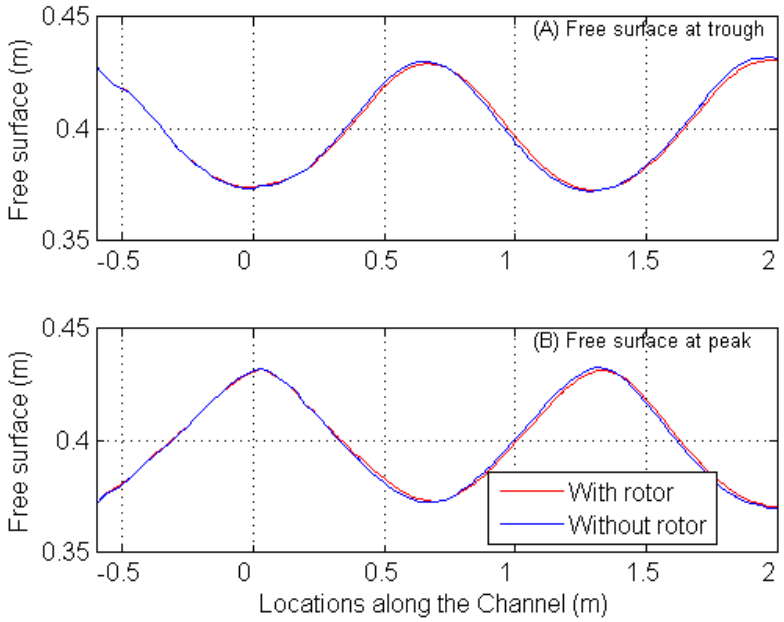

Figure 4.13: Free surfaces of Case 4 (Without rotor) and Case 5 (With rotor) at trough (A) and peak (B). Rotor is place at 0m on the 'Location' axis.

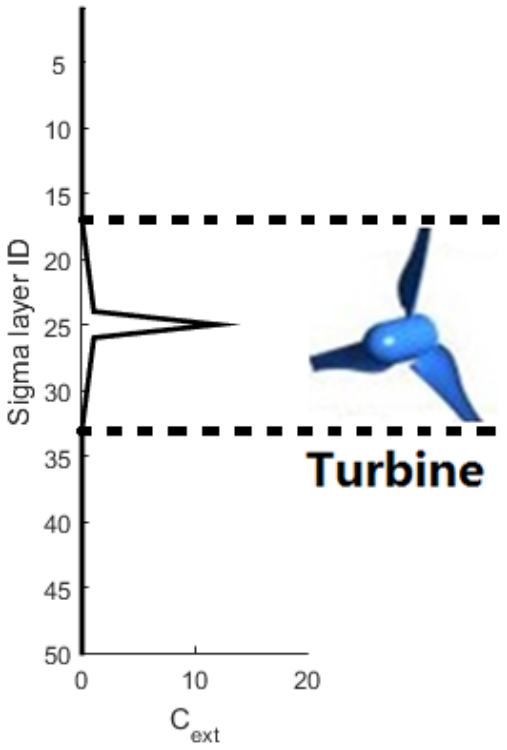

Figure 4.14: Illustration of three-dimensional application of C_{ext}.

coefficient of each sigma layer is treated individually in this research. Figure 4.14 illustrates the three-dimensional application of the C_{ext} set. Layers between the two dotted lines are intercepted by the turbine. These layer are controlled by assigning C_{ext} values. In the present case, 17 out of 50 sigma layers are occupied by the turbine. C_{ext} of the middle layer of these 17 layers is 12. C_{ext} of the other controlled layers vary linearly — decreasing from the hub towards the tip. The equation describing this linear trend is: $\sigma = -6.7C_{ext} + 8$. Layers that do not directly interact with the turbine are called 'free layers'. C_{ext} of these layers are 0. The depth-averaged value of this C_{ext} set is 0.408. Coefficients required to simulate the impacts of the turbine on the turbulence, C_{tp}, C_{td} and C_l, are set to 0.08, 0.1 and 2.8, respectively. These values are the calibrated results based on the above-mentioned experimental data and CFD model predictions. The calibration results are given as below.

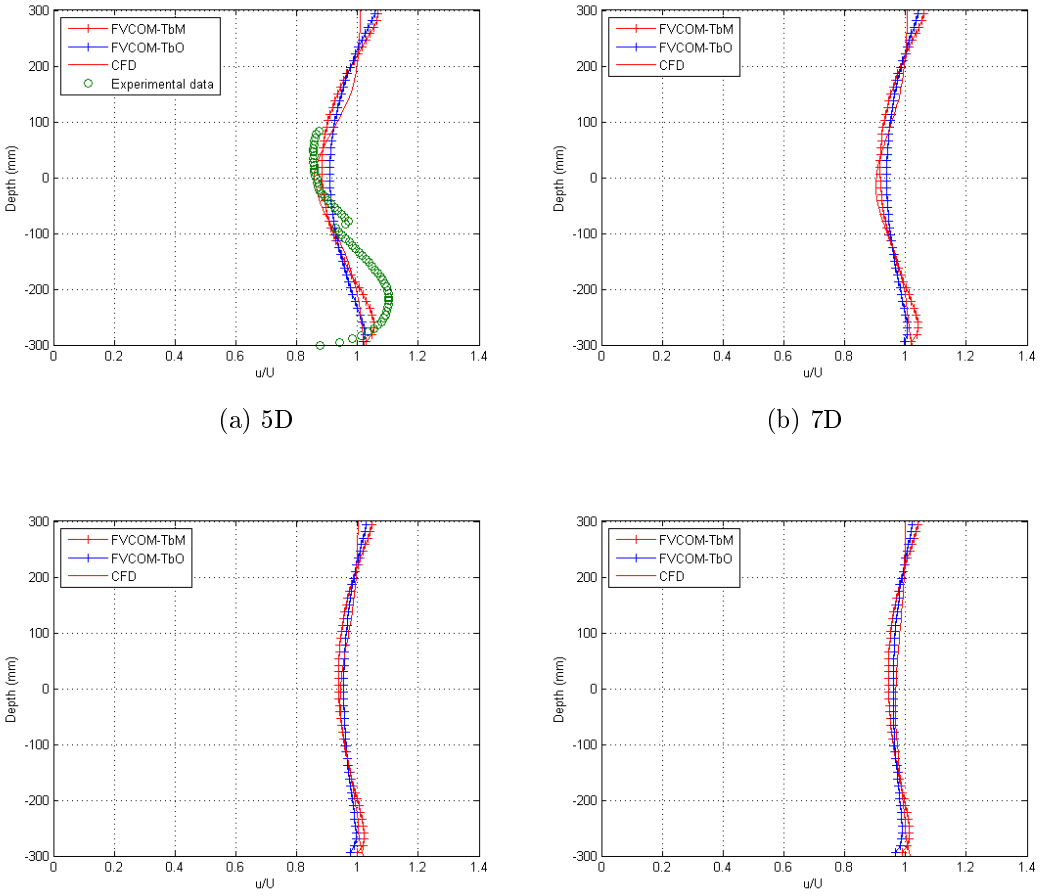

(a) 5D

(b) 7D

(c) 9D

(d) 11D

Figure 4.15: Normalized velocity profiles of two FVCOM cases (with and without turbulence modification terms) against those predicted by the CFD case and measured in the laboratory at 5D, 7D, 9D and 11D downstream of the rotor.

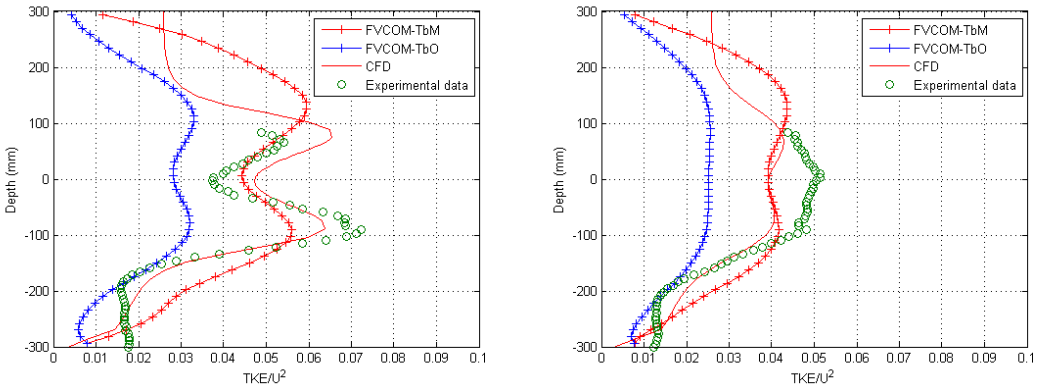

(a) 2D

(b) 4D

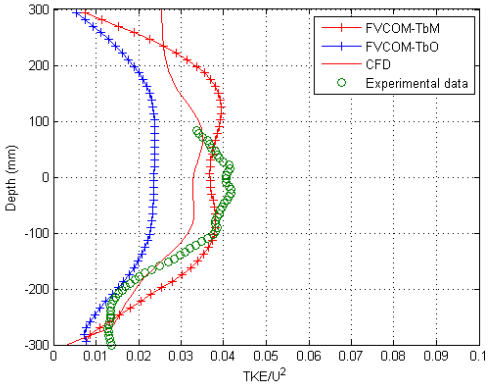

(c) 5D

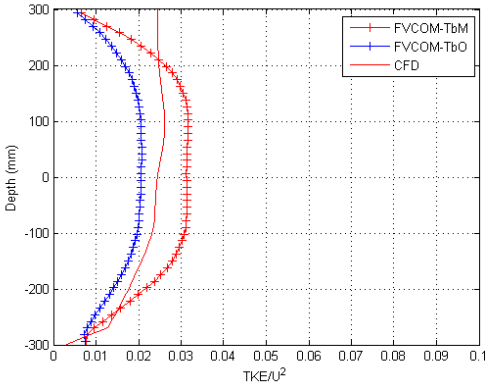

(d) 7D

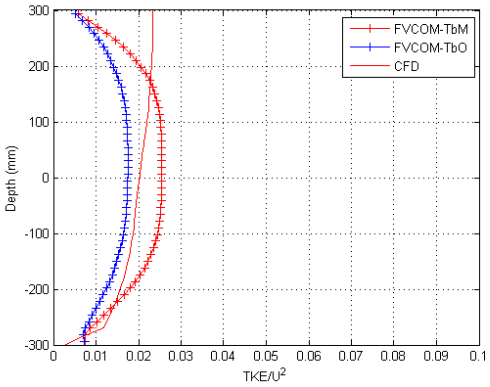

(e) 9D

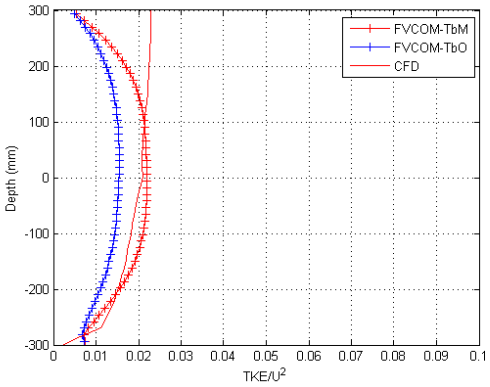

(f) 11D

Figure 4.16: Normalized TKE profiles of two FVCOM cases (with and without turbulence modification terms) against those predicted by the CFD case and measured in the laboratory at 2D, 4D, 5D, 7D, 9D and 11D downstream of the rotor.

To calibrate the model, again, normalized velocity and TKE profiles are selected as the diagnostic variables. These results are compared against data collected at the University of Hull [58] and the CFD predicted results. Two FVCOM cases are tested: with and without the additional turbulence terms as discussed in Section 3.4.2 activated at the

Table 4.6: $\%_{RMSE}$ for the four FVCOM cases

Cases		Velocity				TKE			
		5D	7D	9D	11D	5D	7D	9D	11D
current-	TbM	20.4	13.3	16.7	23.4	16.3	28.0	25.1	15.3
only	TbO	26.9	22.1	12.9	22.1	41.3	22.1	21.7	29.6
wave-	TYO	39.6	38.9	41.7	31.9	-	-	-	-
current	TNO	39.6	39.0	42.3	32.0	-	-	-	-

For TbM and TbO current-only cases at 5D errors are given against the experimental data; and against CFD results otherwise

turbine location. These two cases are hereafter named TbM (with the terms) and TbO (without the terms) respectively.

Comparison of velocity profiles at 5D, 7D, 9D and 11D downstream of the turbine are shown in Figure 4.15 (for $\%_{RMSE}$ of these results refer to Table 4.6). Within the turbine swiping area, velocity profiles of both TbM and TbO show a satisfactory agreement with the experimental measurements at 5D. Slight under-prediction is observed in the near bed boundary layer, which is attributed to the under-predicted bed friction. Further downstream, there is significant overall agreement between the FVCOM and CFD predicted velocities, especially beyond 7D downstream of the turbine. Hence, the new model system is capable of predicting the far-wake of the turbine correctly in terms of velocity, given appropriate C_{ext} values assigned. Beyond 9D downstream, both FVCOM and CFD model results show near uniform distributions of the velocity across the depth, indicating that the flow is less affected by both bottom and upper boundaries as well as the turbine operations in the far-wake.

Comparison of TKE level downstream of the turbine estimated by the FVCOM cases and that measured in the laboratory and predicted by CFD calculation are presented in Figure 4.16, again, for $\%_{RMSE}$ of these results refer to Table 4.6. As the CFD calculated TKE levels are underestimated in comparison with laboratory data (see Section 4.3.1), two more locations within the near-wake, 2D and 4D downstream of the turbine, where the experimental data is available are also included to carry out the calibration. It can be observed that the additional turbulence modification terms discussed in Section 3.4.2 have improved the TKE level predicted by FVCOM noticeably. When the terms are activated at the turbine location, FVCOM calculated TKE profiles agree well with the measurements. Without them, the TKE level is significantly under-estimated. The difference in TKE between case TbM and case TbO becomes less as the wake recovers. In general, the turbulence modification terms are required to model tidal stream energy devices in FVCOM using the MY-2.5 turbulence closure module. The original MY-2.5 module is insufficient to predict the perturbation of turbulence induced by turbines correctly. The additional terms proposed can lead to desired model performance when appropriate coefficients are used.

4.4.2 Wave dynamic modelling

Model set-up

This section discusses the introduction of OBSTACLE in the wave module to model the effects of turbines on wave height and, in particular, the calibration of the wave energy transmission coefficient K_t.

Three cases are tested: baseline case where turbine is absent and the hydrodynamics resemble those of the laboratory experiment; case TNO where the turbine is present but OBSTACLE is deactivated; case TYO where both the turbine and OBSTACLE are implemented. In cases where the turbine is present, the calibrated C_{ext} set is assigned to corresponding sigma layers. The turbulence modification terms are also activated in these cases, with the related coefficients, C_{tp}, C_{td} and C_l, set to the calibrated values. Wave parameters are the same as those used in two of the CFD cases (Case 4 and 5 in Table 4.5) —wave height is 0.06m and wave period is 1s. In case TYO, the wave energy transmission coefficient of OBSTACLE, K_t, is 0.98.

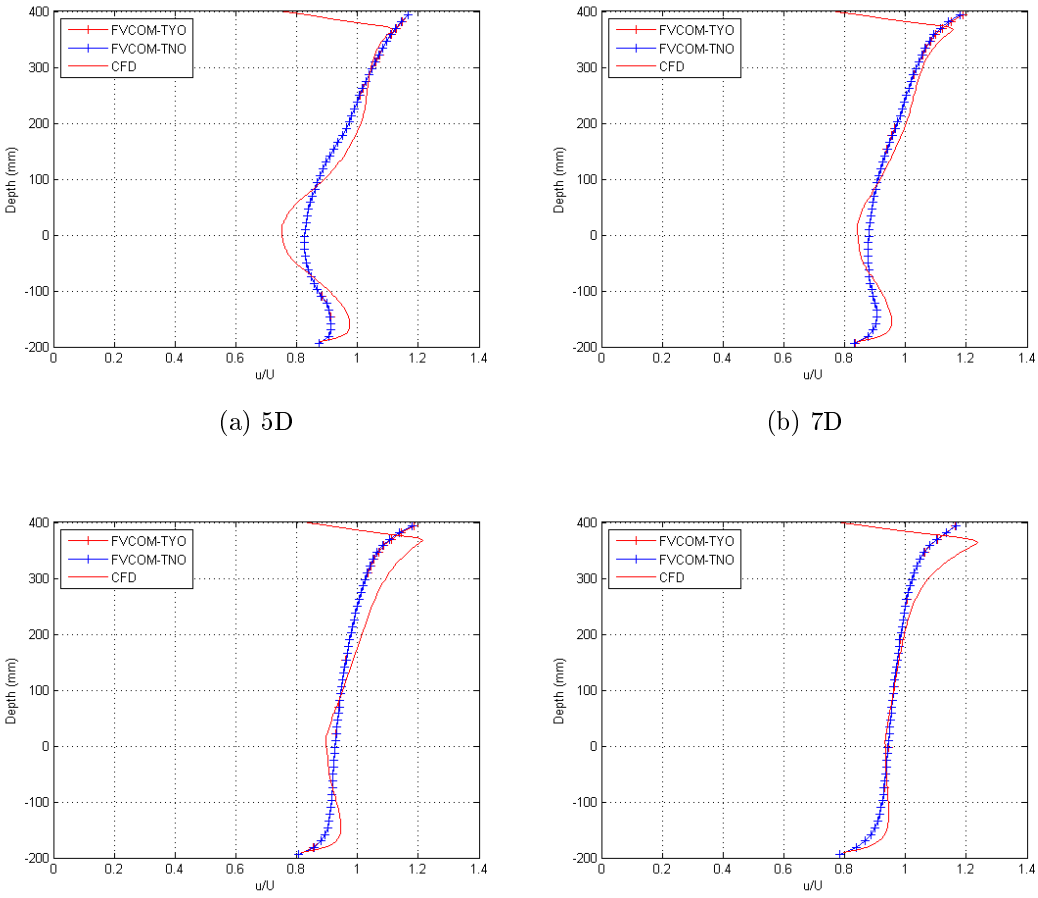

(a) 5D (b) 7D

(c) 9D (d) 11D

Figure 4.17: Normalized velocity profiles of two FVCOM cases, TYO and TNO, against those predicted by a CFD case (Case 5 in Table 4.5) at 5D, 7D, 9D and 11D downstream of the rotor.

Results and discussion

Figure 4.17 demonstrates the normalized velocity profiles of two FVCOM cases, TYO and TNO, against those predicted by one of the CFD cases (Case 5 in Table 4.5) at 5D, 7D, 9D and 11D downstream of the rotor. It is observed that the influence of OBSTACLE on velocity profiles is negligible when K_t is 0.98. Velocity profiles of both FVCOM cases match well with those computed by the CFD case ($\%_{RMSE}$ refer to Table 4.6), especially from 7D downstream of the turbine. The distance within which the wake recovers is slightly shorter in the FVCOM cases than it is in the CFD case: The velocity profile at 5D of the CFD case is in a more obvious W-shape than it is in the FVCOM cases. The difference between the CFD case and FVCOM cases reduces as distance downstream increases. Overall, the significant agreement between velocity profiles indicates the validity of FVCOM in predicting the flow field of a turbine wake under the presence of waves.

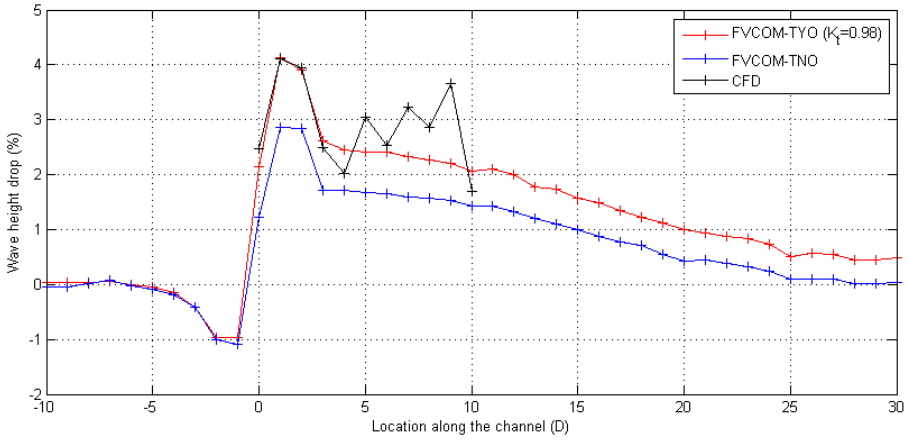

Figure 4.18: Wave height drop in percentage along the channel of two FVCOM cases, TYO and TNO, and of a CFD case (Case 5 in Table 4.5).

Figure 4.18 compares the drop of wave height as a percentage along the channel for the two FVCOM cases, TYO and TNO, and one of the CFD cases (Case 5 in Table 4.5). Wave height drop (in percentage) is defined as the ratio between the decrease in wave height and the background wave height. Case TNO demonstrates the wave height drop under the influence of retarding force and the turbulence closure terms. It is obvious that the wave height drop at the turbine location predicted by TNO is about 1.0% less than that predicted by the CFD case. This difference is quite significant given that the reference (CFD calculated) drop is only about 2.5% at the turbine location. Result of case TYO shows that the wave height drop is increased to the reference level by activating OBSTACLE, and, at the same time, an appropriate value of K_t is used. The wave height drop is enhanced by 0.923% at the turbine location due to the introduction of OBSTACLE.

4.4.3 Suspended Sediment Transport Modelling

Model set-up

This section assesses the sediment transport module of FVCOM in predicting sediment suspension with the presence of a tidal turbine rotor, and calibrates coefficient C_r which is related to turbine enhanced bottom shear stress. To fulfil these objectives, the model is first tuned to replicate the hydrodynamics measured in the laboratory experiment as much as possible, by adjusting the bed roughness. Calculation of suspended sediment transport under the presence of the turbine is then tested with model parameters given in Table 4.7. Among the parameters, settling velocity and critical stress are calculated based on the given D_{50} according to Van Rijn's formulae [65]. The erosion flux (Q_i) is tuned according to the measured suspended sediment concentration at the bottom at 15D downstream of the rotor (See Figure 4.20 and its related discussion). C_{ext}, C_{tp},

Table 4.7: Model parameters for suspended sediment calculation

Model parameter	Value
Bottom roughness	0.04m
D_{50}	$425\mu m$
Settling velocity	50.2 mm s^{-1}
Critical stress	0.2 N m^{-2}
Erosion flux (Q_i)	3×10^{-4} kg m^2 s^{-1}

C_{td} and C_l are set to the corresponding calibrated values.

Results and discussion

In order to achieve a good fit of hydrodynamics, a few numerical experiments are carried out with the bottom roughness varying over the range of 0.005-0.1m. Figure 4.19 compares the velocity profiles at 5 locations (5D, 7.5D, 10D, 12.5D, 15D) downstream of the rotor obtained under different bottom roughness against the measured data. In order to have a better look at the velocities close to the bottom boundary layer, the vertical axis is shown on a logarithmic scale. It can be seen from the figure that the model results agree with the experimental measurements fairly well above the bottom boundary layer (above -1 on the figure). There is, however, noticeable discrepancy within the boundary layer. The bottom roughness (z_0 in Equation 3.65) affects the velocities close to the bed. The performance of the model in terms of predicting velocities at the bottom improves as the bottom roughness increases from 0.005m to 0.04m. However, bottom roughness larger than 0.04m results in under-predictions. Bottom roughness of 0.04m is, therefore, used in the following calibrations in this section. It should be pointed out that $z_0 = 0.04m$ is 100 times greater than D_{50}. In theory, z_0 should be 3-6 times the characteristic length of the surface roughness elements. However, because the D_{50} here is the diameter of the suspended sediment, rather than representing the actual bottom roughness, D_{50} is not the deciding factor of z_0. The value of z_0 used here is decided based on the above-mentioned calibration results to recreate the measured hydrodynamics.

It should be noted that there are negative streamwise velocity values within the bottom boundary layer in the measurements, indicating that water close to the bottom is flowing towards the inlet. It contributes to the discrepancy between the model results and the measured values within this region.

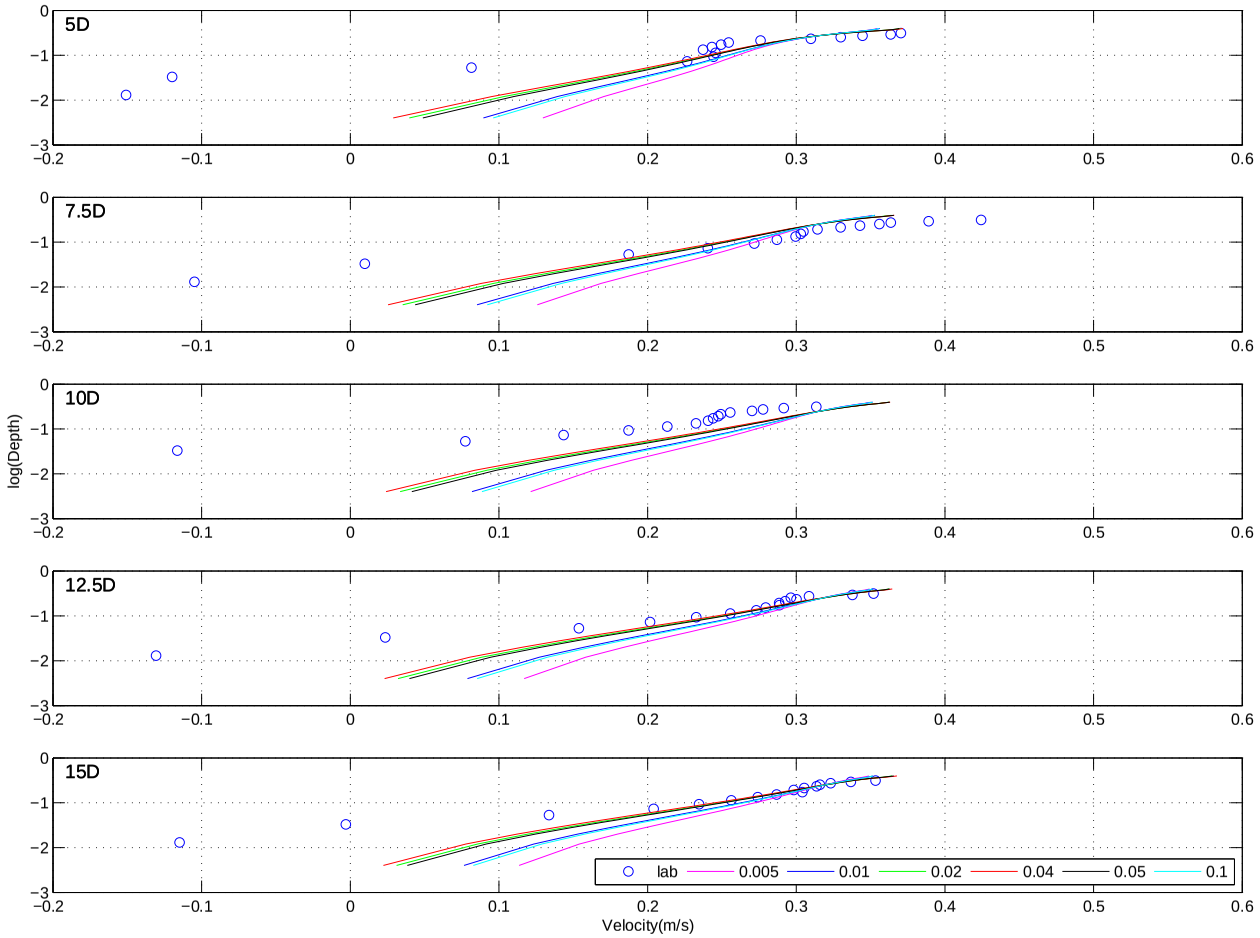

Figure 4.19: Comparison of streamwise velocity profiles obtained under different bottom roughness against the measured data.

With bottom roughness assigned to 0.04m, a series of simulations are carried out to tune the erosion flux Q_i based on the settings given in Table 4.7. Suspended sediment concentration at 1cm above the bed calculated with the erosion flux Q_i set to 3×10^{-4} kg m^2 s^{-1} and without the turbine incurred additional bottom shear stress τ_r activated (hereafter Case 1) is compared against the measured data in Figure 4.20. Due to the lack of baseline measurements, i.e. suspended sediment concentration measured under undisturbed flow, sediment concentration at the bottom layer at 15D downstream of the rotor measured in the laboratory is used as the reference to tune Q_i in the model. In this case, an assumption is made that the impact of the rotor on sediment entrainment has dropped to a negligible level at 15D and beyond. It can be seen from Figure 4.20 that the computed suspended concentration at 15D downstream of the rotor agrees very well with the measured value, indicating a right choice of Q_i. There is, however, obvious disagreement at the other locations. The calculated sediment concentration at the bottom layer is under-estimated in comparison to the laboratory measurements at all other 4 locations.

Suspended sediment concentration profiles of the above-mentioned case (Case 1) at 5 locations downstream of the rotor and those measured in the laboratory are drawn in Figure 4.21. It is observed that without τ_r, even though the calculated concentration at the bottom layer of Case 1 is noticeably underestimated at 5D and 3 other locations $<$ 15D downstream of the rotor, the concentration profile at 5D demonstrates a fairly good agreement with the experimental data. However, substantially underestimated profiles are observed at the other 4 locations further downstream.

Hypothesising that this is caused by the under-predicted concentration at the bottom, two bottom shear stress compensating cases are run with different C_r settings: Case 2, τ_r is activated only at the turbine location and $C_r = 0.5$ and Case 3, τ_r is activated from -1D (1D upstream of the turbine location) to 12D and C_r is 0.035, 0.0325, 0.03, 0.0275, 0.025, 0.0225, 0.02, 0.015, 0.01, 0.0075, 0.005, 0.0035, 0.002, 0.001, respectively. The C_r setting of Case 3 is inspired by a CFD study [113] mentioned in Section 2.4.2.

It can be seen from Figure 4.20 that although by giving τ_r a large value at the turbine location might have increased the bottom sediment concentration immediately downstream of the turbine significantly, not too much change is observed to the sediment concentration at the bottom layer beyond 5D downstream of the turbine. Compared to the almost negligible influence on the bottom sediment concentration beyond 5D, the C_r scheme of Case 2, however, does demonstrate a significant impact on the concentration profiles (see Figure 4.21). The profiles at 5D, 7.5D and 10D are greatly over-estimated. After satisfactory agreement at 12.5D, the profile at 15D starts to indicate a trend of under-estimation. This result suggests that the extra point source of sediment at the turbine location has largely enhanced the suspended sediment concentration in the

water body close to the turbine. However, the sediment concentration drops at a very fast rate as it goes downstream.

Instead of a very strong point source, Case 3 represents a rather mild line source of extra bottom shear stress and hence suspended sediment stretching from -1D to 12D. It can be seen from Figure 4.20 that the calculated sediment concentration at the bottom layer of Case 3 agrees fairly well with the measured result and is generally enhanced at the first 4 out of the 5 investigated locations compared to Case 1 and Case 2. Profile-wise, with a slightly over-estimated bottom sediment concentration at 5D, sediment profile at 5D is again over-estimated, at a larger level in comparison to Case 2. Profiles at 7.5D and 10D are still over-estimated. Satisfactory agreement is obtained at 12.5D and 15D.

There are several conclusions to be drawn from the above discussion:

1. Without any further modification, the background case (Case 1) produced a rather satisfactory profile at 5D downstream of the turbine, despite under-estimated bottom sediment concentration. This result indicates that the suspension capability of the first 5D of the wake is at a correct to over-estimated level;

2. This is further proven by the fact that once there is an extra bottom shear stress source, i.e. sediment source, sediment concentration in the water body at 5D-10D is over-estimated;

3. Sediment concentration drops very quickly after 5D, suggesting an insufficient suspension strength of the far wake.

Following the third conclusion listed above, an exploratory test (Case 4) strengthening the suspension capability, in particular, optimizing values of K_h, in the far wake is carried out. In this case, K_h from 7D to 15D is enhanced by multiplying a coefficient which linearly increases from 1.55 to 1.7. τ_r is overall deactivated. Bottom sediment concentration and sediment profiles are again given respectively in Figure 4.20 and Figure 4.21. Without τ_r, sediment concentration at the bottom is as expected under-estimated. Also, the influence of enhancing K_h on bottom sediment concentration is negligible. It can be seen from Figure 4.21 that by increasing K_h, sediment concentration in the water body in the far wake is enhanced to a reasonable level at all locations. However, interestingly, sediment concentration profile at 5D is slightly affected and over-estimated even though K_h at 5D is not directly modified.

In general, this section discusses the performance of the model in predicting suspended sediment transport behind a tidal turbine. Without any further modification, the inclusion of a retarding force and three turbulent terms is able to produce a good level of suspended sediment at 5D downstream of the turbine. However, suspended sediment concentration further downstream is significantly under-estimated. Under-prediction is also observed in sediment concentration at the bottom layer. Activating

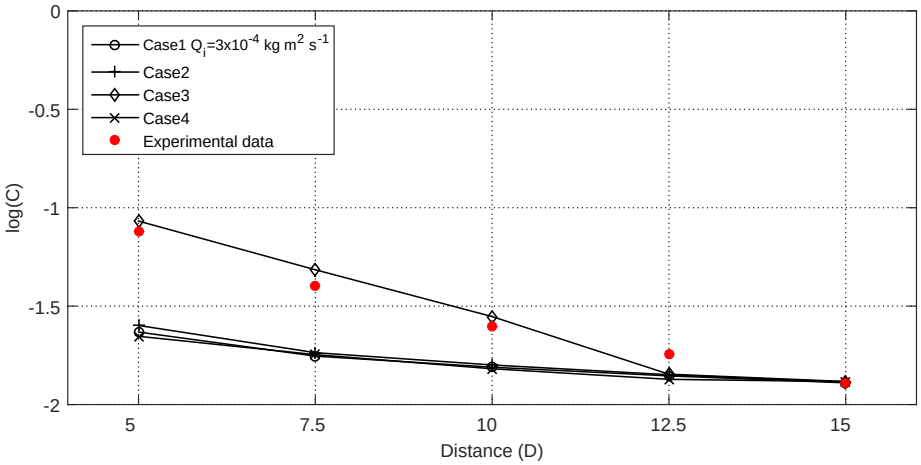

Figure 4.20: Suspended sediment concentration at the bottom layer of cases 1-4. u^*/u^*_{cr} of these four cases are 5.0, 4.8, 4.0 and 4.0, respectively.

the extra bottom shear stress term, especially as a line source, can lead to a fairly good agreement in sediment concentration at the bottom. It, however, causes sediment concentration in the water body to be largely over-estimated at 5D, 7.5D and 10D downstream of the turbine rotor. Also, sediment concentration in the water body drops very quickly after 5D, indicating an under-estimated suspension strength of the far wake. By solely enhancing K_h in the far wake, reasonable profiles are obtained, despite underestimated sediment concentration at the bottom. This result opens a question: Why is the suspension capability of the far wake, specifically K_h, underestimated, given K_m has been shown to be in an acceptable range?

There are two possible reasons. First, the turbulence closure used relates the turbulence stresses to the mean flow and hence only calculates the mean of turbulence. Turbulence in reality could be very much different from the mean calculated and interact with sediment particles differently. For instance, [45] pointed out that, instead of mean turbulence, sediment particles respond to peak stress. Second, the eddy viscosity theory is to parameterize turbulence in continuous fluid medium like water. However, sediment particles are discrete unless they are very small. Therefore, K_h calculated by the turbulence closure could be unsuitable for describing diffusive behaviours of sediment particles, especially particles in strong swirling fluids.

However, due to the lack of similar research, especially laboratory measurements, it is considered as more proper to regard this section as an open discussion. More research and data is required for any solid conclusion.

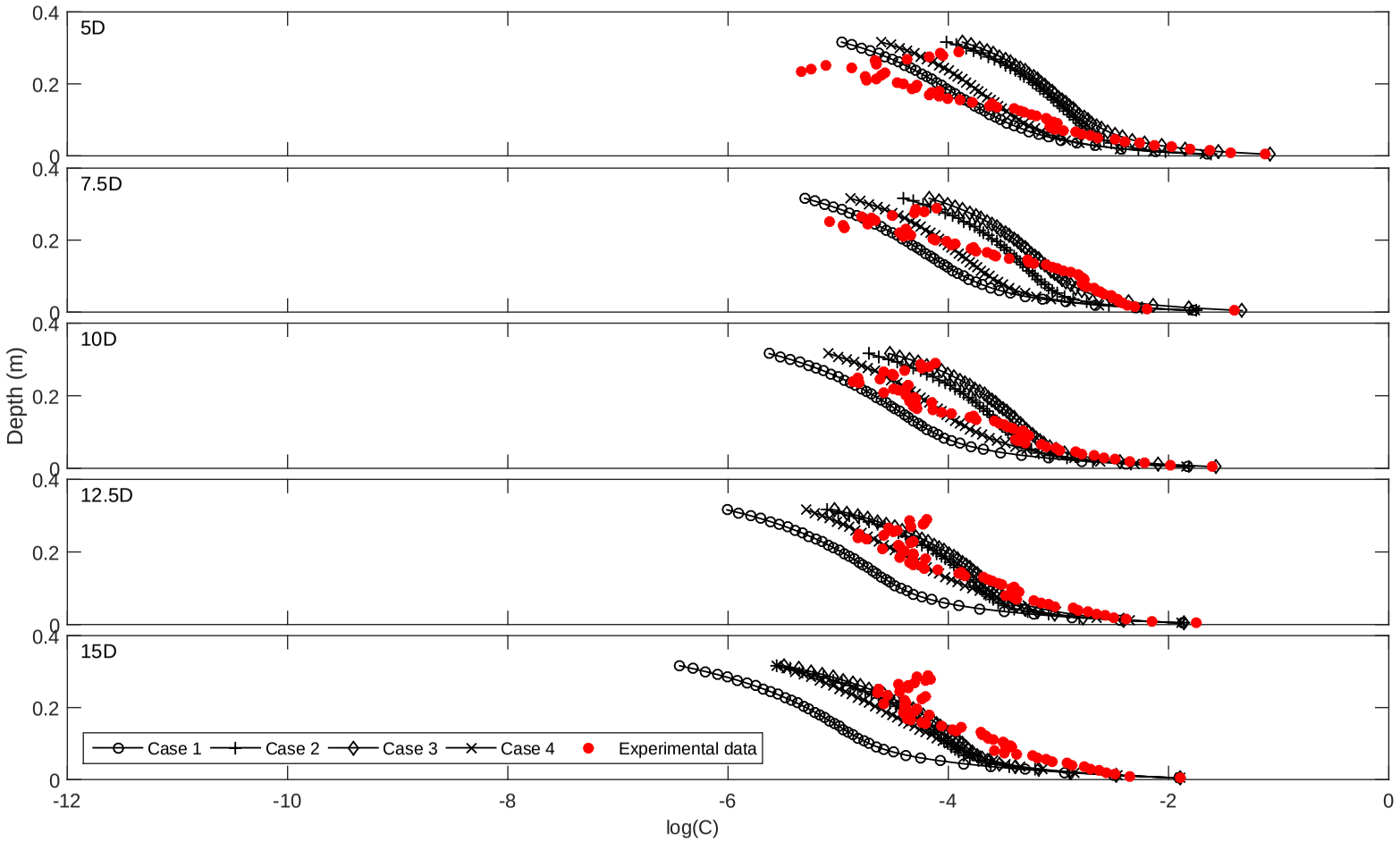

Figure 4.21: Comparison of suspended sediment concentration profiles of cases 1-4.

4.5 Summary

This chapter started with a brief introduction of experimental data collected at the University of Hull, based on which the model calibration was carried out. Before calibrating the turbine simulation platform, a series of CFD models built with ANSYS FLUENT replicating the experimental conditions, including current-only, wave-only and wave-current cases, were run to provide model calibration a wider range of data.

The coefficients to simulate tidal turbines in the developed turbine simulation platform are C_{ext} for retarding force; C_{tp}, C_{td} and C_l for turbulence generation and dissipation; K_t for OBSTACLE and C_r for enhanced bottom shear stress calculation. The results demonstrated that given proper values assigned to C_{ext}, C_{tp}, C_{td}, C_l and K_t, the turbine simulation platform is able to predict reliable hydrodynamics, including velocity field, TKE field and wave height, behind the turbine. More research, however, is required to understand the effects of turbines on sediment suspension and transport and to develop a reliable method of simulating it in an oceanographic numerical model like FVCOM.

Chapter 5

Scale up and sensitivity

5.1 Introduction

In Chapter 4, the developed turbine simulation platform is shown to be able to reproduce hydrodynamic impacts caused by a standalone tidal stream energy device accurately. However, the model coefficients required are based on limited data at laboratory scale. To enable the model's application in realistic large scale natural conditions, these coefficients need to be tested for various physical scales. In addition, the impacts from the variation of these coefficients to the model's overall prediction should also be investigated to reveal the model's application range.

5.2 Scale up

Overall, there are 6 model coefficients related to the turbine implementation in the developed simulation platform: C_{ext} used for flow retarding force; C_{tp}, C_{td} and C_l used for turbulence generation and dissipation; K_t for OBSTACLE implementation in wave simulation and C_r for enhanced sediment transport modelling. This section investigates the consistency of the values of the first 5 coefficients throughout different physical scales, given the protocol that one mesh grid in the model represents one simulated device. This is considered as necessary due to the fact that the calibration of these coefficients is carried out at the laboratory scale and therefore their application to field scale needs to be verified. C_r is not discussed because it is not yet proven to be the right option for solving the problem mentioned in Section 4.4.3 and hence is not applied in later on large scale applications.

As guidelines of performing scaling of fluid dynamics problems, Froude number and Reynolds number are often used to ensure the similitude between two different cases. Where Froude number has the form of:

$$Fr = \frac{inertial forces}{gravity} = \frac{u}{gL} \tag{5.1}$$

and Reynolds number is normally written as:

$$Re = \frac{inertial forces}{viscous forces} = \frac{uL}{\nu} \tag{5.2}$$

where u is the flow velocity; g is the acceleration due to gravity; L is the characteristic length and ν is the kinematic viscosity.

It is obvious that these two scaling guidelines cannot be satisfied simultaneously. In fact, either of them on its own is sufficient to guarantee the similitude as fluid flow is complex enough to be sensitive to changes of any aspects. Thus, a different scaling up approach — achieving the same turbine induced effects in a non-dimensionalized sense — is implemented in this research.

5.2.1 Velocity and turbulence

Two scaled cases, with turbine diameter of 5m and 15m, are carried out to test the consistency of the turbine related coefficients C_{ext}, C_{tp}, C_{td} and C_l. The three dimensions of the flume in the tests are linearly scaled up from the laboratory scale case based on the turbine diameter. Inlet velocity and TSR of the two up-scaled cases are 0.5m/s and 5.5 respectively. The Reynolds numbers of the 0.2m, 5m and 15m cases are $0.1 * 10^6$, $2.5 * 10^6$, $7.5 * 10^6$; all indicating fully turbulent flow.

Figure 5.1 and Figure 5.2 demonstrate the normalized velocity and TKE profiles of the small-scale and the two prototype scaled cases. The turbulence terms are activated at the turbine location in all cases. It can be seen that profiles of both normalized velocity and TKE of the up-scaled cases agree with each other very well and, at the same time, follow those of the small scale case well. The calibrated values of C_{ext}, C_{tp}, C_{td} and C_l, therefore, can be applied to large scale cases to produce the same level of effects.

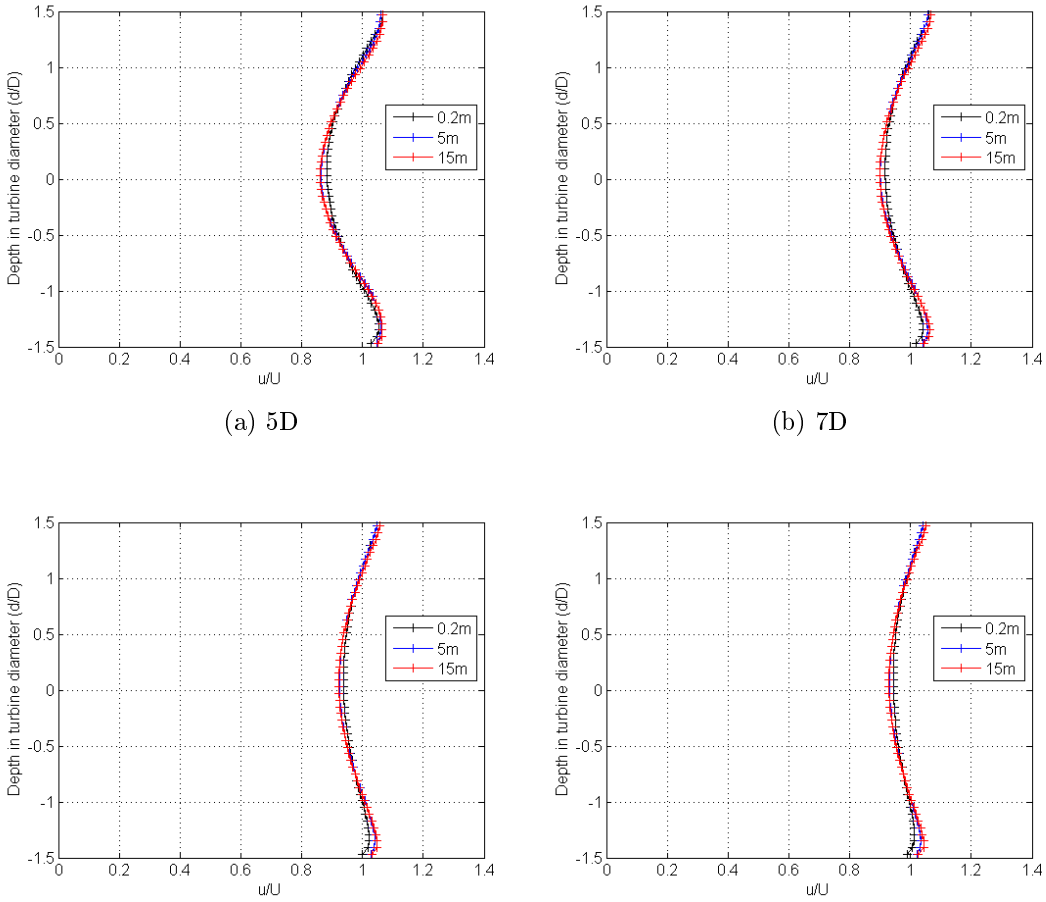

(a) 5D

(b) 7D

(c) 9D

(d) 11D

Figure 5.1: Normalized velocity profiles of case 0.2m, 5m and 15m at 5D, 7D, 9D and 11D downstream of the turbine.

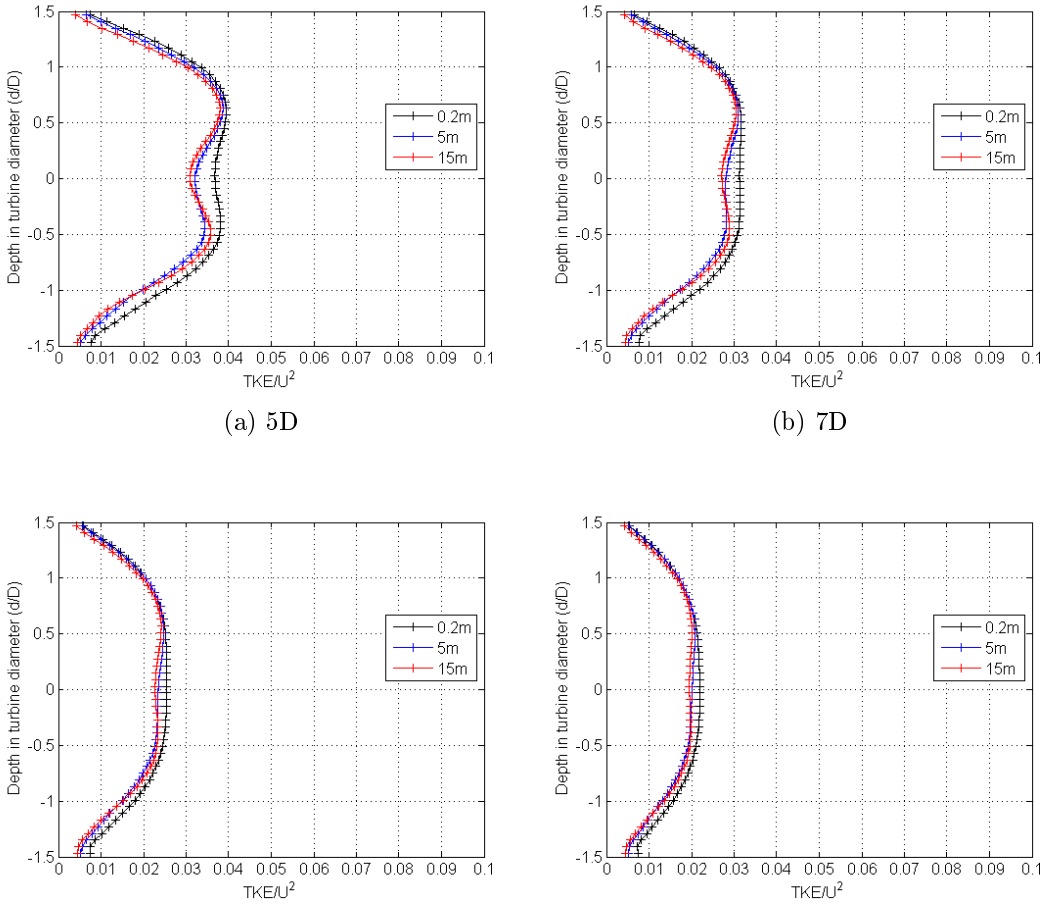

(a) 5D (b) 7D

(c) 9D (d) 11D

Figure 5.2: Normalized TKE profiles of case 0.2m, 5m and 15m at 5D, 7D, 9D and 11D downstream of the turbine.

5.2.2 Waves

Unlike retarding force and the turbulence closure terms which together with some other terms determine the output velocity and turbulence variables through rather complex computations, OBSTACLE, the strength of which is controlled by the energy transmission coefficient K_t, determines directly the percentage of wave energy being transmitted through or over an obstacle. Combined with the numerical procedure explained in Section 3.4.3, it is highly likely that the effect of energy transmission coefficient K_t is not sensitive to the physical scale. To verify this assumption, the two above-mentioned scaled cases are tested and the computed wave height drop behind the turbine is compared. In these two cases, identical incident waves with 2.4m significant wave height and 7s peak period propagate over two turbines with diameter of 15m and 30m respectively. Each of the obstacles takes the size of the turbine it represents as its length.

The obstacles are placed at the same relative locations and apply the same energy transmission coefficient K_t (K_t=0.98). To make sure the environment in which the

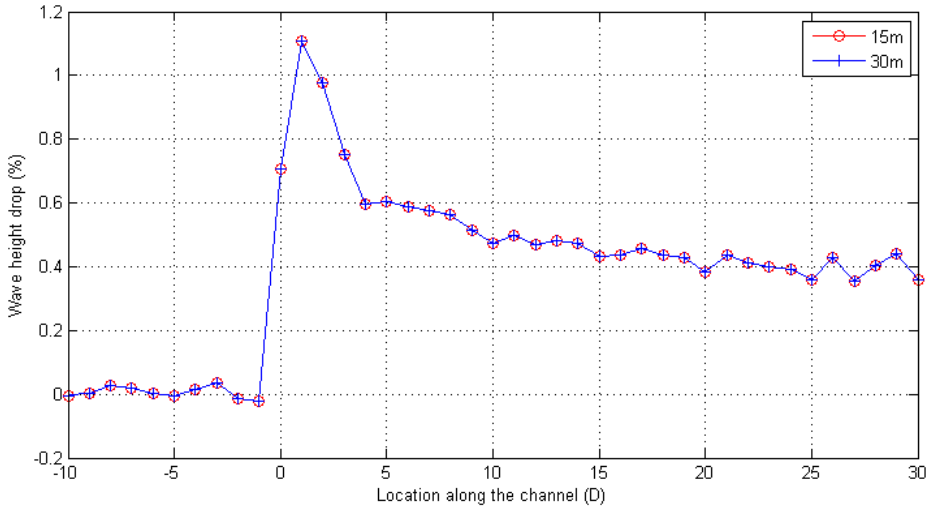

Figure 5.3: Wave height drop as a percentage for two cases with different turbine sizes - 15m and 30m. The trend of wave height drop along the channel is identical, despite the difference in turbine size.

waves propagate is the same, water depth is 45m in both cases. Retarding force is deactivated so that the wave height variation results exclusively from the OBSTACLE.

Figure 5.3 shows the wave height drop along the channel of both cases. It can be seen that the trend of wave height development along the channel in these two cases is identical. The wave energy transmission coefficient produces a same level of wave height drop, despite the difference in physical scale between the two cases. It is therefore concluded that K_t is not sensitive to physical scale, as long as the settings of the turbine simulating OBSTACLE follow the rules mentioned in Section 3.4.3 and the environment in which the waves propagate remains the same.

5.3 Sensitivity

This section discusses the sensitivity of the model's overall prediction to changes in the above-mentioned coefficients. This is done through a series of control experiments in which each of the controlled coefficients is given a $\pm 5\%$ perturbation while the others are held constant. C_r is also included in this discussion. The present discussion is based on the line source scheme of C_r mentioned in Section 4.4.3. To evaluate the sensitivity, velocity and TKE are again selected as the diagnostic variables for hydrodynamics, while suspended sediment concentration is chosen to quantify the sediment transport module's response to coefficient fluctuation.

Results are displayed in Figure 5.4, Figure 5.5 and Figure 5.6 for velocity, TKE and suspended sediment concentration, respectively. In Figure 5.4, the velocity fluctuation in percentage is obtained through dividing the maximum velocity difference by inlet

flow rate (U) which is 1m/s. Similarly, dividing the maximum TKE difference by U^2, the TKE variation in percentage in Figure 5.5 is gained. For sediment concentration, the fluctuation in Figure 5.6 is obtained through dividing the maximum concentration difference by the maximum concentration found in the background case.

It is observed in Figure 5.4 that the model's prediction of velocity is sensitive to C_{ext} which works directly on velocity calculated. Increasing or decreasing C_{ext} by 5% results in roughly 5% fluctuation in calculated velocity. The velocity, however, is slightly more sensitive to the wave OBSTACLE coefficient K_t, suggesting a noticeable impact from wave height to water velocity. However, the greatest affected velocity is at the surface, due to the change in Stokes drift — the mass transport between the wave trough and crest. In the present case, the waves follow the flow direction and hence as the wave height increases, the velocity near the surface also increases. Similar result is reported in [87], where an increase of wave height from 0.15m to 0.3m was reported to accelerate velocity at the surface by about 70%.

The velocity calculation is generally less sensitive to the turbulence modification terms, especially C_{td}. However, there is sensitivity observed to C_{tp} and C_l. Overall, the sensitivity of the model's velocity prediction to turbulence is because the vertical eddy viscosity coefficient K_m seen in Equations 3.59, Equations 3.60 and Equations 3.61, which plays a big role in the vertical distribution of velocity, is calculated based on outputs from the turbulence closure (see Equation 3.68).

Sensitivity response of TKE to variation of turbine simulating coefficients is shown in Figure 5.5. It is seen that the model's prediction of TKE is at a similar sensitivity level to C_{ext}, C_{tp}, C_{td} and C_l, but at a smaller sensitivity level to K_t. However, asymmetry is observed between the two corresponding cases of each coefficient. When C_{ext} is decreased by 5%, the biggest change it causes to the calculated TKE is larger than when C_{ext} is increased by 5%. In fact, the overall change behind the turbine demonstrates the same asymmetry. It is largely because the velocity behind the turbine is larger in the former case when C_{ext} is decreased and it is resulting in a more significant shear production of TKE. The largest changes C_{tp}, C_{td} and C_l respectively cause to TKE are also asymmetrical. A possible explanation is that the changes in TKE caused by varying these three coefficients lead to changes in K_m which alter the shape of the velocity profile and cause secondary changes in TKE production.

In terms of suspended sediment concentration, it can be seen from Figure 5.6 that variation in C_r causes the strongest sensitive response in suspended sediment concentration calculation, which is expected. Very small sensitivity is observed towards C_{ext} and K_t. On the other hand, there is moderate sensitivity seen towards the three turbulence modification terms. This is probably because, as mentioned in Section 4.4.3, turbulent mixing (K_h) decides the suspension ability of the water to some extent and K_h is related to TKE (q^2) and lengthscale (l) through Equation 3.68. Hence, variation

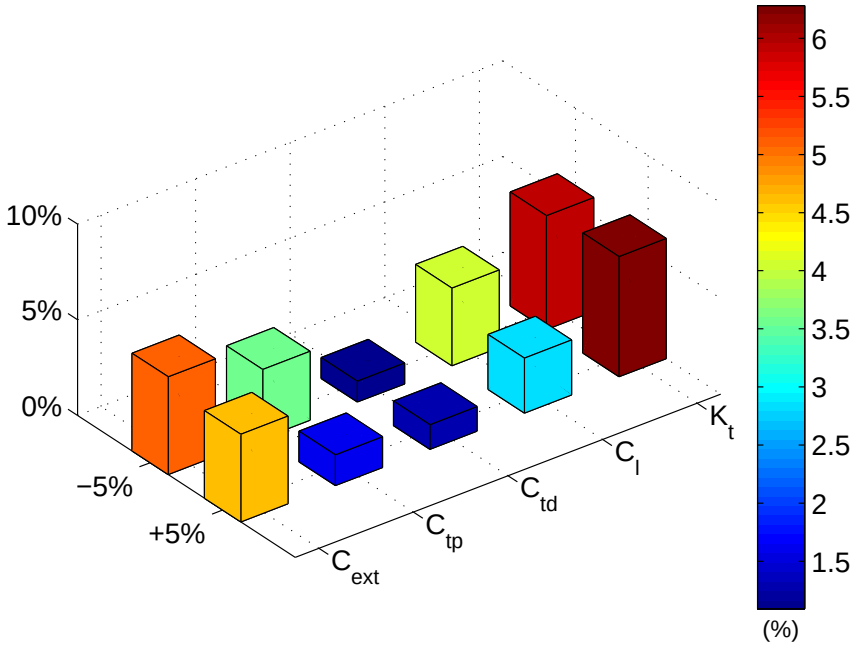

Figure 5.4: Sensitivity response of velocity to variation of turbine simulating coefficients.

in turbulence closure outputs could result in noticeable changes of calculated suspended sediment concentration.

Due to limit in time and computational ability, only a small number of tests are carried out to obtain the observations and discussion given above. In order to obtain more thorough sensitive dependency of the model's performance on the above-listed coefficients and clearer understanding of the sensitive dependency mechanism, more sophisticated and intensive research is recommended.

5.4 Summary

This chapter discussed the dependency of the turbine simulating coefficients on physical scales, under the prerequisite that the mesh around the turbine site is resolved to the size of the simulated turbine and each individual device is represented by a mesh grid. The results showed that the investigated coefficients are not sensitive to the physical scale to predict the same turbine-induced effects on velocity, TKE and wave height in a non-dimensionalized sense.

This chapter also studied impacts from variation of the turbine simulating coefficients to the model's overall prediction. Results of a limited number of tests revealed that the model-calculated velocity is sensitive to C_{ext} and an increase or decrease of 5% in C_{ext} results in roughly 5% fluctuation in calculated velocity. The velocity is slightly more sensitive to the wave OBSTACLE coefficient K_t, due to the change in Stokes drift

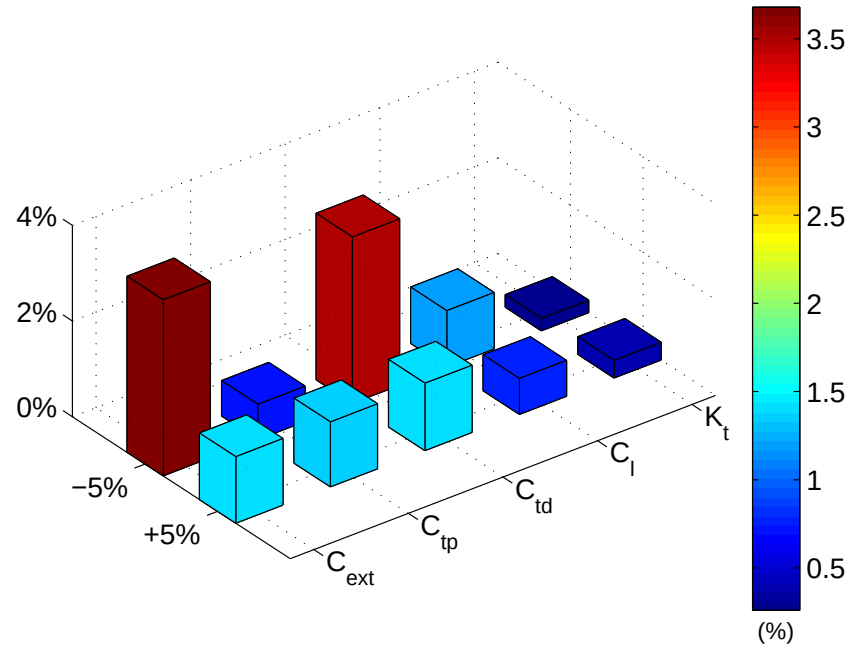

Figure 5.5: Sensitivity response of TKE to variation of turbine simulating coefficients.

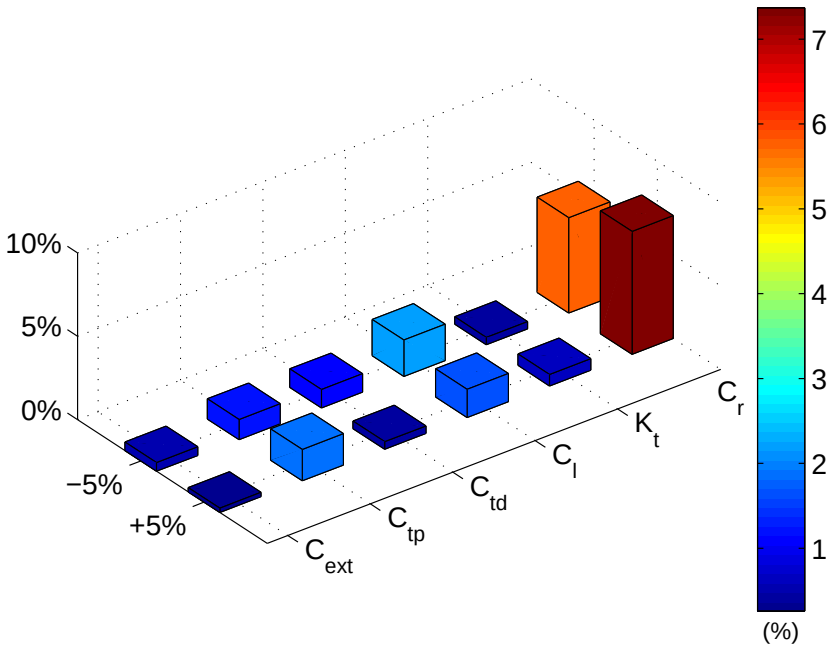

Figure 5.6: Sensitivity response of suspended sediment concentration to variation of turbine simulating coefficients.

level at the surface. The velocity calculation is generally less sensitive to the turbulence modification terms. The slight sensitivity observed can be attributed to the sensitivity of the vertical distribution of velocity to K_m which is calculated based on outputs from the turbulence closure.

The model's prediction of TKE has similar sensitivity level to C_{ext}, C_{tp}, C_{td} and C_l, but is at a smaller sensitivity level to K_t. Asymmetry is observed between the two corresponding cases of each coefficient, possibly because the vertical structure of velocity behind the turbine is different under the two corresponding scenarios.

Suspended sediment concentration is highly sensitive to C_r. Very small sensitivity is observed to C_{ext} and K_t. It however has moderate sensitivity to the turbulence modification terms, mostly because they decide the turbulent mixing (K_h) which strongly affects the strength of suspension in the wake.

Chapter 6

Model application

6.1 Introduction

In this chapter, the model system is applied to single turbine tests under steady current and wave-current combined scenarios within an water channel to examine the impacts to local flow hydrodynamics and sediment suspension. To evaluate the impacts from a large scale turbine farm to regional processes, the model is applied to the Anglesey coast, north-west Wales under realistic natural tidal and wave conditions. Results from hydrodynamics and sediment transport modelling are analysed to reveal potential effects to both coastal and regional processes.

6.2 Single turbine test

A series of tests are carried out to reveal impacts from a single turbine to the surroundings using a prototype scale 15m idealised water channel (825m long, 135m wide and 45m deep) model as the test bed. Flow rate of these cases is 1.0m/s, which is the averaged velocity over a full tide cycle (see Figure 6.1) at a location within the proposed tidal turbine farm off the Anglesey coast. The significant wave height is 2.4m and wave period is 7s. These are of a typical storm condition observed along the Anglesey coast. Sediment tests include clear water and live-bed cases. Parameters required for sediment calculations are listed in Table 6.1. These tests are conducted with and without the turbine implementations, i.e. the coefficients represent turbine effects being switched on and off, in order to reveal the differences between the baseline case (no turbine) and cases with turbine effects. In particular, the focus is placed on the effects of enhanced turbulence and OBSTACLE as shown in the following sections.

6.2.1 Influences of turbulence closure terms

Free-surface elevation and normalized depth-average velocity

Figure 6.2 and Figure 6.3 display the calculated free-surface elevation and normalized depth-average velocity along the water channel of two test cases: TbM —turbulent

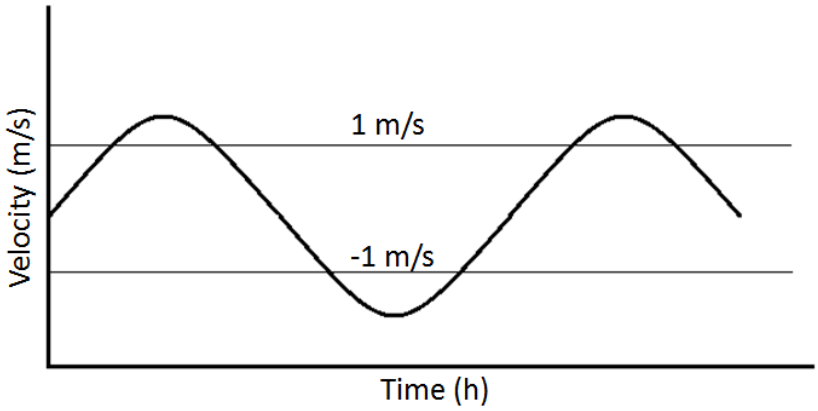

Figure 6.1: A sketch of averaged velocity over a tide cycle (not to scale). The signs indicate directions of the flow.

Table 6.1: Model parameters for suspended sediment calculation

Model parameter	Live-bed	Clear water
D_{50}	0.22mm	4.00mm
Settling velocity	21.0 mm s^{-1}	250.3 mm s^{-1}
Critical stress	0.154 N m^{-2}	2.400 N m^{-2}

terms activated and TbO —turbulent terms deactivated. Retarding force is activated in both cases at the turbine location. Locations upstream and downstream of the turbine are indicated with distance away from the turbine in terms of diameter of the turbine. 0D is where the turbine is placed. A water level increase upstream of the turbine accompanied by a substantial drop of water velocity is observed in both cases. The passing flow is slowed down due to energy loss. The decelerated water accumulates in front of the turbine, causing the water level rise upstream of the turbine. Free-surface elevation drop is observed at the turbine location. The water level keeps dropping until 1D downstream of the turbine while the water velocity commences recovery immediately downstream of the turbine. These behaviours are consistent with measurements from a previously published laboratory experiment [114].

There are slight differences between the free surface elevation and depth-averaged velocity predicted by the two test cases. Water elevation in TbM is lower at 0D and 1D but quickly becomes higher at 2D downstream the turbine. The two lines merge from 3D downstream of the turbine. The depth-averaged velocity predicted by case TbM, on the other hand, is larger at 0D but soon drops lower at 1D until 5D downstream of the turbine and the difference becomes very small from 6D downstream of the turbine. These differences are in general negligible. Both free surface elevation and depth-averaged velocity recover very fast. The depth-averaged velocity has recovered to

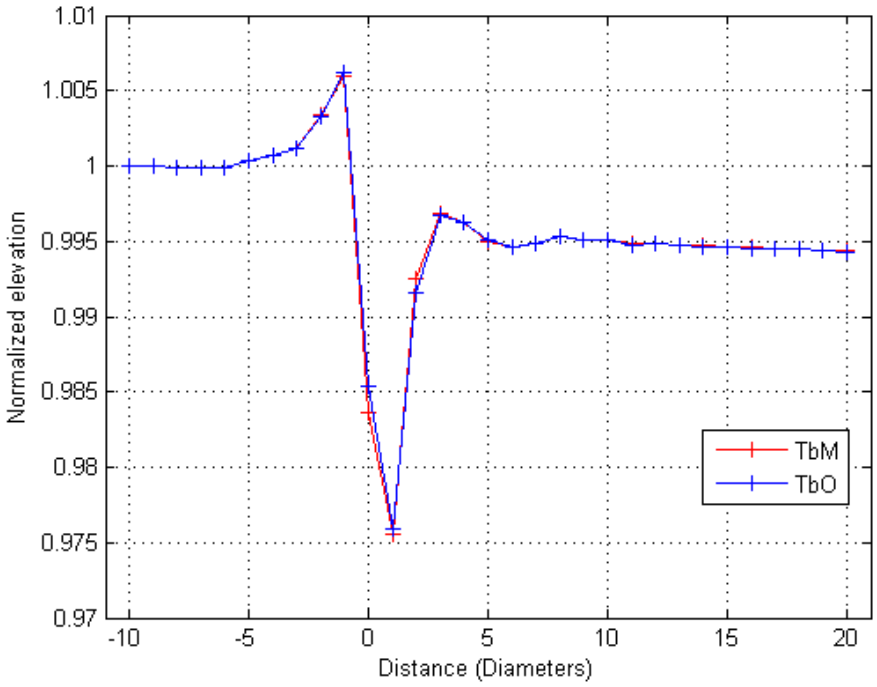

Figure 6.2: Free-surface elevation along the channel.

96% of its original value before the recovery starts to slow down at 2D downstream of the turbine in both scenarios. The recovery of surface water elevation also slows down after the fast recovery region of the first 3D downstream of the turbine. The water elevation is still slightly below its undisturbed value at 20D downstream of the turbine. A full recovery of depth-averaged velocity is not observed within a distance of 20D.

Bottom boundary layer

Water flow velocity, bed shear stress and suspended sediment concentration in the bottom boundary layer along the centreline calculated under different scenarios —with turbine and with turbulent terms being activated (TbM, red lines with markers), with turbine but without turbulent terms being activated (TbO, blue lines with markers) and undisturbed flow (black lines with markers) —are drawn and compared in Figure 6.4. Two sediment transport cases, clear water and live-bed, with respect to the same hydrodynamics are run.

Obvious changes caused by the turbine as well as the turbulent mixing are observed. Influence of the turbine on flow velocity and bed shear stress reaches a maximum roughly at 1D downstream of the turbine. The downstream influential range of the turbine is greater than 25D for bottom layer water velocity and bottom shear stress in both cases TbM and TbO. The presence of the turbine increases the water velocity in the bottom layer, regardless of the calculating scheme of turbulence. However, the increase

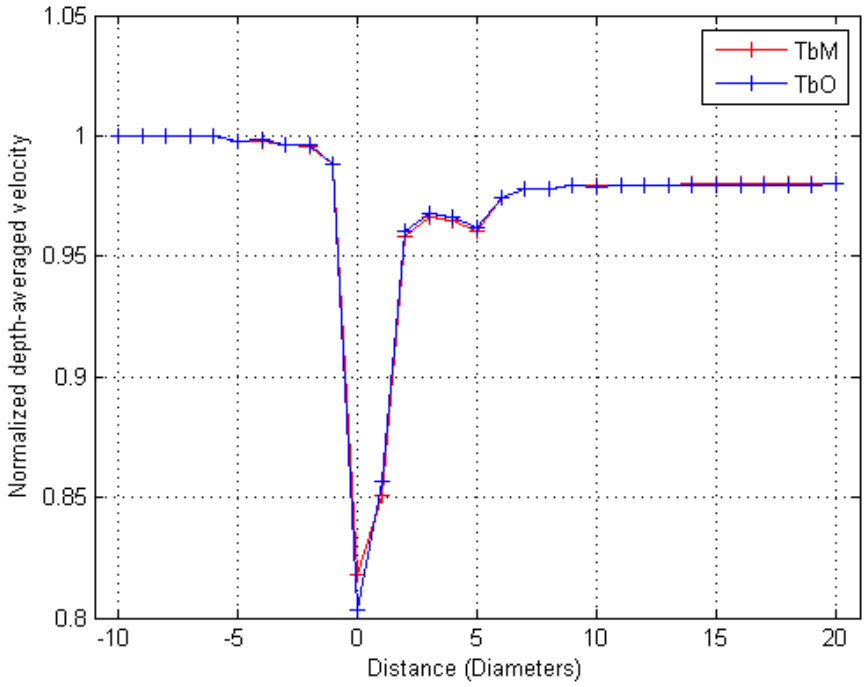

Figure 6.3: Normalized depth-average velocities along the channel.

is noticeably larger when the turbulent terms are activated (case TbM). Bottom shear stress which is largely dependant on water velocity in the bottom layer, expectedly, is also increased. The differences in water velocity in the bottom layer and bottom shear stress caused by the turbulence calculation scheme starts to become negligible from 10D downstream of the turbine.

The changes in suspended sediment concentration can be seen from around 3D upstream of the turbine in both cases. However, downstream, the changes in the live-bed case extend beyond 25D whereas it is within 20D in the clear water case, which demonstrates the grain size effects to the overall sediment suspension.

Suspended sediment concentration in the bottom layer demonstrates opposite behaviours in the clear water (Figure 6.4 (C)) and live-bed (Figure 6.4 (D)) cases. It can be seen from Figure 6.4 (C) that in the clear water case, the bottom stress under the undisturbed flow is below the critical stress. The enhanced bottom shear stress, due to the inclusion of turbine, is above the critical stress, entraining sediment particles into the water column. Sediment concentration in the bottom layer, therefore, is higher in case TbM where the bottom stress is larger in comparison to case TbO.

It is, however, a very different scenario in the live-bed case. Suspended sediment concentration in the bottom layer is decreased in case TbM in the vicinity of the turbine and it is slightly decreased in case TbO at -1D. This result could be counter-intuitive, given an enhanced bottom shear stress within the same area. However, apart from

bottom shear stress, turbulent mixing coefficient K_h close to the device is also increased due to the inclusion of turbine, especially in case TbM. The enhanced mixing is able to mix sediment concentration into a more uniform state close to the bed surface where the concentration is high. In this particular case, the enhanced bottom shear stress and hence increased sediment supply from the bed is not enough to compensate the amount of sediment being transported upwards out of the bottom layer due to the mixing process, suspended sediment concentration in the bottom layer is therefore decreased.

The distribution of suspended sediment concentration along the water channel in case TbO is not exactly the same. The sharp drop of suspended sediment concentration in the vicinity of the turbine seen in case TbM is not observed in case TbO. Instead, only a very slight decrease of suspended sediment concentration is observed at -1D. This is because, without the turbulence modification terms, a much lower turbulent mixing level is found in case TbO in the vicinity of the turbine, and hence less sediment is being transported upwards out of the bottom layer. At 0D, the turbine location, sediment concentration in the bottom boundary layer has a very similar value as that in the undisturbed case. It then rises above the concentration of the undisturbed case from 1D downstream of the turbine. From 3D downstream of the turbine, the suspended sediment concentration of these three cases demonstrates a similar behaviour as that observed in the clear water test: concentration is the highest in case TbM, its value in case TbO is in the middle and it is the lowest in the undisturbed case. This is because the turbulent mixing is gradually recovering to the undisturbed level in the wake and from 3D downstream of the turbine, the mixing level in both turbine present cases has dropped to an extent where the amount of sediment being transported upwards out of the bottom layer is smaller than that being picked up from the bed into the bottom layer through erosion. Under such circumstances, larger bottom shear stress leads to stronger erosion and therefore higher suspended sediment concentration in the bottom layer.

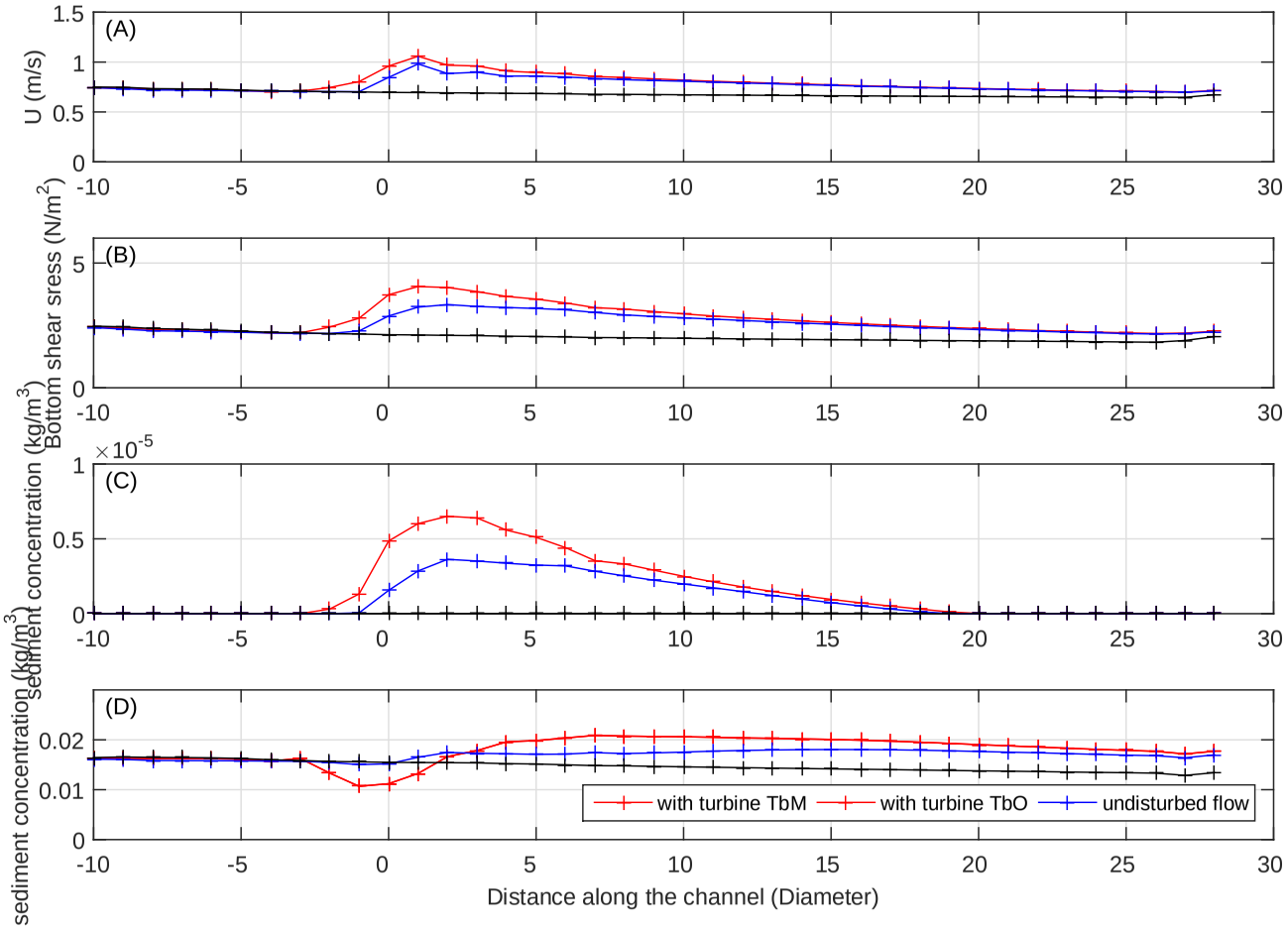

Figure 6.4: (A) Water velocity in the bottom layer, (B) Bottom shear stress, (C) Suspended sediment concentration in the bottom layer along the centreline of a clear water case and (D) Suspended sediment concentration in the bottom layer along the centreline of a live-bed case calculated under different scenarios: TbM - Retarding force + turbulent terms (red lines with markers), TbO - Retarding force (blue lines with markers) and undisturbed flow (black lines with markers).

Suspended sediment distribution across water depth

Figure 6.5 demonstrates the computed suspended sediment concentration across the water depth for the clear water test calculated under scenarios TbM, TbO and undisturbed water. Clearly, due to the size of the particles, vertical transport of sediment from the seabed upwards is very limited. Suspended sediment transport is restricted to the very bottom layers.

Suspended sediment concentration across the water depth for the live-bed test calculated under the three aforementioned scenarios is presented in Figure 6.6. It is observed that sediment suspension is largely restricted to the lower body of the water in the undisturbed flow. Sediment concentration remains constant in this case. Changes in suspension are clearly seen in the other two cases where the turbine is present. Consistent with results discussed in Figure 6.4, sediment concentration close to the bottom is reduced in case TbM around the turbine where changes in concentration within the same region in case TbO is less apparent. Sediment concentration close to the bed further downstream is observed to be increased in both cases TbM and TbO and the increase is more apparent in case TbM.

Apart from changes caused to sediment distribution close to the bed, sediment concentration at the upper part of the water column is also affected. It can be seen from Figure 6.6 that the turbine clearly enhances the turbulence-induced mixing and results in a higher sediment concentration at the upper part of the water in both case TbM and case TbO. This is more apparent in case TbM where the turbulent terms are activated, resulting in a higher TKE level.

Sediment transport rate

Figure 6.7 and Figure 6.8 demonstrate suspended sediment transport rates along the channel calculated under three scenarios of the clear water test and the live-bed test, respectively. The suspended sediment transport rate is calculated according to the following equation at each location:

$$R = \int_{h_b}^{h_s} U_z * C_z dz \tag{6.1}$$

where h_b is the height at bottom, h_s is the height at surface, U_z and C_z are the water velocity and suspended sediment concentration.

Similar to the distribution of sediment concentration at the bottom layer, the suspended sediment transport rate is increased due to the presence of the turbine in the clear water case and it is further increased when the turbulence closure terms are activated. The sediment transport rate reaches its maximum at 2D downstream of the turbine and then starts to fall thereafter. In the live-bed case, on the contrary, the presence of the turbine slightly reduces the suspended sediment transport rate upstream of

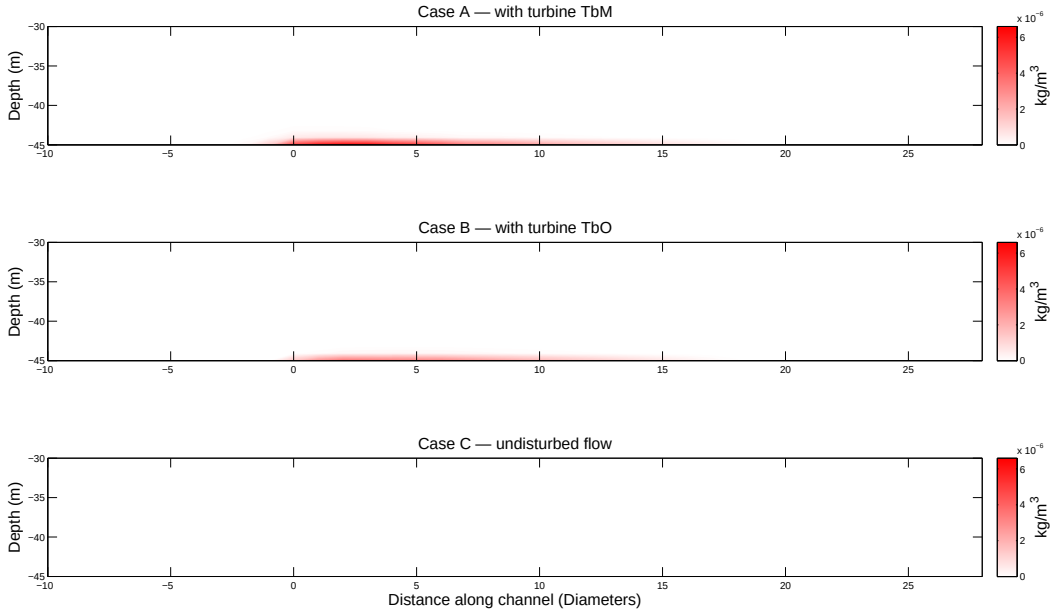

Figure 6.5: Suspended sediment concentration contours of the clear water test: Case A (TbM) —with turbine and with turbulent terms being activated, Case B (TbO) —with turbine but without turbulent terms being activated and Case C —undisturbed flow.

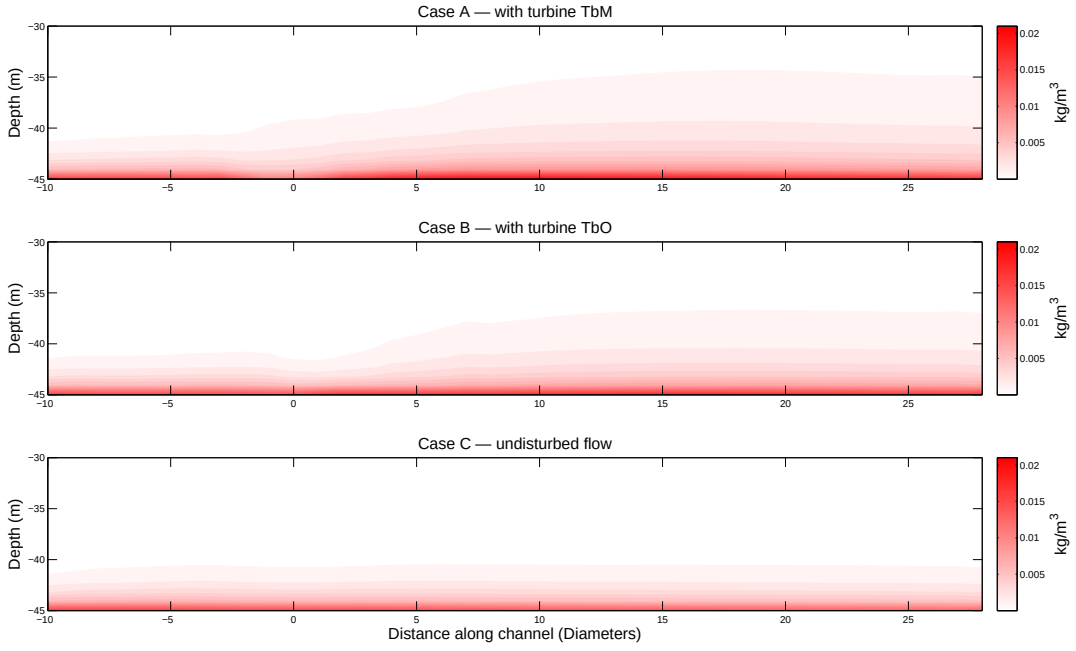

Figure 6.6: Suspended sediment concentration contours of the live-bed test: Case A (TbM) —with turbine and with turbulent terms being activated, Case B (TbO) —with turbine but without turbulent terms being activated and Case C —undisturbed flow.

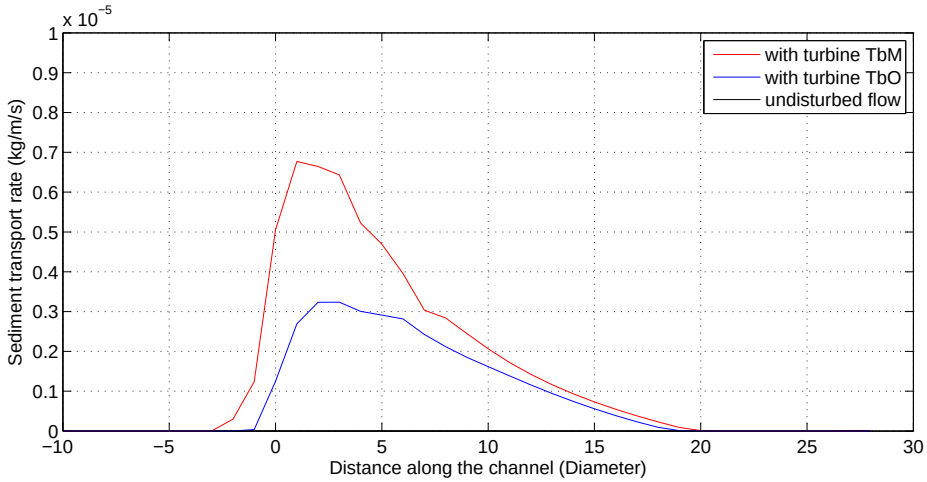

Figure 6.7: Suspended sediment transport rates along the channel of the clear water test under three scenarios.

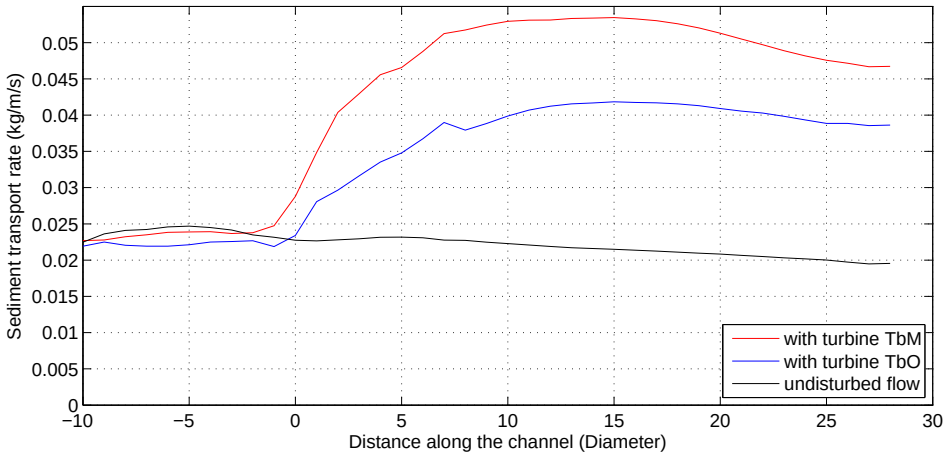

Figure 6.8: Suspended sediment transport rates along the channel of the live-bed test under three scenarios.

the turbine. But it increases in the downstream. The sediment transport rate becomes larger than that of the undisturbed case at 0D in case TbO and at -2D in case TbM. In general, the transport rate of case TbM is larger than that of case TbO.

It can be seen from the above tests that the influences of turbine operation on sediment suspension are not always the same. In the clear water condition, the enhanced turbulence and bed shear stress both tend to increase the sediment suspension and hence lead to a rise in sediment concentration. On the contrary, in the live bed condition, the rise in bed shear stress certainly increases the sediment entrainment from the bed surface. The enhanced turbulence, however, mixes the sediment more uniformly and hence demands a high level of sediment supply. With the right grain size, starvation of sediment in suspension is seen under these two competing mechanisms, which leads to the reduction of concentration near the bottom.

It is therefore noted that the sediment grain size contributes to the fundamental effects on the results. The tests carried out are certainly not exclusive and further experiments with a wider range of grain size should be tested to verify these findings.

6.2.2 Influence of waves and OBSTACLE

This section discusses the extent to which the inclusion of waves affects the bottom shear stress and sediment transport under the presence of turbine. This is done by comparing the results of a current-only TbM case and a wave-imposed TbM case without OBSTACLE. This case is hereafter named as case TNO15. Another wave-current-sediment coupled case with OBSTACLE activated is also tested in this section to further discuss how OBSTACLE affects the bottom shear stress and sediment transport. This case is named as TYO15. Sediment conditions for the live-bed case mentioned above in Table 6.1 are used in this section. Bottom shear stress of these three cases are calculated through BBL.

In the two tests with wave present, waves with 2.4m significant wave height and 7s peak period propagate over the calculation domain which is discretized into a mesh with a constant resolution of 15m. The turbine-representing OBSTACLE is 15m long and K_t is set to the calibrated value of 0.98.

Figure 6.9 compares the computed bottom shear stress, suspended sediment concentration in the bottom boundary layer and sediment transport rate for cases TbM, TNO15 and TYO15. It is observed that the inclusion of surface waves increases bottom shear stress by 7% in general upstream of the turbine and in the far wake (9D beyond) of the turbine. This agrees with the conclusions 'Due to the presence to surface waves, the bottom boundary layer is affected and the shear stress is much higher than that due to current alone.' by [65] which inspired the implementation of the BBL module. Difference in bottom shear stress caused by the waves from the turbine location to 9D downstream is relatively small. The retarding force which represents the turbine opera-

tion is playing the major role within this region enhancing the bottom shear stress of all three cases. In the far wake region, as expected, OBSTACLE slightly reduces bottom shear stress in comparison with case TNO15.

Suspended sediment concentration in the bottom layer in the vicinity of the turbine is decreased in all three cases for the reason given in Section 6.2.1. In general, compared to case TbM, suspended sediment concentration in the bottom layer of the other two cases is reduced by the presence of waves by roughly 4%, due to the fact that the inclusion of waves increases turbulent mixing level, in particular K_h, of the water and hence, more sediment particles are being transported upwards out of the bottom layer. In terms of suspended sediment transport rate, the change in the vicinity of the turbine is small. In the wake region, suspended sediment transport rate is depressed by the inclusion of waves.

In general, although the changes caused by waves and OBSTACLE to the above-mentioned processes are detectable, they are small in the particular case considered here.

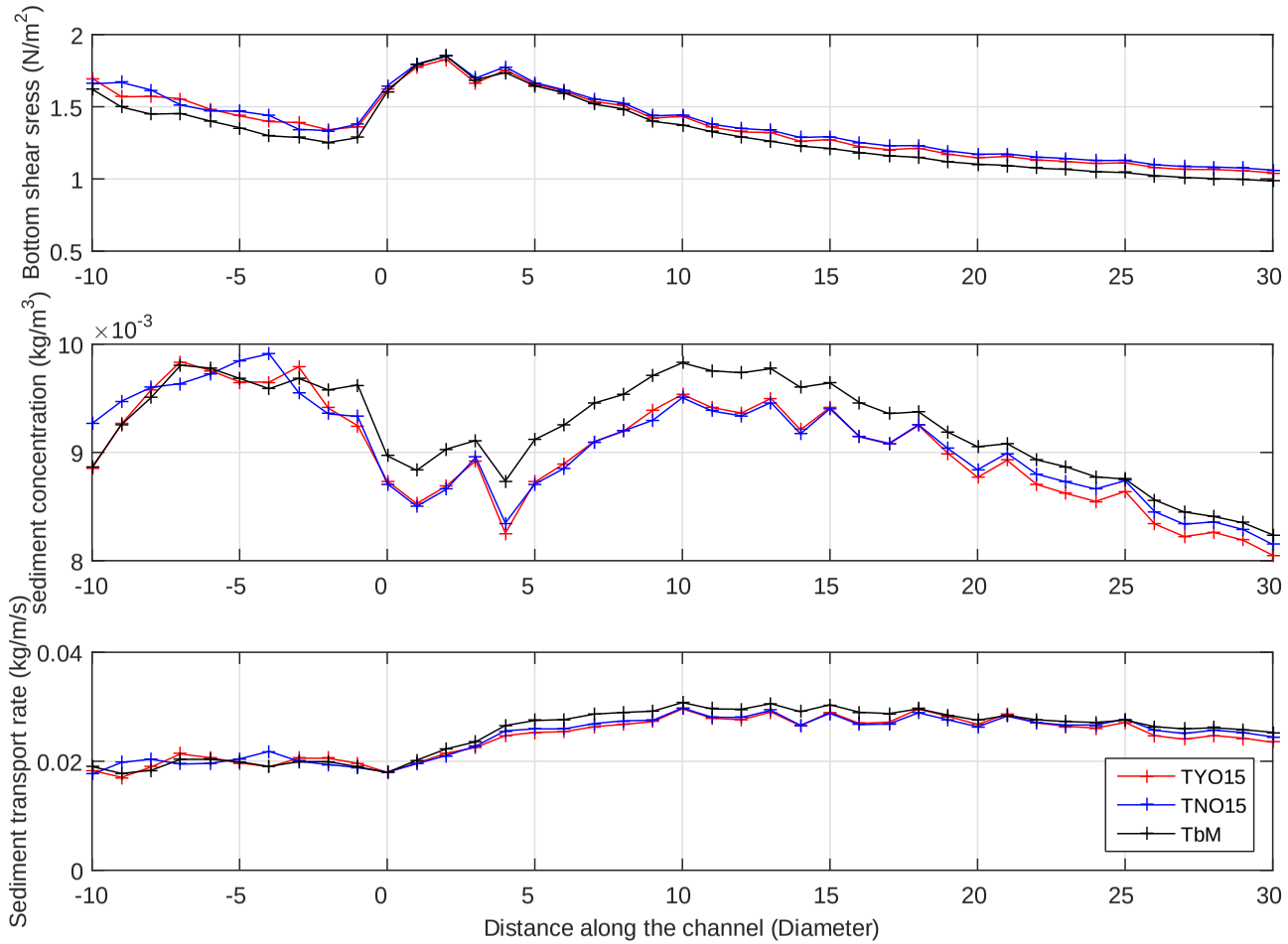

Figure 6.9: (A) Bottom shear stress, (B) Suspended sediment concentration in the bottom layer along the centreline of a live-bed test and (C) Suspended sediment transport rate calculated under three different scenarios: TYO15 - Retarding force + turbulent terms + waves + OBSTACLE (red lines with markers), TNO15 - Retarding force + turbulent terms + waves (blue lines with markers) and TbM - Retarding force + turbulent terms (black lines with markers).

6.3 Irish Sea test

This section applies the model to a sea region identified to have potential for tidal current energy extraction, the Anglesey coast, north-west Wales (denoted by a red box in Figure 6.10). As a part of the Irish Sea which is a high-energy shelf sea region, the Anglesey coast features high tidal ranges and relatively large current velocities as the water flow here is constricted between the mainland and a group of small rocky islands known as the Skerries [34]. Location of the Skerries is again depicted by a red box in Figure 6.11. The vision of converting this coastal sea region into a tidal energy extraction site, therefore, is promising. In fact, this site has been identified as one of the seven sites of interest for tidal current energy exploitation in the UK [14]. Attention has been drawn to tidal current power potential assessment at this site [124, 104, 57, 50, 66, 100].

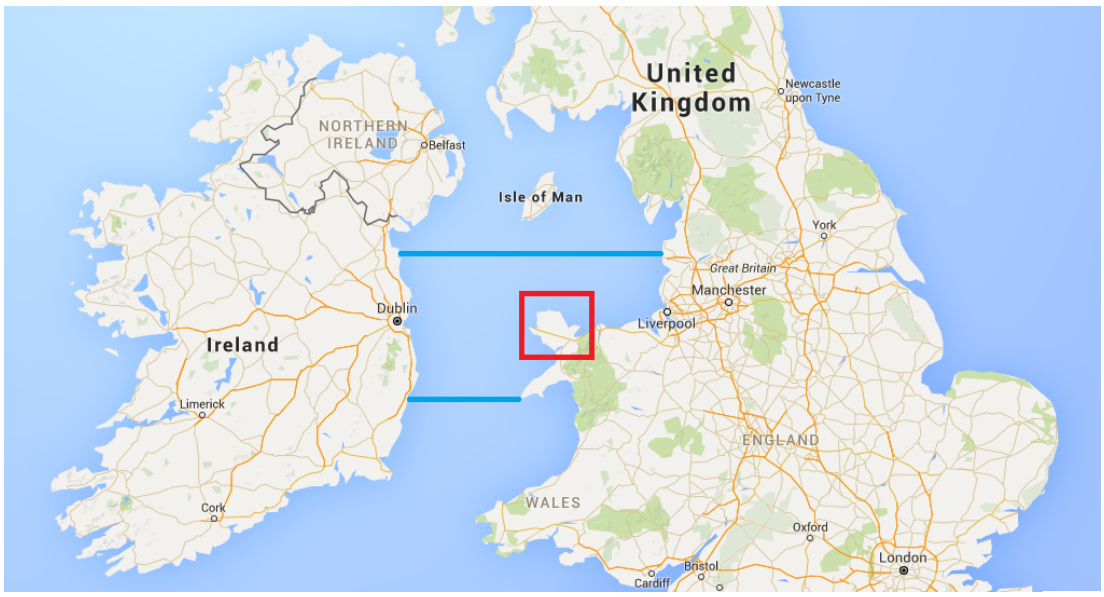

Figure 6.10: Location of the Anglesey Coast and the study domain of the model. Anglesey Coast is depicted by the red box and the study domain is enclosed by the blue lines (open boundaries) and two natural coasts.

In addition, this site has been selected by a tidal current turbine company, Sea Generation, to install a 10MW array of its SeaGen S 2MW devices. This project is named the Anglesey Skerries Tidal Array (ASTA). According to the project website, the location of the proposed array is in the Sound between the Skerries and Carmel Head on mainland Anglesey, where the water depth is approximately 20 to 40m.

6.3.1 Model set up

The study domain, enclosed by the two natural coasts, east coast of Ireland and the west coast of England, and two blue lines, latitudes of which are 52.808°N and 53.842°N, shown on Figure 6.10, is discretized into 67,066 triangular elements. The largest element

Figure 6.11: Location of the Skerries.

size is $1600m$ at the north and south open boundaries. The smallest element size is $15m$ at the turbine farm location to allow turbines within the farm to be presented individually. Suitable element sizes are assigned to coastal areas to allow good resolution of coastlines and islands. This is a three-dimensional model and the water column is divided into 50 sigma layers with identical layer thickness. The bathymetry of the model is extracted from a model covering the west coast of the United Kingdom [21]. Figure 6.12 demonstrates the bathymetry of the model with locations of tidal level, tidal current, waves and sediment validation datasets imposed.

The model is driven by tidal level time series imposed on each of the nodes on the two open boundaries, with the initial mean sea level set as static and at a constant elevation of $0m$. The tidal level time series is obtained through harmonic analysis of 15 tidal constituents (M_2 Q_1 O_1 P_1 S_1 K_1 $2N_2$ MU_2 N_2 NU_2 L_2 T_2 S_2 K_2 M_4) extracted from the High Resolution UK Continental Shelf Model (CS20-15HC3) developed and maintained by the National Oceanography Centre (NOC).

Coriolis effect is considered in this research and the turbulence is modelled using the MY-2.5 model. River discharge is not included despite the presence of several fresh water inflows, considering that first the river discharges are far away from the focused study area and second the water volume carried by the rivers is small compared to the total water volume exists in the modelled area.

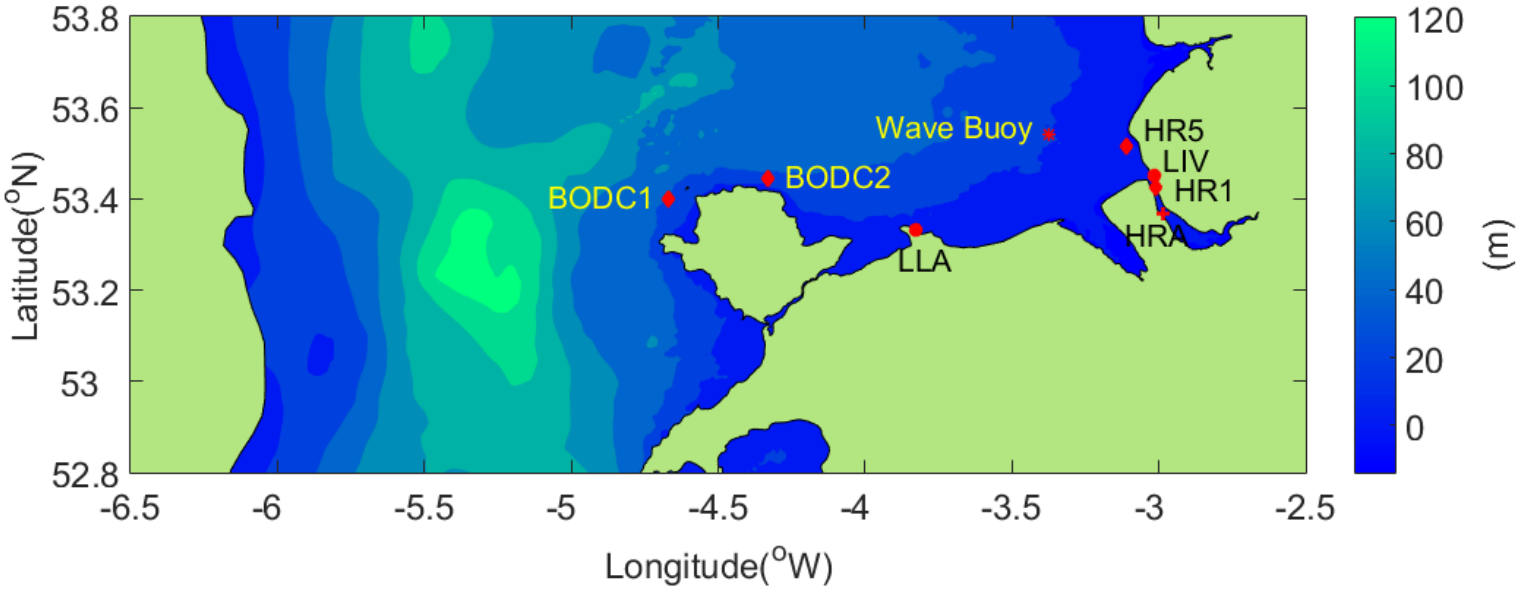

Figure 6.12: Bathymetry of the model and locations of validation datasets. Circles are locations of tide gauges; Diamonds are where tidal current data was collected; Star denotes the location of the WaveNet Buoy; Cross indicates where the sediment data was measured.

Table 6.2: Locations of the tidal gauge sites

Site name	Latitude	Longtitude
Liverpool-Gladstone Dock (LIV)	53.44969°N	3.01800°W
Llandudno (LLA)	53.33167°N	3.82522°W

Table 6.3: Tidal harmonic analysis comparison for M_2 constituent

Site name	Observations		FVCOM	
	$H_n(m)$	$\varphi_n(^\circ)$	$H_n(m)$	$\varphi_n(^\circ)$
LIV	3.08	320.12	3.00	318.78
LLA	2.72	309.83	2.83	309.32

6.3.2 Model calibration

Tidal level

The model predicted tidal water level is calibrated against measurements at two gauges provided by the UK Tide Gauge Network located within the study domain. Table 6.2 gives the locations of these two gauges. They are also indicated as circles on Figure 6.12. The model is run over a month and two days, covering the period from 28/04/2006 00:00:00am to 01/06/2006 00:00:00am. The free surface elevation comparison presented in Figure6.13 shows 750-hour results out from the total model running period.

The model results show overall good agreement with the tide gauge measurements at both sites. No obvious phase lag is observed. The comparison at site LLA shows a slight better agreement. There are some discrepancies in amplitude at site LIV during several spring tides, although the error is small. To quantify the difference, harmonic analysis is carried out at both sites. In total, 29 tidal constituents are recognized by the analysis and M_2 and S_2 are suggested as the dominant constituents. Table 6.3 and Table 6.4 compare the model predicted tidal harmonic constants of M_2 and S_2 against those measured on-site. The model results agree very well with the observations for both amplitude and phase at both sites. The discrepancy between model predicted and measured results in terms of amplitude is within 4.5% at site LLA and 8.1% at site LIV. The model predicted tidal amplitude and angles are slightly smaller than those measured on-site, suggesting that the high tide in the model arrives ahead of that obtained in the observation. However, the phase difference is within 3 minutes. These differences could be due to the uncertainties in the bottom bathymetry at the gauge sites. Also the wind effect is not considered in the simulation which may contribute to these errors. Overall, the model is able to provide accurate predictions in tidal elevation within this particular region.

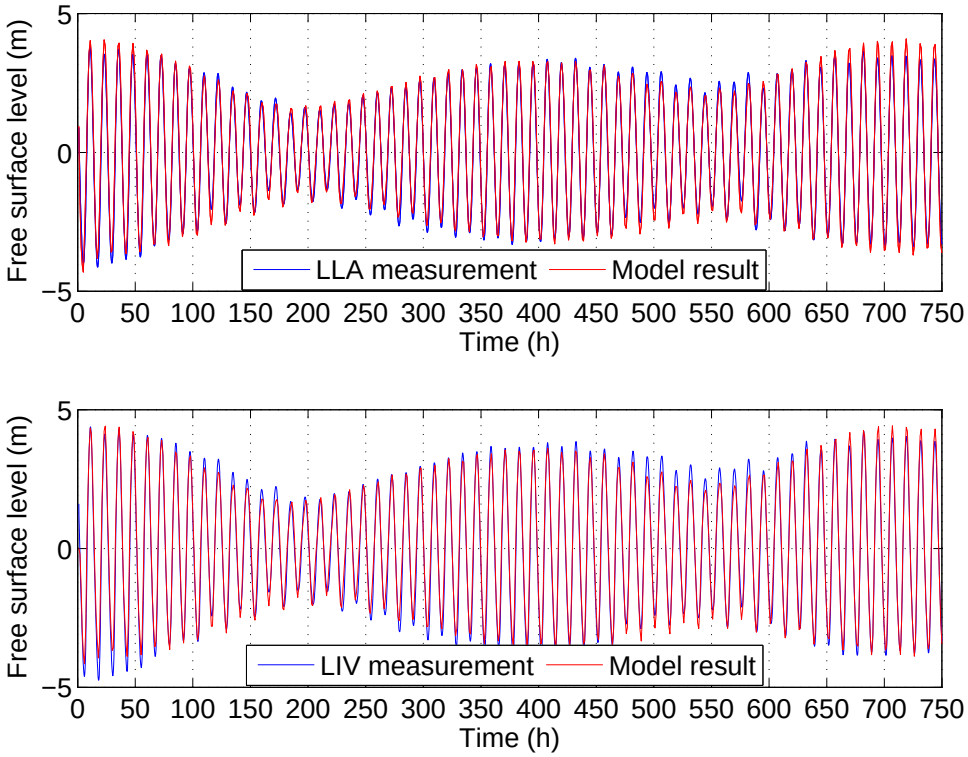

Figure 6.13: Comparison of free surface elevation at the two tide gauge sites.

Table 6.4: Tidal harmonic analysis comparison for S_2 constituent

Site name	Observations		FVCOM	
	$H_{\mathrm{n}}(m)$	$\varphi_{\mathrm{n}}(^{\circ})$	$H_{\mathrm{n}}(m)$	$\varphi_{\mathrm{n}}(^{\circ})$
LIV	0.92	345.05	0.88	344.08
LLA	0.83	332.07	0.83	331.35

Table 6.5: A brief summary of the tidal current validation data

Site name		Coordinates (°)		Time	Surface	Mid-depth	Bottom
		Latitude	Longitude				
HR	1	53.426	-3.01	1983	Yes	Yes	Yes
	5	53.515	-3.11	1983	Yes	No	Yes
BODC	1	53.4	-4.67	1970	No	10/35	30/35
	2	53.445	-4.33	1982	No	No	35/38

Tidal current

To exam the reliability of the model in terms of predicting tidal current, model predicted velocities at the sea surface, mid-depth and bottom layers are compared against two measured data sources. These two data sources are:

- Measurements taken by HR Wallingford during the Mersey Barrage study back in the year of 1983 [126]. Velocities at the surface, mid-depth and bottom layers were measured at five locations within the Liverpool Bay, among which four sites were located at the mouth of the Mersey Estuary and were very close to each other. The other one was located off the Formby coast. Data measured at two of these sites is used for validation in the present research. Coordinates of these two sites are given in Table 6.5. They are marked in Figure 6.12 as diamonds.

- Current meter data downloaded from the British Oceanographic Data Centre (BODC). The BODC current meter data archive was obtained through a number of projects covering a large area as well as a long time span. Vertical coverage of this data source varies among datasets. Data collected at two sites, one located off the north-west coast of the Anglesey island and another one located off the north coast of the Anglesey island which is very close to the proposed turbine farm site, is used in the present research to check the reliability of the model in predicting tidal current. These two datasets date back to years 1970 and 1982, respectively. Locations of these two sites are given in Table 6.5. They are also marked as diamonds in Figure 6.12.

Table 6.5 gives a brief summary of the tidal current validation data. Data availability along the water depth varies among these sites. For example, the current was measured at three depth at site HR1 while it was only measured very close to the bottom at site BODC2.

Figure 6.14 and Figure 6.15 present the model computed tidal current velocities against HR Wallingford measured data at locations HR1 and HR5. Model predictions and on-site measurements agree very well at three depth at site HR1. Predicted peak velocities during flood and ebb tides are fairly close to the on-site measurements. A

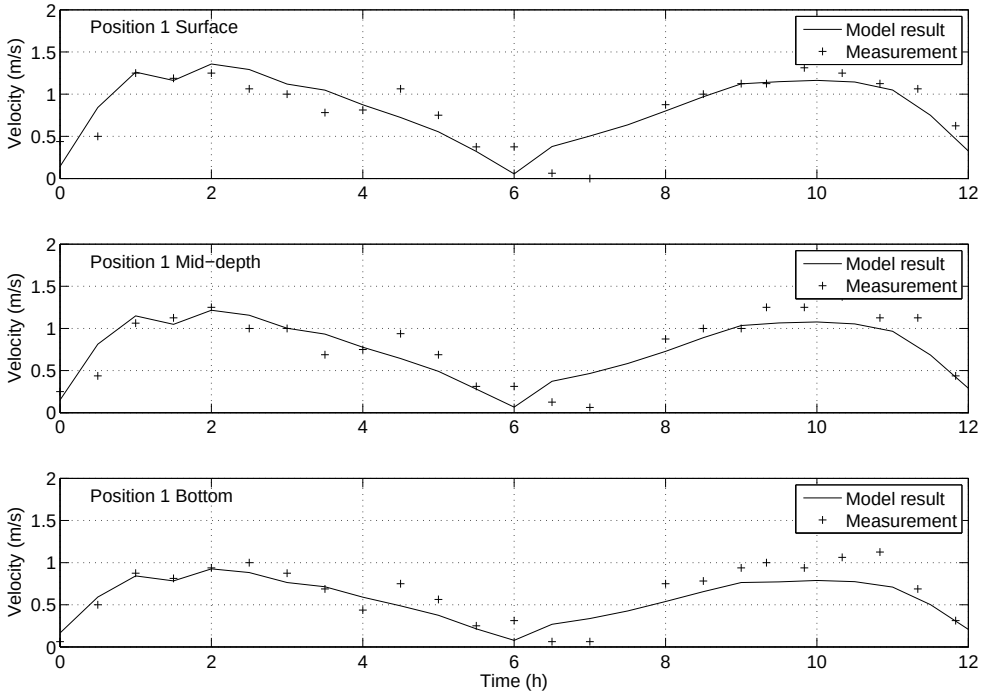

Figure 6.14: Comparison of model predicted and measured flow velocity at three levels at HR1.

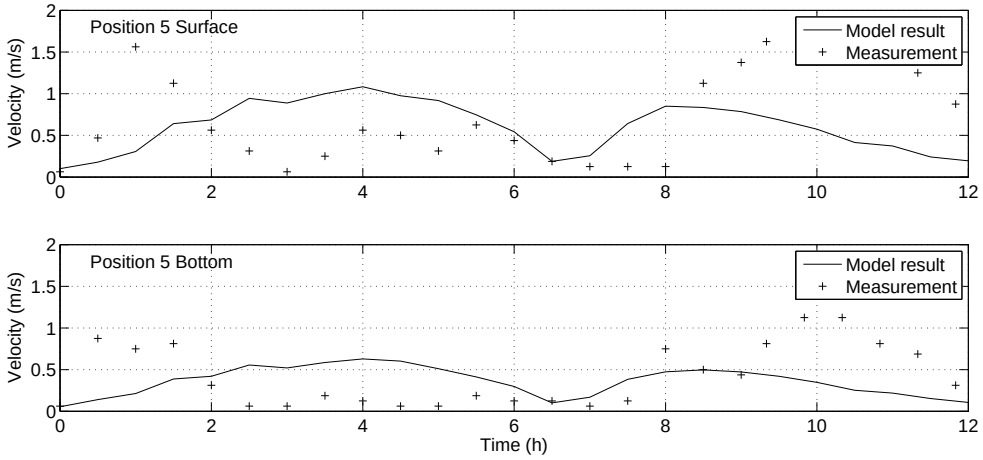

Figure 6.15: Comparison of model predicted and measured flow velocity at two levels at HR5.

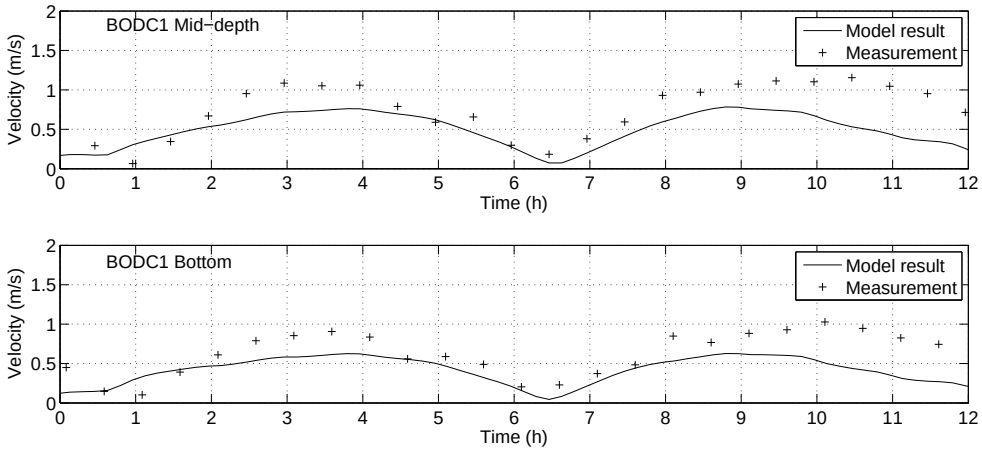

Figure 6.16: Comparison of model predicted and measured flow velocity at two levels at BODC1.

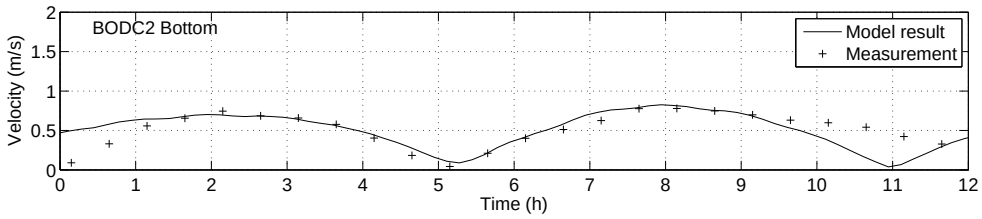

Figure 6.17: Comparison of model predicted and measured flow velocity at bottom at BODC2.

noticeable feature of the current at site HR1, i.e. rapid increase and prolonged decrease of flow speed during flood tide and, conversely, prolonged increase and sharp decrease of flow speed during ebb tide, is also being simulated correctly by the model. The model's performance at site HR5, however, is less accurate. Peak velocity during flood tide is over-estimated and it is largely under-estimated during ebb tide. These discrepancies could be attributed to the inaccurate bathymetry used in the model. It should be noted that HR5 is positioned further inside the estuary and close to the bank, where the uncertainty in the bed level in the model is large.

Figure 6.16 and Figure 6.17 show the model's performance at the 2 BODC measuring sites. In general, the result is in good agreement with the measurements. Peak velocity is slightly under-estimated during both flood and ebb tides at site BODC1. The model clearly shows a very good agreement with the measurements at site BODC2. Again, inaccurate bathymetry used in the model could contribute to the discrepancies mentioned above. Unfortunately, no detailed bathymetry data is available. In addition, the surface wind which is not included in the present simulation could also have had effects on the measured data as discussed. Nonetheless, the general performance of the model in terms of simulating three-dimensional current flow structure is satisfactory.

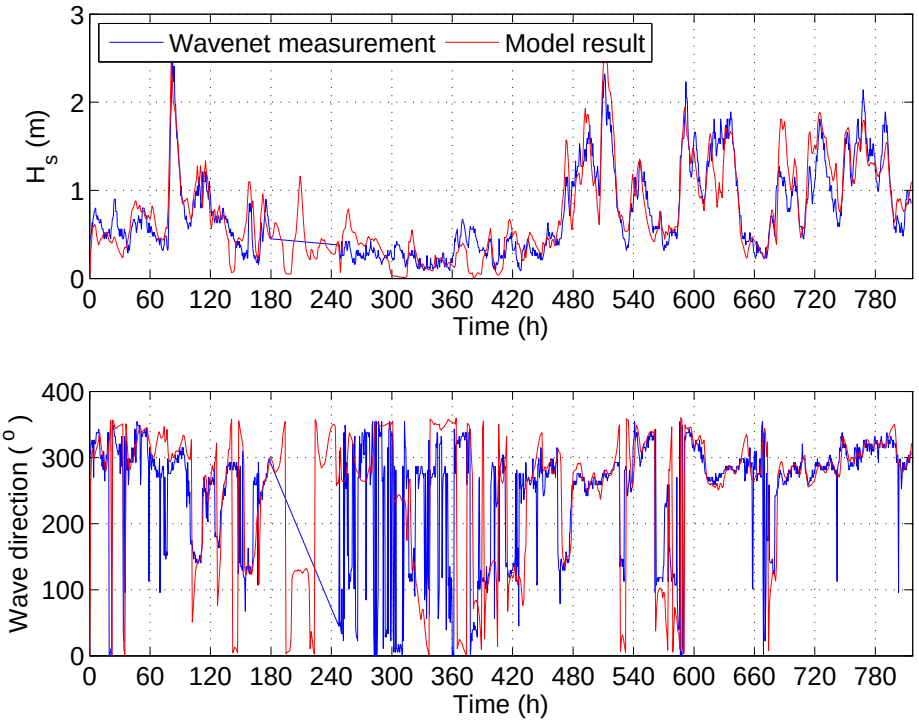

Figure 6.18: Comparison of modelled significant wave height and wave direction against measurements over a month.

Wind and waves

To validate the reliability of the model in terms of predicting waves, the current-wave-sediment fully coupled system is tested against measurements. A time series of wave condition is imposed on each open boundary mesh point according to dataset 'ERA-Interim' available on the European Centre for Medium-Range Weather Forecasts (ECMWF) website. A time varying uniform wind field created based on data measured at the Hilbre Island weather station is applied to all the nodes within the mesh. White-capping is considered in the model using the method introduced in [64]. The calculation of wave breaking follows the approach proposed by [11]. Formulation accounting for bottom friction is the JONSWAP formulation [51]. The friction coefficient is set to $0.067 \mathrm{m}^2\mathrm{s}^{-3}$ in the present study.

As for current validation case, the wave model is run over a month and two days, covering the period from 28/04/2006 00:00:00am to 01/06/2006 00:00:00am. The computed results are validated against data collected by a WaveNet buoy. The coordinates of the buoy deployment location are 53.5315°N, 3.3713°W and the location of the buoy is marked by a star marker in Figure 6.12.

Figure 6.18 presents the modelled wave height and direction of 820-hour results against the WaveNet buoy data. The on-site data is missing at 180-240 hours. In general, the model-predicted values agree with the data well. The model is capable of predicting the magnitude and phase changes of wave height and direction, particularly for the large storms at 80-100 hours, 480-540 hours and 590-610 hours.

Sediment transport

The predicted sediment concentrations at various phases over two tidal processes, spring tide and neap tide, are compared with measurements from a Mersey barrage feasibility study carried out in year 1990 by HR Wallingford [125]. Suspended sediment concentrations were collected at point HRA (point A in [125]). The coordinates of point HRA are 53.368°N, 2.984°W. The relative location of point HRA can be found in Figure 6.12. The measurements were taken over a spring tide as well as a neap tide at several heights above the seabed. Model time and parameters required to calculate the suspended sediment concentration were adjusted accordingly. The sediment particle size is specified as $D_{50} = 0.22mm$ across the entire study domain according to [125]. Uniform distribution of sediment with $D_{50} = 0.22mm$ is also used in [29]. Waves are absent in this simulation.

Figure 6.19 and Figure 6.20 present the model predicted and measured flow velocity and suspended sediment concentration at point HRA along the water depth, over tidal cycles of a spring tide and a neap tide. The model results demonstrate a good agreement over the tidal cycles in terms of predicting the flow velocity. There are differences in the computed suspended sediment concentration in the region close to the bed surface, which could be attributed to the uncertainties in the measurements. The measurements were also collected sequentially which may lead to uncertainties in the timing of the data that is different from the simulation. In addition, the model used a uniform grain size which is different from the real size distribution across the computational domain. The involvement of mud material in the computational domain is not considered in the present study. Absence of waves might also have contributed to the errors. Nevertheless, the overall performance of the model in predicting concentration of suspended sediment is considered to be good.

6.3.3 Model application

After calibration, the model is applied to assess the impact of a tidal turbine farm on coastal processes around the Anglesey coast. Model results obtained through a wave-current-sediment fully coupled system are analysed in detail to identify short term impacts of the farm. Turbine simulating terms introduced in the previous chapters are activated with each of the coefficients set to the calibrated value except the bottom stress term. The additional bottom stress term is not activated because it is not yet proven to be the right option for solving the problem mentioned in Section 4.4.3.

The model is run from 17/05/2006 07:00:00am to 20/05/2006 05:00:00am which includes five and a half tidal cycles. Averaged tide range of these tidal cycles at LLA is 5.71m. The reason to select this time period is that the wave height peaks at 2.32m at the wave buoy location and 3.62m at the selected farm location (see Figure 6.21) during this time slot, representing moderate wave to stormy wave conditions. Free surface level

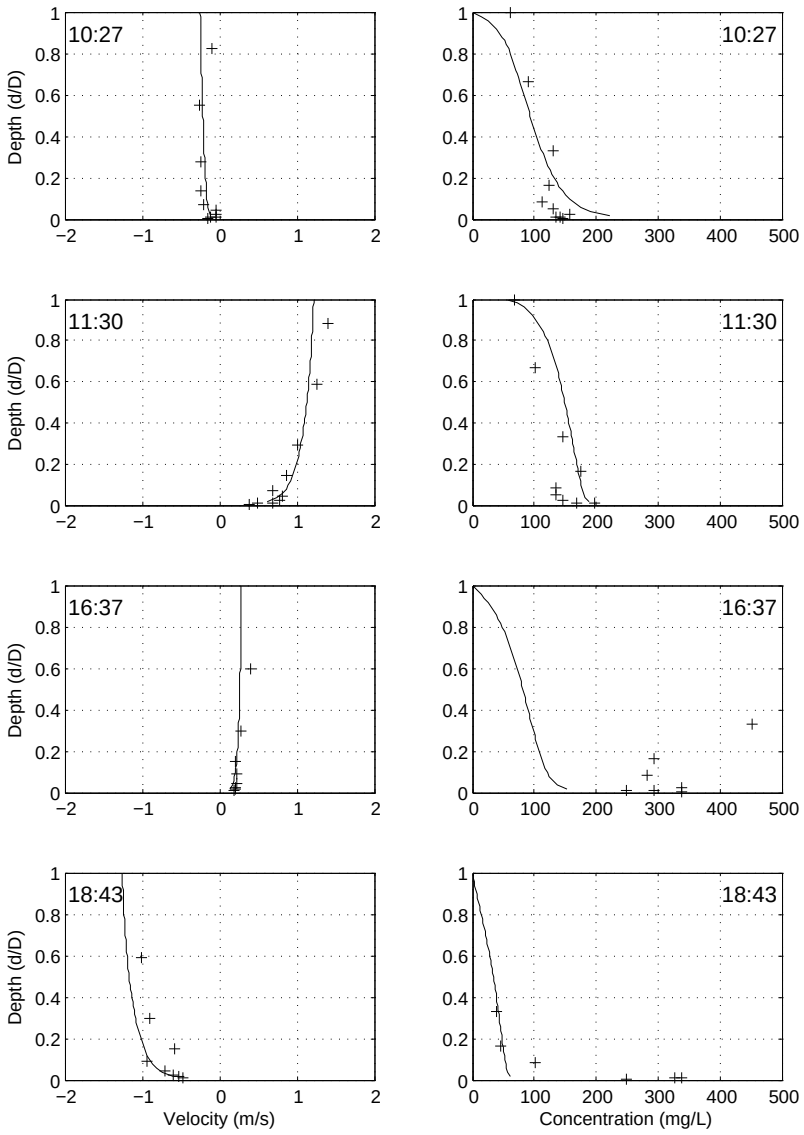

Figure 6.19: Comparison of model predicted and measured flow velocity and suspended sediment concentration at different height above the bed at point HRA over a spring tide. Four panels on the left-hand side are flow velocity profiles and the four panels on the right-hand side are suspended sediment concentration profiles. The solid lines denote model calculated values and the symbols are for the measured results.

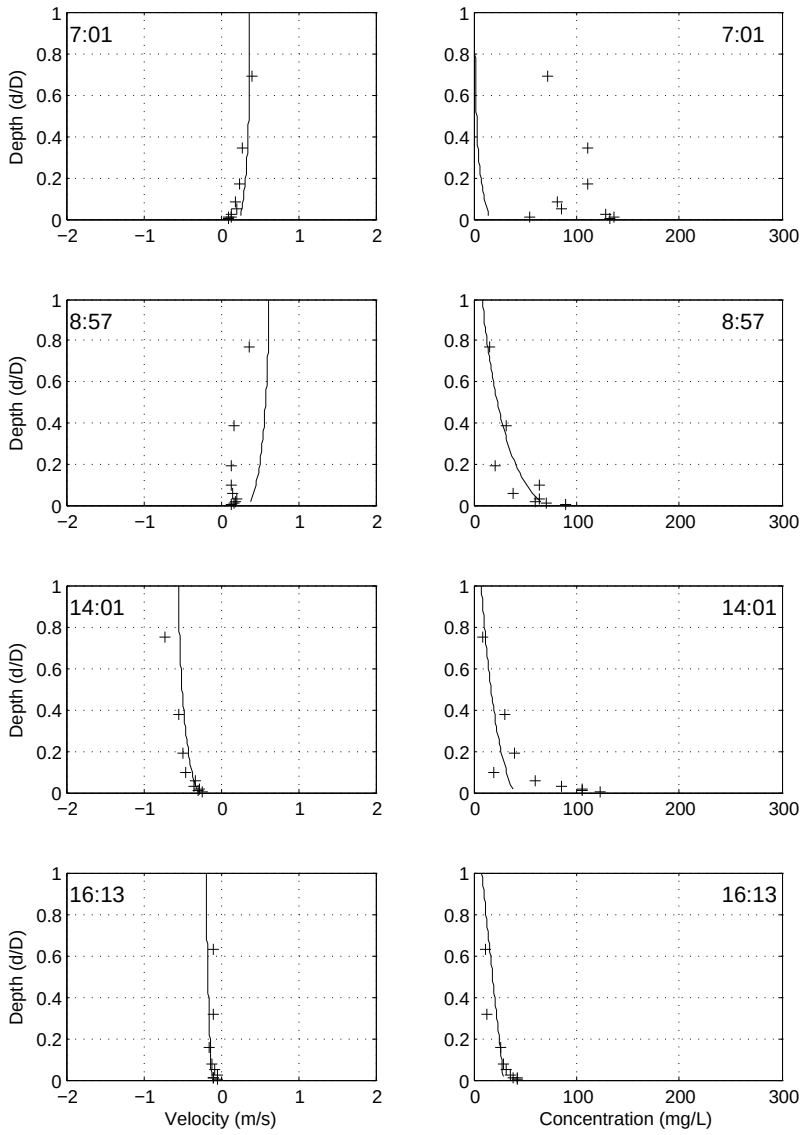

Figure 6.20: Comparison of model predicted and measured flow velocity and suspended sediment concentration at different height above the bed at point HRA over a neap tide. Four panels on the left-hand side are flow velocity profiles and the four panels on the right-hand side are suspended sediment concentration profiles. The solid lines denote model calculated values and the symbols are for the measured results.

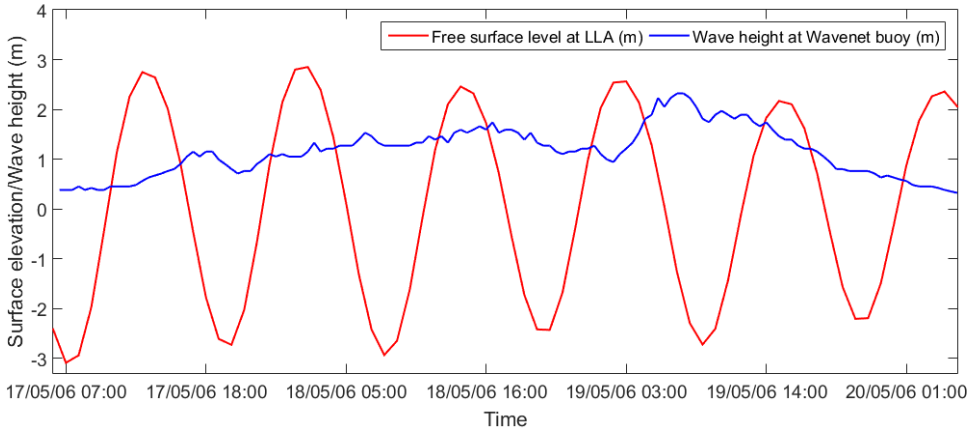

(a) Free surface level at LLA and wave height measured by the Wavenet buoy.

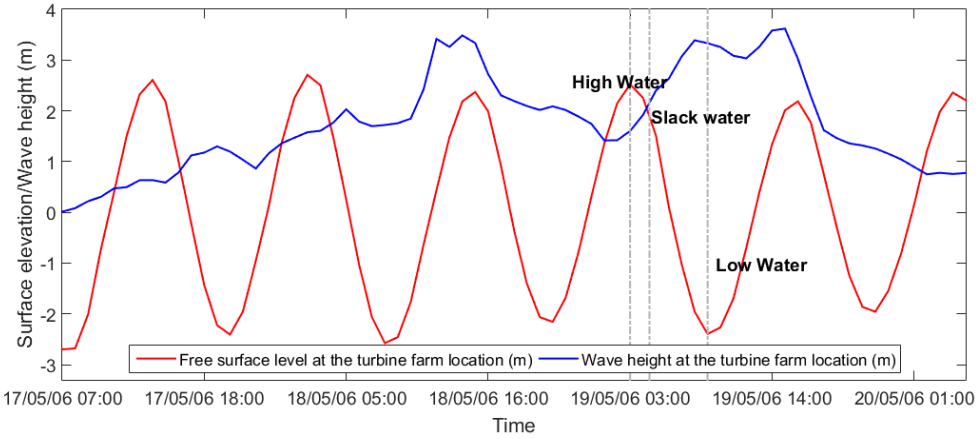

(b) Model calculated free surface level and wave height at the turbine farm location.

Figure 6.21: Sea conditions from 17/05/2006 07:00:00am to 20/05/2006 05:00:00am.

at LLA and wave height measured by the Wavenet buoy during this time period are given in Figure 6.21 (a). Model calculated free surface level and wave height at the farm location are given in Figure 6.21 (b). The three grey dash-dot lines indicate three moments, High Water, Slack water and Low Water, at which some analysis in Section 6.3.4 and Section 6.3.5 is made.

The model domain shown in Figure 6.12 covers an area larger than the focused region off the Anglesey coast. Figure 6.22 presents the water depth over the focused area. It can be seen from the figure that the water depth increases gradually towards the open sea. The water depth between north-west Anglesey and the Skerries is approximately 30m which is acceptable for tidal turbine installation. Figure 6.23 depicts a typical flow pattern based on depth-averaged velocity between north-west Anglesey and the Skerries, with the locations of the tidal turbines highlighted. The location of the farm is chosen based on the above-mentioned two factors, i.e. acceptable water depth and large flow rate. The farm is also located in the middle of the waterway to minimize its

impacts on the local shores. The farm consists of 18 turbines. In the current research, each turbine is assigned a diameter of 15m and is represented by an individual mesh cell. Vertically, the turbines are located at the mid-depth. The turbines in the farm are aligned in a staggered way. They are separated from each other by 8D laterally and 15D in the up/downstream flow direction. The staggered layout is suggested by a few researches to be efficient, as it can reduce wake interference between consecutive rows and the flow upon which the downstream row turbines extract energy is accelerated and thus carries more available kinetic energy [81, 6, 79].

The two black solid lines indicate slices of which samples of computed free surface elevation and bottom shear stress and vertical contours of velocity and TKE are drawn in Section 6.3.4. The one parallel to the Skerries, namely 'slice 1', crosses through the device farm along the direction of the dominant flow (east-westerly). Two individual turbines sit on slice 1 with another one very close to it. The other one, namely 'slice 2', crosses through the device farm perpendicularly to the direction of the dominant flow. It has a close proximity to the third row of devices counting from the left-hand side of the figure. In general, it is about 3D away from the third row of devices counting from left-hand side of the figure and 12D from the second row of devices counted in the same manner. It provides information to study the near wake of the third row of devices at High Water, when water flows from north-east towards south-west. At Low Water, when the water flows in the opposite direction, it provides information of hydrodynamics in front of the 5 turbines in the third row of devices.

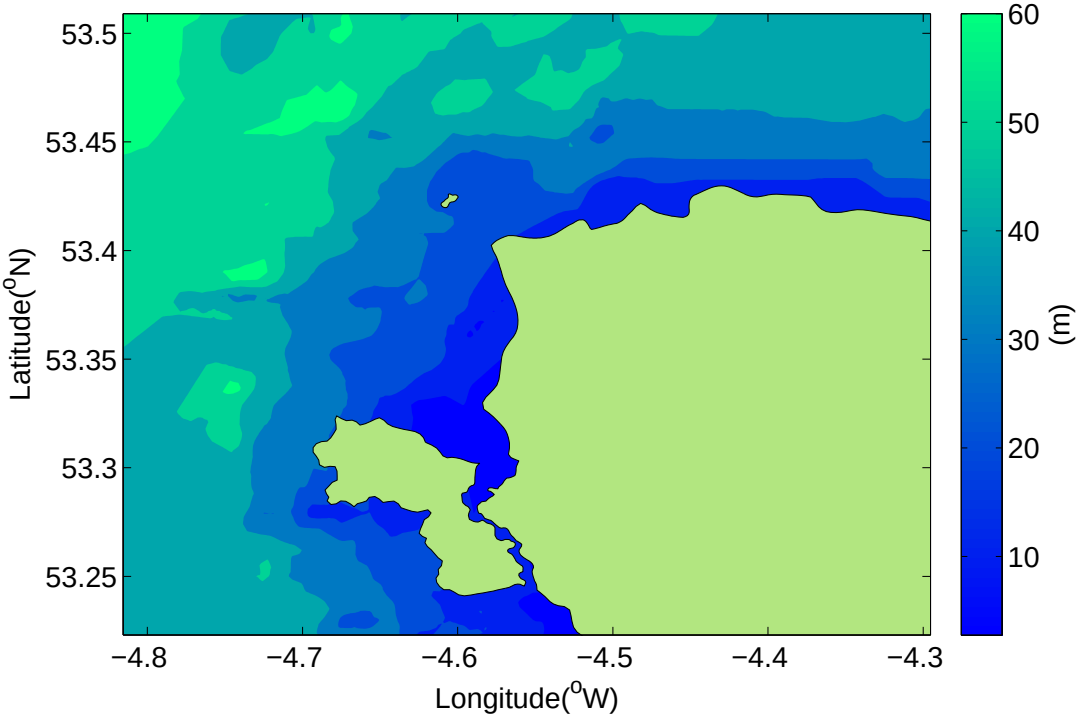

Figure 6.22: Water depth off the Anglesey coast.

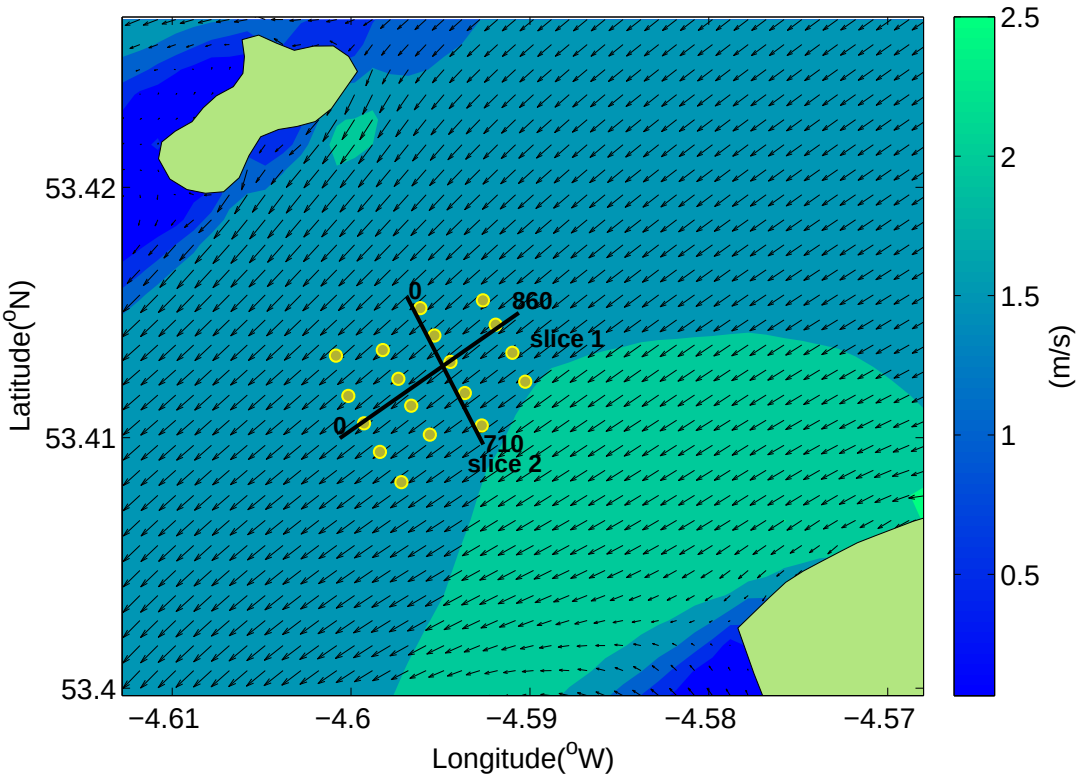

Figure 6.23: A typical pattern of water depth averaged velocity between the north-west Anglesey and the Skerries, with the locations of the tidal turbines highlighted (arrows imposed just to indicate the flow direction). The two black solid lines indicate locations at which trend lines of free surface elevation and bottom shear stress and vertical contours of velocity and TKE are drawn in Section 6.3.4.

6.3.4 Results — Local impacts

This section studies local impacts of the turbine farm on hydrodynamics and suspended sediment concentration in the vicinity of the farm within the waterway between the north-west Anglesey and the Skerries. Analysis features horizontal slices at the surface, the mid-layer and the bottom of the area depicted in Figure 6.23 at the three selected phases of the tide indicated in Figure 6.21 (b). The computed free surface elevation, flow velocity, TKE and bottom shear stress are drawn along two vertical slices, locations of which are displayed as solid black lines in Figure 6.23.

Surface elevation

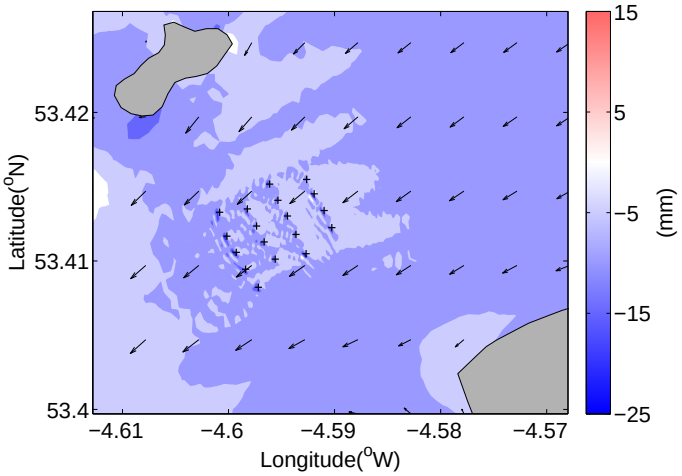

(a) High Water

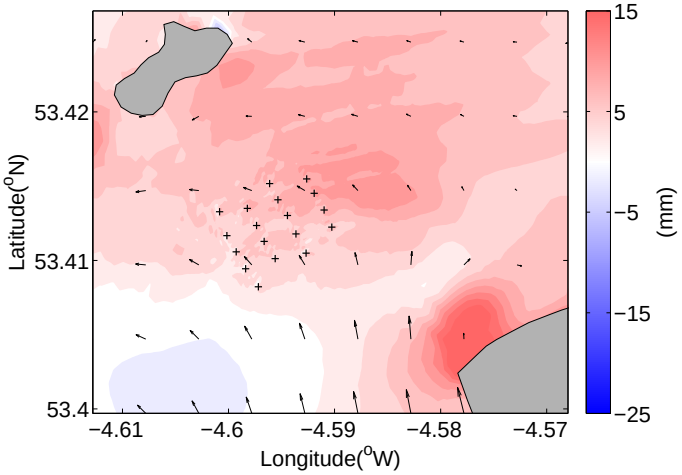

(b) Slack water

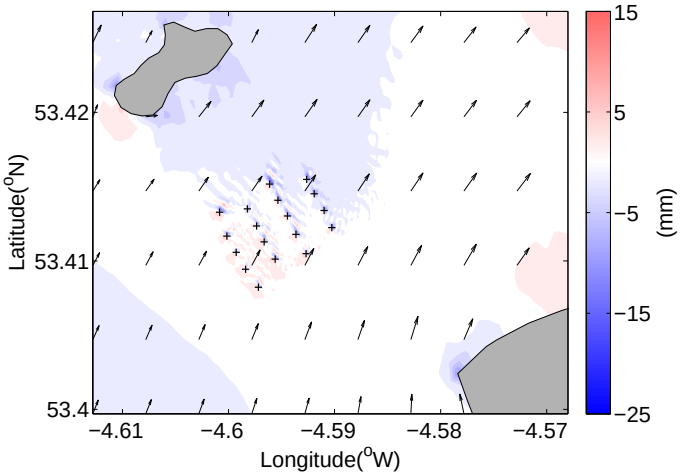

(c) Low Water

Figure 6.24: Surface elevation changes in the vicinity of the farm (arrows imposed to indicate the flow direction).

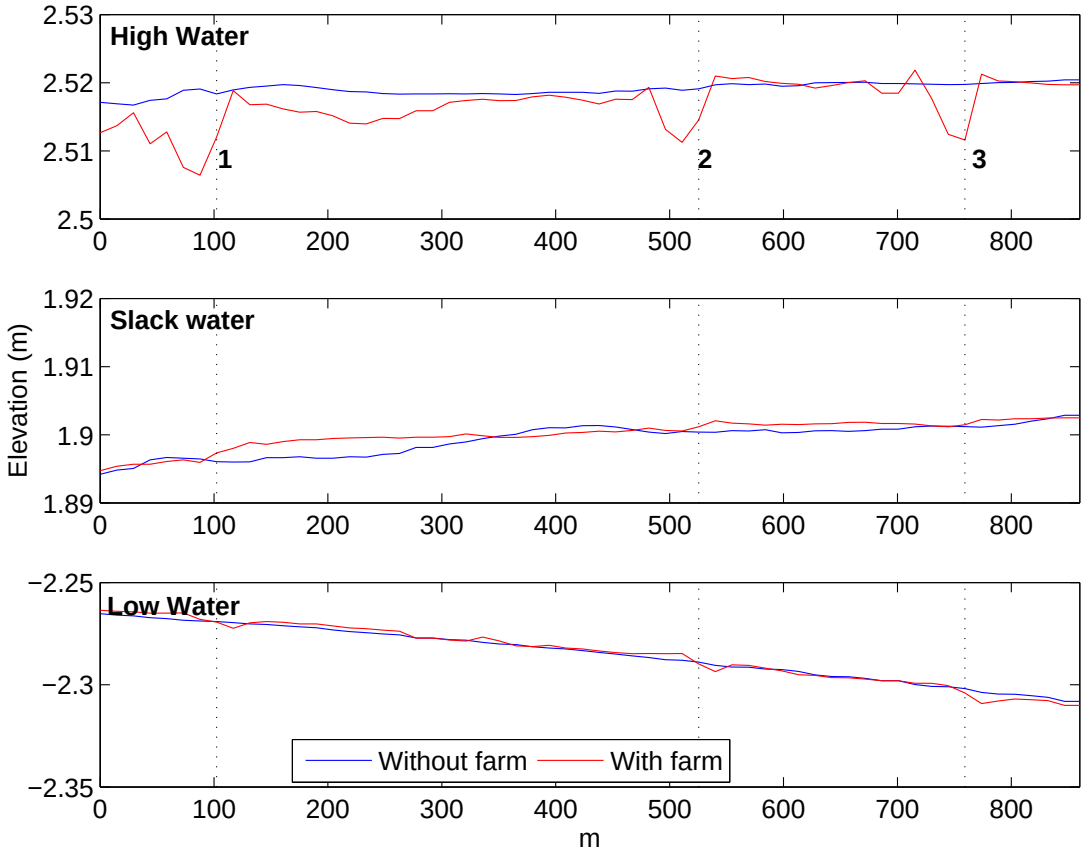

Figure 6.25: Surface elevation with and without turbine farm along slice 1 at the three selected phases of the tide.

Changes in the computed surface elevation due to the implementation of the turbine farm at High Water (HW), Slack water and Low Water (LW) are presented in Figure 6.24. Positive values indicate rise in water surface and negative numbers refer to drop in surface. At HW, the current flows towards south-west, the surface elevation around the farm site reduces by 5-15mm. Close to the turbine structures, the elevation change shows a serrated pattern in the near-field of the farm at the downstream of the turbines. The serrated pattern is also observed at LW, when the current flows towards north-east. However, at LW, slight increase in water level around the first 2 rows upstream of the farm is observed, indicating a strong obstruction of the farm. This agrees with what was seen in Figure 6.2. As expected, water level downstream the farm reduces, but at a less extent in comparison to that at HW. At Slack water, at south of the turbine farm the current flows northwards, meeting a westwards flow within and around the farm. The blockage effect of the turbine farm and the confining Skerries together is causing the surface elevation within the area to increase by a range of 5-15mm.

Figure 6.25 shows surface elevation with and without the device farm along slice 1 at the three selected phases of the tide. The black dotted lines indicate locations where turbines are present (locations 1 and 2) or nearby (location 3). Typical influence of

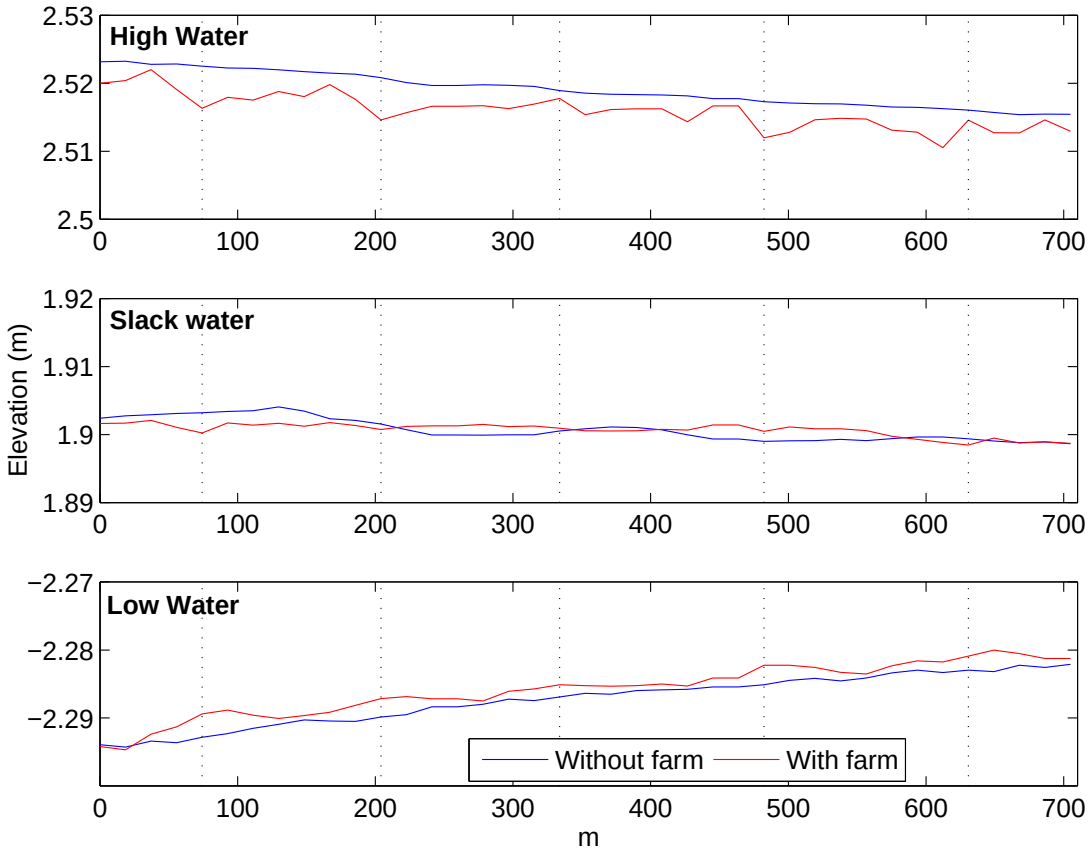

Figure 6.26: Surface elevation with and without turbine farm along slice 2 at the three selected phases of the tide.

turbines on surface elevation is observed at both HW and LW. During HW, the flow direction is, in the figure, from 800m to 0m. Compared to the no turbine case, elevation around turbine present locations 2 and 3 undergoes a slight increase followed by a substantial decrease then an increase back to the undisturbed level. Similar disturbance to the elevation is observed at turbine present location 1. However, the elevation is generally reduced which could be attributed to the overall decrease of surface elevation at the downstream end of the farm. Similar behaviour is observed during LW, when the water flows, in the figure, from 0m to 800m, but with a smaller magnitude than that at HW. The typical disturbance pattern is not observed at Slack water. Increase in surface elevation is the rather dominant process which agrees with that observed in Figure 6.24.

Figure 6.26 shows surface elevation with and without the device farm along slice 2 at the three selected phases of the tide. The black dotted lines indicate locations of the 5 turbines on the third row of devices counting from the left-hand side of Figure 6.23. Figure 6.25 at HW shows influence of the 5 turbines on surface elevation in the near wake. It is observed that the presence of the turbine row has, overall, reduced the elevation in the near downstream. On the other hand, the comparison at LW demonstrates changes the surface elevation undergoes in front of the 5 turbines on the third row of devices. It can be seen that at all five turbine locations, surface elevation is increased due to the blockage effect of the turbine. Another useful observation is the rather small gaps between the two curves in between two neighbouring turbines observed at LW. It indicates that influence of the upstream second row of devices on elevation in front of the third row of devices has diminished to a negligible level. Plots at the Slack water, again, do not show any typical pattern. However, compared to the dominant increase in elevation observed in Figure 6.25, elevation along slice 2 experiences both increase and decrease across the slice.

Flow Hydrodynamics

Figure 6.27 and Figure 6.29 present the flow fields in the vicinity of the farm at HW and LW across the surface layer, middle layer and bottom layer, together with the corresponding differences between the with- and without-turbine cases. The wake of each turbine can be seen clearly at both phases of the tide. It is found on the right panels that while the surface and the mid-layer mainly undergo water deceleration, and the depth averaged flow fields constantly suggest overall decelerated flow in the wake, the water at the bottom in the vicinity of the farm is accelerated at both phases of the tide, indicating that, vertically, the decelerated water due to the blockage of the farm squeezes its way through the bottom layers. This is bound to increase the bottom shear stress calculated. In comparison, the near wake length during LW in Figure 6.29 is shorter than that during HW in Figure 6.27, largely due to the weaker flow speed at

that time. Figure 6.28 displays the flow fields in the vicinity of the farm at Slack water. Instead of the typical wake pattern observed above at HW and LW, the flow field in the vicinity of the farm is rather chaotic at this phase of the tide, due to the complicated combination of the turbine farm and the meeting of the northerly flowing water from the south and the westerly-going water from the east. Changes caused to the velocity are also the least strongest, mainly due to the weakest flow speed in comparison to the other two phases of the tide.

Figure 6.30 shows the velocity changes through the depth along slice 1 at the three selected phases of the tide. Flow speed deceleration at and above mid-layer is clearly observed during HW and LW at locations 1 and 2 where turbines are present and location 3 where a turbine is nearby. The deceleration is less strong at location 3 as expected. Such deceleration at and above mid-layer is also seen at Slack water at locations 1 and 2, but with a less extent, possibly due to the reason mentioned above. It is however absent at location 3. On the other hand, flow acceleration is observed at nearly 1/3 of the water depth near the bottom at the investigated locations except location 3 during Slack water. However, the spatial span of the accelerated flow is in general shorter than that of the decelerated flow. Another finding is that the turbines are still very likely to operate within the wake of the devices at the upstream, despite the rather large spatial spacings and the staggered layout design.

Figure 6.31 demonstrate the velocity changes across the depth along slice 2 at the three selected phases of the tide. The contour at HW indicates the wake at roughly 3D downstream of the third row of devices counting from the left-hand side of Figure 6.23. The five turbines are clearly reflected on the figure. The flow speed in between two adjacent turbines is decelerated, instead of being accelerated, under the present lateral spacing. The turbines are weakly reflected in the contour at Slack water. Flow acceleration near the bottom is also observed in the contour at LW, implying that the influence of the turbines can reach 3D upstream or even beyond. Flow at and above mid-layer at this phase of the tide is decelerated, which is a combined result of the blockage of the turbines on the third row of devices and the wake from the upstream turbines.

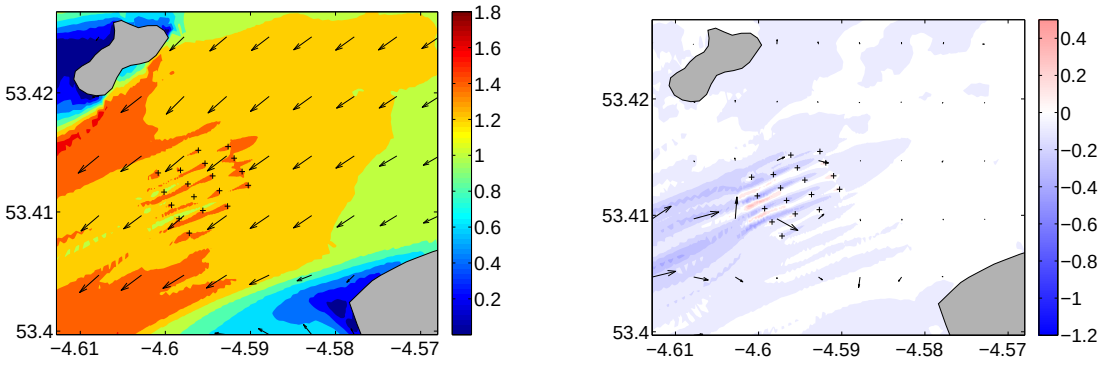

(a) With turbine, surface

(b) Difference, surface

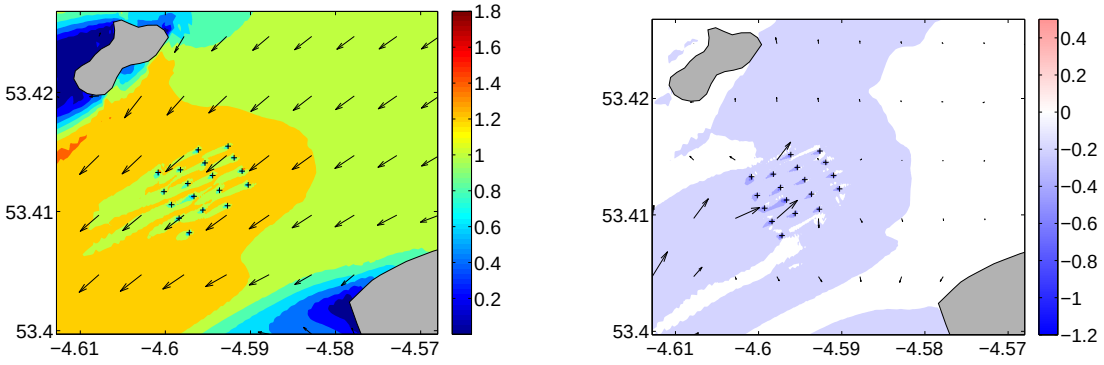

(c) With turbine, mid-layer

(d) Difference, mid-layer

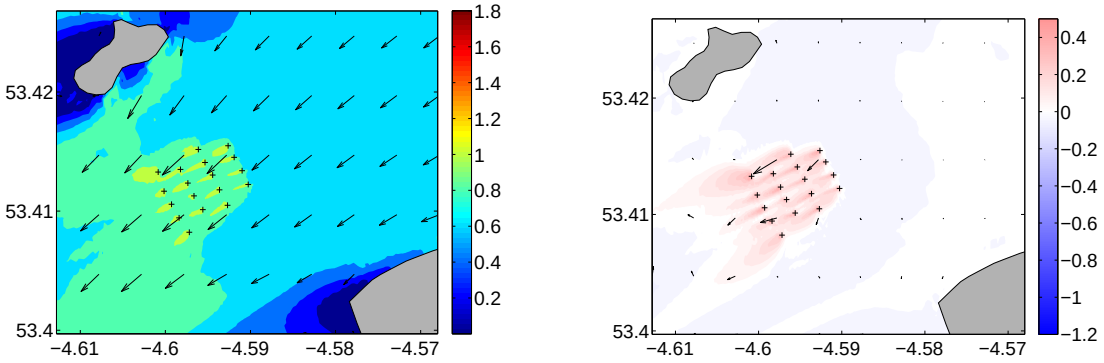

(e) With turbine, bottom

(f) Difference, bottom

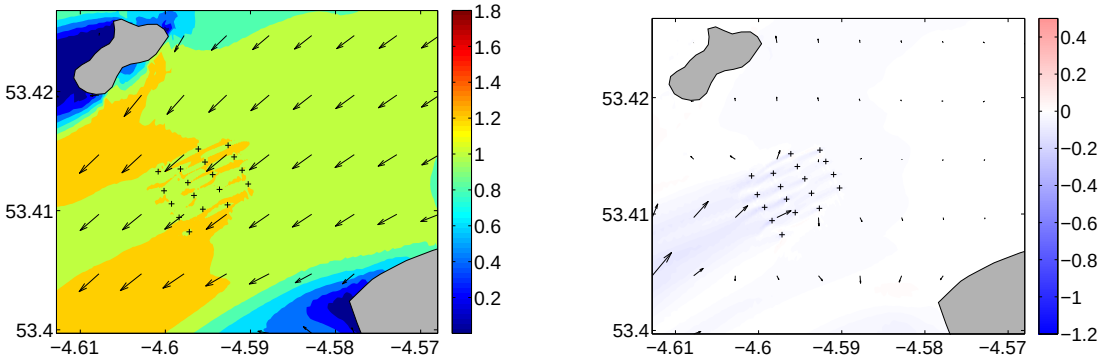

(g) With turbine, depth averaged

(h) Difference, depth averaged

Figure 6.27: Flow fields with turbine farm and flow field change contours in the vicinity of the farm imposed with velocity vectors and turbine locations at HW. (unit: m/s)

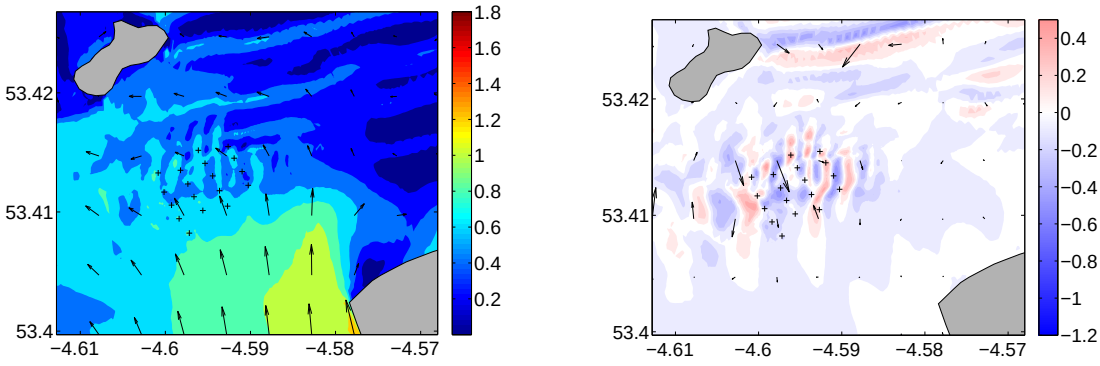

(a) With turbine, surface

(b) Difference, surface

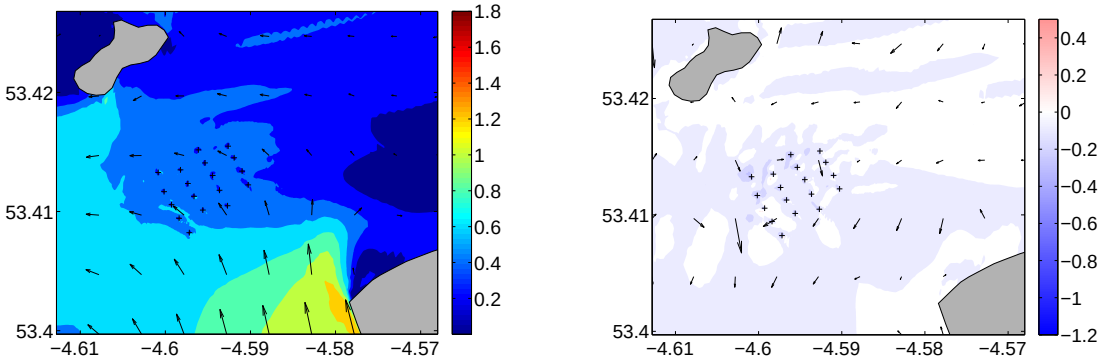

(c) With turbine, mid-layer

(d) Difference, mid-layer

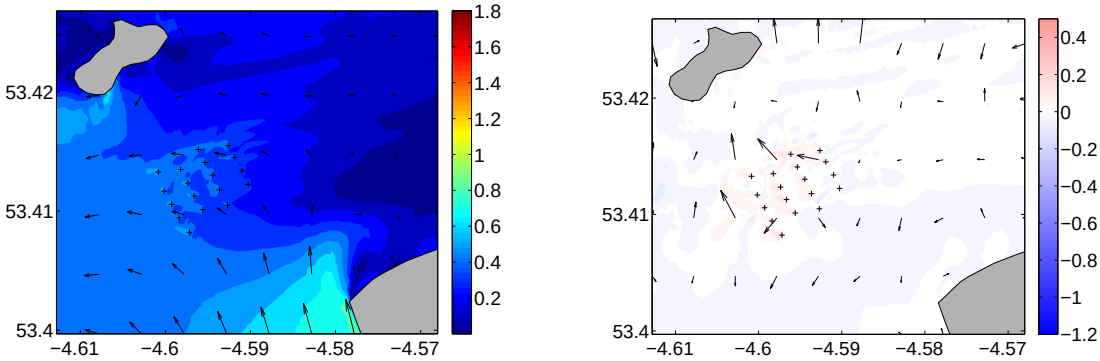

(e) With turbine, bottom

(f) Difference, bottom

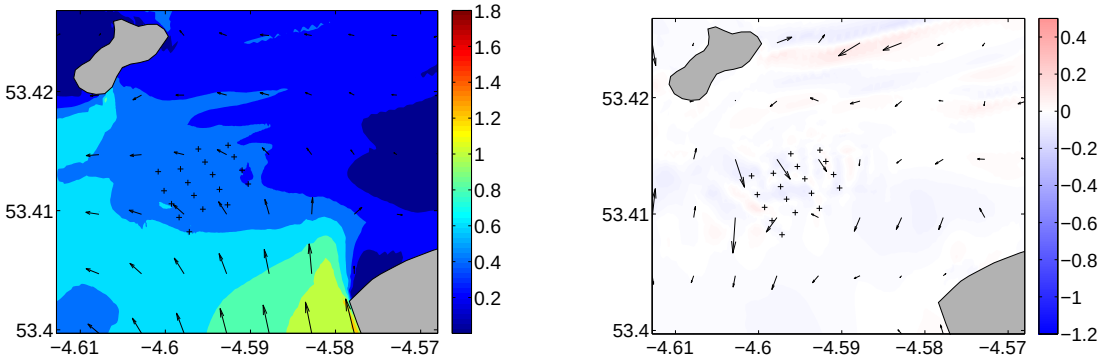

(g) With turbine, depth averaged

(h) Difference, depth averaged

Figure 6.28: Flow fields with turbine farm and flow field change contours in the vicinity of the farm imposed with velocity vectors and turbine locations at Slack water. (unit: m/s)

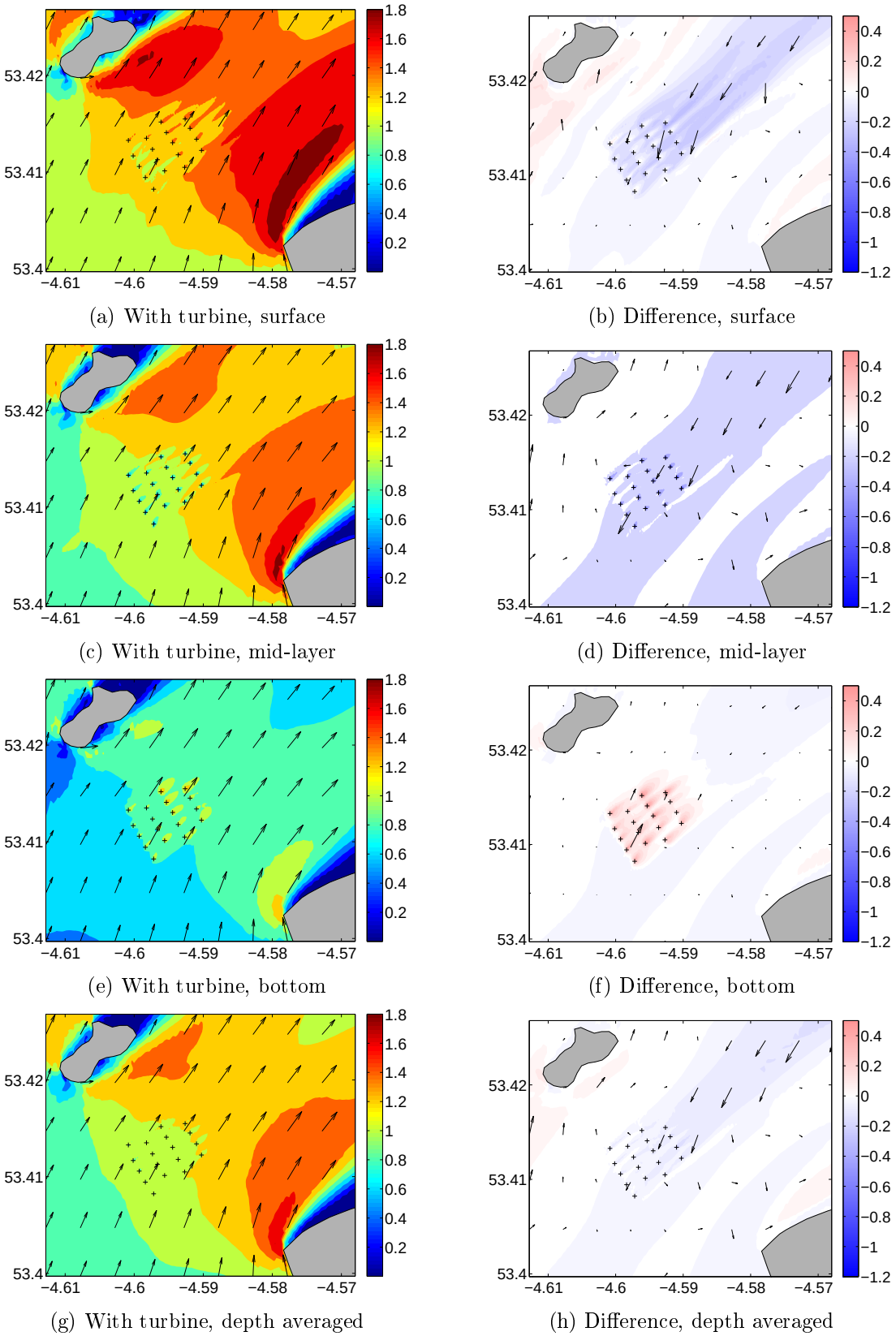

(a) With turbine, surface

(b) Difference, surface

(c) With turbine, mid-layer

(d) Difference, mid-layer

(e) With turbine, bottom

(f) Difference, bottom

(g) With turbine, depth averaged

(h) Difference, depth averaged

Figure 6.29: Flow fields with turbine farm and flow field change contours in the vicinity of the farm imposed with velocity vectors and turbine locations at LW. (unit: m/s)

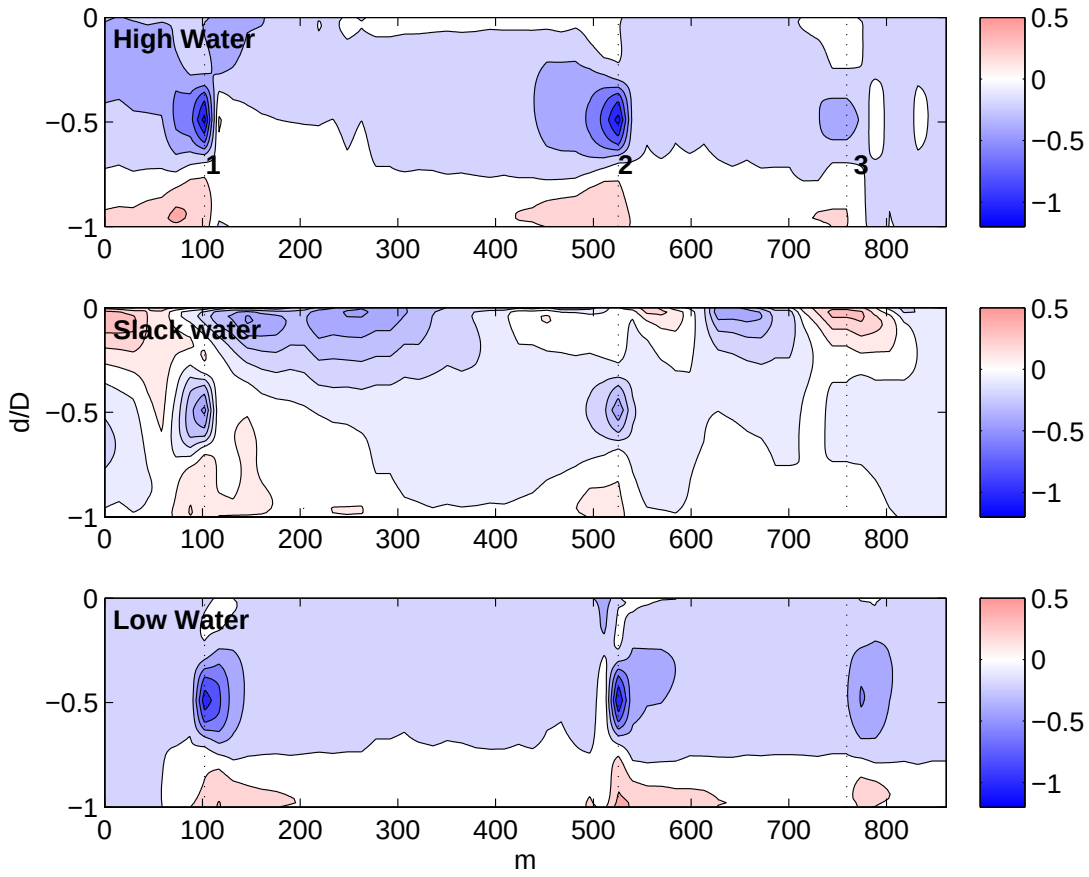

Figure 6.30: Velocity changes along slice 1 at the three selected phases of the tide. (unit: m/s)

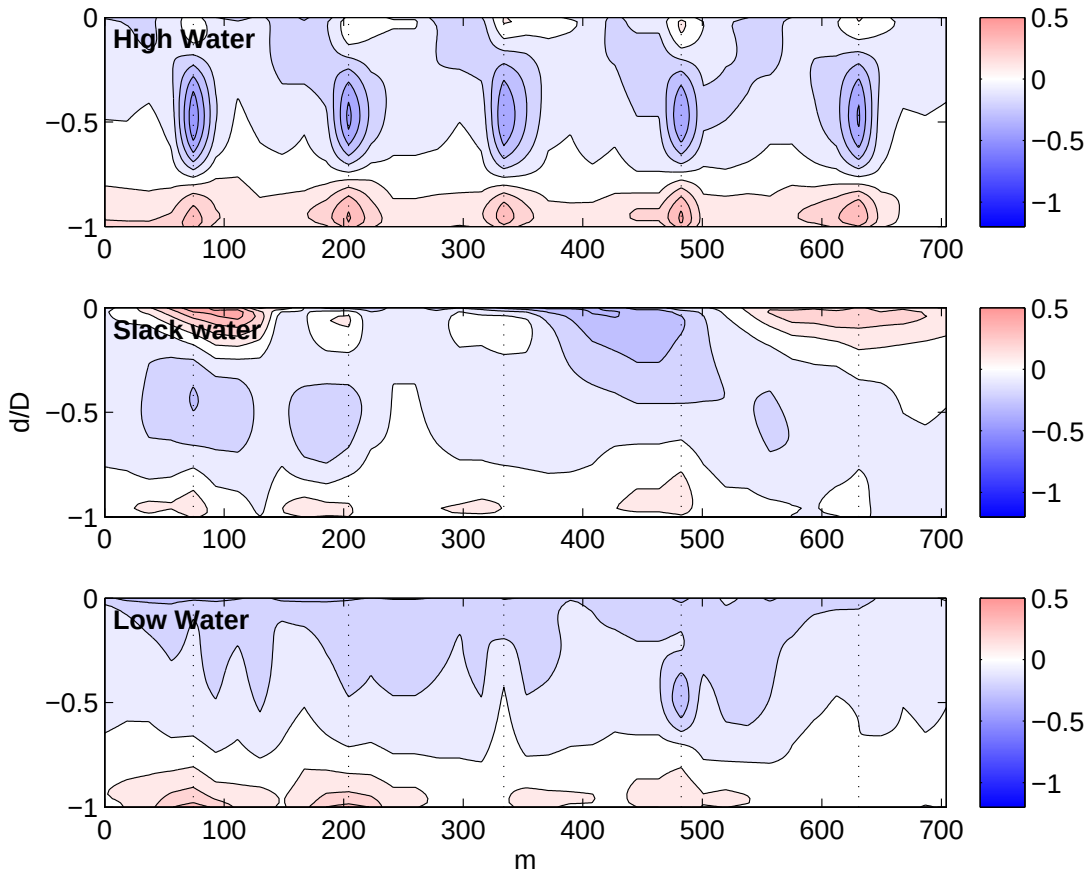

Figure 6.31: Velocity changes along slice 2 at the three selected phases of the tide. (unit: m/s)

Turbulence kinetic energy

Figure 6.32 to Figure 6.34 present the TKE level in the vicinity of the farm at the surface, middle and bottom layers. It can be seen from the figures that the changes in TKE downstream of each of the turbines stretch up to a distance of approximately 15D and the farm as a whole does not extend the length any longer. Comparing to the other 2 layers, the TKE level is the highest in the middle layer due to the presence of turbine. The pattern of TKE difference in Figure 6.32 and Figure 6.34 on the right hand side panel changes: as the turbine-produced TKE is transported downstream, it spreads laterally, forming a cone-shaped highly turbulent area. The width of the cone-shaped area reaches its maximum of roughly 8D before the impact becomes negligible. The TKE level and TKE level changes at the three investigated depths observed at Slack water in Figure 6.33 are both weaker compared to those at the other two phases of the tide.

Figure 6.35 shows the TKE changes across the depth along slice 1 at the three selected phases of the tide. The inclusion of turbines, without exception, increases the downstream TKE level. It is observed that, throughout the depth, there are two TKE

peaks, one above and one below the hub of the turbines, for some of the well developed wakes. Similar behaviour is reported in [117]. This is because the vortex shed from the tip of the blades is being represented by the three turbulence modification terms in the model. The peaks however almost always occur at about 1D downstream of the turbines. This is probably because even though the three additional turbulence terms are activated at the turbine locations, the velocities at the turbine locations are substantially smaller than those at a certain distance downstream of the turbines, resulting in a rather weaker TKE production. The longitudinal stretch of the wake in terms of TKE is in general longer during HW when compared to that during LW. However, it is very likely that the wake of most of the turbines has recovered to a very weak turbulent level after a distance of 15D. As a result, among the investigated turbines and phases of the tide, only the turbine at location 2 is likely to operate in a slight turbulent environment due to the turbine upstream during HW.

Figure 6.36 shows the TKE changes across the depth along slice 2 at the three selected phases of the tide. Again, the five turbines on the third row of devices counting from the left-hand side of Figure 6.23 are clearly reflected in the contour at HW. Gaps where TKE is not affected by the presence of the turbines are observed between adjacent devices. At LW, slight increase of TKE is detected in front of the 5 turbines on the third row of devices. TKE between the neighbouring turbines is also slightly increased, meaning that the turbulence caused by the turbines on the second row of devices is not yet completely dissipated after a distance of roughly 13D. But, overall, a latitudinal spatial interval of 8D and a longitudinal spatial interval of 15D is a good choice for the turbines of the current case to avoid operating in highly turbulent flows.

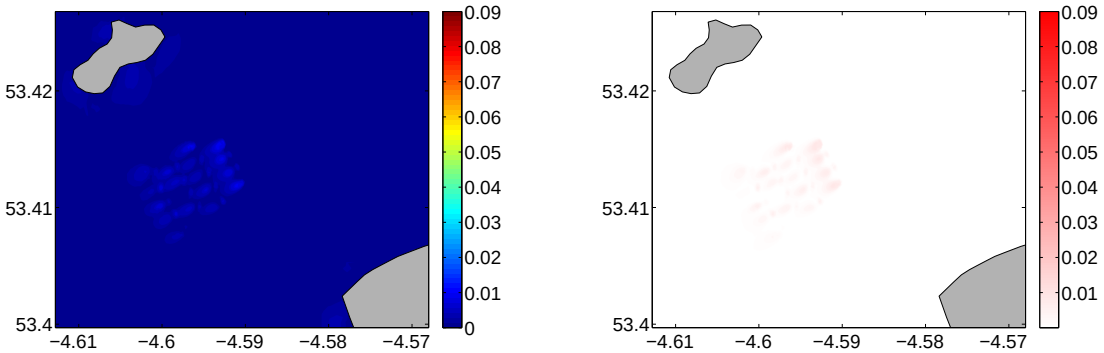

(a) With turbine, surface

(b) Difference, surface

(c) With turbine, mid-layer

(d) Difference, mid-layer

(e) With turbine, bottom

(f) Difference, bottom

Figure 6.32: TKE fields with turbine farm and TKE field change contours in the vicinity of the farm at HW. (unit: m^2/s^2)

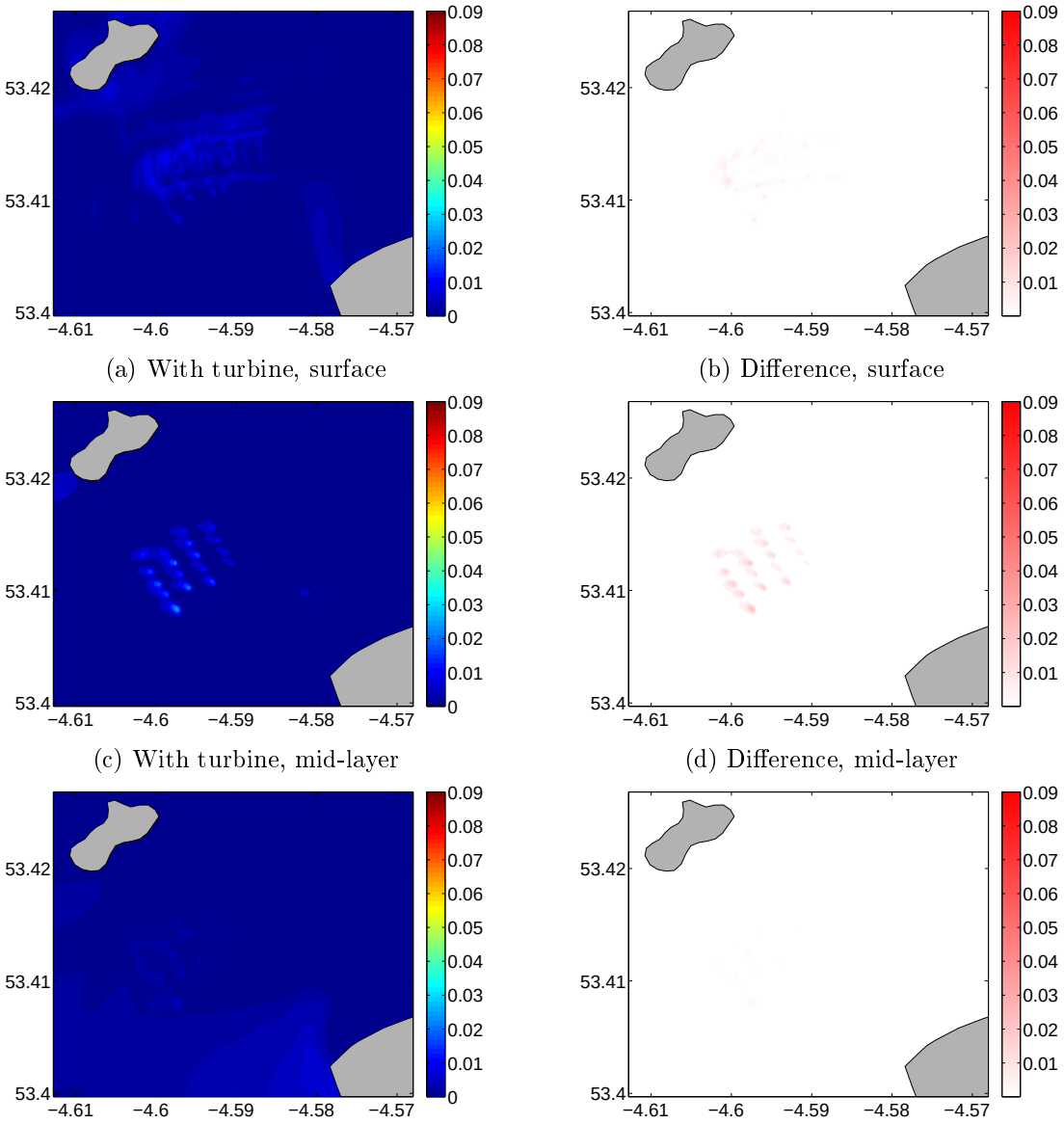

(a) With turbine, surface

(b) Difference, surface

(c) With turbine, mid-layer

(d) Difference, mid-layer

(e) With turbine, bottom

(f) Difference, bottom

Figure 6.33: TKE fields with turbine farm and TKE field change contours in the vicinity of the farm at Slack water. (unit: m^2/s^2)

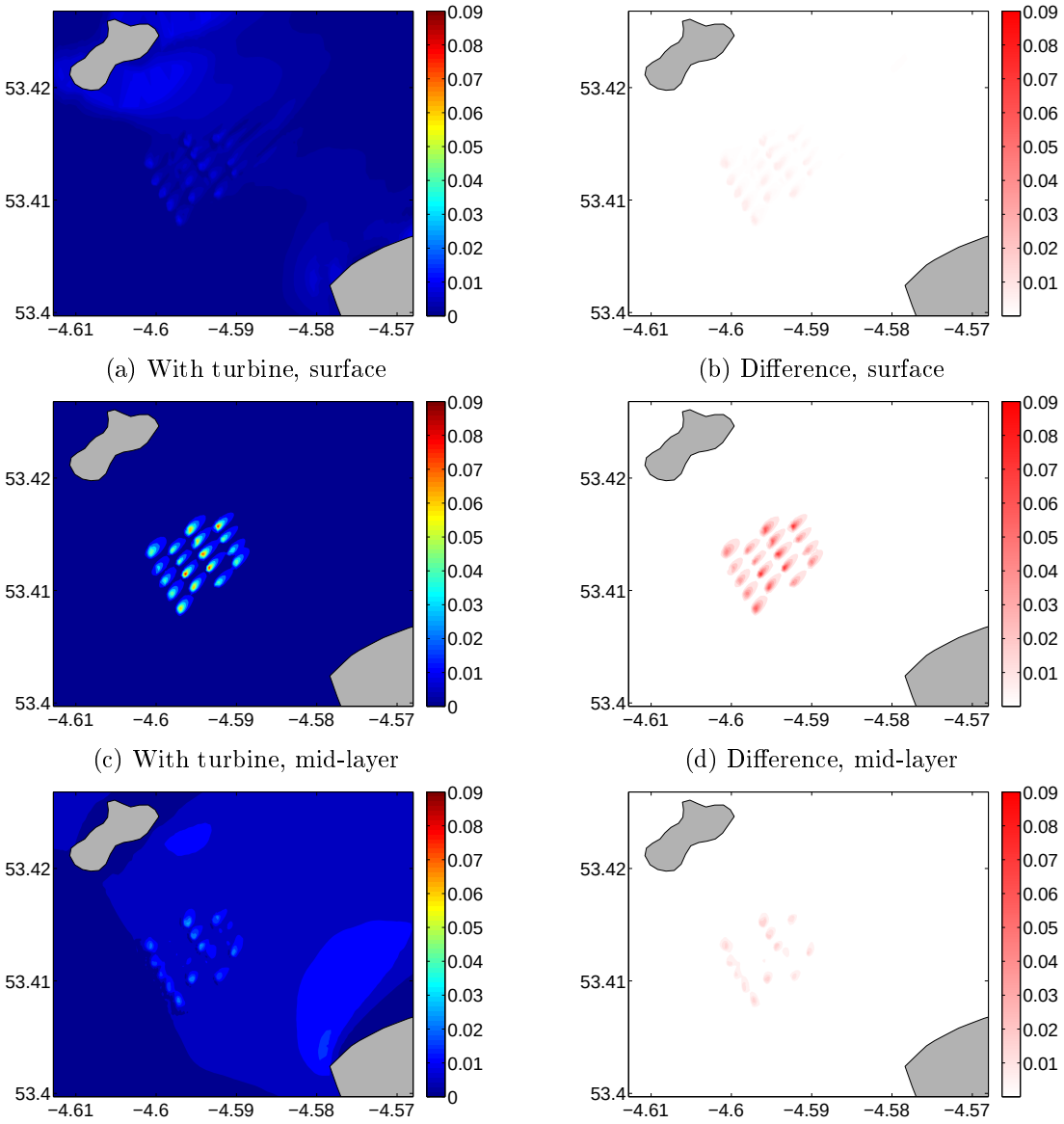

(a) With turbine, surface

(b) Difference, surface

(c) With turbine, mid-layer

(d) Difference, mid-layer

(e) With turbine, bottom

(f) Difference, bottom

Figure 6.34: TKE fields with turbine farm and TKE field change contours in the vicinity of the farm at LW. (unit: m^2/s^2)

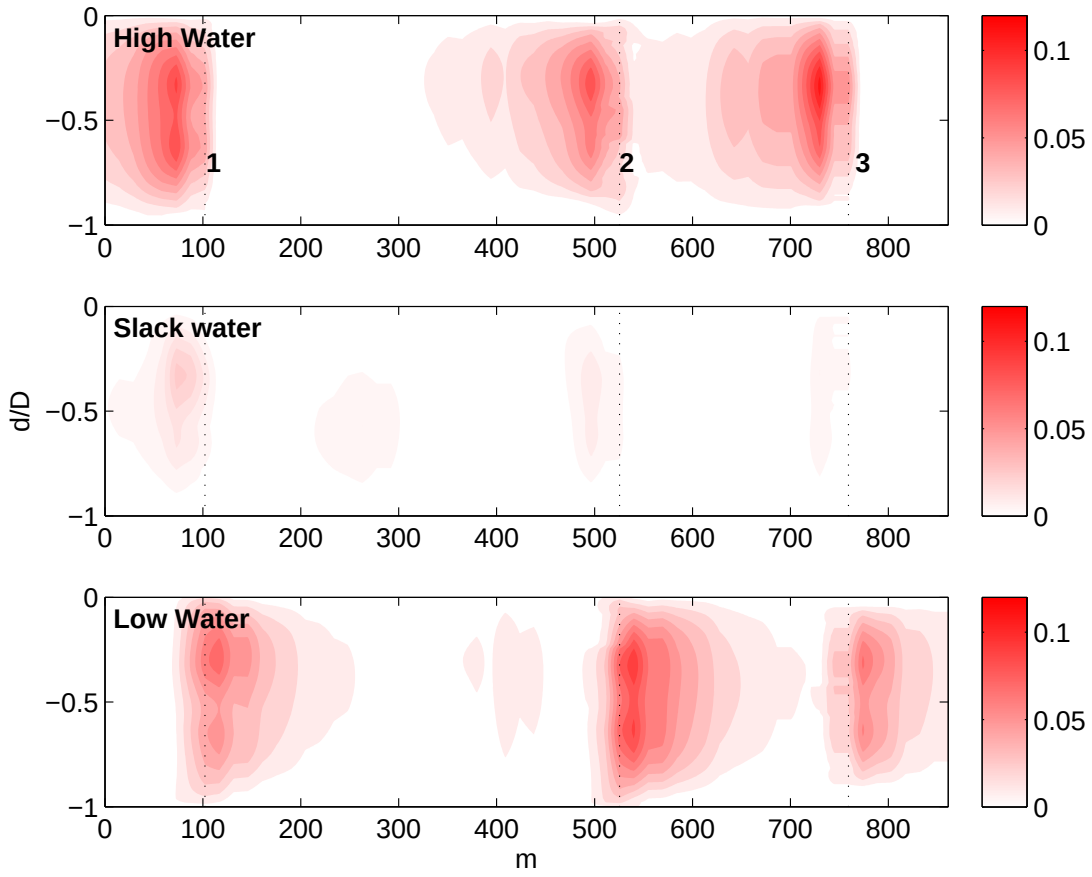

Figure 6.35: TKE changes along slice 1 at the three selected phases of the tide. (unit: m^2/s^2)

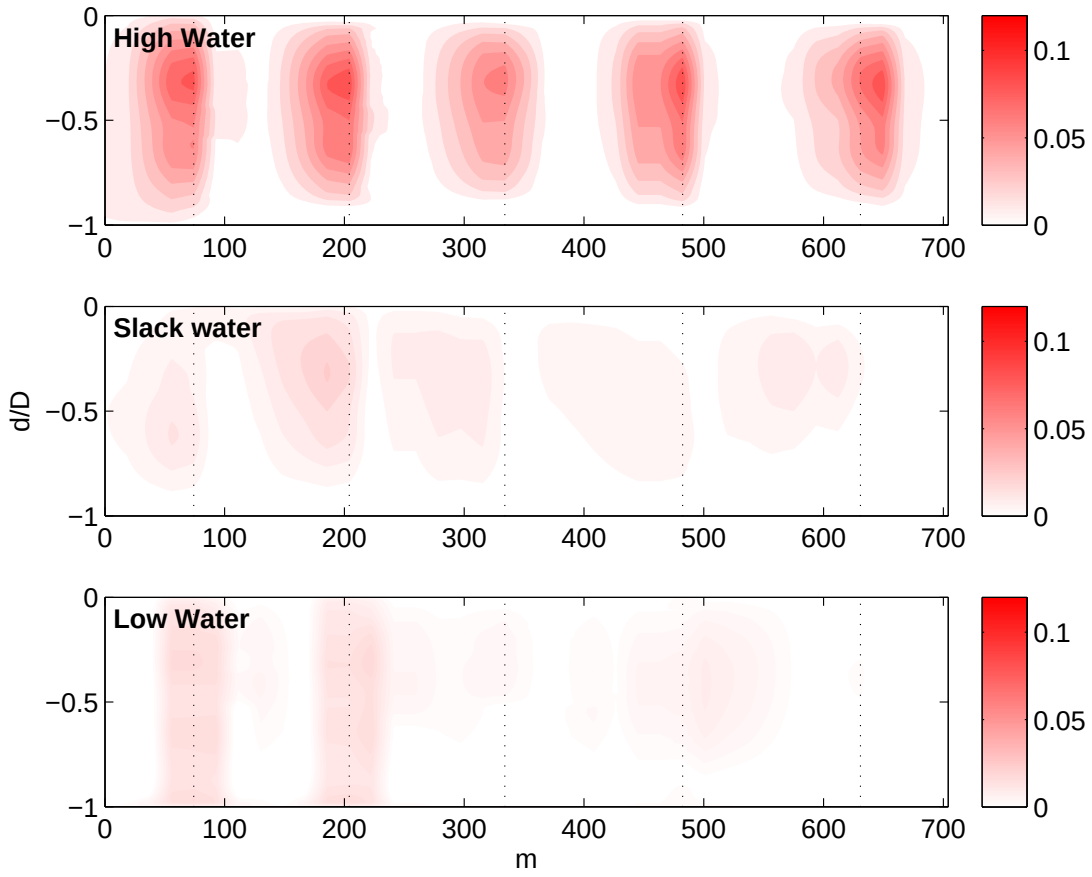

Figure 6.36: TKE changes along slice 2 at the three selected phases of the tide. (unit: m^2/s^2)

Surface Wave Dynamics

Figure 6.37 looks at wave height in the vicinity of the structures at the 3 instances. It is observed that at both HW and LW, wave height reduces immediately behind the turbines. However, wave height downstream of the farm is affected by the turbines in opposite ways at HW and LW. During HW, wave height downstream of the farm is decreased by maximum of 7% of the baseline wave height. On the other hand, during LW, wave height downstream of the farm is increased by maximum of 2% of the baseline wave height. However, instead of direct impact from the turbine farm, changes in wave height are more likely to result from variations in flow dynamics. After all, the more obvious wave height changes are observed along the flow directions while the waves are propagating at almost perpendicular directions to them.

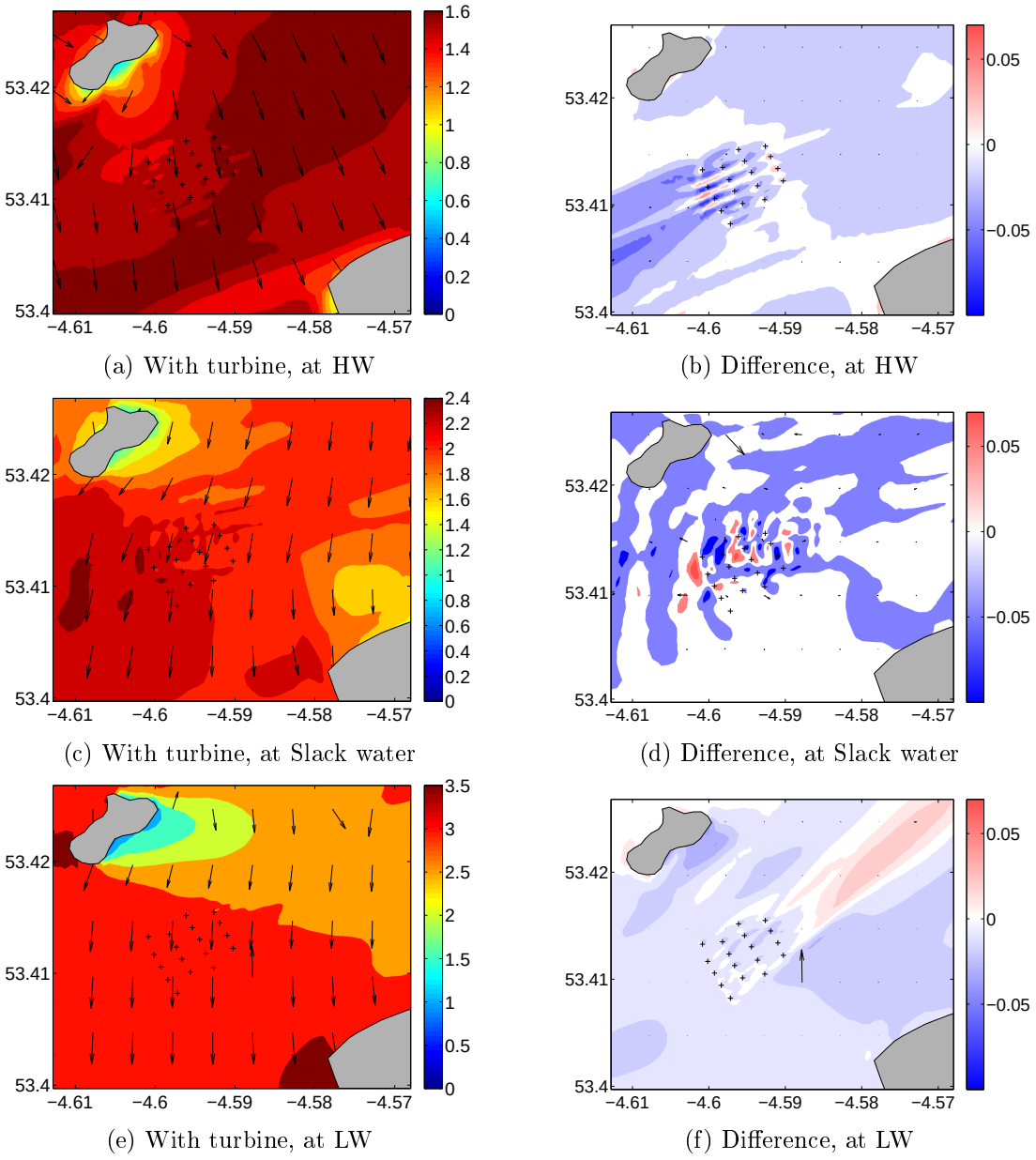

(a) With turbine, at HW

(b) Difference, at HW

(c) With turbine, at Slack water

(d) Difference, at Slack water

(e) With turbine, at LW

(f) Difference, at LW

Figure 6.37: Significant wave height fields with turbine and significant wave height field change contours in the vicinity of the farm imposed with wave direction vectors and turbine locations at HW, Slack water and LW. (unit: m on the left panel and % on the right panel)

Bed Shear Stress

Bottom shear stress and changes of it caused by the turbines in the vicinity of the device farm are presented in Figure 6.38. The maximum bottom shear stress at LW is 4.5 N/m^2, about 2 N/m^2 larger than it is at HW, mainly due to shallower water depth and similar flow speed. Also, wave height is larger at LW. The shear stress is the weakest at Slack water in spite of a medium wave height at this moment, thanks to the slow current.

Different from reduced bottom shear stress observed in most two-dimensional studies reviewed in Section 2.4.3, bottom shear stress in the vicinity of the turbine farm is observed to be enhanced by the devices in the present study and the enhancement can be up to $2.5N/m^2$ (120%) around the structures at both HW and LW. This is mainly due to the accelerated flow near the bottom in the wake. This result agrees with observations obtained in the laboratory [53, 58] and results predicted by three-dimensional CFD simulations [113].

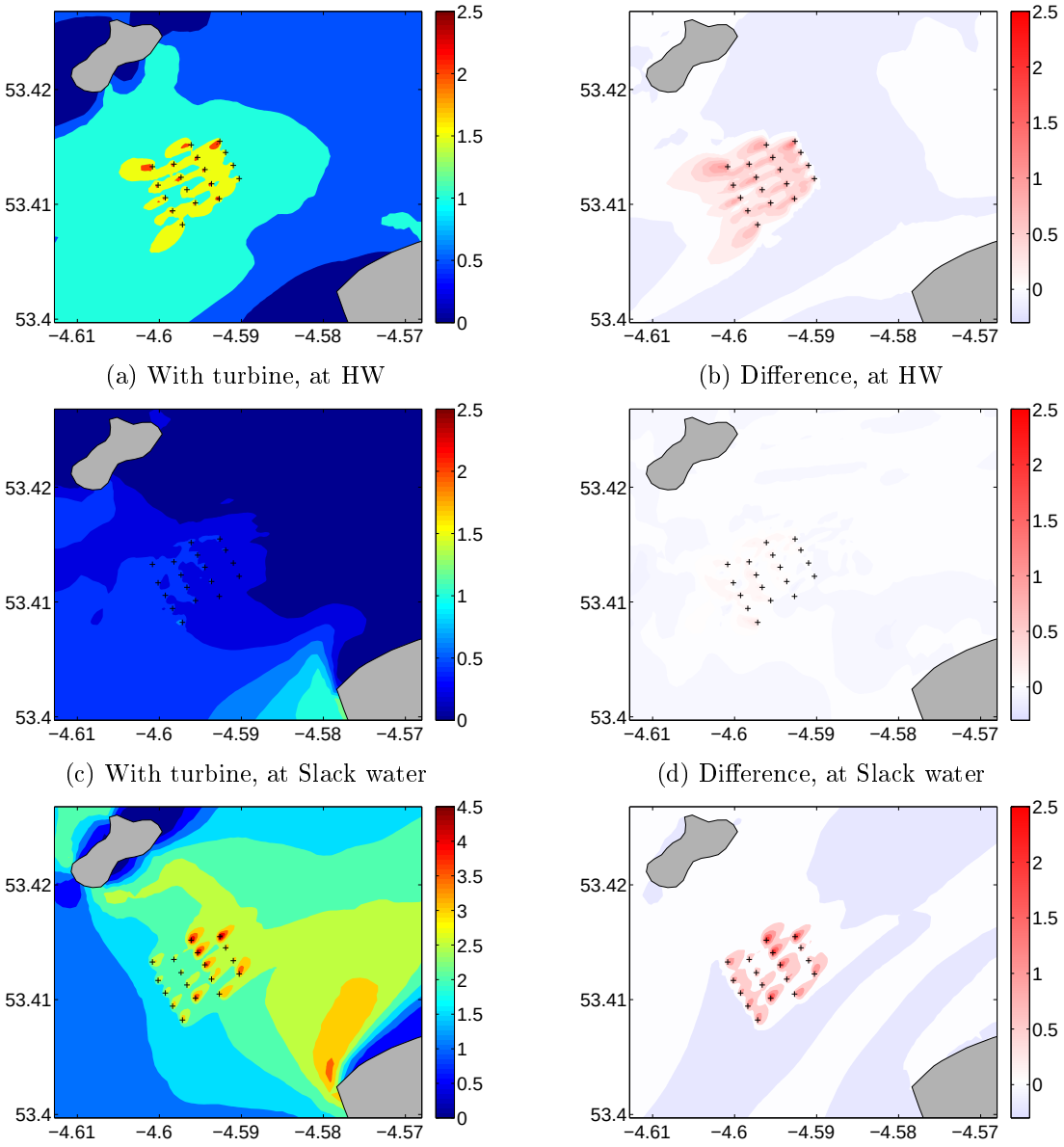

(a) With turbine, at HW

(b) Difference, at HW

(c) With turbine, at Slack water

(d) Difference, at Slack water

(e) With turbine, at LW

(f) Difference, at LW

Figure 6.38: Bottom stress field with turbine and bottom stress field change contours in the vicinity of the farm. (unit: N/m^2)

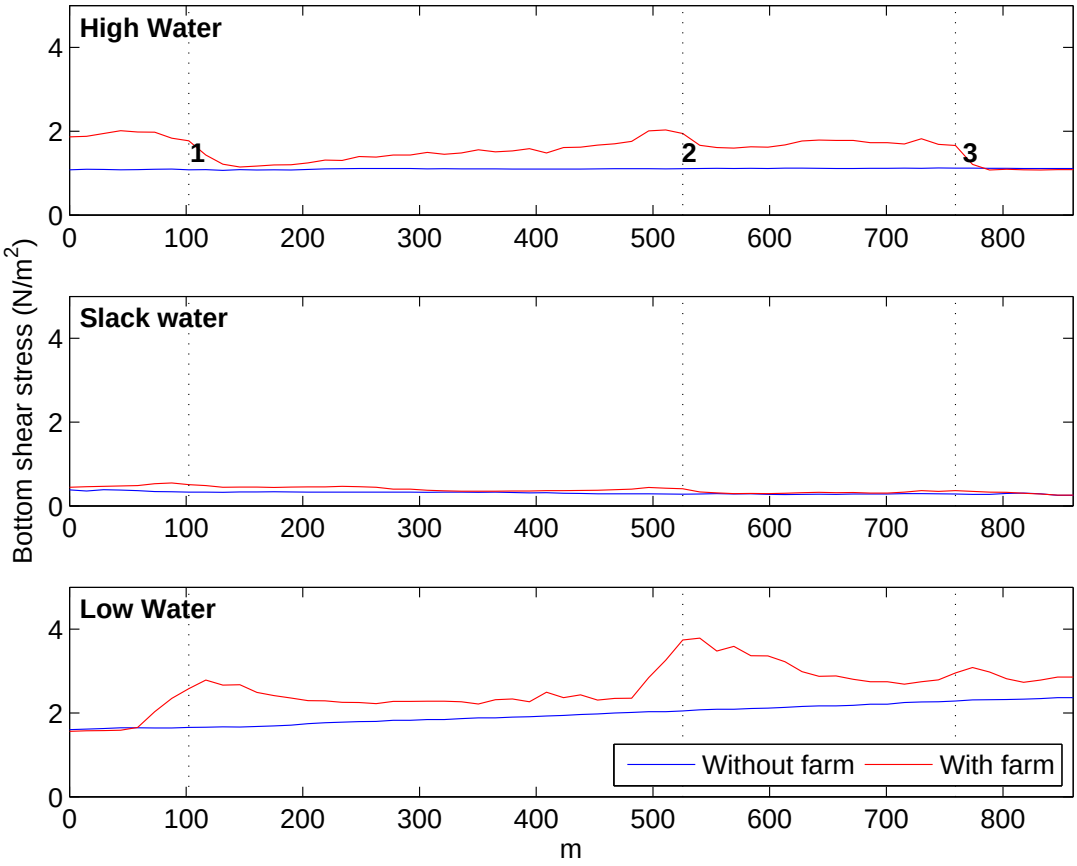

Figure 6.39: Bottom shear stress with and without the farm along slice 1 at the three selected phases of the tide. (unit: N/m^2)

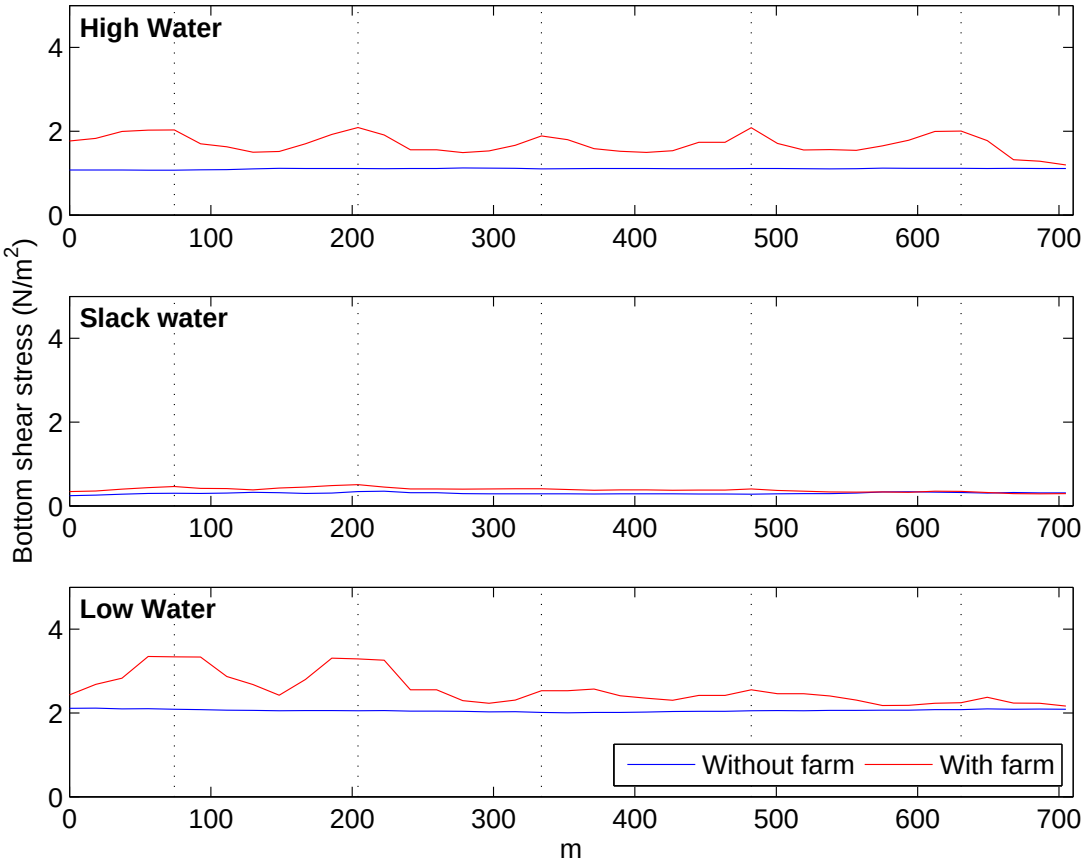

Figure 6.40: Bottom shear stress with and without the farm along slice 2 at the three selected phases of the tide. (unit: N/m^2)

Figure 6.39 shows the calculated bottom shear stress of scenarios with and without the farm along slice 1 at the three selected phases of the tide. Turbine-induced shear stress enhancement is seen in both figures and at all three phases of the tide, although the baseline bottom shear stress and its enhancement are both quite weak at Slack water. It is observed from Figure 6.39 that the influential range of individual turbines on bottom shear stress can be longer than the longitudinal spatial spacing between two adjacent turbines at both HW and LW. Also, it is seen that the bottom shear stress increases gradually towards the direction of north-east (on the figure 0-800). It is caused by a smooth rise of wave height resulting from a steadily decreasing water depth in the same direction.

Figure 6.40 presents the calculated bottom shear stress of the two scenarios along slice 2 at the three selected phases of the tide. Again the turbine-induced bottom shear stress enhancement is clearly seen at HW, curves of which reflect the near wake impact of the turbines on the third row of devices counting from the left-hand side of Figure 6.23. It is observed that shear stress in the area between two neighbouring turbines is also enhanced, agreeing with the pattern shown in Figure 6.31. Similarly, bottom shear stress enhancement seen at LW is corresponding to flow dynamic variations at the same

moment in Figure 6.31 and it is likely to be showing the impact of the third row of devices on the shear stress at the upstream.

Suspended Sediment Transport

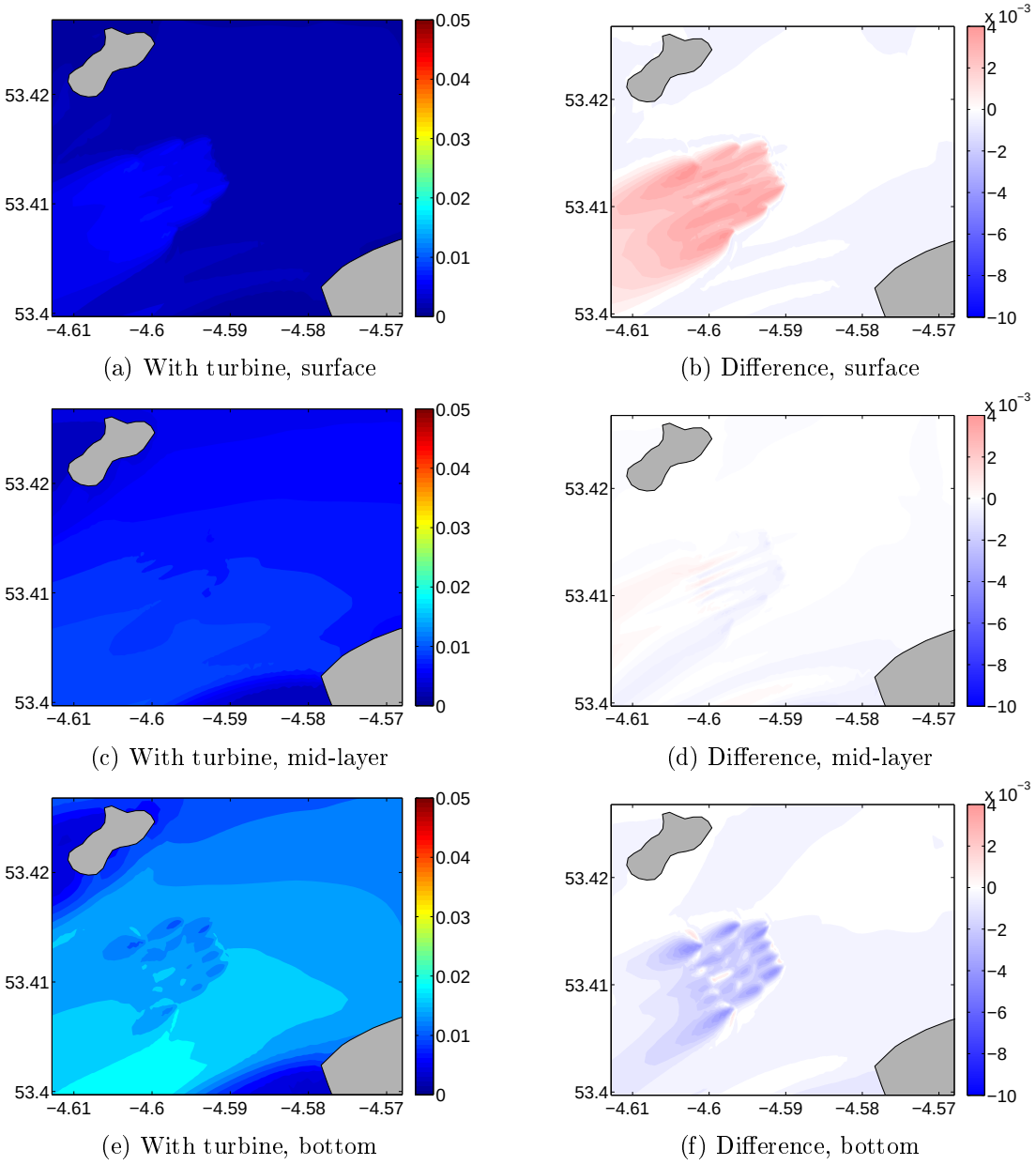

(a) With turbine, surface

(b) Difference, surface

(c) With turbine, mid-layer

(d) Difference, mid-layer

(e) With turbine, bottom

(f) Difference, bottom

Figure 6.41: Suspended sediment concentration fields with turbine farm and suspended sediment concentration field change contours in the vicinity of the farm at HW. (unit: kg/m^3)

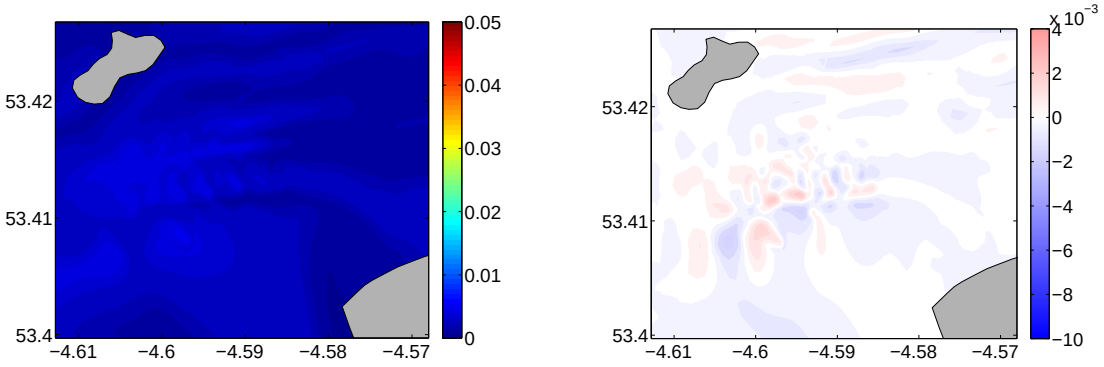

(a) With turbine, surface

(b) Difference, surface

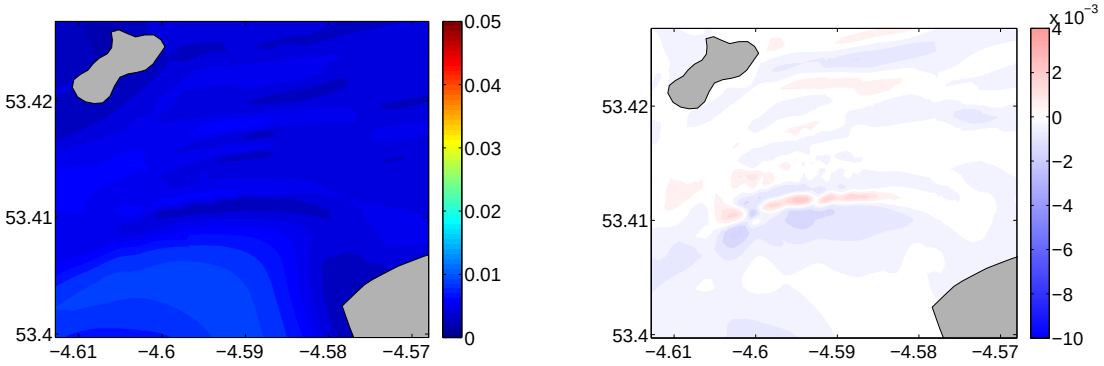

(c) With turbine, mid-layer

(d) Difference, mid-layer

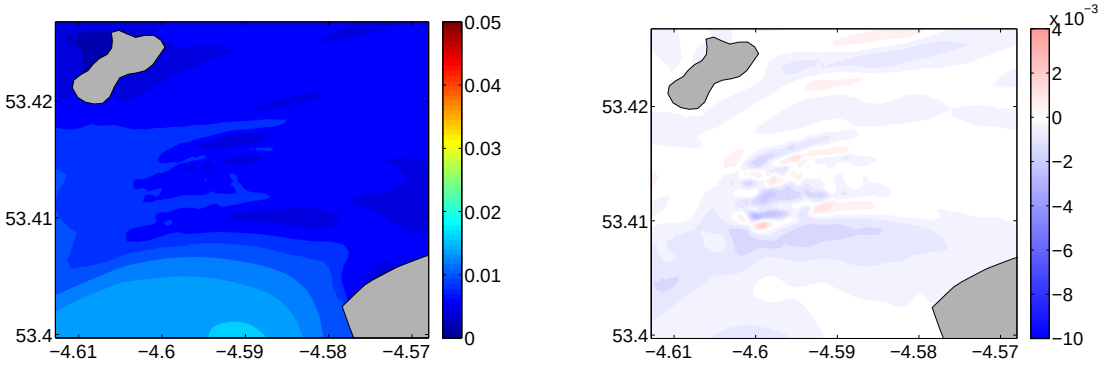

(e) With turbine, bottom

(f) Difference, bottom

Figure 6.42: Suspended sediment concentration fields with turbine farm and suspended sediment concentration field change contours in the vicinity of the farm at Slack water. (unit: kg/m^3)

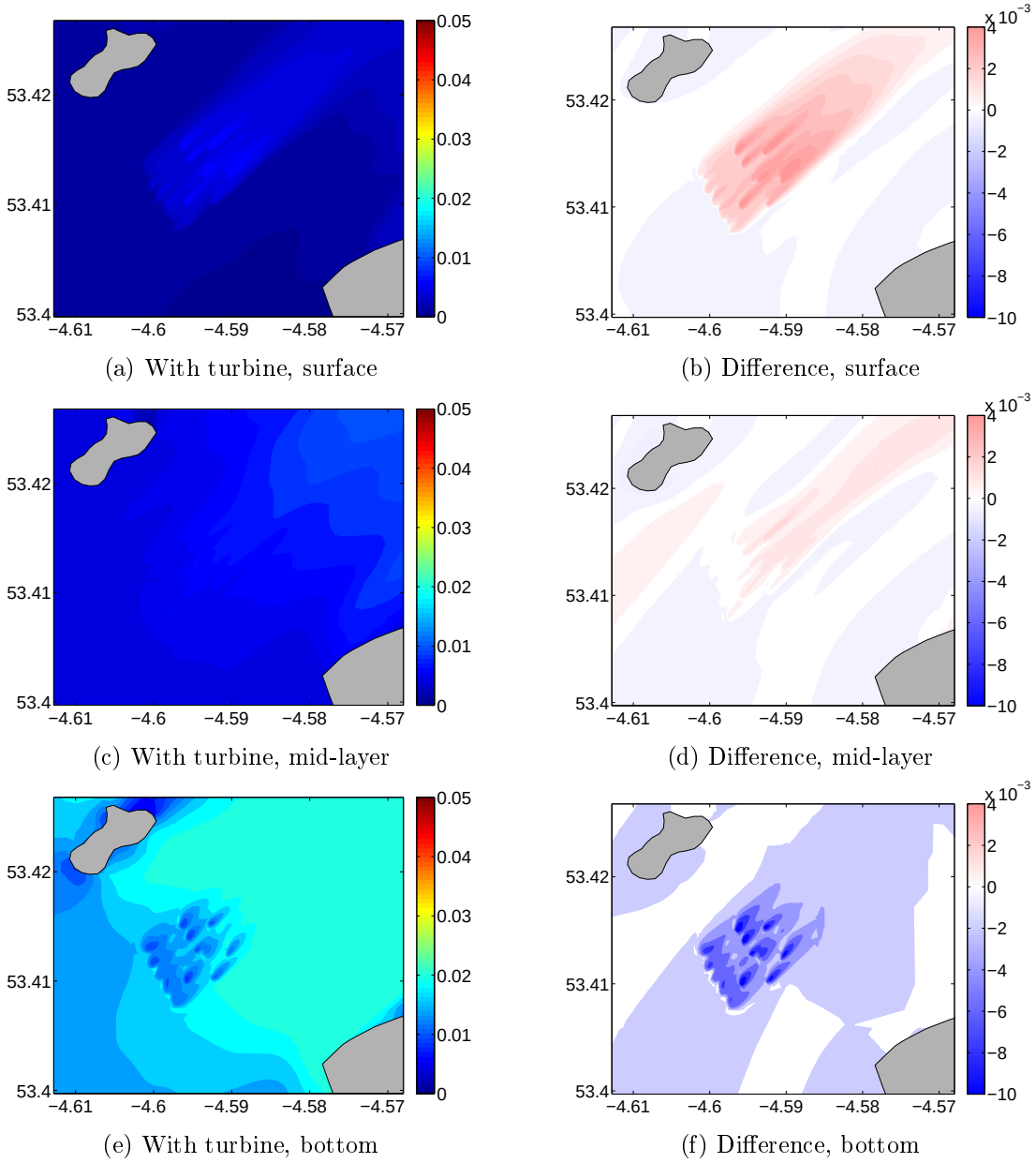

(a) With turbine, surface

(b) Difference, surface

(c) With turbine, mid-layer

(d) Difference, mid-layer

(e) With turbine, bottom

(f) Difference, bottom

Figure 6.43: Suspended sediment concentration fields with turbine farm and suspended sediment concentration field change contours in the vicinity of the farm at LW. (unit: kg/m^3)

Figure 6.41 to Figure 6.43 present suspended sediment concentration in the vicinity of the turbine farm at the three selected phases of the tide. Again, at Slack water, the patterns are rather chaotic. However, clear patterns are observed at the other two phases of the tide. Sediment concentration near the bottom is reduced due to the presence of the turbines. This is largely due to the fact the same grain size as that used in Section 6.2.1, has been tested. The choice of the grain size leads to a live-bed condition at the turbine site. Consequently, the sediment concentration near the bottom is reduced as discussed in Section 6.2.1. It is, however, increased in the upper

part of the water, especially close to the free surface. These results suggest that the turbines have a strong influence on the vertical dispersion of the sediment particles. The significant increase of suspended sediment in the surface layer is clearly visible along a very long wake, which could cause noticeable changes in sea surface colour and potential ecological consequences.

6.3.5 Results — regional impacts

This section looks at impacts of the turbine farm on hydrodynamics and suspended sediment concentration on a regional scale. The study area includes most of the north coast of Anglesey and coast around Holy island. Analysis features horizontal slices at the surface, the mid-layer and the bottom of the area, at the three selected phases of the tide.

Surface elevation

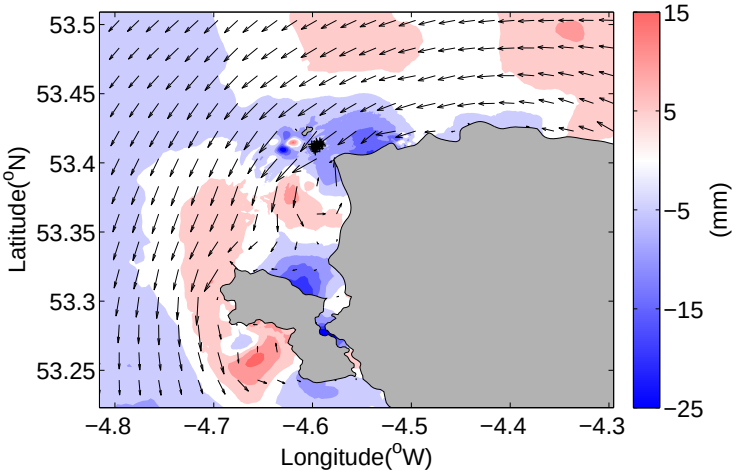

(a) High water

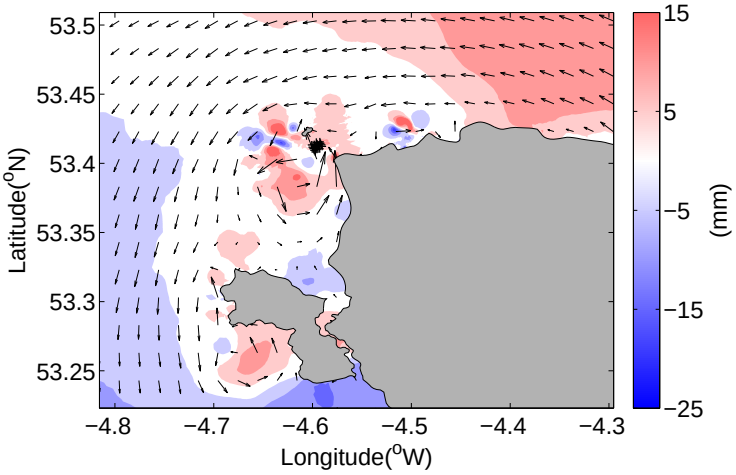

(b) Slack water

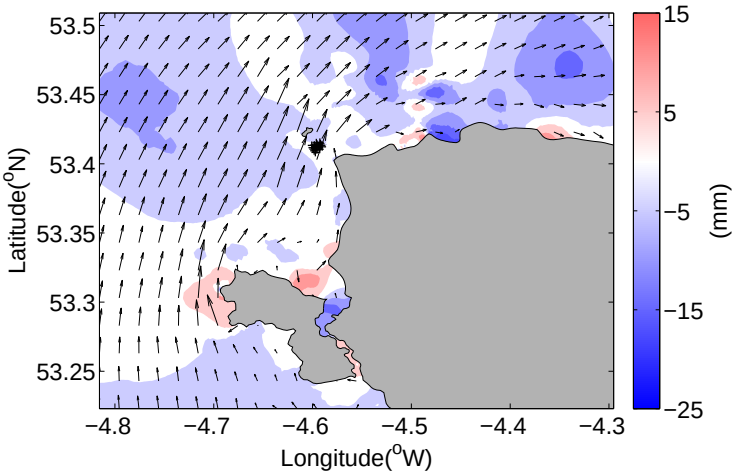

(c) Low water

Figure 6.44: Surface elevation changes at the three selected phases of the tide (arrows imposed to indicate the flow direction).

Figure 6.44 shows surface elevation changes due to the presence of the device farm at the three selected phases of the tide, with flow vectors imposed. At HW, the current flows towards the south-west, the surface elevation around the farm site reduces by 5-15mm. The reduction continues to be observed west of the Skerries and it expands both southerly and northerly at the west edge of the figure. Elevation reduction at this moment is also observed within the Cymyran strait separating Holy island from Anglesey. Increase of elevation can be seen both further upstream and downstream of the device farm. Two eddies are observed — one slightly south-west of the farm and another one off the west coast of Holy island. Elevation increase is seen at the centres of these two eddies.

At Slack water, the flow field pattern is similar to that at HW, but with a much smaller flow rate. Surface elevation within the local area of the farm is mostly increased. A stripe of decreased elevation is seen along the main flow direction at the downstream of the farm. Further upstream is dominated by increased elevation and the opposite within the further downstream area. Changes in the Cymyran strait at this phase of the tide are a mix of increase and decrease. The two eddies are still observed at almost the same locations, and so are the two hotspots of increased surface elevation.

At LW, the current flows towards the north-east, and in comparison, the surface elevation change around the farm site is less significant. Reduction is observed west of the Skerries and a large area downstream of the farm, with four hot spots where the elevation is increased dot about in this region. Changes in the Cymyran strait at this phase of the tide is again a mix of increase and decrease. Another patch of increased elevation is found off the very west point of the Holy island.

In general, the affected area in terms of surface elevation at all three phases of the tide is very likely to be larger than the region covered by the graphs which is roughly $1540km^2$. The change is within the range of -25mm to +15mm, which is very slight compared to the tidal range in this area.

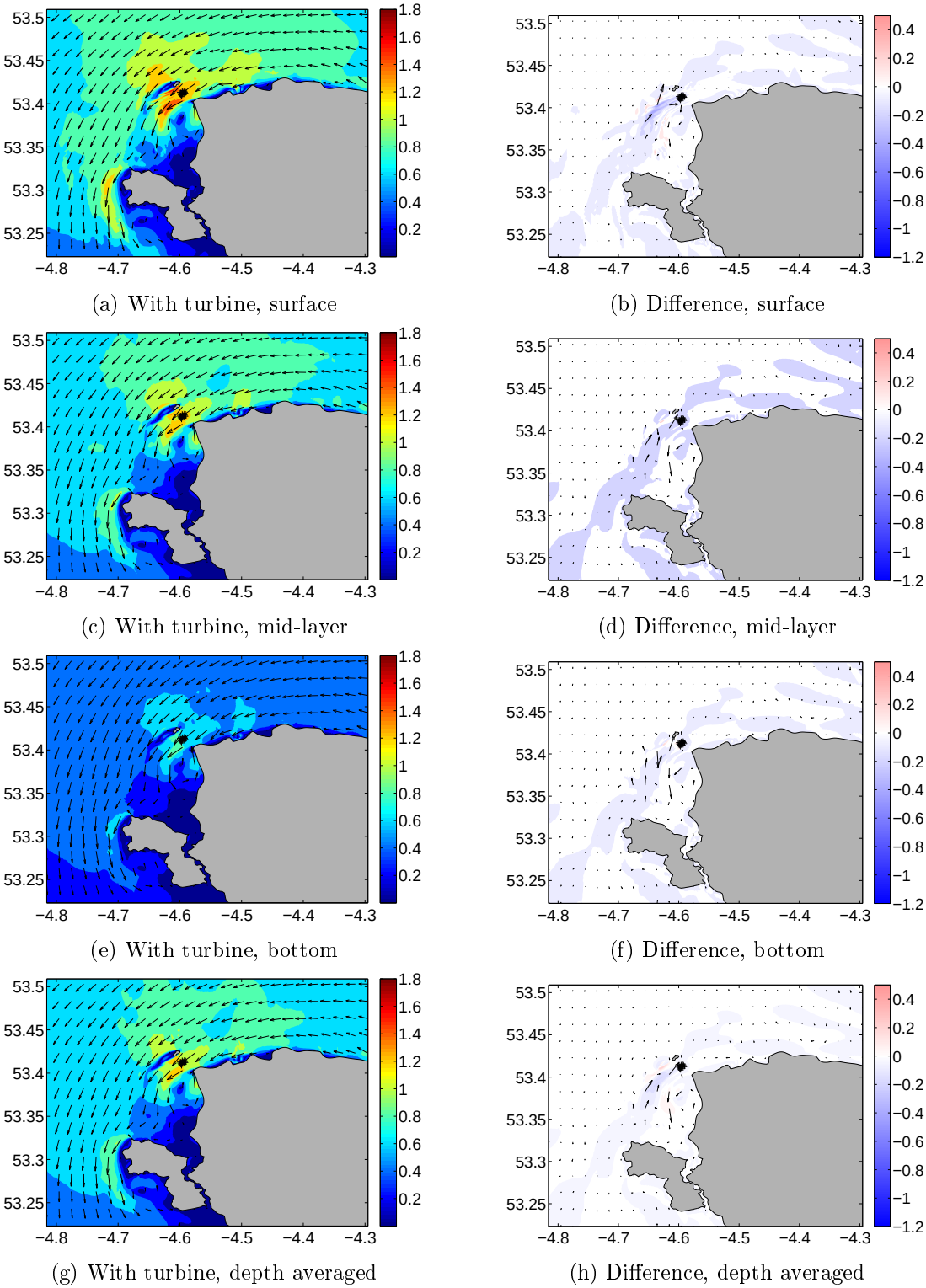

(a) With turbine, surface

(b) Difference, surface

(c) With turbine, mid-layer

(d) Difference, mid-layer

(e) With turbine, bottom

(f) Difference, bottom

(g) With turbine, depth averaged

(h) Difference, depth averaged

Figure 6.45: Flow fields with turbine farm and flow field change contours imposed with velocity vectors and turbine locations at HW. (unit: m/s)

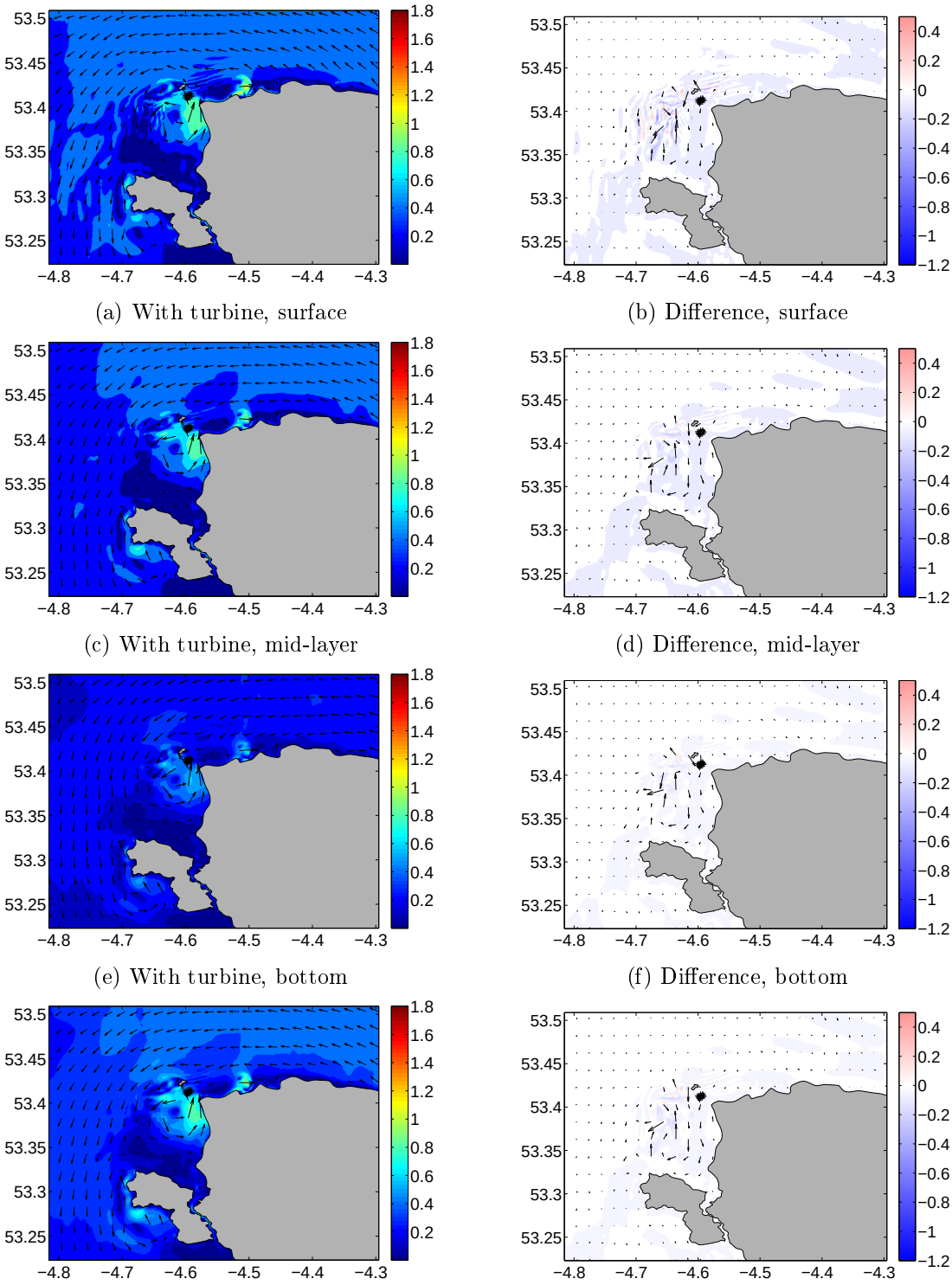

(a) With turbine, surface

(b) Difference, surface

(c) With turbine, mid-layer

(d) Difference, mid-layer

(e) With turbine, bottom

(f) Difference, bottom

(g) With turbine, depth averaged

(h) Difference, depth averaged

Figure 6.46: Flow fields with turbine farm and flow field change contours imposed with velocity vectors and turbine locations at Slack water. (unit: m/s)

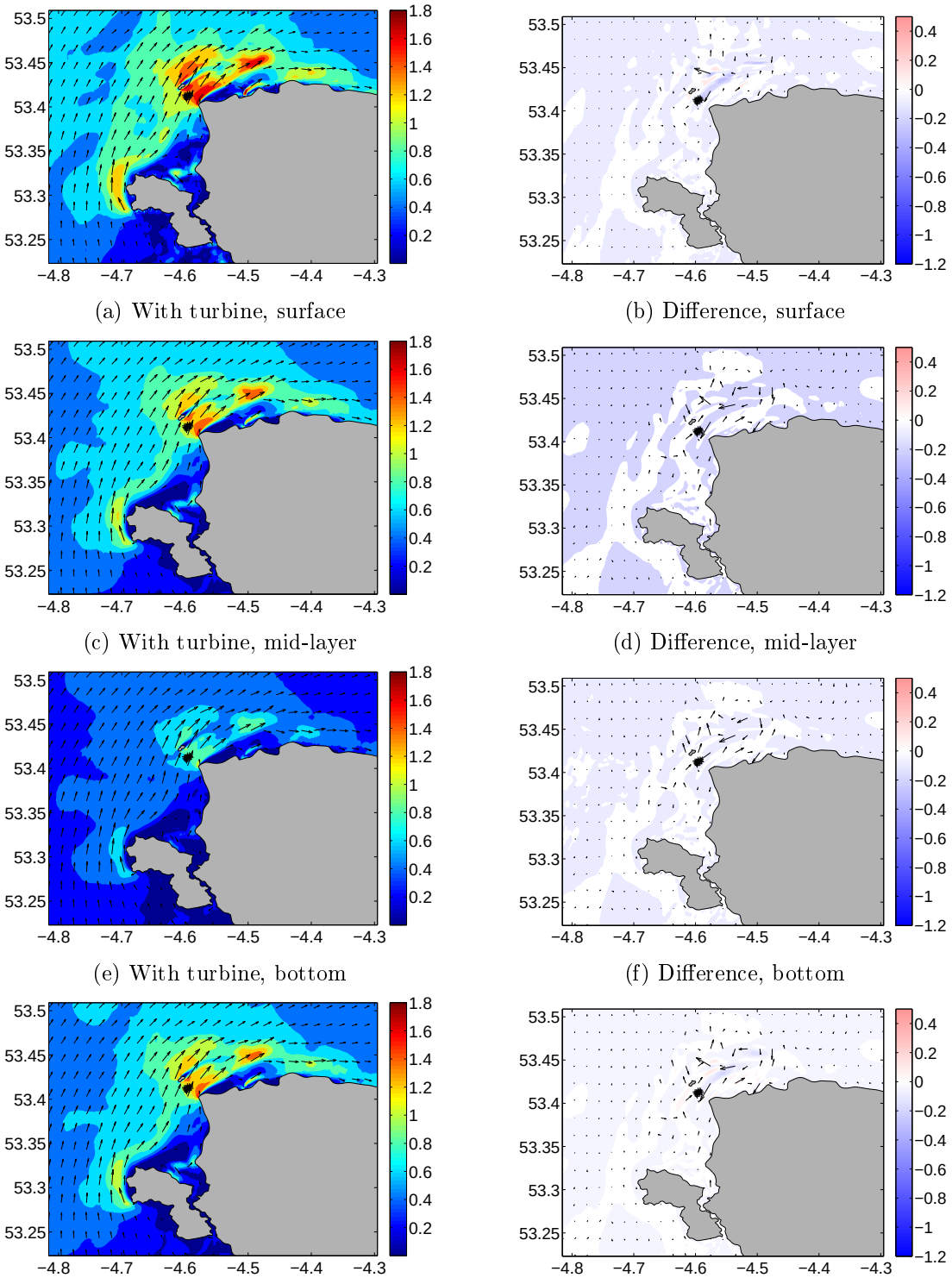

(a) With turbine, surface

(b) Difference, surface

(c) With turbine, mid-layer

(d) Difference, mid-layer

(e) With turbine, bottom

(f) Difference, bottom

(g) With turbine, depth averaged

(h) Difference, depth averaged

Figure 6.47: Flow fields with turbine farm and flow field change contours imposed with velocity vectors and turbine locations at LW. (unit: m/s)

Figure 6.45 displays flow fields at the surface, the mid-layer and the bottom as well as depth-averaged flow fields for the case with the turbine farm on the left panel and

the changes caused by the farm to the flow fields on the right panel at HW, when the current is flowing towards the south-west. An eddy is observed off the west coast of Anglesey. A strong jet of decelerated flow downstream of the farm is observed at the surface layer, sandwiched by two jets of accelerated flow, suggesting that the flow is diverted due to the blockage effect of the farm. The length of the decelerated flow jet (the wake) is roughly 4.5 km (300D). The accelerated flow jets are also observed in the depth-averaged flow field. They are however much less visible at the mid-layer and the bottom. The mid-layer shows the maximum decrease of water velocity due to the strongest C_{ext} it undergoes. The affected area in terms of water velocity is consistent throughout the water depth and, unlike surface elevation, it mainly follows the flow direction. Area south to the Holy island also undergoes flow deceleration.

The above-mentioned two panels at Slack water are presented in Figure 6.46. The eddy observed at HW off the west coast of Anglesey is still visible. A chaotic pattern of changes caused by the farm to the flow field is observed at the surface layer. The jet of decelerated flow along the main flow direction is not observed. Changes at the other two depths are slight, with also chaotic patterns.

Figure 6.47 displays the similar distribution at LW when the current is flowing towards north-east. Impact of turbine operation on the current is largely flow reduction around the farm site. The wake at this phase of the tide is slightly shorter with a length of roughly 3.5 km (230D). Flow diversion is again clearly seen at the surface, but not the mid-layer and the bottom. The maximum decrease in flow velocity is also found at the mid-layer for the same reason mentioned above. However, at this particular instant, the affected area is no longer along the main flow direction. Instead, a much larger area towards the open sea is under the influence of the turbine farm.

Turbulence kinetic energy

Figure 6.48 to Figure 6.50 show TKE fields at the surface, the mid-layer and the bottom of the case with turbine farm on the left panel and changes due to the implementation of the farm on the right panel at HW, Slack water and LW, respectively. It can be seen from the figures that the impact of the turbines on TKE is very much restricted to the local area of the device farm. Although the presence of the turbine farm increases local TKE around the devices from nearly 0 to 0.09 m^2/s^2 at the mid-layer and causes less significant, but detectable, local TKE enhancement at the other layers, no TKE changes is detected elsewhere within the investigated region.

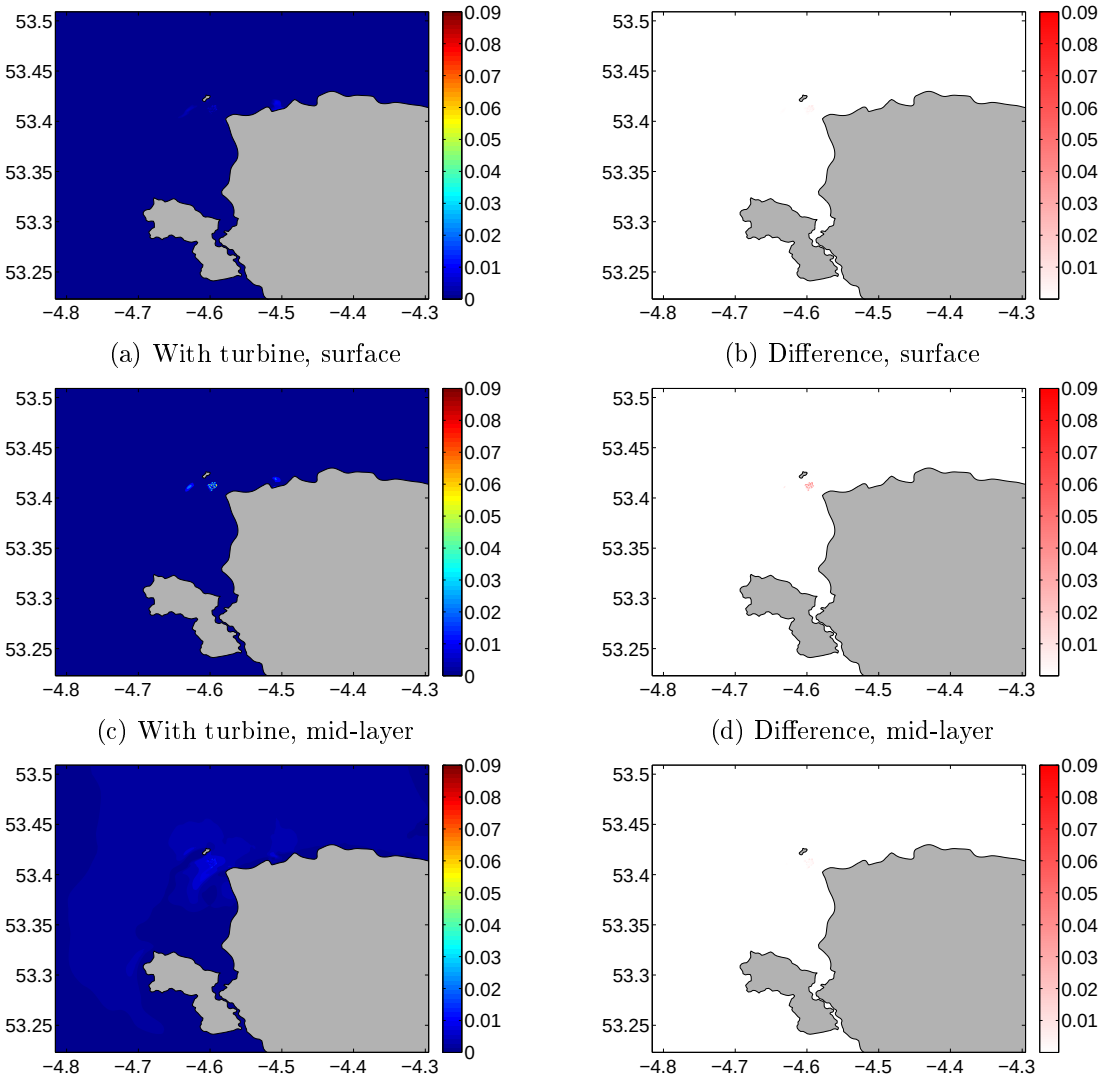

(a) With turbine, surface

(b) Difference, surface

(c) With turbine, mid-layer

(d) Difference, mid-layer

(e) With turbine, bottom

(f) Difference, bottom

Figure 6.48: TKE fields with turbine farm and TKE field change contours at HW. (unit: m^2/s^2)

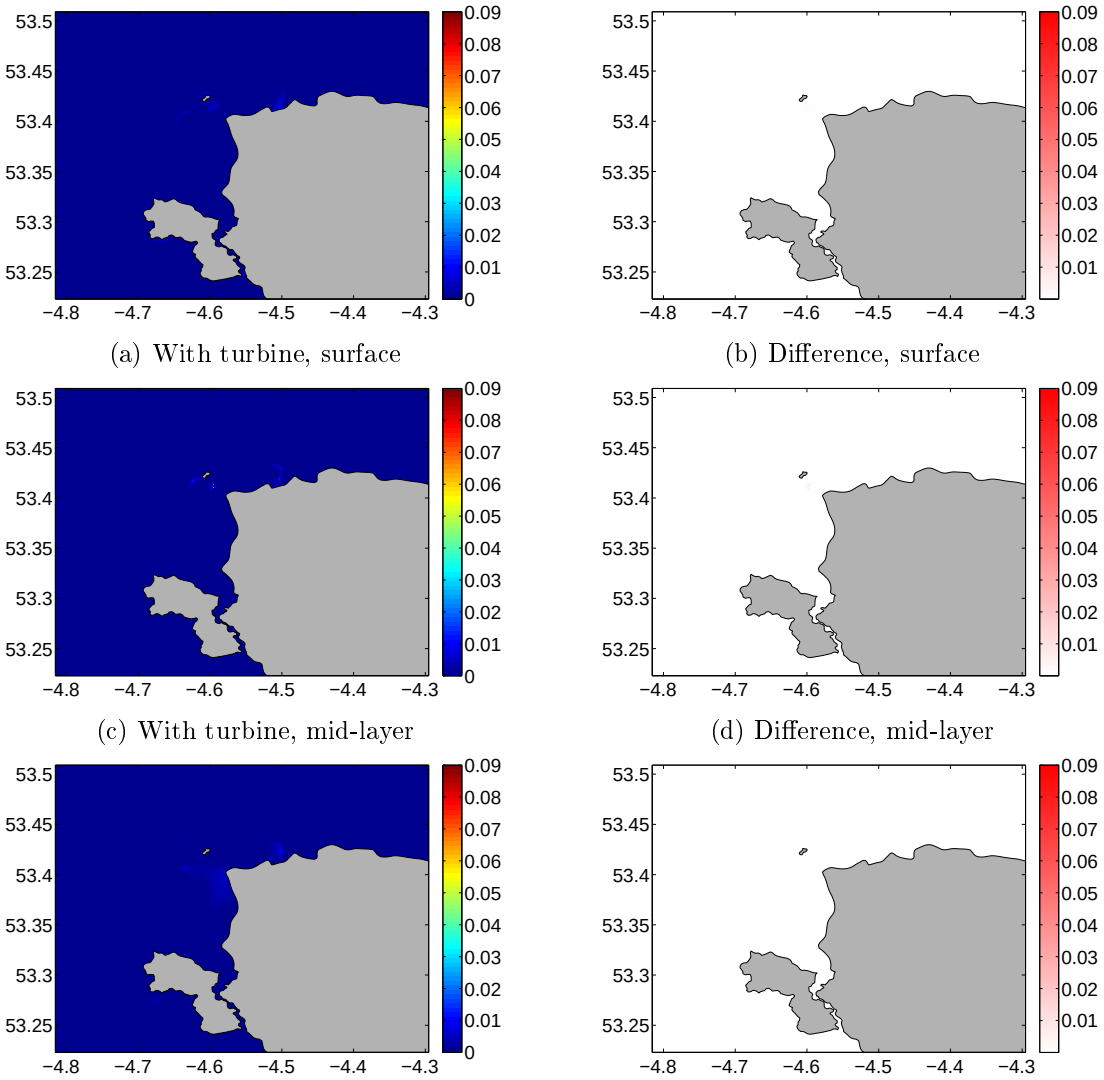

(a) With turbine, surface

(b) Difference, surface

(c) With turbine, mid-layer

(d) Difference, mid-layer

(e) With turbine, bottom

(f) Difference, bottom

Figure 6.49: TKE fields with turbine farm and TKE field change contours at Slack water. (unit: m^2/s^2)

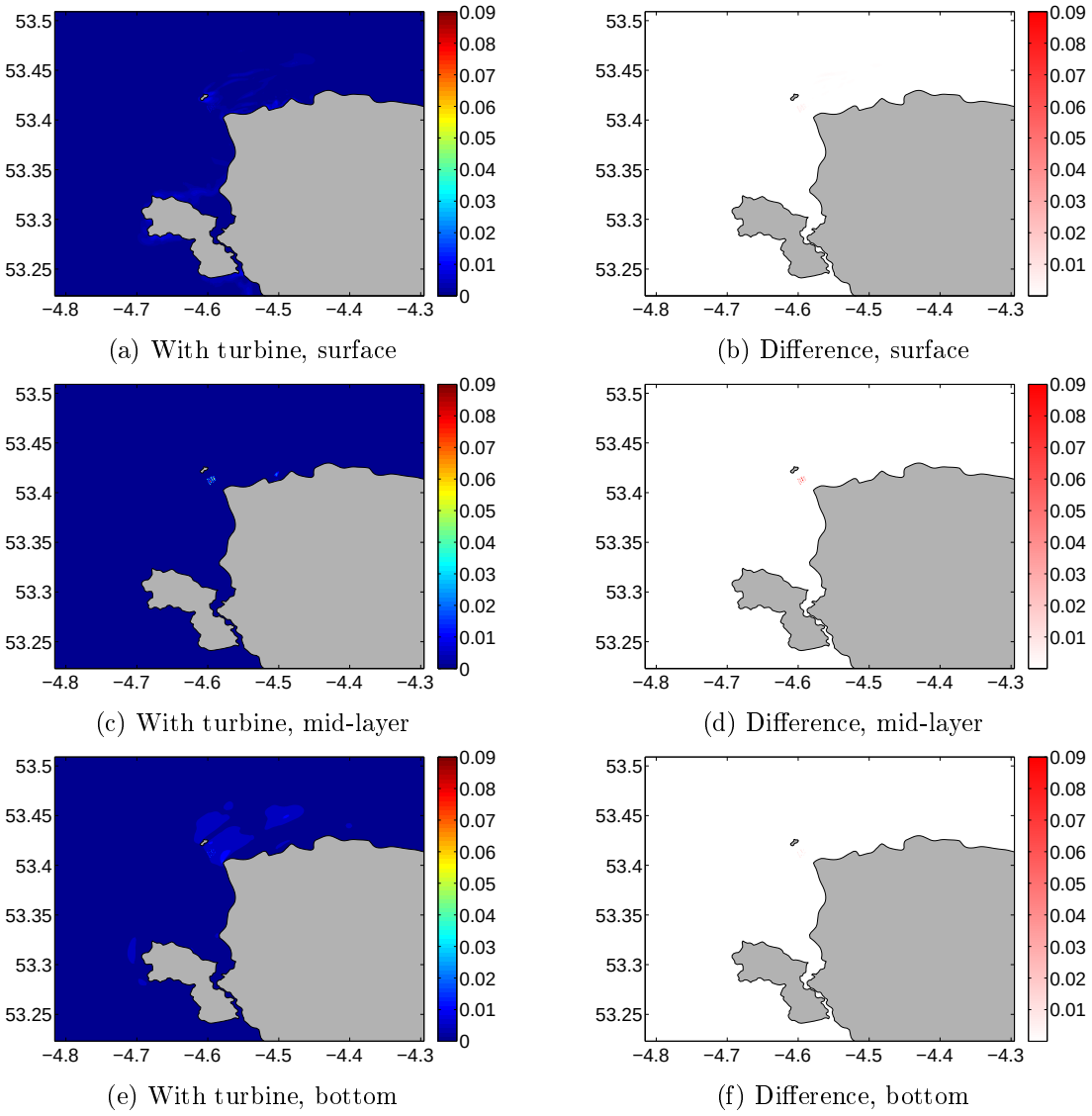

(a) With turbine, surface

(b) Difference, surface

(c) With turbine, mid-layer

(d) Difference, mid-layer

(e) With turbine, bottom

(f) Difference, bottom

Figure 6.50: TKE fields with turbine farm and TKE field change contours at LW. (unit: m^2/s^2)

Surface wave dynamics

Figure 6.51 shows significant wave height distribution with the turbine farm on the left panel and its changes caused by the turbine farm on the right panel at HW, Slack water and LW, respectively. It can be seen from the figures that a fairly large area is affected by the implementation of the turbines, even though the effect is quite small outside the vicinity of the farm. At HW, when the current is flowing towards the south-west, the effect at regional scale is mainly a reduction of wave height in both the vicinity and downstream of the farm. Wave height in the upstream is also slightly reduced. Three small hotspots of increased wave height are found with far distance from each other. On the other hand, when the current is flowing towards north-east at LW, apart from the decreased wave height in the very vicinity of the farm and in the far field, wave height

is found to be increased within a large area downstream of the farm. The dominant cause of wave height changes, as pointed out in early sections, is very likely to be the corresponding flow field variations which affect surface waves under the wave-current interaction framework, instead of OBSTACLE. This is supported by the fact that the wave height change observed during Slack water has a chaotic pattern very similar to the one of the flow field at the surface (see Figure 6.46 (b)).

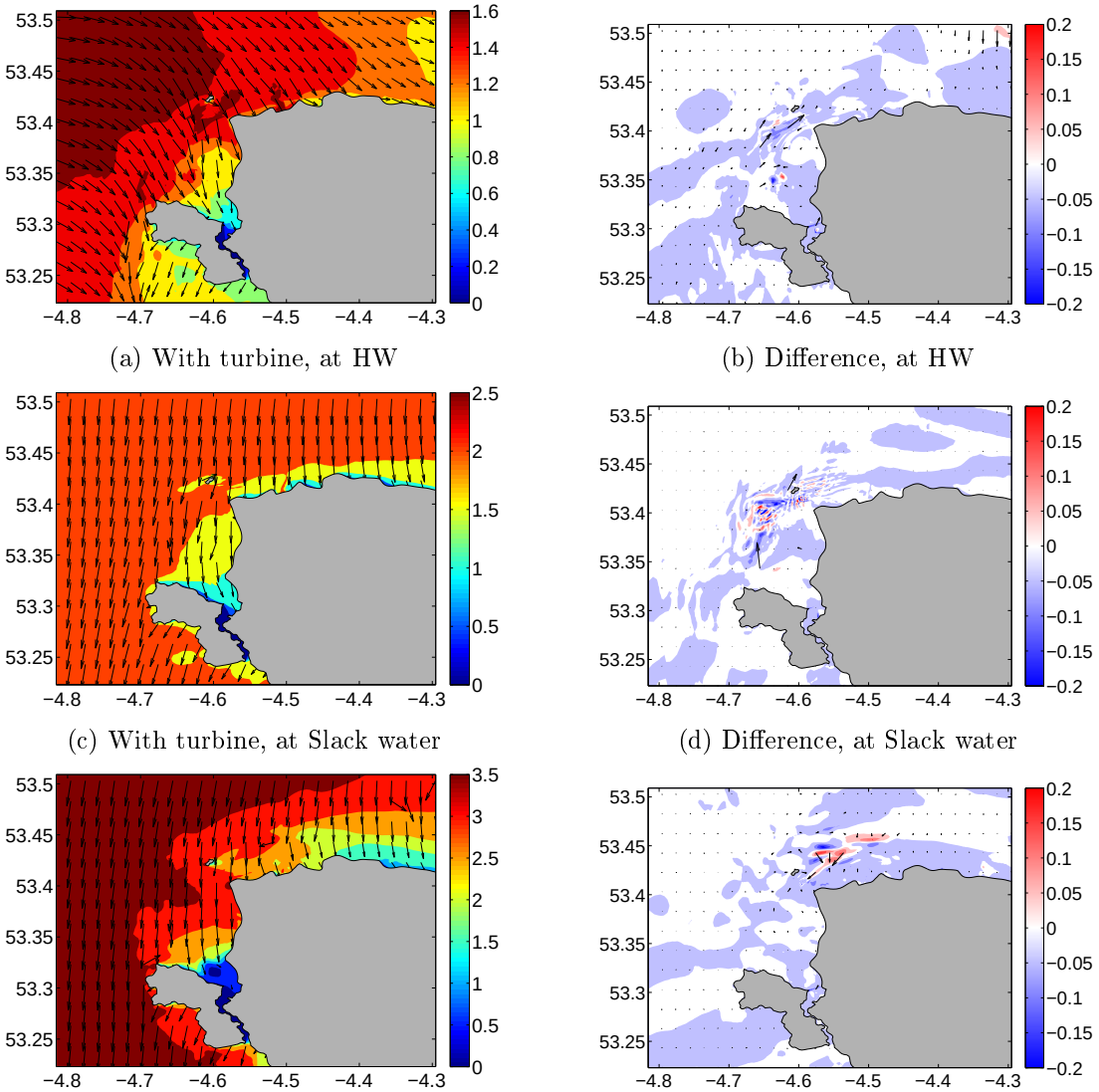

(a) With turbine, at HW

(b) Difference, at HW

(c) With turbine, at Slack water

(d) Difference, at Slack water

(e) With turbine, at LW

(f) Difference, at LW

Figure 6.51: Significant wave height fields with turbine and significant wave height field change contours imposed with wave direction vectors. (unit: m)

Bed shear stress

Figure 6.52 shows bed shear stress distribution with the turbine farm on the left panel and its changes on the right panel at HW, Slack water and LW respectively. It can be seen from the figure that the presence of the turbine farm alters the bed shear stress of

a large area. This is not surprising as the calculation of bottom shear stress depends highly on flow velocity and wave height, both of which undergo regional changes due to the implementation of the turbine farm. However, with the turbine-induced shear stress enhancement reaching a maximum of about $2.5N/m^2$ within the device farm, reduction in bottom shear stress observed outside the turbine farm is relatively small — the most severe reduction being about $0.3N/m^2$.

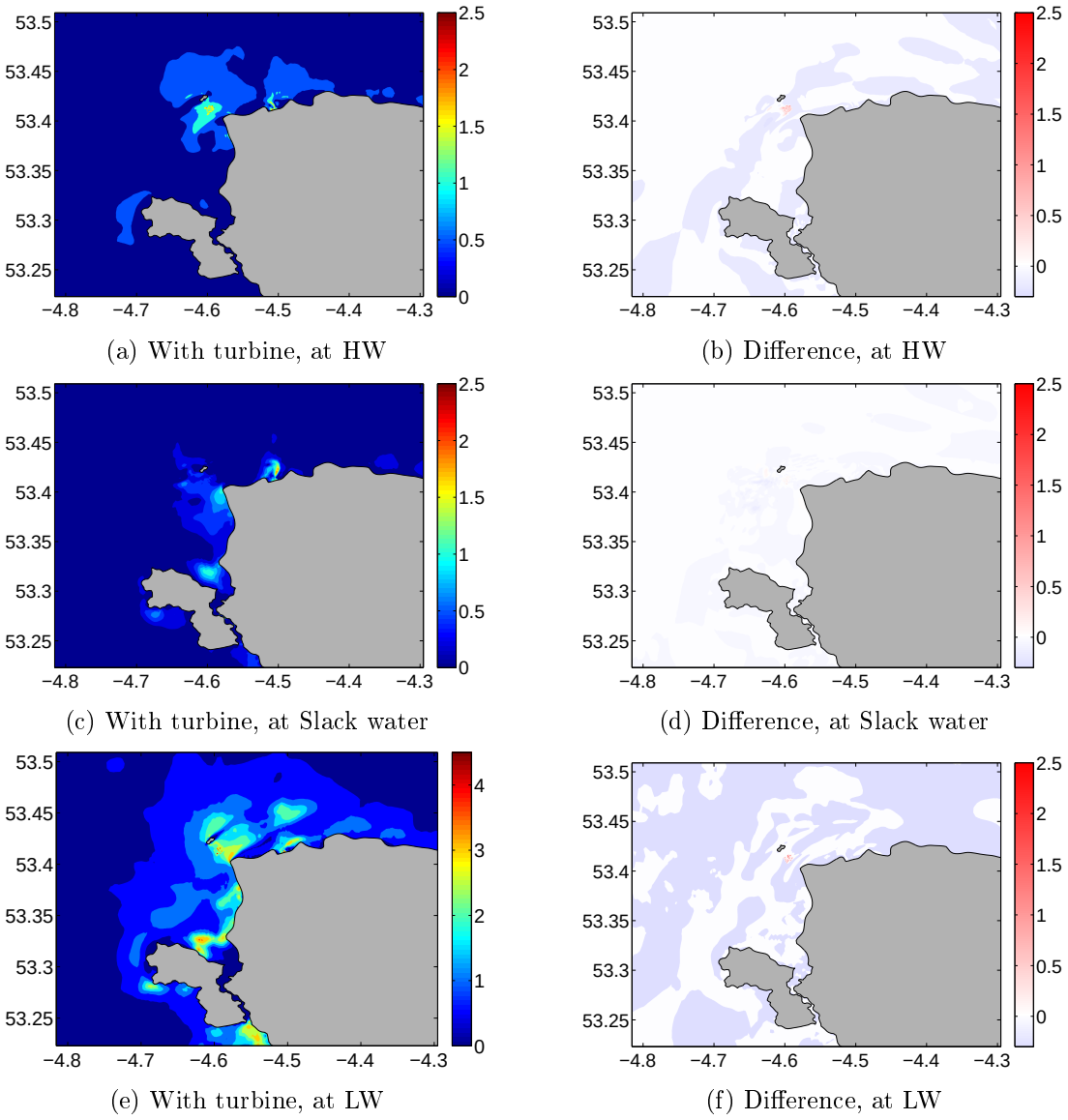

(a) With turbine, at HW

(b) Difference, at HW

(c) With turbine, at Slack water

(d) Difference, at Slack water

(e) With turbine, at LW

(f) Difference, at LW

Figure 6.52: Bottom stress fields with turbine and bottom stress field change contours. (unit: N/m^2)

Suspended sediment transport

Figure 6.53 to Figure 6.55 show suspended sediment concentration fields at the surface, the mid-layer and the bottom for the case with the turbine farm on the left panel and changes due to the implementation of the farm on the right panel at HW, Slack

water and LW, respectively. An eddy-like pattern is observed off the west coast of Anglesey at both HW and Slack water, with suspended sediment concentration generally higher at HW. The location of the eddy-like pattern agrees with the location of the eddy observed in Figure 6.45 and Figure 6.46. Changes caused by the turbine farm to sediment concentration are mainly along the eddy at these two phases of the tide. At HW, a jet of increased suspended sediment concentration, sandwiched by decreased sediment concentration, is clearly observed along the eddy at the surface. A similar pattern is observed at the mid-layer, with the changes being less significant. Sediment concentration in the vicinity of the farm is decreased at the bottom at HW, but with sediment concentration still increased at the downstream of the eddy. Changes at Slack water demonstrate similar patterns, but more chaotic. The changes are also generally less significant in comparison.

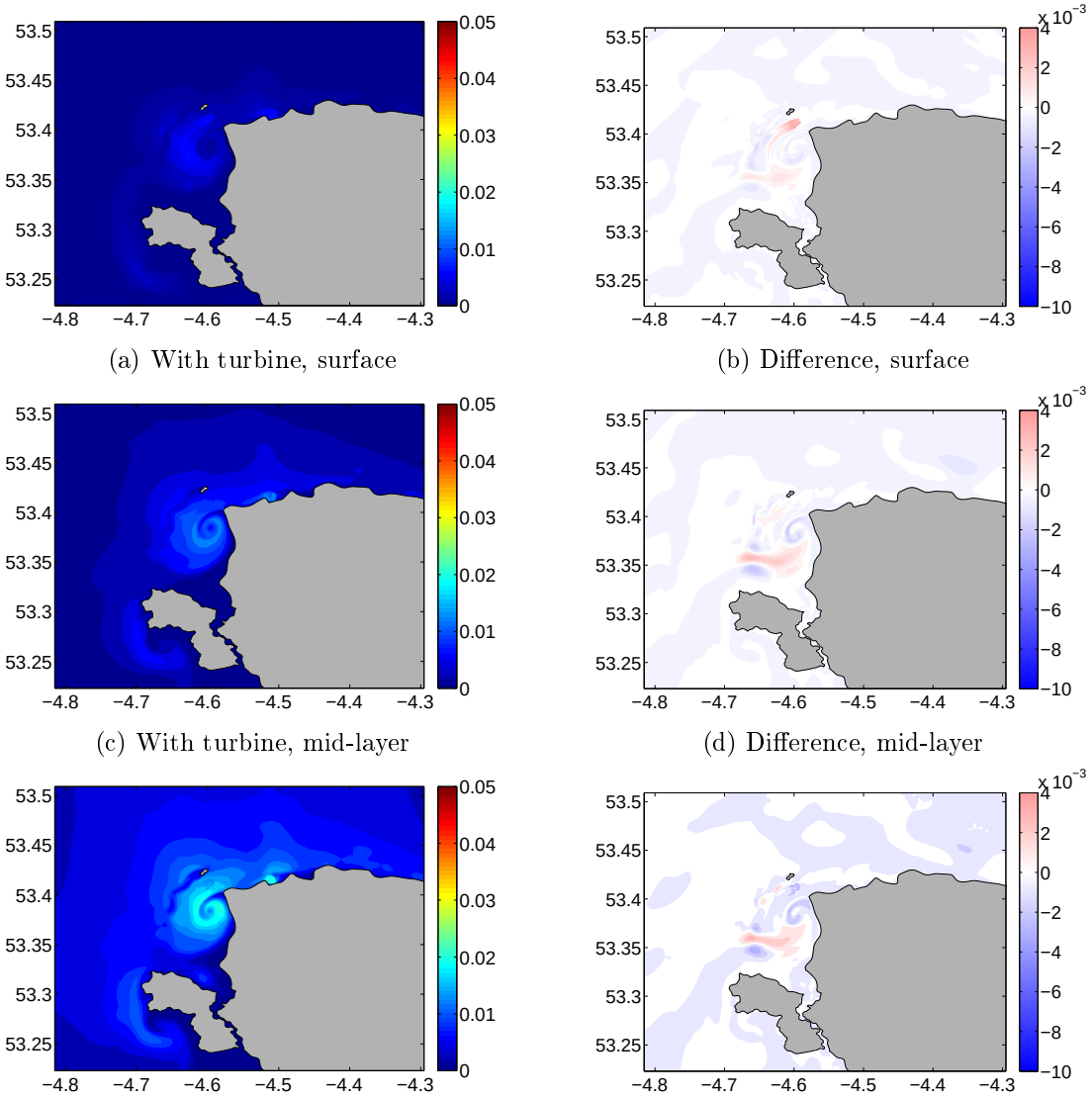

(a) With turbine, surface

(b) Difference, surface

(c) With turbine, mid-layer

(d) Difference, mid-layer

(e) With turbine, bottom

(f) Difference, bottom

Figure 6.53: Suspended sediment concentration fields with turbine farm and suspended sediment concentration field change contours at HW. (unit: kg/m^3)

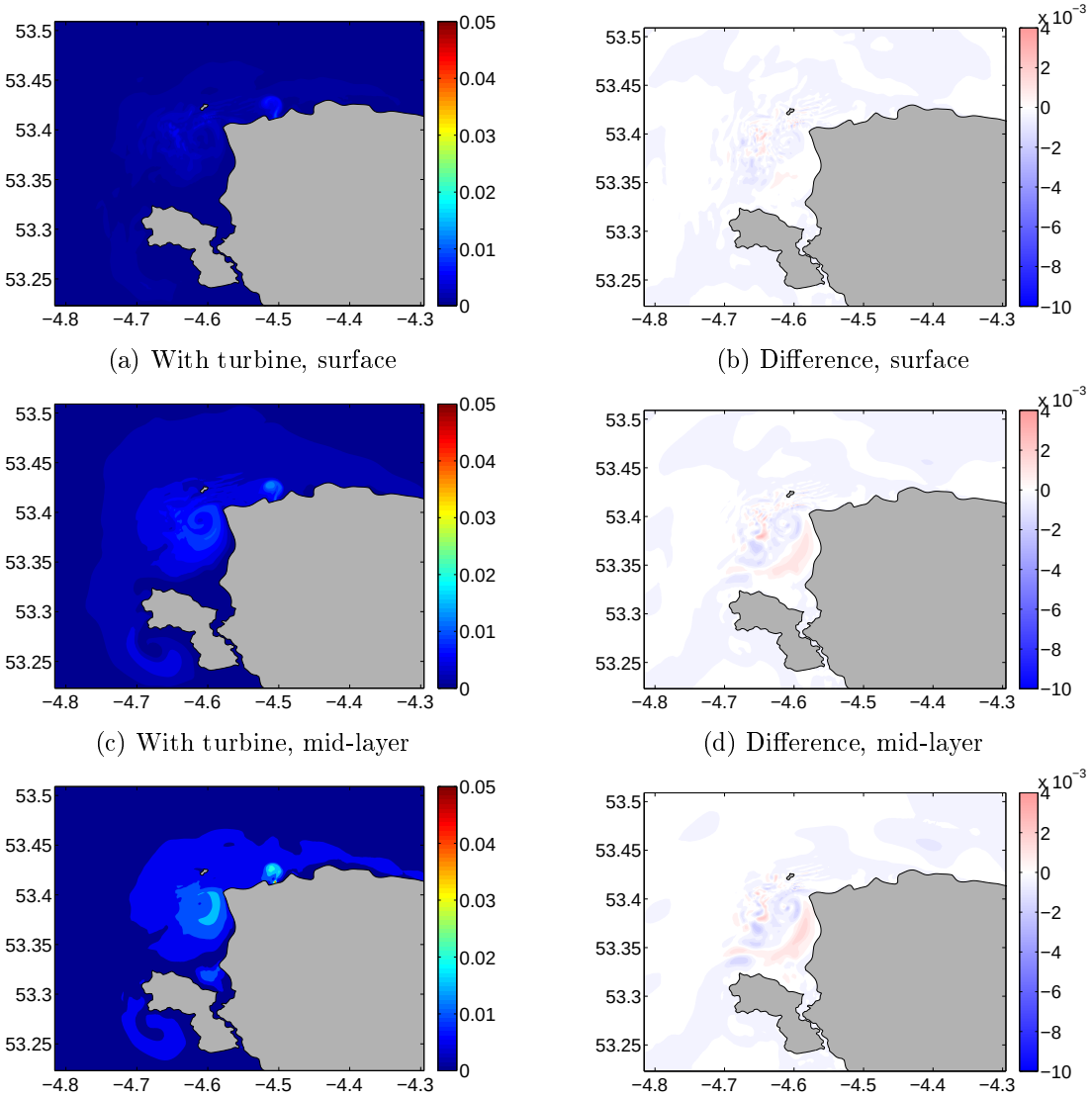

(a) With turbine, surface

(b) Difference, surface

(c) With turbine, mid-layer

(d) Difference, mid-layer

(e) With turbine, bottom

(f) Difference, bottom

Figure 6.54: Suspended sediment concentration fields with turbine farm and suspended sediment concentration field change contours at Slack water. (unit: kg/m^3)

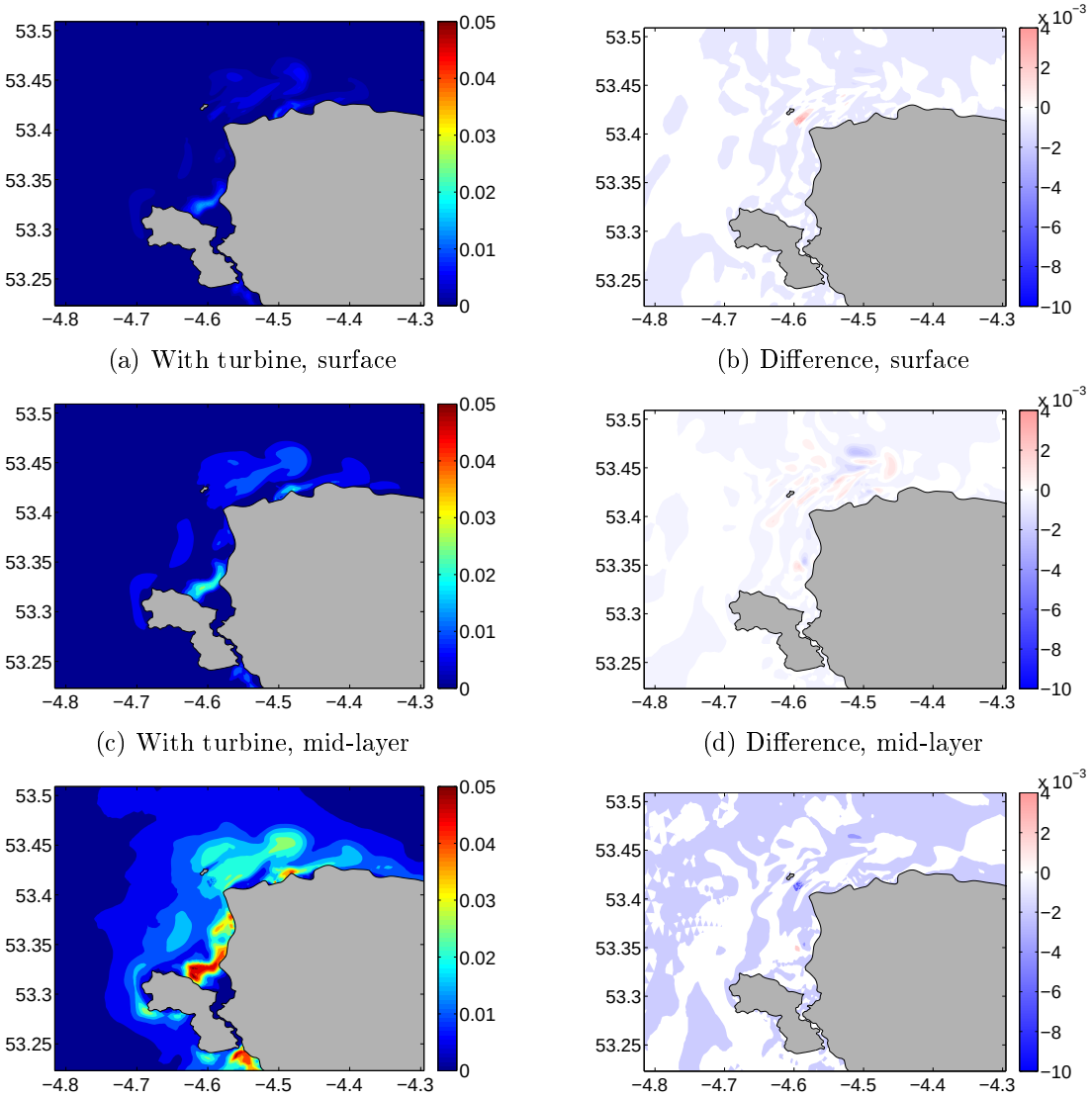

(a) With turbine, surface

(b) Difference, surface

(c) With turbine, mid-layer

(d) Difference, mid-layer

(e) With turbine, bottom

(f) Difference, bottom

Figure 6.55: Suspended sediment concentration fields with turbine farm and suspended sediment concentration field change contours at LW. (unit: kg/m^3)

At LW, no eddy-like pattern is observed within the investigated area. Again, in the vicinity of the farm, sediment concentration is increased at the surface and mid-layer and is decreased at the bottom. The influenced area, however, is smaller in comparison to that at LW. Outside the obvious wake, a patchy pattern of decreased concentration is observed across the investigated area at the surface and bottom and it is a mix of increase and decrease at the mid-layer. These changes are, however, very small, compared to the changes the vicinity of the farm undergoes.

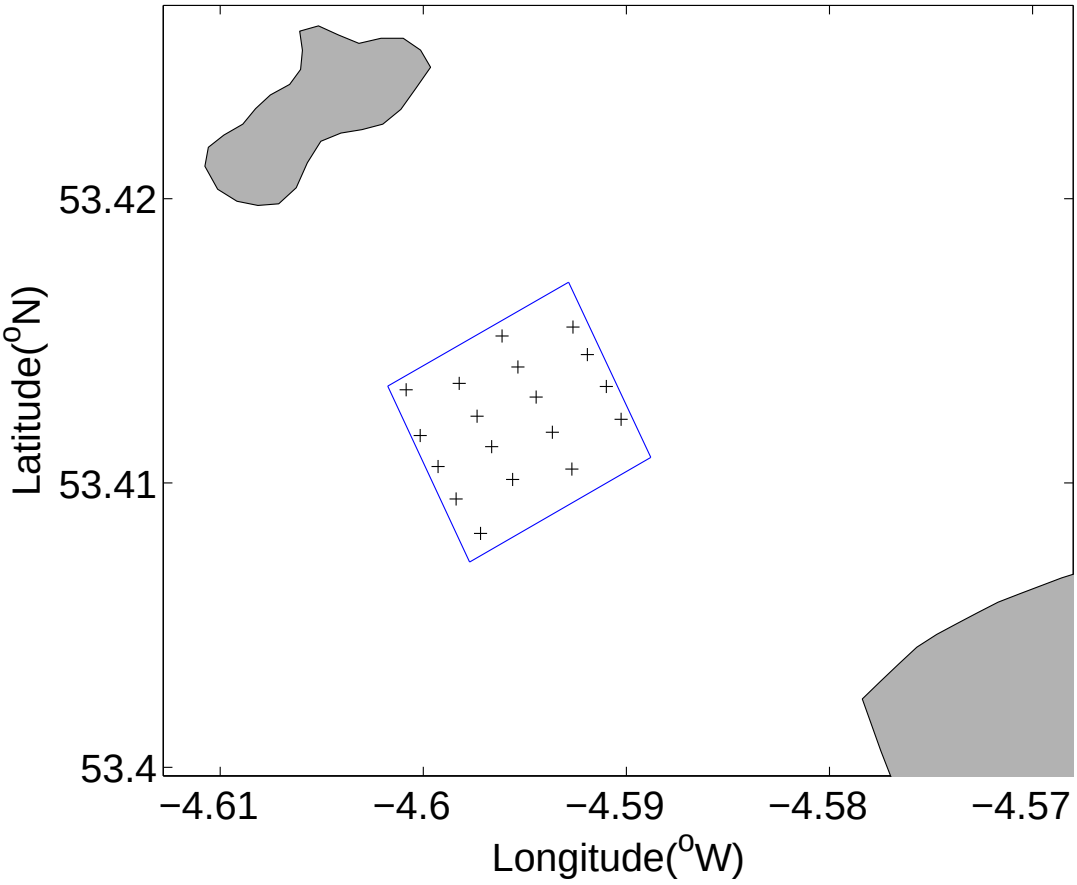

Figure 6.56: Box for integrating suspended sediment transport rate into and out of the turbine farm.

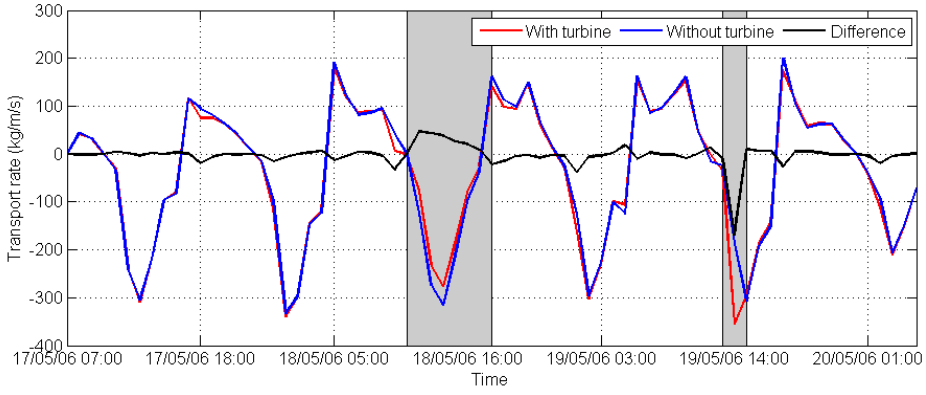

Figure 6.57: Time series of suspended sediment transport rate calculated with and without the turbine farm and changes caused by the turbine farm to suspended sediment transport rate around the turbine farm.

Suspended sediment transport flux

This section studies suspended sediment transport flux in and out of the turbine farm. It is calculated by integrating the transport rate along the edges of a box surrounding the farm as shown in Figure 6.56. Transport rates on the left, right, top and bottom lines of the box are calculated separately according to Equation 6.1. The individual transport rates are then summed up to get the transport fluxes in and out of the box.

Figure 6.57 shows the transport flux around the box under scenarios with and without the device farm. Difference in transport flux between these two scenarios is also given in the figure. Positive and negative values on lines suggest net flux into and out of the box respectively. In general, the influence of the particular turbine farm considered in the present study on suspended sediment transport rate in the vicinity of the farm is small. Sudden big change in transport flux is observed during the two time periods highlighted by grey boxes. These two instances also correspond to the large wave height and High Water shown in Figure 6.21.

Residual sediment transport

This section looks at the impacts of the turbine farm on regional residual sediment transport pathways. Figure 6.58 (a) shows the residual sediment transport pathways of the baseline case (no turbine farm) around the Anglesey coast, based on calculations of suspended sediment and velocity fields over one tidal cycle from High Water at 19/05/2006 03:00 to the next High Water as shown in Figure 6.21. One dominant feature of the sediment transport pathways observed from the figure is the large residual sediment transport directed eastwards along the north coast of Anglesey. Similar sediment transport pathways within this region are documented in earlier researches [112, 89]. Also, an anti-clockwise eddy-like residual sediment transport is observed in front of the turbine farm location, which is likely caused by the blockage effect of the headland opposite the Skerries on the current.

Figure 6.58 (b) gives the changes in residual sediment transport caused by the turbine farm. The impact of the farm is not localized. The large residual sediment transport along the entire north coast of Anglesey observed in the baseline case is reduced by the inclusion of the turbine farm by 2.3 kg/m/s (3%). The sediment transport is reduced by a larger extent just off the coast, east of the headland opposite the Skerries. The largest reduction in this area is 17.1 kg/m/s (11%). These two observations suggest that over a long period of time, coastal and offshore geomorphic structures off the north coast of Anglesey are under risk of erosion. The residual sediment transport rate west of the turbine farm is enhanced by 8.8 kg/m/s (10%). This could be attributed to the blockage effect caused by the turbine farm.

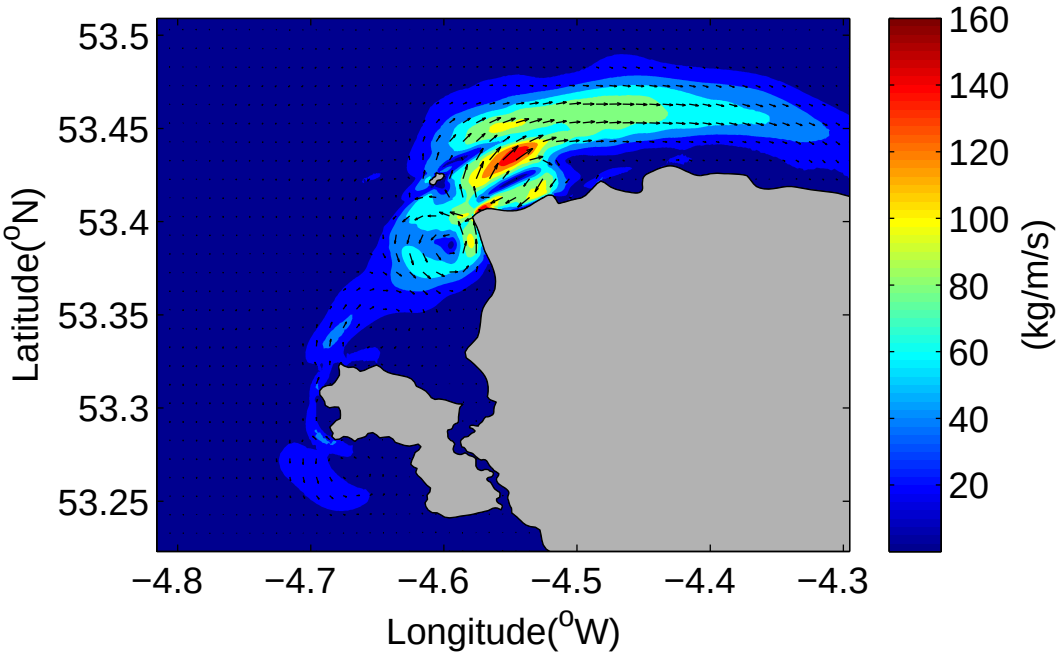

(a) Baseline case (no turbine farm)

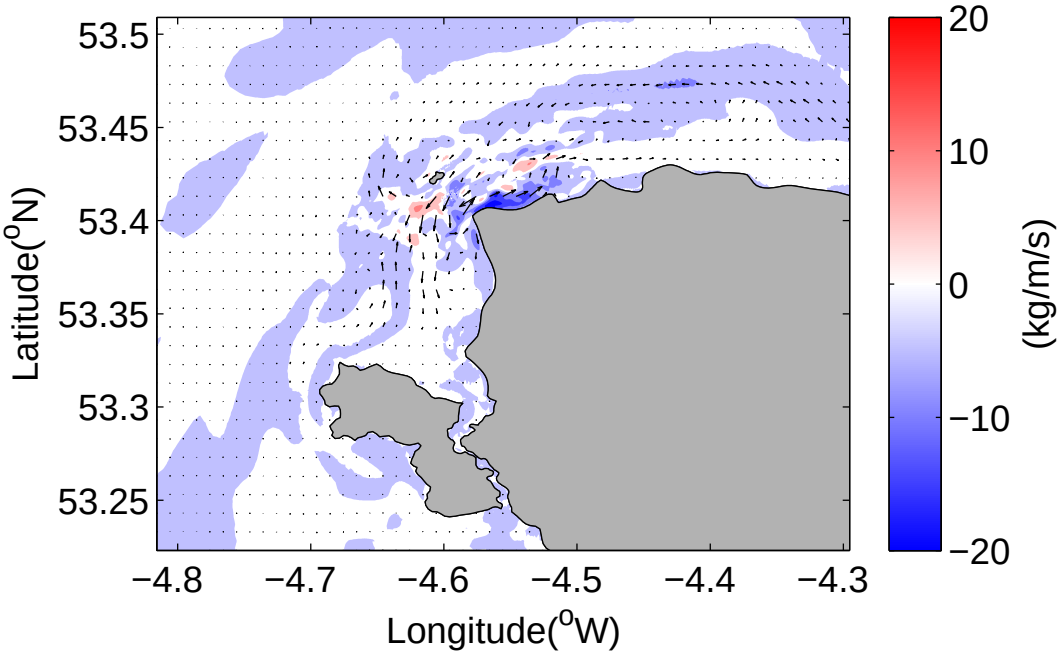

(b) Difference

Figure 6.58: Residual sediment transport pathways around the Anglesey coast.

Chapter 7

Conclusions and future research

7.1 Introduction

The current study aimed to develop a new model system for investigation of large scale tidal stream turbine farm impact to the surrounding environment. The three-dimensional coastal-oceanographic model FVCOM was used as the basis and several important parameterisations have been implemented in the model system to adapt it for the intended studies. These parameterisations include application of CFD model FLUENT with the VBM method to examine details of flow and turbulence characteristics around an individual turbine device at near field scale, together with analysis of available experimental data for a range of flow conditions. Based on these parameterisations and model simulations, several important findings were obtained.

7.2 Major Findings

The major findings of the present study have been listed below:

7.2.1 Model development

- The comparison between the FVCOM calculated results and the data obtained through laboratory experiments and CFD simulations suggested that calculations of flow field, turbulence field, wave height and sediment transport dynamics in FVCOM needed further modification in order to predict the above-mentioned processes in the wake of a turbine correctly.

  Through comparing FVCOM calculated results with laboratory experimental data and CFD simulations,

- The approaches implemented in the present study, i.e. retarding force for flow field, three additional terms for turbulence field and the built-in feature 'OBSTACLE' in SWAN for wave height, can improve the performance of the model

in predicting hydrodynamics and wave dynamics in the wake of a turbine, given corresponding coefficients assigned properly.

- Preliminary tests of the additional bottom shear stress term proposed to simulate impact of tidal turbines on sediment transport suggest that the additional stress term could potentially be a good way to simulate the initial pick-up of sediment particles under the presence of turbines. However, further modifications could also be required to obtain a correct suspension capability at the far wake.

- The model is sensitive to C_{ext} and K_t in terms of velocity calculation. The sensitivity is observed to be symmetrical. The model's prediction of TKE has similar sensitivity level to C_{ext}, C_{tp}, C_{td} and C_l. The sensitive responses, however, are asymmetrical. Suspended sediment concentration is highly sensitive to C_r, then moderately sensitive to the turbulence modification terms. Very small sensitivity is observed to C_{ext} and K_t.

7.2.2 Physics

- A tidal turbine simulation platform developed based on a wave-current-sediment fully coupled numerical model is applied to a single turbine flume test. Under a steady current, despite the fact that the turbine is causing flow deceleration in the water column, velocity near the bottom is increased, which also leads to enhancement of bottom shear stress. For the sediment types used in the single turbine tests, sediment concentration near the bottom responds in opposite ways to the inclusion of turbines. While sediment concentration near the bottom is increased in the clear water case, it is decreased in the live bed case due to the deficit in the sediment pick-up and suspension balance caused by the turbine. However, in general, the inclusion of a turbine increases sediment concentration in the upper part of the water.

- Waves and OBSTACLE considered in the single turbine flume test cause a very small variation to bottom shear stress and sediment transport patterns.

- The tidal turbine simulating platform has also been applied to the Anglesey coast, NW Wales for a case study. By using a very fine mesh resolution at the turbine farm site, hydrodynamic features and sediment transport patterns in the near wake of the turbines are identified. The particular turbine farm considered in the present study causes regional impact to free surface elevation. The impact, however, is generally small (-25mm to +15mm, i.e. $\sim 0.5\%$) compared to the usual large tidal range in this area. Thanks to the three-dimensional model used in the present study, apart from flow deceleration observed at the upper levels of the water and from the depth-averaged flow fields, accelerated flow is commonly observed at

layers near the bottom in the wake, together with enhanced bottom shear stress within the wake. This result agrees with observations obtained in the laboratory and results predicted by three-dimensional CFD simulations and is very different from conclusions drawn in work applying two-dimensional models in which bottom stress was weakened due to decelerated depth-averaged flow (see Section 2.4.3). The variation in velocity is not localized to the turbine farm, but extended a distance of up to 4.5 km from the farm. However, impact from the devices on TKE is very much restricted to the local area of the farm. Wave energy immediately downstream of the individual turbines is slightly dissipated; this is reflected by the drop in near-wake wave height observed. However, further downstream of the farm, the dominant factor determining changes in wave height is instead variations in flow field which affect the wave dynamics through the interactive mechanism of waves and current. The device farm has a strong influence on the vertical mixing of suspended sediment in the wake: sediment concentration near the bottom is reduced yet that near the surface is increased. Regionally, the strong residual sediment transport directed eastwards along the north coast of Anglesey is found to be weakened by the device farm, which, in the long run, may put the nearby coastal and offshore geomorphic structures under risk of erosion.

7.3 Future Research

The present study only starts to look into the potential impacts from a tidal turbine farm for limited scenarios. There are many limitations that restrict the application of current findings to a wider range of natural conditions. The follow-on study can therefore aim to overcome these limitations and extend and improve the findings for more realistic applications in the future. Some general remarks are given in the following list:

- Better representations of turbine.

  A three-dimensional extension of retarding force, even though resolves the velocity profiles in the wave very well, still lacks of rotation motion, resulting in under-predicted turbulent mixing and subsequent suspended sediment transport. Also, the mechanism of turbine-wave interaction is not fully resolved by the model, but relies on simple application of OBSTACLE.

- Use higher order turbulence closures.

  Higher order turbulence closures, such as Shear Stress Transport (SST) models or Large Eddy Simulation (LES) model, can lead to better simulation of eddy shedding.

- Further model sensitivity tests.

Due to limit in time, sensitivity test on the model in the present study focused only on limited variables (velocity, TKE and suspended sediment concentration). Sensitivity tests on more variables and deeper analysis on the sensitive response mechanism are suggested.

- Turbine-sediment interaction.

  Future research can focus on the dynamics of sediment transport under the presence of the turbine and its representation in numerical models. Further testing on responses of grains with different sizes to the inclusion of turbine is also recommended.

- Include more physical processes.

  Apart from hydrodynamics, wave dynamics and suspended sediment transport, future work on assessment of changes in bed scour, temperature and salinity structure and biological system is also possible. Further, bedload sediment transport is not yet considered in this research due to the reasons mentioned in previous chapters — it can be included in future studies.

Bibliography

[1] Reza Ahmadian, Roger Falconer, and Bettina Bockelmann-Evans. Far-field modelling of the hydro-environmental impact of tidal stream turbines. *Renewable Energy*, 38(1):107–116, 2012.

[2] PH Alfredsson and JA Dahlberg. A preliminary wind tunnel study of windmill wake dispersion in various flow conditions. *Technical note AU-1499, part 7*, 1979.

[3] Sanderse B. Aerodynamics of wind turbine wakes literature review. *EnergyResearch Centre of Netherlands ECN-E-09-016*, 2009.

[4] AS Bahaj, LE Myers, RI Rawlinson-Smith, and Matthew Thomson. The effect of boundary proximity upon the wake structure of horizontal axis marine current turbines. In *Proceedings of the 27th International Conference on Offshore Mechanics and Arctic Engineering, Estoril, Portugal*, 2012.

[5] AS Bahaj, LE Myers, MD Thomson, and N Jorge. Characterising the wake of horizontal axis marine current turbines. In *Proceedings of the 7th European Wave and Tidal Energy Conference, Port, Portugal*, 2007.

[6] Luolin Bai, Roy RG Spence, and Grégory Dudziak. Investigation of the influence of array arrangement and spacing on tidal energy converter (TEC) performance using a 3-dimensional CFD model. In *Proceedings of the 8th European Wave and Tidal Energy Conference, Uppsala, Sweden*, pages 654–660, 2009.

[7] N Barltrop, KS Varyani, A Grant, D Clelland, and XP Pham. Investigation into wave-current interactions in marine current turbines. *Proceedings of the Institution of Mechanical Engineers, Part A: Journal of Power and Energy*, 221(2):233–242, 2007.

[8] N Barltrop, KS Varyani, A Grant, D Clelland, and Xuan Pham. Wave-current interactions in marine current turbines. *Proceedings of the Institution of Mechanical Engineers, Part M: Journal of Engineering for the Maritime Environment*, 220(4):195–203, 2006.

[9] WMJ Batten, AS Bahaj, AF Molland, and JR Chaplin. Hydrodynamics of marine current turbines. *Renewable energy*, 31(2):249–256, 2006.

[10] WMJ Batten, AS Bahaj, AF Molland, and JR Chaplin. The prediction of the hydrodynamic performance of marine current turbines. *Renewable energy*, 33(5):1085–1096, 2008.

[11] JA Battjes and JPFM Janssen. Energy loss and set-up due to breaking of random waves. In *Proceedings of the 16th International Conference on Coastal Engineering*, volume 1, pages 569–587, 1978.

[12] Albert Betz. *Wind-energie und ihre ausnutzung durch windmühlen*. Vandenhoeck, 1926.

[13] Fatih Birol et al. World energy outlook. Technical report, Paris: International Energy Agency, 2008.

[14] Veatch Black. Phase II. UK tidal stream energy resource assessment. Carbon Trust Marine Energy Challenge. Technical report, 2005.

[15] LS Blunden and AS Bahaj. Initial evaluation of tidal stream energy resources at portland bill, uk. *Renewable Energy*, 31(2):121–132, 2006.

[16] Rodolfo Bolanos, Judith Wolf, Jennifer Brown, Pedro Osuna, Jaak Monbaliu, and Agustin Sanchez-Arcilla. Comparison of wave-current interaction formulation using the polcoms-wam wave-current model. In *Proceedings of the 31st International Conference on Coastal Engineering*, volume 1, pages 521–533. World Scientific, 2008.

[17] N Booij, RC Ris, and Leo H Holthuijsen. A third-generation wave model for coastal regions: 1. model description and validation. *Journal of Geophysical Research: Oceans (1978–2012)*, 104(C4):7649–7666, 1999.

[18] Judith Bosboom and Gert Klopman. Intra-wave sediment transport modelling. In *Proceedings of the 27st International Conference on Coastal Engineering*, volume 3, pages 2453–2466, 2001.

[19] Ian G Bryden and Scott J Couch. Me1 marine energy extraction: tidal resource analysis. *Renewable Energy*, 31(2):133–139, 2006.

[20] IG Bryden, SJ Couch, A Owen, and G Melville. Tidal current resource assessment. *Proceedings of the Institution of Mechanical Engineers, Part A: Journal of Power and Energy*, 221(2):125–135, 2007.

[21] R Burrows, IA Walkington, NC Yates, TS Hedges, J Wolf, and J Holt. The tidal range energy potential of the west coast of the united kingdom. *Applied Ocean Research*, 31(4):229–238, 2009.

[22] Tony Burton, David Sharpe, Nick Jenkins, and Ervin Bossanyi. *Wind energy handbook*. John Wiley & Sons, 2001.

[23] Glenn Cada, James Ahlgrimm, Michael Bahleda, Tom Bigford, Stefanie Damiani Stavrakas, Douglas Hall, Russell Moursund, and Michael Sale. Potential impacts of hydrokinetic and wave energy conversion technologies on aquatic environments. *Fisheries*, 32(4):174–181, 2007.

[24] Changsheng Chen, Geoffery Cowles, and RC Beardsley. An unstructured grid, finite-volume coastal ocean model: Fvcom user manual. *SMAST/UMASSD*, 2006.

[25] Changsheng Chen, Hedong Liu, and Robert C Beardsley. An unstructured grid, finite-volume, three-dimensional, primitive equations ocean model: application to coastal ocean and estuaries. *Journal of atmospheric and oceanic technology*, 20(1):159–186, 2003.

[26] Long Chen and Wei-Haur Lam. Methods for predicting seabed scour around marine current turbine. *Renewable and Sustainable Energy Reviews*, 29:683–692, 2014.

[27] Long Chen and Wei-Haur Lam. Slipstream between marine current turbine and seabed. *Energy*, 68:801–810, 2014.

[28] Y-S Chen and S-W Kim. Computation of turbulent flows using an extended k-epsilon turbulence closure model. Technical report, NASA, 1987.

[29] Elizabeth Christie. *Numerical Modeling of Morphological Impacts of Offshore Wind Farms*. PhD thesis, School of Engineering, University of Liverpool, 1 2015.

[30] Scott J Couch and Ian G Bryden. The impact of energy extraction on tidal flow development. In *Proceedings of the 3rd International Conference on Marine Renewable Energy, Blyth, UK*, 2004.

[31] Geoffrey W Cowles. An investigation of dynamical processes influencing sediment transport and morphological change in skagit bay using an unstructured grid coastal ocean model. Technical report, DTIC Document, 2011.

[32] TA de Jesus Henriques, SC Tedds, A Botsari, G Najafian, TS Hedges, CJ Sutcliffe, Ieuan Owen, and RJ Poole. The effects of wave–current interaction on the performance of a model horizontal axis tidal turbine. *International Journal of Marine Energy*, 8:17–35, 2014.

[33] Zafer Defne, Kevin A Haas, and Hermann M Fritz. Numerical modeling of tidal currents and the effects of power extraction on estuarine hydrodynamics along the georgia coast, usa. *Renewable Energy*, 36(12):3461–3471, 2011.

[34] MR Dobson, WE Evans, and KH James. The sediment on the floor of the southern irish sea. *Marine Geology*, 11(1):27–69, 1971.

[35] Scott Draper, GT Houlsby, MLG Oldfield, and AGL Borthwick. Modelling tidal energy extraction in a depth-averaged coastal domain. *IET renewable power generation*, 4(6):545–554, 2010.

[36] Amina El Kasmi and Christian Masson. An extended k–ε model for turbulent flow through horizontal-axis wind turbines. *Journal of Wind Engineering and Industrial Aerodynamics*, 96(1):103–122, 2008.

[37] David Fallon, Michael Hartnett, Agnieszka Olbert, and Stephen Nash. The effects of array configuration on the hydro-environmental impacts of tidal turbines. *Renewable Energy*, 64:10–25, 2014.

[38] Céline Faudot and Ole Gunnar Dahlhaug. Prediction of wave loads on tidal turbine blades. *Energy Procedia*, 20:116–133, 2012.

[39] Inc Fluent. Fluent users guide, 2006.

[40] Pascal W Galloway, Luke E Myers, and AbuBakr S Bahaj. Quantifying wave and yaw effects on a scale tidal stream turbine. *Renewable energy*, 63:297–307, 2014.

[41] B Galperin, LH Kantha, S Hassid, and A Rosati. A quasi-equilibrium turbulent energy model for geophysical flows. *Journal of the Atmospheric Sciences*, 45(1):55–62, 1988.

[42] Chris Garrett and Patrick Cummins. The efficiency of a turbine in a tidal channel. *Journal of fluid mechanics*, 588:243–251, 2007.

[43] Chris Garrett and Patrick Cummins. Limits to tidal current power. *Renewable Energy*, 33(11):2485–2490, 2008.

[44] Benoît Gaurier, Peter Davies, Albert Deuff, and Grégory Germain. Flume tank characterization of marine current turbine blade behaviour under current and wave loading. *Renewable Energy*, 59:1–12, 2013.

[45] Anthony J Grass. Structural features of turbulent flow over smooth and rough boundaries. *Journal of Fluid Mechanics*, 50(02):233–255, 1971.

[46] SR Green. Modelling turbulent air flow in a stand of widely-spaced trees. *Phoenics J*, 5(3):294–312, 1992.

[47] Gareth I Gretton, Tom Bruce, and David M Ingram. Hydrodynamic modelling of a vertical axis tidal current turbine using cfd. In *Proceedings of the 8th European Wave and Tidal Energy Conference*, pages 468–476, 2009.

[48] ME Harrison, WMJ Batten, LE Myers, and AS Bahaj. Comparison between cfd simulations and experiments for predicting the far wake of horizontal axis tidal turbines. *IET Renewable Power Generation*, 4(6):613–627, 2010.

[49] M Reza Hashemi and Simon P Neill. The role of tides in shelf-scale simulations of the wave energy resource. *Renewable Energy*, 69:300–310, 2014.

[50] M Reza Hashemi, Simon P Neill, Peter E Robins, Alan G Davies, and Matt J Lewis. Effect of waves on the tidal energy resource at a planned tidal stream array. *Renewable Energy*, 75:626–639, 2015.

[51] Klaus Hasselmann, TP Barnett, E Bouws, H Carlson, DE Cartwright, K Enke, JA Ewing, H Gienapp, DE Hasselmann, P Kruseman, et al. Measurements of wind-wave growth and swell decay during the joint north sea wave project (jonswap). Technical report, Deutches Hydrographisches Institut, 1973.

[52] TS Hedges. Regions of validity of analytical wave theories. *Oceanographic Literature Review*, 1(43):10, 1996.

[53] Craig Hill, Mirko Musa, Leonardo P Chamorro, Chris Ellis, and Michele Guala. Local scour around a model hydrokinetic turbine in an erodible channel. *Journal of Hydraulic Engineering*, 140(8):04014037, 2014.

[54] Leo H Holthuijsen. *Waves in oceanic and coastal waters*. Cambridge University Press, 2007.

[55] GT Houlsby, S Draper, MLG Oldfield, et al. Application of linear momentum actuator disc theory to open channel flow. *Report no. OUEL*, 2296(08), 2008.

[56] Tai-Wen Hsu, Jian-Ming Liau, Shin-Jye Liang, Shiaw-Yih Tzang, and Dong-Jiing Doong. Assessment of kuroshio current power test site of green island, taiwan. *Renewable Energy*, 81:853–863, 2015.

[57] AS Iyer, SJ Couch, GP Harrison, and AR Wallace. Variability and phasing of tidal current energy around the united kingdom. *Renewable Energy*, 51:343–357, 2013.

[58] Luara Beth Jordan, Simmons, and McLelland. The impact of tidal stream turbines on 3d flow and bed shear stress measured with particle image velocimetry in a laboratory flume. In *Proceedings of the 11th European Wave and Tidal Energy Conference, Nantes, France*, pages 654–660, 2015.

[59] RH Karsten, JM McMillan, MJ Lickley, and RD Haynes. Assessment of tidal current energy in the minas passage, bay of fundy. *Proceedings of the Institution*

of Mechanical Engineers, Part A: Journal of Power and Energy, 222(5):493–507, 2008.

[60] PH Kemp and RR Simons. The interaction between waves and a turbulent current: waves propagating with the current. *Journal of Fluid Mechanics*, 116:227–250, 1982.

[61] PH Kemp and RR Simons. The interaction of waves and a turbulent current: waves propagating against the current. *Journal of Fluid Mechanics*, 130:73–89, 1983.

[62] Hyoseob Kim, Brian A O'Connor, Inbo Park, and Younggyu Lee. Modeling effect of intersection angle on near-bed flows for waves and currents. *Journal of waterway, port, coastal, and ocean engineering*, 127(6):308–318, 2001.

[63] G Klopman. Vertical structure of the flow due to waves and currents. *Progress report, Delft Hydraulics H*, 840, 1994.

[64] GJ Komen, K Hasselmann, and K1 Hasselmann. On the existence of a fully developed wind-sea spectrum. *Journal of physical oceanography*, 14(8):1271–1285, 1984.

[65] Van Rijn Leonardus Cornelis. *Principles of sediment transport in rivers, estuaries and coastal seas*, volume 1006. Aqua publications Amsterdam, 1993.

[66] M Lewis, SP Neill, PE Robins, and MR Hashemi. Resource assessment for future generations of tidal-stream energy arrays. *Energy*, 83:403–415, 2015.

[67] Ethan E Lust, Luksa Luznik, Karen A Flack, Jessica M Walker, and Max C Van Benthem. The influence of surface gravity waves on marine current turbine performance. *International Journal of Marine Energy*, 3:27–40, 2013.

[68] Luksa Luznik, Karen A Flack, Ethan E Lust, and Katharin Taylor. The effect of surface waves on the performance characteristics of a model tidal turbine. *Renewable energy*, 58:108–114, 2013.

[69] Ole Secher Madsen. Spectral wave-current bottom boundary layer flows. In *Proceedings of the 24th International Conference on Coastal Engineering*, volume 1, pages 384–398, 1994.

[70] Fabrice Maganga, Gregory Germain, Jacob King, G Pinon, and E Rivoalen. Experimental characterisation of flow effects on marine current turbine behaviour and on its wake properties. *IET Renewable Power Generation*, 4(6):498–509, 2010.

[71] R Martin-Short, J Hill, SC Kramer, A Avdis, PA Allison, and MD Piggott. Tidal resource extraction in the pentland firth, uk: Potential impacts on flow regime and sediment transport in the inner sound of stroma. *Renewable Energy*, 76:596–607, 2015.

[72] Richard McSherry, Jamie Grimwade, Ian Jones, Simon Mathias, Andrew Wells, and Andre Mateus. 3D CFD modelling of tidal turbine performance with validation against laboratory experiments. In *Proceedings of the 9th European Wave and Tidal Energy Conference, Southampton, UK*, 2011.

[73] George Mellor. The three-dimensional current and surface wave equations. *Journal of Physical Oceanography*, 33(9):1978–1989, 2003.

[74] George Mellor. Some consequences of the three-dimensional current and surface wave equations. *Journal of Physical Oceanography*, 35(11):2291–2298, 2005.

[75] George L Mellor, Mark A Donelan, and Lie-Yauw Oey. A surface wave model for coupling with numerical ocean circulation models. *Journal of Atmospheric and Oceanic Technology*, 25(10):1785–1807, 2008.

[76] IA Milne, AH Day, RN Sharma, and RGJ Flay. Blade loads on tidal turbines in planar oscillatory flow. *Ocean Engineering*, 60:163–174, 2013.

[77] Benjamin D Moate, Peter D Thorne, and Richard D Cooke. Field deployment and evaluation of a prototype autonomous two dimensional acoustic backscatter instrument: The bedform and suspended sediment imager (bassi). *Continental Shelf Research*, 112:78–91, 2016.

[78] Amir Teymour Javaherchi Mozafari. Numerical modeling of tidal turbines: Methodology development and potential physical environmental effects. Master's thesis, Mechanical Engineering, University of Washington, 2010.

[79] Paul Mycek, Benoît Gaurier, Grégory Germain, Grégory Pinon, and Elie Rivoalen. Experimental study of the turbulence intensity effects on marine current turbines behaviour. part i: One single turbine. *Renewable Energy*, 66:729–746, 2014.

[80] LE Myers and AS Bahaj. Experimental analysis of the flow field around horizontal axis tidal turbines by use of scale mesh disk rotor simulators. *Ocean Engineering*, 37(2):218–227, 2010.

[81] LE Myers and AS Bahaj. An experimental investigation simulating flow effects in first generation marine current energy converter arrays. *Renewable Energy*, 37(1):28–36, 2012.

[82] Luke Myers, AS Bahaj, Gregory Germain, and Jack Giles. Flow boundary interaction effects for marine current energy conversion devices. In *Proceedings of the World Renewable Energy Congress (WREC X), Glasgow, UK*, 2008.

[83] E Nap and A Van Kampen. Sediment transport in irregular non-breaking waves. *Coastal Engineering Department, Delft University of Technology, Delft, The Netherlands*, 1988.

[84] Simon P Neill, James R Jordan, and Scott J Couch. Impact of tidal energy converter (tec) arrays on the dynamics of headland sand banks. *Renewable Energy*, 37(1):387–397, 2012.

[85] Simon P Neill, Emmer J Litt, Scott J Couch, and Alan G Davies. The impact of tidal stream turbines on large-scale sediment dynamics. *Renewable Energy*, 34(12):2803–2812, 2009.

[86] Peter Nielsen. *Coastal bottom boundary layers and sediment transport*, volume 4. World scientific, 1992.

[87] Maitane Olabarrieta, Raul Medina, and Sonia Castanedo. Effects of wave–current interaction on the current profile. *Coastal Engineering*, 57(7):643–655, 2010.

[88] Alex Olczak, Tim Stallard, and Peter Stansby. Tidal turbine wake recovery due to turbulent flow and opposing waves. In *Proceedings of the 2nd Oxford tidal energy workshop*, 2013.

[89] RD Pingree and DK Griffiths. Sand transport paths around the british isles resulting from m 2 and m 4 tidal interactions. *Journal of the Marine Biological Association of the United Kingdom*, 59(02):497–513, 1979.

[90] Andrey Pleskachevsky, Dieter P Eppel, and Hartmut Kapitza. Interaction of waves, currents and tides, and wave-energy impact on the beach area of sylt island. *Ocean Dynamics*, 59(3):451–461, 2009.

[91] David R Plew and Craig L Stevens. Numerical modelling of the effect of turbines on currents in a tidal channel–tory channel, new zealand. *Renewable Energy*, 57:269–282, 2013.

[92] Sheerin PM Sforza and M Smorto. Three-dimensional wakes of simulated wind turbines. *AIAA Journal*, 19(9):1101–1107, 1981.

[93] Power, Verdant. Roosevelt Island Tidal Energy (RITE) environmental assessment project. Final Report. NYSERDA Report 11-04. Prepared for the New York State Energy Research and Development Authority, 2011.

[94] KG Rados, JM Prospathopoulos, N Ch Stefanatos, ES Politis, PK Chaviaropoulos, and A Zervos. CFD modeling issues of wind turbine wakes under stable atmospheric conditions. In *European wind energy conference and exhibition proceedings, Parc Chanot, Marseille, France*, pages 16–19, 2009.

[95] Rafael Ramirez Mendoza, Laurent Amoudry, Peter Thorne, Richard Cooke, Stephen Simmons, Stuart McLelland, Brendan Murphy, Daniel Parsons, Laura-Beth Jordan, and Lada Vybulkova. Impact of scaled tidal stream turbine over mobile sediment beds. In *Proceedings of the 11th European Wave and Tidal Energy Conference, Nantes, France*, 2015.

[96] V Ramos, R Carballo, M Sanchez, M Veigas, and G Iglesias. Tidal stream energy impacts on estuarine circulation. *Energy Conversion and Management*, 80:137–149, 2014.

[97] MR Raupach and RH Shaw. Averaging procedures for flow within vegetation canopies. *Boundary-Layer Meteorology*, 22(1):79–90, 1982.

[98] Pierre-Elouan Mikael Rethore, Niels N Sørensen, Andreas Bechmann, and Frederik Zahle. Study of the atmospheric wake turbulence of a CFD actuator disc model. In *European wind energy conference and exhibition proceedings, Parc Chanot, Marseille, France*, 2009.

[99] Peter E Robins, Simon P Neill, and Matt J Lewis. Impact of tidal-stream arrays in relation to the natural variability of sedimentary processes. *Renewable Energy*, 72:311–321, 2014.

[100] Peter E Robins, Simon P Neill, Matt J Lewis, and Sophie L Ward. Characterising the spatial and temporal variability of the tidal-stream energy resource over the northwest european shelf seas. *Applied Energy*, 147:510–522, 2015.

[101] Thomas Roc, Daniel C Conley, and Deborah Greaves. Methodology for tidal turbine representation in ocean circulation model. *Renewable Energy*, 51:448–464, 2013.

[102] Dano Roelvink and AJHM Reniers. *A guide to modeling coastal morphology.* World Scientific, 2012.

[103] Christophe Sanz. A note on k-ε modelling of vegetation canopy air-flows. *Boundary-Layer Meteorology*, 108(1):191–197, 2003.

[104] Sena Serhadlıoğlu, Thomas AA Adcock, Guy T Houlsby, Scott Draper, and Alistair GL Borthwick. Tidal stream energy resource assessment of the anglesey skerries. *International Journal of Marine Energy*, 3:e98–e111, 2013.

[105] Mark A Shields, Lora Jane Dillon, David K Woolf, and Alex T Ford. Strategic priorities for assessing ecological impacts of marine renewable energy devices in the pentland firth (scotland, uk). *Marine Policy*, 33(4):635–642, 2009.

[106] Michael Shives and Curran Crawford. Adapted two-equation turbulence closures for actuator disk rans simulations of wind & tidal turbine wakes. *Renewable Energy*, 92:273–292, 2016.

[107] SM Simmons, SJ McLelland, DR Parsons, BJ Murphy, LB Jordan, and L Vybulkova. Flume measurements of the wake of two model horizontal-axis tidal stream turbines. In *the 2nd international workshop on Hydraulic Structures, Coimbra, Portugal*, 2015.

[108] Joseph Smagorinsky. General circulation experiments with the primitive equations: I. the basic experiment*. *Monthly weather review*, 91(3):99–164, 1963.

[109] Andrey Sogachev. A note on two-equation closure modelling of canopy flow. *Boundary-layer meteorology*, 130(3):423–435, 2009.

[110] Jens Norkær Sorensen and Wen Zhong Shen. Numerical modeling of wind turbine wakes. *Journal of fluids engineering*, 124(2):393–399, 2002.

[111] Richard Soulsby. *Dynamics of marine sands: a manual for practical applications*. Thomas Telford, 1997.

[112] AH Stride. Sediment transport by the north sea. In *North Sea Science, Aviemore, Scotland*. M.I.T Press, 1973.

[113] Sufian Sufian. *Numerical Modeling of Impacts from Horizontal Axis Tidal Turbines*. PhD thesis, School of Engineering, University of Liverpool, 12 2016.

[114] X Sun, JP Chick, and IG Bryden. Laboratory-scale simulation of energy extraction from tidal currents. *Renewable Energy*, 33(6):1267–1274, 2008.

[115] G Sutherland, M Foreman, and C Garrett. Tidal current energy assessment for Johnstone Strait, Vancouver Island. *Proceedings of the Institution of Mechanical Engineers, Part A: Journal of Power and Energy*, 221(2):147–157, 2007.

[116] SWANTeam. *SWAN Cycle III version 40.51 user manual*. Delft University of Technology, Faculty of Civil Engineering and Geosciences, Environmental Fluid Mechanics Section, 2006.

[117] SC Tedds, Ieuan Owen, and RJ Poole. Near-wake characteristics of a model horizontal axis tidal stream turbine. *Renewable Energy*, 63:222–235, 2014.

[118] The Energy and Climate Change Committee, the House of Commons. The Future of Marine Renewables in the UK, the Eleventh Report of Session 2010-12. Technical report, 2012.

[119] Jérôme Thiébot, Pascal Bailly du Bois, and Sylvain Guillou. Numerical modeling of the effect of tidal stream turbines on the hydrodynamics and the sediment transport–application to the alderney race (raz blanchard), france. *Renewable Energy*, 75:356–365, 2015.

[120] Stephen R Turnock, Alexander B Phillips, Joe Banks, and Rachel Nicholls-Lee. Modelling tidal current turbine wakes using a coupled rans-bemt approach as a tool for analysing power capture of arrays of turbines. *Ocean Engineering*, 38(11):1300–1307, 2011.

[121] RE Uittenbogaard. 1DV simulation of wave current interaction. In *Proceedings of the 27th International Conference on Coastal Engineering*, volume 1, pages 255–268, 2001.

[122] Motohiko Umeyama. Reynolds stresses and velocity distributions in a wave-current coexisting environment. *Journal of waterway, port, coastal, and ocean engineering*, 131(5):203–212, 2005.

[123] LJ Vermeer, Jens Nørkær Sørensen, and A Crespo. Wind turbine wake aerodynamics. *Progress in aerospace sciences*, 39(6):467–510, 2003.

[124] Ian Walkington and Richard Burrows. Modelling tidal stream power potential. *Applied Ocean Research*, 31(4):239–245, 2009.

[125] HR Wallingford. Mersey barrage feasibility study: stage II, Hydraulic and sedimentation study, sand flux measurement. Report EX 2225. Technical report, 1990.

[126] HR Wallingford. Mersey barrage feasibility study: stage IIIA, 3D Mathematical Modelling of Tidal flows and Sedimentation. Technical report, 1992.

[127] John C Warner, Christopher R Sherwood, Richard P Signell, Courtney K Harris, and Hernan G Arango. Development of a three-dimensional, regional, coupled wave, current, and sediment-transport model. *Computers & Geosciences*, 34(10):1284–1306, 2008.

[128] J Whelan, M Thomson, JMR Graham, and J Peiro. Modelling of free surface proximity and wave induced velocities around a horizontal axis tidal stream turbine. In *Proceedings of the 7th European Wave and Tidal Energy Conference*, 2007.

[129] JI Whelan, JMR Graham, and J Peiro. A free-surface and blockage correction for tidal turbines. *Journal of Fluid Mechanics*, 624:281–291, 2009.

[130] JI Whelan, JMR Graham, and J Peiro. Inertia effects on horizontal axis tidal-stream turbines. In *Proceedings of the 8th European Wave and Tidal Energy Conference*, 2009.

[131] Patricia L Wiberg and Courtney K Harris. Ripple geometry in wave-dominated environments. *Journal of Geophysical Research: Oceans (1978–2012)*, 99(C1):775–789, 1994.

[132] Patricia L Wiberg and David M Rubin. Bed roughness produced by saltating sediment. *Journal of Geophysical Research: Oceans (1978–2012)*, 94(C4):5011–5016, 1989.

[133] B Wilson, RS Batty, F Daunt, and C Carter. Collision risks between marine renewable energy devices and mammals, fish and diving birds: Report to the Scottish Executive. 2006.

[134] J Wolf and D Prandle. Some observations of wave–current interaction. *Coastal Engineering*, 37(3):471–485, 1999.

[135] Yongsheng Wu, Jason Chaffey, David A Greenberg, Keir Colbo, and Peter C Smith. Tidally-induced sediment transport patterns in the upper bay of fundy: a numerical study. *Continental Shelf Research*, 31(19):2041–2053, 2011.

[136] Zhaoqing Yang, Taiping Wang, and Andrea E Copping. Modeling tidal stream energy extraction and its effects on transport processes in a tidal channel and bay system using a three-dimensional coastal ocean model. *Renewable Energy*, 50:605–613, 2013.

[137] Laith AJ Zori and R Ganesh Rajagopalan. Navier-Stokes calculations of rotor-airframe interaction in forward flight. *Journal of the American Helicopter Society*, 40(2):57–67, 1995.

Appendix A

Nomenclature

$\%_{RMSE}$ % Root Mean Square Error

δ_{wc} The wave boundary layer thickness

ϵ The phase difference

η_r The ripple height

κ The von Karman constant

λ_r The ripple wavelength

ν The kinematic viscosity

ω The wave frequency

ω_e The effectivewave frequency

ω_r The angular wave frequency

ρ_0 The density of water

ρ_s The density of sediment particles

σ The relative frequency

τ_0 The shear stress experienced by sediment particles

τ_b The bottom shear stress

τ_r The additional bottom shear stress caused by the rotation of the turbine

τ_{bt} The total bottom shear stress

τ_{bx} The bottom stress in the x direction

τ_{by} The bottom stress in the y direction

τ_{ce} The critical erosion stress

τ_{ci} The critical shear stress of the ith sediment class

τ_{cw} The maximum wave-current combined bottom shear stress

τ_c The current component of the maximum wave-current combined bottom shear stress

τ_{sx} The surface wind stress in the x direction

τ_{sy} The surface wind stress in the y direction

τ_w The wave component of the maximum wave-current combined bottom shear stress

θ The wave direction

θ_c The critical Shields parameter

$\tilde{W}$ The wall proximity function

ε The turbulent kinetic energy dissipation rate

$\vec{C}_g$ The group velocity vector

$\vec{V}$ The ambient water current vector

$\vec{V}$ The flow velocity vector

ζ The height of the free surface

A The wave amplitude

A_H The horizontal eddy viscosity

B_1 A model coefficient $B_1 = 16.60$

c The wave speed

C_σ The wave propagation velocity in frequency space

C_θ The wave propagation velocity in directional space

C_d The drag coefficient

C_i The concentration of the ith sediment class

C_r A coefficient analogue to the drag coefficient

C_{ext} The energy extraction coefficient

$c_{L,D}$ The lift/drag coefficient

C_l The coefficient of term P_l

C_{td} The coefficient of term P_{td}

C_{tp} The coefficient of term P_{tp}

d The diameter of sediment particles

D_i The depositional rate of the ith sediment class

Dir The wave directions

E_1 A model coefficient $E_1 = 1.80$

E_2 A model coefficient $E_2 = 1.33$

E_i The erosion rate of the ith sediment class

f The Coriolis parameter

F_l The horizontal diffusion of the marcroscale

F_q The horizontal diffusion of the turbulent kinetic energy

F_u The horizontal momentum term in the x direction

F_v The horizontal momentum term in the y direction

F_{bi} The fraction of the ith sediment class

$F_{L,D}$ The lift/drag force

g The acceleration due to gravity

H The bottom depth

h The total water column depth

H_s The significant wave height

k The wave number

K_h The vertical eddy viscosity

K_m The vertical eddy viscosity coefficient

K_q The vertical eddy diffusion coefficient of the turbulent kinetic energy

K_t The wave energy transmission coefficient of OBSTACLE

L The average wave length

l The macroscale

N The wave action density spectrum

n The number of records in the validation data

N_b The number of blades

P_a The air pressure at sea surface

P_b The bottom porosity

P_b The buoyancy production terms of turbulent kinetic energy

P_H The hydrostatic pressure

P_s The shear production terms of turbulent kinetic energy

P_l The turbine-induced interference for the turbulence length-scale (l)

P_{td} The turbine-induced turbulence dissipation term

P_{tp} The turbine-induced turbulence generation term

q The non-hydrostatic pressure

q^2 The turbulent kinetic energy

Q_i The erosive flux of the ith sediment class

q_i One record in the validation data

q_{iest} One record in the calculated result

q_{max} The maximum record in the calculated result

q_{min} The minimum record in the calculated result

S_h A stability function

S_m A stability function

S_{tot} The source-sink terms

S_{xx}, S_{yy}, S_{xy}, S_{yx}, S_{px},S_{py} The radiation stress terms

t Time

T_b The bottom wave period

T_p The surface wave relative peak period

u The velocity component in the x direction

u^* The shear velocity

u^*_{cr} The critical shear velocity

U_b The wave bottom orbit velocity

U_r The tip speed of the turbine

u_{*cw} The friction velocity due to combined waves and current

u_{*c} The friction velocity due to current

u_{*w} The friction velocity due to waves

$u_{\tau b}$ The water friction velocity associated with the bottom

$u_{\tau s}$ The water friction velocity associated with the surface

u_{br} The wave-orbital velocity amplitude outside the wave boundary layer

u_{cr} The current velocity at a reference elevation

v The velocity component in the y direction

w The velocity component in the z direction

w_i The settling velocity of the ith sediment class

x The east axis in the Cartesian coordinate system

y The north axis in the Cartesian coordinate system

z The vertical axis in the Cartesian coordinate system

z_0 The bottom roughness parameter

z_r The refernce elevation

z_{0BF} The roughness length associated with bedform

z_{0N} The roughness length associated with grain roughness

z_{0ST} The roughness length associated with sediment transport

z_{ab} The reference hight

CFD Computational Fluid Dynamics

D The diameter of turbine

EMEC European Marine Energy Centre

FVCOM Finite Volume Coastal Ocean Model

HATT Horizontal Axis Tidal Turbine

RITE Roosevelt Island Tidal Energy

SWAN Simulating Waves Nearshore

TEC Tidal Energy Converter

TKE Turbulent Kinetic Energy

TSR Tip Speed Ratio

VATT Vertical Axis Tidal Turbine

VOF The Volume of Fluid method

WBL The wave boundary layer

Appendix B

Publications

X. Li, M. Li, X. Chen, P.D. Thorne. (2014). 3D numerical modelling of large scale impact of tidal turbine arrays using an oceanographic model. In *Proceedings of the 34th International Conference on Coastal Engineering*, 1(34), 31.

X. Li, M. Li, S. J. McLelland, L. B. Jordan, L. O. Amoudry, R Ramírez-Mendoza, P. D. Thorne. <Modelling tidal stream turbines in a three-dimensional wave-current fully coupled oceanographic model>. <*Renewable Energy*> (2017), http://dx.doi.org/10.1016/j.renene.2017.02.033.